Dipole Orientation Induced Effects
in
Dipolar Bose-Einstein Condensates

A thesis
submitted in partial fulfillment of the requirement of the degree of
Doctor of Philosophy
in Physics by

Chinmayee Mishra

Registration number: 20143351

IISER PUNE

Department of Physics

Indian Institute of Science Education and Research

Pune 411 008, India

2020

CERTIFICATE

Certified that the work entitled in the thesis entitled "Dipole Orientation Induced Effects in Dipolar Bose-Einstein Condensates" submitted by Chinmayee Mishra was carried out by the candidate, under my supervision. The work presented here or any part of it has not been included in any other thesis submitted previously for the award of any degree or diploma from any other university or institution.

Date: 20 March, 2020

Dr Rejish Nath

(supervisor)

DECLARATION

I declare that the written submission represents my ideas in my own words and where others ideas have been included, I have adequately cited and referred original sources. I also declare that I have adhered to all principles of academic honesty and integrity and have not misrepresented or fabricated or falsified any idea/data/fact/source in my submission. I understand that violation of the above will be cause for disciplinary action by the institute and can also evoke penal action from the sources which have thus not been properly cited or from whom proper permission has not been taken when needed. The work presented in this thesis was done under the guidance of Dr. Rejish Nath at the Indian Institute of Science Education and Research, Pune.

Date : 19 March, 2020

Dr Chinmayee Mishra

(Reg: 20143351)

Dedicated to Bou and Baba

"If I have seen further it is by standing on the shoulders of Giants"
-Isaac Newton, in his letter to Robert Hooke.

Acknowledgements

The years spent in completing the work in this thesis, unquestionably, have changed my life. I owe my gratitude to many people for their help and support. First, I'd like to thank my supervisor, Dr Rejish Nath for his guidance and introducing me to atomic Bose-Einstein condensates. He has been patient through many of my blunders and helped me improve. As the first PhD student in the group, I had the unique opportunity to exploit the maximum of his time and it has been an unforgettable roller coaster ride.

I would like to thank Prof. Luis Santos, who I had the opportunity to collaborate with on multiple projects. His suggestions have been valuable and his enthusiasm for research is contagious. I am extremely grateful towards him for providing me the opportunity to visit ITP, Leibniz University, Hanover and work in his group for three months. I thank my collaborators Dr Kazimierz Łakomy and Dr Subhashis Sinha as well for their contributions.

I thank my Research Advisory Committee (RAC) members, Dr Umakant Rapol and Dr. Sachin Jain for their timely discussions and advice.

I owe gratitude to Department of Science and Technology(DST) for the INSPIRE fellowship during my PhD. I would also like to extend my gratitude to DST for supporting me during my B.Sc. and M.Sc. through INSPIRE scholarship. I thank Leibniz University for funding my visit to ITP, Leibniz University, Hanover for three months.

IISER Pune has a special place in my heart. It has funded me in my first year, provided me accommodation during my PhD and also given me occasional travel support. I thank the former and current Physics Chair for promoting a healthy research environment. The staff in Physics office (Prabhakar Sir, Dhanashree Ma'am) and the administrative department (Tushar Sir, Sayali Ma'am) have the helped official work go smoother.

My group members have been my surrogate family in IISER Pune. Yashwant is the most hard working bee of our group. He has always been passionate, although sometimes bordering on bullheadedness, about whatever he puts his mind to. Having shared an office space with him for the longest period, I have benefited from our discussions on Physics, argued about philosophy, shared laughs on memes and been subjected to an overdose of Joana Ceddia. I am thankful to Ankita for our engaging discussions on research and technical problems. Her unique perspective of looking at a problem has been very helpful. Our early morning and late night movie jaunts and whimsical shopping spree will be

List of Publications

Included in the thesis

- Meghana Raghunandan, **Chinmayee Mishra**, Kazimierz Łakomy, Paolo Pedri, Luis Santos, and Rejish Nath, Two-dimensional bright solitons in dipolar Bose-Einstein condensates with tilted dipoles, Phys. Rev. A **92**, 013637 (2015) https://link.aps.org/doi/10.1103/PhysRevA.92.013637

- **Chinmayee Mishra** and Rejish Nath, Dipolar condensates with tilted dipoles in a pancake-shaped confinement, Phys. Rev. A **94**, 033633 (2016) https://link.aps.org/doi/10.1103/PhysRevA.94.033633

- **Chinmayee Mishra**, Luis Santos, and Rejish Nath, Self-Bound Doubly Dipolar Bose-Einstein Condensates, Phys. Rev. Lett. **124**, 073402 (2020) https://link.aps.org/doi/10.1103/PhysRevLett.124.073402

- **Chinmayee Mishra**, and Rejish Nath, Periodically Driven Quasi-1D Dipolar Bose-Einstein Condensates, *Manuscript under preparation*

Not included in the thesis

- Daniel Edler, **Chinmayee Mishra**, Falk Wächtler, Rejish Nath, Subhashis Sinha, and Luis Santos, Quantum Fluctuations in Quasi-One-Dimensional Dipolar Bose-Einstein Condensates, Phys. Rev. Lett. **119**, 050403 (2017) https://link.aps.org/doi/10.1103/PhysRevLett.119.050403

Abstract

Ultracold quantum gases have thrived as an interdisciplinary field of condensed matter physics, quantum optics, atomic and molecular physics. It boasts set-ups with precisely controllable and highly tuneable interaction parameters. Research in this area has sparked after the realisation of Bose-Einstein condensation in alkali atoms in 1995. The goal is to continuously seek quantum gas systems where more and more complex interactions may be embedded. Bose-Einstein condensation were, later, achieved in atoms like Cr, Er, and Dy which have significant dipole moments, bringing anisotropic interactions to the quantum gas systems. In the last 15 years, dipolar Bose-Einstein condensates have consistently been found at the forefront of ultracold atomic research.

Our goal is to explore the tunability of the dipole-dipole interaction. The simplest way is via an external field which can easily tune the polarisation direction of the dipole moment. Effectively it tunes the dipole-dipole interaction between the atoms, potentially from repulsive to attractive. The effect of this on the collective behaviour of dipolar Bose-Einstein condensates are dramatic. Below our findings have been outlined for reference.

We begin by reviewing the advent of the theory of Bose gas and the general short-range two-body interactions in Chapter 1. We introduce dipolar interactions and prescribe the available methods for tuning these interactions. Theoretically these systems are addressed using mean-field theory. We list the conditions under which mean-field theory is applicable and show a glimpse of beyond the mean-field theory, which becomes crucial in the final chapter.

In Chapter 2, we review the stability of both homogeneous and trapped Bose-Einstein condensates by studying the elementary excitations in the system. The theoretical methodologies for calculating Bogoliubov excitations and the low-lying modes of the condensates have been explained along with important discoveries from the experimental counterpart. The last section in Chapter 2 contains the theory of parametric modulation, a technique that has become widely popular in ultracold systems due to availability of precise tuning of interactions parameters.

In Chapter 3, the effect of tilting of dipole moment have been explored in dipolar Bose-Einstein condensates in the quasi-2D. We emphasize on the effect of trapping geometry on the stability followed by characterizing various stable and unstable domains with the help of phase diagrams in experimentally relevant parameter space. Post instability

dynamics under different instabilities reveal markedly different features, capturing the essence of anisotropic nature of dipole-dipole interactions. Anisotropic solitons, new kind of self-trapped solutions and their respective stabilities have been analysed in detail and succinctly put as a phase diagram. In the end, we propose experimental preparation of the so far elusive quasi-2D soliton via adiabatic tuning of tilting of dipole moment.

Chapter 4 consists of an ongoing work on dipolar Bose-Einstein condensation in quasi-1D. We consider multiple cigar-shaped condensates under parametric modulation. Consequently, some non-intuitive yet interesting phenomena have come to light. In homogeneous systems, we show emergence and transfer of Faraday patterns from layer to layer when only one layer is modulated. The selection of pattern relies on the Bogoliubov spectrum, which can be changed dramatically by tuning the dipole moment. We also show the transfer of mode-locking phenomenon in trapped bilayer condensates. Interestingly, this excitation transfer may be enhanced or suppressed again by tuning the dipole moment polarisation direction. We also find that the center of mass motion and the widths oscillations in multilayer dipolar systems are coupled, giving rise to energy transfer between them as well.

In the final chapter, we introduce doubly-dipolar BECs with purely 3D calculations. The system has magnetic and electric dipole-dipole interaction and the polarisation angle between the two dipole moments is now the most important tuneable parameter. In the context of beyond-mean-field effects, we show the presence of self-bound droplet solutions in doubly-dipolar BECs. Most interestingly, the droplet is shown to undergo a shape transition from the traditional cigar-shaped to a new pancake-shape by tuning the polarisation angle. Further we prove that not only a structural transition, but also it is a dimensional crossover instigated purely by internal interactions in the absence of any external trapping geometry.

This thesis is a detailed work on the effects of tilting angle of the dipole moment in dipolar BECs in quasi-2D, quasi-1D and 3D geometries. We present the stability analysis and instability dynamics and consequent emergence of some novel solutions. Recent experimental results in tuning the strength of dipole-dipole interaction as well as the polarisation angle will provide a much necessary boost for future explorations of this topic.

Symbols & Abbreviations

Physical constants

$\hbar \rightarrow$ Planck's constant

$k_B \rightarrow$ Boltzmann constant

$\mu_0 \rightarrow$ Vacuum permeability

$\epsilon_0 \rightarrow$ Vacuum permittivity

Abbreviations

BEC $\rightarrow$ Bose-Einstein condensate

DDI $\rightarrow$ Dipole-dipole interaction

ODLRO $\rightarrow$ Off-diagonal long-range order

GPE $\rightarrow$ Gross-Pitaevskii equation

DS $\rightarrow$ Dark soliton

LHY correction $\rightarrow$ Lee-Huang-Yang correction

eGPE$\rightarrow$ Extedned Gross-Pitaevskii equation

BdG$\rightarrow$ Bogoliubov-de Gennes

Q2D$\rightarrow$ Quasi Two Dimension

Q1D$\rightarrow$ Quasi One Dimension

EI$\rightarrow$ Expansion instability

CI$\rightarrow$ Collapse instability

DDDI$\rightarrow$ Doubly dipole-dipole interaction

DDBEC$\rightarrow$ Doubly dipolar Bose-Einstein condensate

EDM$\rightarrow$ Electric dipole moment

MDM$\rightarrow$ Magnetic dipole moment

Contents

List of Figures

Chapter 1

Bose-Einstein Condensation

Quantum physics has established itself as the backbone of modern science for decades now. It has become an indispensable tool in the fundamental understanding of condensed matter physics, atomic and molecular physics, nuclear and particle physics, chemistry and information science at microscopic scales. Researchers are in pursuit of pushing the boundaries of these fields whose potential applications span from computers to sensors, metrology, electronics, and cryptography etc. But the behaviour of matters in quantum realm are fundamentally different from their classical counterparts, especially in presence of many particles who interact with each other. The most popular manifestations of such quantum many-body effects are superconductivity and superfluidity. They emerge as a macroscopic collective phenomena from the constituent microscopic entities. Understanding or capturing the accurate description of quantum many-body systems has proven to be a challenge, both theoretically and in a lab. Theoretically, one of the apparent problems stems from difficulty in modeling the huge number of degrees of freedom. Another difficulty pertains to the inherent nonlinearities in the systems which is a byproduct of interparticle interactions. Experimental complexities include lack of precise control mechanisms and constructing idealized systems for fundamental analysis.

A triumph came in the form of dramatic developments in cooling and trapping of atoms in the 1980s. While it is next to impossible to address atoms individually in solids and liquids, in ultracold temperature regime, people were able to observe single atomic energy transitions for the first time. Halting the thermal motion of atoms ultimately enabled ultracold atoms as the 'quantum simulators' of many-body physics. At ultracold temperature the atoms and their mutual interactions can be controlled as never before. It was possible to mimic systems from solid state physics or even cosmology because they all have the common factor i.e. interacting bodies.

Ultracold quantum gases have come up as the fundamental testing bed for studying quantum matter. At nanokelvin temperatures precise tunability of interatomic interaction can be achieved. After experimental realisation of long predicted Bose-Einstein condensation, the fifth state of matter, the field has come a long way in last couple of decades
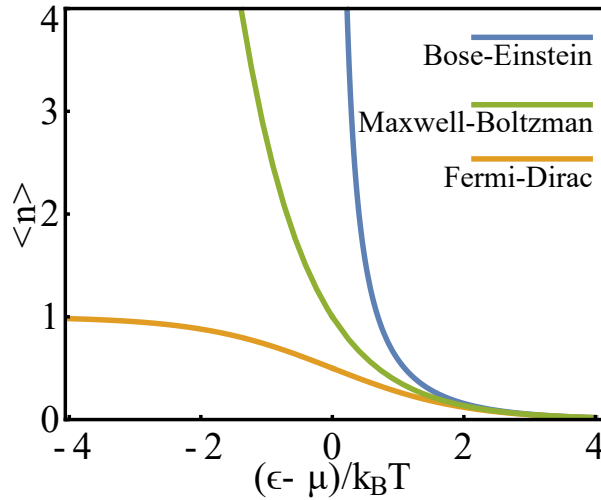
Figure 1.1: Average occupancy under three different statistics. As $\mu \to \epsilon$ the Bose-Einstein statistics shows that the occupancy blows up while Fermi-Dirac statistics shows a maximum occupancy of 1 owing to the Pauli's exclusion principle.

and found its niche at the intersection of condensed matter physics, quantum optics, atomic and molecular physics. Here, we expand upon the fundamentals of Bose-Einstein condensation, starting from the ideal bose gas.

1.1 Ideal Bose gas

Transition of ice to water and then to steam are the common occurrences of phase transitions that all of us witness in our daily lives. These are typical thermodynamic transitions between the widely known states of matter. In rare occasions a transition to plasma can also be observed. Still, there exists a fifth state of matter, first proposed in an ensemble of non-interacting particles. A phase transition to the fifth state of matter was first theorized by Einstein [1] using the Bose statistics for indistinguishable bosons, proposed by S.N. Bose, in 1924 [2]. It predicts the condensation of a non-interacting Bose gas to a single quantum state under extremely cold temperatures. Multiple bosons, unlike fermions that follow Fermi-Dirac statistics, can occupy a single quantum state and the average occupation number of bosons with energy ϵ is [3, 4],

$$\langle n \rangle = f(\epsilon_p) = \frac{1}{e^{\frac{\epsilon - \mu}{k_B T}} - 1} \tag{1.1}$$

where μ is the chemical potential, the energy required to add one particle to system. It should be noted that for (1.1) to be physically meaningful μ must take negative values with zero being the maximum if $\epsilon_{min} = 0$. The total number of particle is $N = \sum_\epsilon \langle n \rangle$. But in thermodynamic limit $N \to \infty$ and volume $V \to \infty$ such that $N/V = $ constant, we

convert the sum to an integral as follows,

$$n = \frac{N}{V} = \frac{1}{V} \sum_{\epsilon} f(\epsilon) = \int_0^{\infty} d\epsilon f(\epsilon) g(\epsilon) \tag{1.2}$$

where $\epsilon = \frac{p^2}{2m}$ and $g(\epsilon)$ is the density of states of a 3D homogeneous distribution $g(\epsilon) = \frac{V}{4\pi^2} \left(\frac{2m}{\hbar^2} \right)^{\frac{3}{2}} \sqrt{\epsilon}$. Replacing appropriately we obtain the following expression for the constant density,

$$n = \frac{1}{4\pi^2} \left(\frac{2m}{\hbar^2} \right)^{\frac{3}{2}} \int_0^{\infty} d\epsilon \frac{\sqrt{\epsilon}}{e^{\frac{\epsilon - \mu}{k_B T}} - 1} \tag{1.3}$$

The way to increase n would be to increase the chemical potential, but the chemical potential has an upper bound as already mentioned. In the limit $\mu \to 0 (\epsilon_{min} = 0)$, we have,

$$
\begin{aligned}
n_{\mu \to 0} = n_c &= \frac{1}{4\pi^2} \left(\frac{2m}{\hbar^2} \right)^{\frac{3}{2}} \int_0^{\infty} d\epsilon \frac{\sqrt{\epsilon}}{e^{\frac{\epsilon}{k_B T}} - 1} \\
&= \frac{1}{4\pi^2} \left(\frac{2m k_B T}{\hbar^2} \right)^{\frac{3}{2}} \zeta \left(\frac{3}{2} \right) \Gamma \left(\frac{3}{2} \right)
\end{aligned}
\tag{1.4}
$$

where, $\zeta(\frac{3}{2}) = \sum_{n=1}^{\infty} n^{-\frac{3}{2}}$, $\Gamma(\frac{3}{2}) = \int_0^{\infty} dx e^{-x} \sqrt{x}$. The interpretation is, at constant temperature the density continues to remain constant even if more number of bosons are added to the system. This conundrum is a result of the conversion of discrete sum to a continuous integral without addressing the singular case of $\epsilon_{min} = 0$ individually, in which case the integrand blows up. This is easily fixed by separating the lowest energy state before taking the limit $\mu \to 0$.

$$
\begin{aligned}
n &= n_0 + n_{\text{exc}} \\
\implies n_{\mu \to 0} &= \lim_{\mu \to 0} \frac{1}{V} \frac{1}{e^{-\frac{\mu}{k_B T}} - 1} + n_c
\end{aligned}
\tag{1.5}
$$

The first term accommodates infinite number of bosons even though n_c is capped or in other words all the extra bosons added will accumulate in the ground state. Such a macroscopic occupation of bosons in a single state is called the Bose-Einstein condensation(BEC). For a fixed density, the critical temperature may be obtained by further simplifying (1.4),

$$n_c \approx 2.612 \frac{1}{\lambda_{T_c}^3} \tag{1.6}$$

where, $\lambda_{T_c} = \sqrt{\frac{2\pi\hbar^2}{m k_B T_c}}$. For temperature $T << T_c$ almost all particles are in the ground state i.e. $N_0 >> N_{\text{excited}}$ and theoretically at $T = 0$, $N = N_0$. Following (1.5) this relation

can be captured in the following equation,

$$\frac{N_0}{N} = 1 - \left(\frac{T}{T_c}\right)^{3/2} \tag{1.7}$$

Until many-body theory was understood, Einstein's prediction survived only as a beautiful academic model. It was a challenge also to find a substance which doesn't liquefy/solidify as temperature decreases in its ground state. This is the reason why BEC was initially probed in Hydrogen atoms [5] for a long time which remained weakly interacting during cooling processes. After rapid development in cooling techniques [6] in the 70s and 80s, it became possible to cool the atoms too fast for them to reach the true ground state(a solid state) and instead simply slow them down to a meta-stable condensate state. Using dilute gas ($\sim 10^{14}$ cm^{-3}), which is much less than both solid ($\sim 10^{23}$ cm^{-3}) or air ($\sim 10^{19}$ cm^{-3}) density, life times achieved are up to the order of seconds. In 1995 dilute gases of the alkali elements rubidium [7], sodium [8], and lithium [9] were condensed in lab for the first time for which 2001 Nobel prize was awarded.

1.2 Two-body interactions

While a thermal gas can be often well approximated to an ideal gas, in conditions of high pressure or low temperature the interaction between particles can no more be neglected. Under ultracold temperature condition, the ideal gas picture of BEC falls short and it becomes important to understand the interactions inherent in the system, which govern the fundamental properties of a BEC [10, 11]. The interaction properties are understood from the scattering of two atoms, specifically the corresponding scattering length for low energy scattering processes. Generally, the inter particle separation is much larger than the scattering length which determines the strength of the interaction. The diluteness ensures that the relevant scattering processes are always two-body in nature and a theoretical study using scattering theory is feasible. Below a brief introduction has been given to the two types of interactions: short-range interactions and long-range interactions. The short-range interaction can be replaced by a zero-range potential and the long-range part is separately dealt with.

1.2.1 Contact interaction

We shall first review the short-range interaction case where the interaction potential is $U(r) \sim \frac{1}{r^n}$ for any $n > 3$. Consider the simple case of elastic collision of two particles [11–13]. In relative mass coordinate, the wave function in far-field may be written as,

$$\psi(\mathbf{r}) = e^{i\mathbf{k}\cdot\mathbf{z}} + \frac{e^{i\mathbf{k}\cdot\mathbf{r}}}{r} f_k(\theta) \tag{1.8}$$
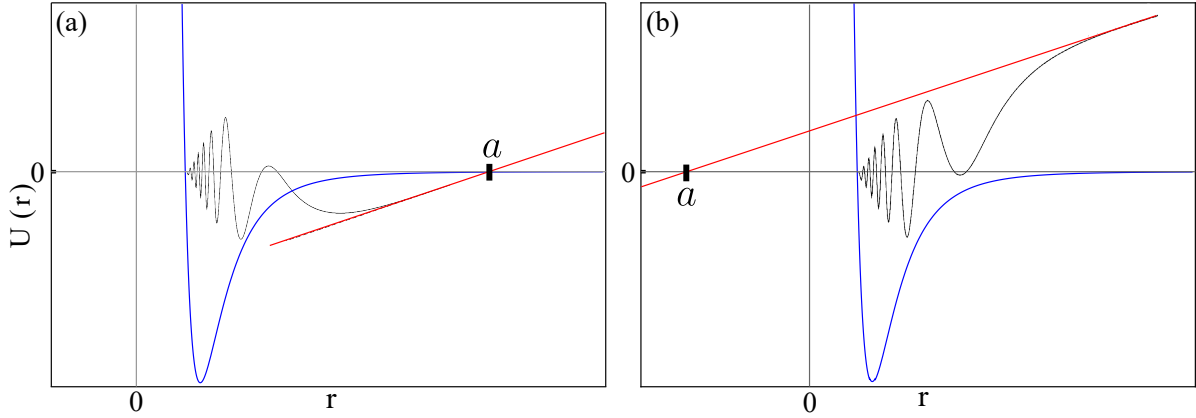
Figure 1.2: Typical shape of the interaction potential between two atoms, as function of the inter-atomic distance r. When $r \to 0$ the coulomb repulsion dominates and as r increases it becomes attractive due to presence of exchange interaction and supports bound states as its global ground state. Farther away, weak attraction prevails due to van-der Waals interaction $\propto -1/r^6$. But the diluteness condition and strategic cooling prevents formation of molecular ground state and ensures the gas is in a long-lived metastable BEC state [4]. a represents the scattering length, which is obtained by extrapolating the asymptotic wave function backwards which can be either positive (a) or negative(b).

It is assumed that the interaction potential is spherically symmetric with finite range, the internal degrees of freedom of the particle are frozen and only a single scattering channel is available. The first term is the incoming plane wave along the z direction. The second term represents an outgoing spherical wave with wave vector k. $f_k(\theta)$ is the scattering amplitude independent of r,

$$f_k(\theta) \;=\; -\frac{m_{red}}{2\pi\hbar^2} \int d^3\mathbf{r}' e^{-ik\mathbf{n}.\mathbf{r}} U(\mathbf{r}')\psi(\mathbf{r}') \tag{1.9}$$

where m_{red} is the reduced mass and $\mathbf{n}$ is the direction of scattering. The actual form of the potential $U(r)$ consists of the van der Waals potential and considers the details of the structure of the atom. This makes solving for $\psi(r)$ extremely nontrivial. In fact the most relevant information on $U(r)$ is obtained by measuring the scattering length in laboratory in ultracold temperature. This complex potential cannot be treated using Born approximation either as it supports many bound states. Instead it is ideal to use a model potential which reproduces the same scattering amplitude for the sparsely dense BEC. Such a model potential is known as pseudo-potential. Owing to low energy scattering we can work in the limit $k \to 0$ and only the s-wave scattering term contributes. Using intuitive calculations, we can write the relative velocity v of colliding particles in terms of de-Broglie wavelength λ of the individual atoms. Following this the angular momenta involved in the collision, $\hbar l = m_{red}vr = \frac{hr}{\lambda}$. Since r/λ is quite small i.e. the atomic wave lengths are spread much wider than inter-atomic separation and also the quantum

number l must take integer values, logically we obtain, $l(< \frac{2\pi r}{\lambda}) = 0$. Implementation in calculation simplifies the scattering amplitude to a constant value $-a$ and the wave function becomes,

$$\psi = 1 - \frac{a}{r} \tag{1.10}$$

a is the scattering length which is determined by the form of the interaction potential. But once a is known, the details of the interaction potential becomes irrelevant. It is easier to use a form of pseudo-potential which gives the same value of scattering length at low energy and can be treated using Born approximation. The simplest potential satisfying the above requirements [14],

$$U(r)\psi(r) = g\delta(r)\frac{\partial}{\partial r}[r\psi(r)] \tag{1.11}$$

where the short-range coupling strength or the contact interaction strength $(m = 2m_{red})$,

$$g = \frac{4\pi\hbar^2 a}{m} \tag{1.12}$$

The pseudo-potential has a Dirac delta function and a regularization operator. The regularization operator has no effect when $r \to 0$ and the pseudopotential merely becomes $g\delta(r)$. However, if the wave function has a form with $1/r$ divergence the regularization operator removes this divergence $\frac{\partial}{\partial r}\left(r \cdot \frac{A}{r}\right) = 0$. This kind of divergence is a result of zero-range pseudopotential. Replacing (1.11) in (1.8) we may now obtain,

$$\psi(\mathbf{r}) = e^{i\mathbf{k}\cdot\mathbf{z}} - \frac{a}{1 + ika}\frac{e^{i\mathbf{k}\cdot\mathbf{r}}}{r} \tag{1.13}$$

From here, it is clear that we must always satisfy the condition $|ka| << 1$ for the Dirac delta pseudo-potential to faithfully explain the physical observations in the system. This approach is a valuable asset when mean-field approximation is used to describe the system later in this thesis.

1.2.2 Tuning contact interaction

One of the biggest cause of the success of ultracold atomic research lies in the extraordinary amount of control the systems have to offer. In case of atomic BEC, it is the ability to tune the atom-atom interaction with great precision and steer the system into desired parametric regimes. This includes even flipping the interactions from strongly repulsive to strongly attractive and it has allowed the ultracold systems to be testing beds for many condensed matter phenomena as well. Below we briefly go through the procedure to tune the contact interaction.

Controlling the strength of the short-range contact interaction is done via an experimental tool called the Feshbach resonance which was first theoretically predicted in 1976 [15] and experimentally verified later in 1998 [16, 17]. A Feshbach resonance occurs when a bound state in the closed channel is coupled to the scattering state in the open channel in a scattering process as shown in Fig. 1.4(a). This coupling alters the scattering in the open channel significantly and the scattering length. This in turn changes the strength of short-range interaction ranging from positive(repulsive) to negative(attractive) values.

A scattering channel is connection between the initial and final internal states in a scattering process. An open channel is energetically favored while closed channels are those that are not. Considering two molecular potentials of two atom collision as shown in Fig. 1.4(a). If two atoms in an open channel can resonantly couple with a bound state of a closed channel, given that the energy of the bound state is close to the energy of the incident energy. An externally applied magnetic field is used to tune the energy of the bound state if the channels have different magnetic moments. Since the asymptotic behaviour of the collision is quite sensitive to this resonance the scattering length thus become a function of the applied magnetic field. The relation for such magnetic resonance is [18],

$$a(B) = a_{bg} \left(1 - \frac{\Delta}{B - B_0} \right) \tag{1.14}$$

where, a_{bg} is the background scattering length, Δ is the resonance width and B_0 is the magnetic field when the energies of the bound state and the incident energy match. In Fig. 1.4(b) the behaviour of the above relation is shown.

The magnetic Feshbach resonances are distinct for each species, thus it is limited by their spatial modulation. However, there have been alternate proposals for couplings other than magnetic in nature for modification of scattering lengths. The coupling schemes include external radio-frequency fields [19], static electric fields [20] and optical fields [21, 22]. Recently optical Feshbach resonance has been realised via intercombination transition [23], and stimulated Raman coupling [24] etc. Collapse and expansion of Strontium atom BEC has also been achieved using optical Feshbach resonance [25].

1.2.3 Dipole-dipole interaction

Unlike short-range interaction, the long-range dipole-dipole interaction(DDI), which has a $1/r^3$ dependence, cannot be dealt easily using scattering processes as all the partial waves contribute to the scattering process of dipolar particles. Due to the anisotropy angular momentum is also not conserved during the collision process. The DDI potential is given by,

$$V_d(r) = \frac{g_d}{r^3}(1 - 3\cos^2 \theta) \tag{1.15}$$
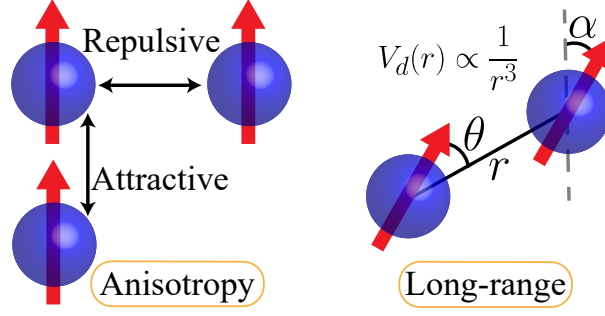
Figure 1.3: The anisotropic and long-range interaction of dipolar atoms. (a) A head-to-tail configuration leads to attractive interaction while side-by-side configuration gives repulsive interaction. In 1.2.4 it is shown that effective strength of interaction can undergo a sign change followed by a flipping of nature of interactions in the above configurations. (b) The $1/r^n$ for $n = 3$ character ensures a long-range nature while in general $n > 3$ is considered short-range in nature.

where the strength of the dipole-dipole interaction $g_d = \frac{\mu_0 d_m^2}{4\pi}\left(\frac{d_e^2}{4\pi\epsilon_0}\right)$ for magnetic(electric) DDI with $d_m(d_e)$ being the magnetic(electric) dipole moment. θ is the angle between the dipole moment and the inter-particle separation $\mathbf{r}$. While the bare short-range potential consists of multiple complicated potentials, the DDI bare potential is simple and the same expression is used for the pseudo-potential of the long-range interaction [26, 27].

At $r = 0$ the DDI potential blows up but in a condensate the likelihood of approaching this regime is small not only because of the diluteness factor but also due to the existence of a strong repulsive Coulomb interaction at extremely short distances, a detail which is accounted for with the help of scattering length described in the previous section. To overcome the issue during theoretical calculations, DDI term is often treated in momentum space with truncation at sufficiently large momenta. Although no scattering length may be attributed to the DDI, a characteristic length maybe associated with it as a method for comparison with its short-range counterpart.

$$a_d = \frac{m g_d}{3\hbar^2} \tag{1.16}$$

This quantity is chosen such that a 3D homogeneous dipolar condensate becomes unstable when $a_d > a$ i.e. the DDI becomes dominant. So, it is useful to work with the ratio between the interaction strengths,

$$\beta = \frac{g_d}{g} = \frac{4\pi a_d}{3a} \tag{1.17}$$

The two most important features of the DDI are 1) Anisotropy and the 2) Long-range nature. Due to this, the dipolar condensates have shown remarkably different and novel features in contrast to a non-dipolar condensate governed by short-range interaction. Not all particles have (sufficient) dipole moment for DDI to be significant. Below we itemize

some relevant ultracold gases with strong dipole moment [28].

BEC was first achieved in alkali atoms and the maximum value of dipole moment in them are $1\mu_B$ which is too weak to observe any dipolar effect, although some effect has been observed in spinor ^{8}7Rb condensate with extremely small scattering lengths [29–31]. Strong dipolar effects were observed 2005 onward after the condensation of Chromium atom [32] which has the magnetic dipole-moment of $6\mu_B$. Since the DDI is proportional to the square of the dipole moment, Cr has 36 times stronger dipolar effect than alkali atoms. Later Er [33] and Dy [34] with magnetic dipole moments $7\mu_b$ and $10\mu_B$ were Bose condensed in the year 2012 and 2011 respectively. So far, study of DDI in dipolar atomic BECs are the most successful.

Polar hetero-nuclear molecules in their low rovibrational states offer extremely strong dipole moments of the order of 1 Debye. A BEC of such molecules would be dominated by DDI. Despite the progress in cooling polar molecules [35, 36], its falls short in comparison with the atomic counterpart. A quantum degenerate state of polar molecules are yet to be achieved as requisite temperature and density still remain a challenge in the lab [37].

A Rydberg atom is an atom with at least one electron excited to very high principal quantum number n.Rydberg excited atoms are another strongly dipolar candidate as the dipole moment scales as n^4. The lifetime of a single Rydberg atom scales as n^{-3}. But a dense cloud of moving Rydberg atoms have a much shorter lifetime than any hydrodynamic timescales. This has resulted in studies such as excitation of Rydberg atoms in BEC and ion-atom interactions [38, 39].

Observation of both magnetic and electric dipole moments simultaneously [40, 41] has been a subject of intense research in recent years. A pair of quasi-degenerate energy levels of opposite parity states available in Dysprosium makes it an ideal candidate [42]. In presence of magnetic field the two energy levels split into their respective Zeeman sub-levels and the atom maybe prepared in the ground state of the lowest Zeeman sub-level. Now in presence of an external electric field, the sub-levels of opposite parities get coupled and an induced electric dipole moment results. The theoretical outcome of such a doubly-dipolar degenerate Bose gas has been probed in detail later.

1.2.4   Tuning the DDI

In case of magnetic atoms, the desired tuning of DDI can also be achieved such that the effective strength of the interaction changes sign from positive to negative values. This is achieved by using a fast rotating external field along with a static polarising field component and taking the time averaged dipole-dipole interaction [44, 45]. We start with a time dependent magnetic field $B(t) = B\cos\phi\hat{k} + B\sin\phi[\cos\Omega t\hat{i} + \sin\Omega t\hat{j}]$ where the rotating frequency Ω satisfies the condition, $\omega_{\text{trap}} < \Omega < \mu B/\hbar$ where $\mu B/\hbar$ represents
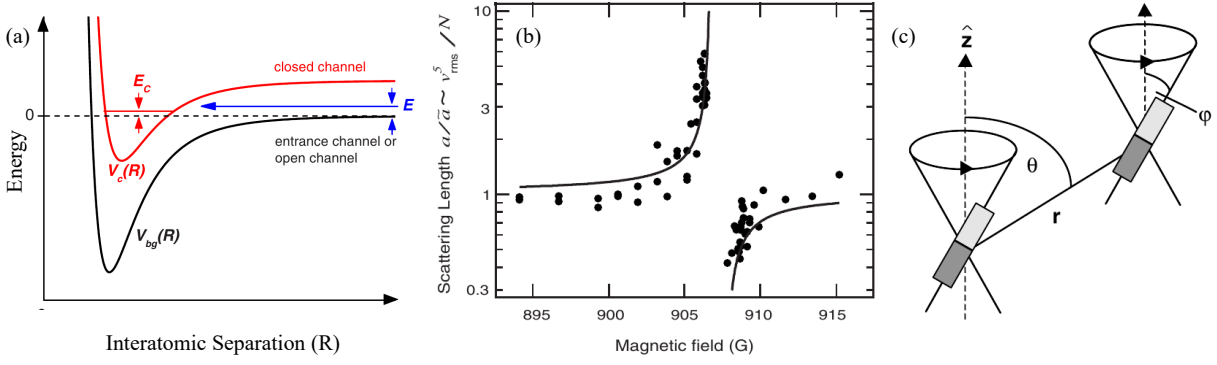
Figure 1.4: (a) A two channel model showing the coupling between an entrance channel of collision energy E and bound state supporting closed channel of energy E_c. This coupling is done with the help of external magnetic field by bringing E_c close to E, which tends to zero in ultracold regime [43]. (b) Observation of a magnetically tuned Feshbach resonance in an optically trapped BEC of Na atoms. It the dispersive shape of the scattering length a near the resonance, as determined from measurements of the mean-field interaction by expansion of the condensate after release from the trap. a is scaled with respect to a_{bg}. (c) Tunability of the magnetic dipole interaction. Using time-varying magnetic fields $B(t)$, the dipoles are rapidly rotated around the z axis. The angle ϕ between the dipole orientation and the z axis determines the strength and sign of the effective interaction. Images taken from [43] and [44].

the Larmor frequency. The time average DDI over the relevant period of $2\pi/\Omega$ is,

$$\langle V_d(r) \rangle = \frac{g_d}{r^3}(1 - 3\cos^2\nu)\left[\frac{3\cos^2\phi - 1}{2}\right] \tag{1.18}$$

where ν is the angle between inter-atomic separation and the static field. The factor within the square brackets may be tuned by changing the angle ϕ and it changes the value from 1 to $-1/2$. This allows tuning the DDI from repulsive to attractive or vice versa. At $\phi = \theta_m = 54.7^o$ known as the magic angle, the DDI completely vanishes.

In the above section we saw that using an external orienting field the polarisation direction and effectively the strength of the DDI may be changed. Although in 3D it has no effect, in quasi-2D this has the effect of tuning the degree of anisotropy and in quasi-1D it can be used to tune the strength of the DDI as will be discussed in detail. Tilting of dipoles introduces a previously unexplored parameter regime which has been extensively studied in this thesis.

One specific case deals with tuning the induced electric dipole moment following introduction of doubly-dipolar interaction in Dy atoms in previous section. This may be achieved by controlling the strength of the applied electric field and the angle between the electric and magnetic field [42]. The relevant quasi-degenerate energy levels (angular moment $J = 10$ and 9) of opposite parity of Dy atom, when placed in external magnetic and electric field, splits into Zeeman sublevels and gets coupled. The coupling, which
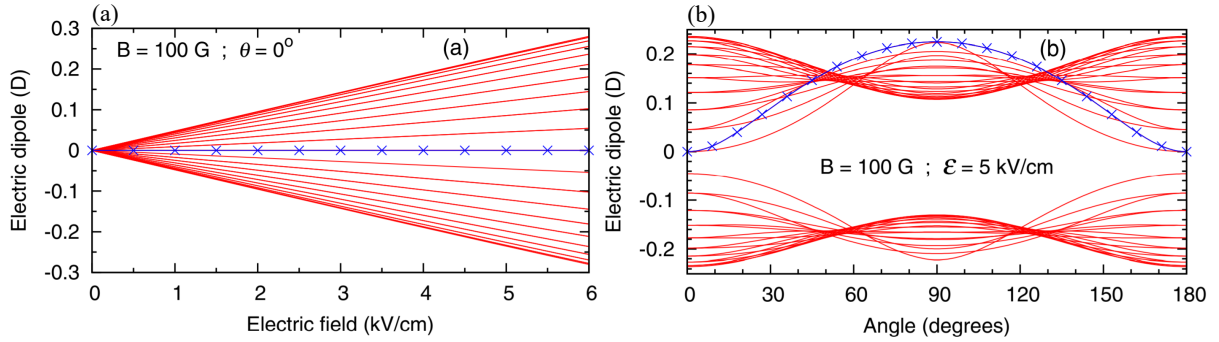
Figure 1.5: The crossed line(blue) is the state of interest in which the Dysprosium atom is prepared. (a) For angle between the external magnetic and electric field $\theta = 0^o$ the electric dipole moment remains zero. Once $\theta \neq 0^o$, electric field affects the magnitude of the electric dipole moment. (b) Shows how the electric dipole moment varies with θ for a fixed magnitude of magnetic and electric field strength. Image taken from [42].

induces the electric dipole moment, is controlled by the electric field strength. When the electric field and magnetic field are aligned along the same axis, the particular Zeeman sublevel ($|M = -10\rangle$) where the atom is prepared is unaffected and doesn't get coupled to any other state since it lacks an opposite parity sublevel counterpart. This is because the number of sublevels for both parities are different. However, when the electric field is tilted, the Zeeman sublevels are no longer the good quantum numbers and all the sublevels get mixed. The mixing induces electric dipole moment and reaches a maximum at angle 90°. This is demonstrated in the Fig. 1.5.

1.3   Dipolar Bose gas

Dipolar Bose gas owe their success to the added richness in the interaction potential due to anisotropy and long-range effects of the DDI, in contrast to a contact interacting BEC. The very first change noticed due to additional DDI is the change in critical temperature of condensation [46, 47]. However, the most exciting effects are visible in the post-condensation period. In Chromium BEC [48], the anisotropic effect was shown to manifest in the collapse and following explosion of the cloud. In rotating condensates, the vortex lattice ground state undergoes several symmetry configurations, e.g. triangular, square, stripe, and bubble phase, as DDI strength is increased compared to the contact strength g [49]. This tuning is achieved by decreasing g via Feshbach resonance.

However, in spinor condensates, where atoms occupy multiple Zeeman states, energy associated with the spin-changing collisions are already very small as it is proportional to difference between scattering lengths in different spin channels [50]. This allows for the dipolar energy of even alkali atoms to have comparable strengths and evidence of dipolar effects in spinor condensates. The spin-1 BEC phase diagram with weak magnetic

field in presence of DDI presents three distinct ground state spin textures a) polar-core vortex phase, b)flower phase, and c) chiral spin-vortex phase [51]. The dipolar nature of Rubidium was experimentally probed in [52] where spontaneous decay of helical spin textures leads to formation of spatial domains of spin structures. In Cr BEC also spinor dynamics is influenced by the strong DDI, which does not preserve the spin projection along the quantization axis, unlike the contact interaction. This mean DDI facilitates spin transfer between Zeeman sublevels. In cylindrically symmetric system from an initial state with all atoms in $-F$ state, where F is the total spin, DDI violate spin projection. It leads to transfer of angular momentum to center of mass and generation of dynamic vorticity [53, 54]. This is similar to Einstein-de Haas effect. This experiment requires extremely weak magnetic field less than 1 mG where system shows regularized DDI.

Some of the highest rewarding systems in ultracold gases consist of optical lattices which can easily mimic traditional condensed matter and solid state physics and beyond. Placing atoms in such periodic potential allows for almost lossless control of the idealistic systems. [55] was one of the first experiments to show the effect of DDI in alkali atoms in 1D optical lattice. It was shown that interaction induced decoherence can be reduced by manipulating the competition between DDI and contact interaction. In 2D lattices, novel phases such as chekerboard phase and supersolid phase has been studied [56, 57]. Haldance Bose insulator phase with similarities to famous Haldance gapped phase is found in 1D optical lattices with long-range DDI [58]. Insulating states [59] and self-assembled structures [60–62] are also predicted in lattices in presence of long-range interactions.

1.3.1 Mean-field description

The study of N-atoms in BEC consists of multitude of two-body interactions and a many-body Hamiltonian is used to include all the terms. However, it is difficult to solve for the N-body problem and usually it is dealt by converting it to a single body problem with the help of mean-field approach. This is also known as the Hartree-Fock approximation where the total wave function Φ is a product of single particle states ψ of N bosons. In other words, instead of considering individual interaction of a single atom with all the rest in the gas, it is prudent to approximate the particle being in a potential which is averaged over all two-body interactions. The pseudo-potential interaction terms are compatible with such a picture. In addition to simplifying the problem considerably, mean-field approach makes it easy to understand the underlying physics in terms of a set of parameters. The mean-field approximation requires a large number of atoms in the condensate, $N >> 1$ at ultracold temperatures to be valid [11, 63]. The condition $k|a| << 1$ must also be satisfied to ensure the interactions should be from low-energy scattering processes. N interacting

bosons can be described using the following many-body Hamiltonian, [4, 12, 10],

$$\hat{H} = \int d\mathbf{r}\hat{\Psi}^\dagger(\mathbf{r}) \left[-\frac{\hbar^2}{2m}\nabla^2 \right] \hat{\Psi}(\mathbf{r}) + \frac{1}{2} \int d\mathbf{r} \int d\mathbf{r}'\hat{\Psi}^\dagger(\mathbf{r})\hat{\Psi}^\dagger(\mathbf{r}')V(r-r')\hat{\Psi}(\mathbf{r}')\hat{\Psi}(\mathbf{r}) \quad (1.19)$$

where $\hat{\Psi}(\mathbf{r})$ and $\hat{\Psi}^\dagger(\mathbf{r})$ are the bosonic field operators annihilating and creating particles at position $\mathbf{r}$ and $V(r - r')$ is the two-body inter-atomic potential. The first term is the kinetic energy and the second term is a two-body term. The bosonic operators obey the usual bosonic commutation relations and are related to the creation and annihilation operators as,

$$\hat{\Psi}^\dagger(\mathbf{r}) = \sum_k \phi_k(\mathbf{r})\hat{a}_k^\dagger \qquad \text{and} \qquad \hat{\Psi}(\mathbf{r}) = \sum_k \phi_k(\mathbf{r})\hat{a}_k \quad (1.20)$$

where $\phi_k(\mathbf{r})$ is the single particle states. Assuming N is large in the single particle state ϕ_0, then $N + 1 \approx N$ and the creation and annihilation operators can be replaced by numbers as $\hat{a}_0 = \hat{a}_0^\dagger = \sqrt{N}$. The field operator,

$$\hat{\Psi}(\mathbf{r}) = \sqrt{N}\phi_0(\mathbf{r}) + \sum_{k>0} \phi_k(\mathbf{r})\hat{a}_k = \psi(\mathbf{r}) + \delta\hat{\Psi}(\mathbf{r}) \quad (1.21)$$

where $\psi(\mathbf{r})$ is a complex valued function defined as the expectation value of the field operator, $\langle\hat{\Psi}(\mathbf{r})\rangle = \psi(\mathbf{r}) = |\psi(\mathbf{r})|e^{iS(\mathbf{r})}$ where $S(\mathbf{r})$ determines the coherence. $\psi(\mathbf{r})$ acts as the order parameter in Bose-Einstein condensation transition as it has a fixed phase factor associated with broken gauge symmetry. In this context, the gauge symmetry refers to the idea that one should be able to multiply any phase factor $e^{i\alpha}$ without changing any physical property. But in BEC phase transition the condensate, by making an explicit choice for the value of order parameter, spontaneously chooses a particular phase $S(\mathbf{r})$, thereby breaks the gauge symmetry. The modulus of this classical field $\psi(\mathbf{r})$ gives the square root of the density of the condensate where for a uniform gas this density becomes a constant $\approx N/V$. The off-diagonal long range order(ODLRO) of the BEC is also characterised by $\psi(\mathbf{r})$, which is also known as the wave function of the condensate, as follows. Consider the one particle density matrix,

$$\rho(\mathbf{r}' - \mathbf{r}) = \langle\hat{\Psi}^\dagger(\mathbf{r})\hat{\Psi}(\mathbf{r}')\rangle \quad (1.22)$$

In the limit $\mathbf{r}' - \mathbf{r} \to 0$ if the density matrix $\rho(\mathbf{r}' - \mathbf{r}) \neq 0$, the system is said to possess ODLRO. Using (1.21),

$$\lim_{(\mathbf{r}'-\mathbf{r})\to 0} \rho(\mathbf{r}' - \mathbf{r}) = \langle\hat{\Psi}^\dagger(\mathbf{r})\rangle\langle\hat{\Psi}(\mathbf{r})\rangle = \psi^*(\mathbf{r})\psi(\mathbf{r}) \approx \frac{N}{V} \quad (1.23)$$

The wave function is also applicable to non-equilibrium states of the condensate.

1.3.2 Gross-Pitaevskii equation

We shall now derive the equation for the wave function using the Heisenberg equation with many-body Hamiltonian for the time evolution of the field operator. Considering N atoms now in an external confinement potential $V_{ext}(\mathbf{r})$,

$$
\begin{aligned}
i\hbar\frac{\partial}{\partial t}\hat{\Psi}(\mathbf{r},t) &= [\hat{\Psi}(\mathbf{r},t),\hat{H}] \\
&= \left[-\frac{\hbar^2\nabla^2}{2m} + V_{ext}(\mathbf{r}) + \int d\mathbf{r}'\hat{\Psi}^\dagger(\mathbf{r}',t)V(\mathbf{r}'-\mathbf{r})\hat{\Psi}(\mathbf{r}',t)\right]\hat{\Psi}(\mathbf{r},t)
\end{aligned}
\tag{1.24}
$$

As introduced previously the field operators needs to be replaced by their classical counterparts. Under diluteness condition correlations between particles can be ignored, and the many-body wave function can be factorised to single particle basis, $\Phi(\mathbf{r}_1,...,\mathbf{r}_N) \propto \psi(\mathbf{r}_1)...\psi(\mathbf{r}_N)$, a.k.a. Hartree-Fock approximation. ψ is the order parameter. The two-body interaction is replaced by the effective pseudo-potential encompassing both the short-range and long-range interactions as shown in section 1.2. Please note that the true short range potential is not a delta function, rather in pseudo-potential treatment the replacement by delta function effectively captures the physics and eases the mathematical complications.

$$
V(\mathbf{r}'-\mathbf{r}) = g\delta(\mathbf{r}'-\mathbf{r}) + \frac{g_d}{|\mathbf{r}'-\mathbf{r}|^3}(1-3\cos^2\theta)
\tag{1.25}
$$

Neglecting the fluctuation term $\delta\hat{\Psi}(\mathbf{r},t)$, we obtain a nonlinear schrödinger's equation describing N atoms in trap,

$$
\begin{aligned}
i\hbar\frac{\partial}{\partial t}\psi(\mathbf{r},t) = \Bigg[&-\frac{\hbar^2\nabla^2}{2m} + V_{ext}(\mathbf{r}) + g|\psi(\mathbf{r},t)|^2 \\
&+g_d\int d\mathbf{r}'\psi^*(\mathbf{r}',t)\frac{1-3\cos^2\theta}{|\mathbf{r}'-\mathbf{r}|^3}\psi(\mathbf{r}',t)\Bigg]\psi(\mathbf{r},t)
\end{aligned}
\tag{1.26}
$$

This is known as the time dependent Gross-Pitaevskii equation(GPE) for the dipolar BEC. The interaction terms make the equation nonlinear and the final term adds a non-local character to the condensate wave function. Assuming $\psi(\mathbf{r},t) = \psi(\mathbf{r})e^{-\frac{i\mu t}{\hbar}}$, a stationary counterpart of the above equation maybe obtained,

$$
\mu\psi(\mathbf{r}) = \left[-\frac{\hbar^2\nabla^2}{2m} + V_{ext}(\mathbf{r}) + g|\psi(\mathbf{r})|^2 + g_d\int d\mathbf{r}'\psi^*(\mathbf{r}')\frac{1-3\cos^2\theta}{|\mathbf{r}'-\mathbf{r}|^3}\psi(\mathbf{r}')\right]\psi(\mathbf{r})
\tag{1.27}
$$

where μ is the chemical potential. The GPE describes the macroscopic behavior of the condensate where the variations in the wave functions are much larger than the mean interatomic distances at low energy limits. Other validity conditions include N being much larger than 1, the de-Broglie wavelength being much larger than the range of the short-

range interactions, the system energy should be small compared to the dipolar energy $E_D = \frac{\hbar^6}{m_{red}^3 g_d^4}$ [64], and the diluteness parameter $\bar{n}a^3$ must be very small compared to 1. $\bar{n}$ is the mean density and $m_{red} = m/2$ is the reduced mass. For Chromium BEC Monte-Carlo simulations have shown the validity of dipolar mean-field equation [65]. The dipole length $a_d \propto \hbar^2/mE_d$ should be smaller than short-range interaction radius to ensure absence of bound states in the dipolar states [66] but this condition is expected to be violated in strongly magnetic Dysprosium BEC. But still the GPE remains valid because the dipolar effects on the s-wave scattering length is included in the contact interaction term.

For numerical purposes it is prudent to scale out the dimensions from the GPE. This allows seamless calculations without worrying too much about physical details. In presence of strong confinements, usually the GPE is scaled with the trap energy $\hbar\omega$, where ω is the tight trap frequency. In absence of traps, GPE can be scaled with energy scales associated with healing length ξ, chemical potential μm or the DDI, E_d.

1.3.3 Low-dimensional GPE

The properties of the condensate offer surprisingly different dynamics in lower dimensions than in 3D that have been studied both theoretically [67–70] and experimentally [71–74]. So it becomes imperative to understand the conditions under which a system becomes low-dimensional and understand dimension-specific properties. The key idea is, when a system is lower-dimensional the dynamics of the system along constrained direction is frozen such that it can be ignored. In theoretical calculations, the GPE also can be reduced to fewer coordinates for simplification. This is usually done by having a tight trap along the constrained direction. We shall compare the characteristic length scales of the system to gain further intuition. Consider a cylindrically symmetric trap of the form,

$$V_{ext}(r) = \frac{1}{2}m\omega_\rho^2\rho^2 + \frac{1}{2}m\omega_z^2z^2 \tag{1.28}$$

where $\rho^2 = x^2 + y^2$ and ω_ρ, ω_z are the harmonic oscillator frequencies. The lengths associated with this confinement potential are $l_\rho = \sqrt{\hbar/m\omega_\rho}$ and $l_z = \sqrt{\hbar/m\omega_z}$. We also have interaction-dependent length scales healing length, ξ, and condensate radii R_x, R_y and R_z. In the simple case where the dipoles are also orientated adhering to the confinement symmetry, we may write $R_x = R_y \propto R_\rho$. The healing length is defined as the distance over which the system smooths over any defects. Mathematically, $\xi = \sqrt{4\pi na}$. When $R_\rho, R_z >> \xi >> a$, we are in the 3D regime.
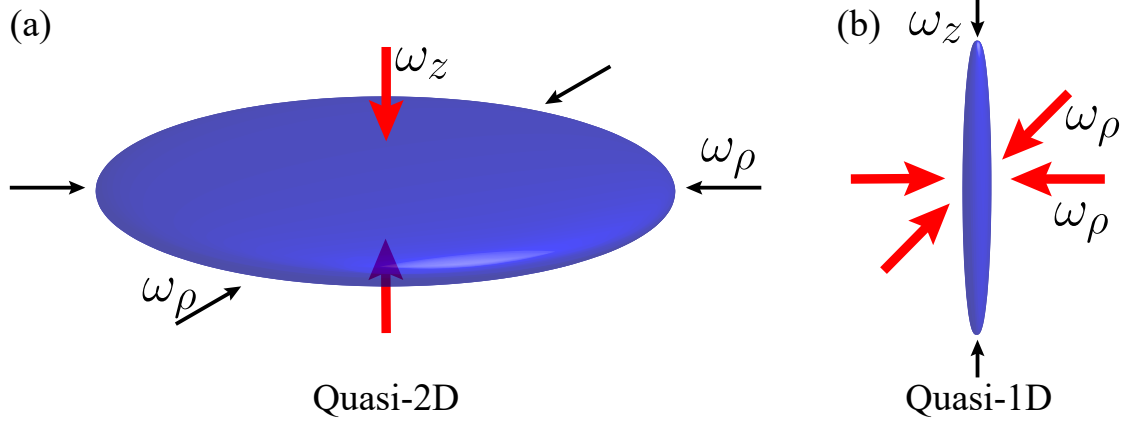
Figure 1.6: (a) To achieve a the quasi-$2D$ BEC, the confinement frequency $\omega_z >> \omega_\rho$. This gives the condensate a pancake shape. (b) A cigar-shaped BEC is achieved by having strong radial trap frequency compared to the axial one i.e. $\omega_\rho >> \omega_z$.

Quasi-2D BEC

This happens when $l_\rho >> \xi >> l_z$ or in other words when the trap frequency $\omega_z >> \omega_\rho$. Under this condition, the condensate lacks energy to rise out of the ground state of the confinement along z-direction. Using single mode approximation, the wave function can be factorized as $\psi(r,t) = \psi(\rho,t)\phi(z)$ where $\phi(z)$ is the ground state of the harmonic potential confinement $\phi(z) = \frac{exp(-z^2/2l_z^2)}{\pi^{1/4}\sqrt{l_z}}$. Inserting this in (1.26) we obtain a quasi-2D GPE:

$$i\hbar\frac{\partial\psi(\rho,t)}{\partial t} = \left[-\frac{\hbar^2\nabla_\rho^2}{2m} + \frac{1}{2}m\omega_\rho^2\rho^2 + \frac{g}{\sqrt{2\pi}l_z}|\psi(\rho,t)|^2 \right.$$
$$\left. + \int dz|\phi(z)|^2 \int d\mathbf{r}'\psi^*(\mathbf{r}',t)V_d(\mathbf{r}'-\mathbf{r})\psi(\mathbf{r}',t)\right]\psi(\rho,t) \quad (1.29)$$

where $V_d(\mathbf{r}'-\mathbf{r})$ is the DDI potential. The quasi-2D GPE maybe used when the associated chemical potential $\mu << \hbar\omega_z$ at all times. Violation of this condition results in a non-Gaussian distribution of the wave function along z and a full 3D treatment becomes necessary. In quasi-2D regime the condensate is pancake-shaped. Also while working with dipolar BEC the stabilizing effect of the finite-sized tightly confined direction cannot be ignored when the dipoles are oriented along the trap axis.

The two-body scattering of dipolar atoms in two-dimension have been studied in [75, 76]. When anisoropy of the interaction is present in quasi-2D configuration, it translates to anisotropy in the superfluidity [77], which is also a signature of existence of roton [78].

Quasi-1D BEC

Following in similar footsteps as the previous paragraph the validity conditions for a quasi-1D BEC are, $l_z >> \xi >> l_\rho$ where $\omega_z << \omega_\rho$. The dynamics along radial ρ-direction is frozen and it allows the separation of degrees of freedom as $\psi(r,t) = \phi(\rho)\psi(z,t)$. The chemical potential must satisfy $\mu << \hbar\omega_\rho$. For $\phi(\rho) = \frac{exp[-\rho^2/2l_\rho^2]}{\sqrt{\pi}l_\rho}$ the quasi-1D GPE can be written as,

$$
\begin{aligned}
i\hbar\frac{\partial\psi(z,t)}{\partial t} &= \left[-\frac{\hbar^2\nabla_z^2}{2m} + \frac{1}{2}m\omega_z^2 z^2 + \frac{g}{2\pi l_z^2}|\psi(z,t)|^2 \right. \\
&\quad \left. + \int d\rho|\phi(\rho)|^2 \int d\mathbf{r}'\psi^*(\mathbf{r}',t)V_d(\mathbf{r}'-\mathbf{r})\psi(\mathbf{r}',t) \right]\psi(z,t) \quad (1.30)
\end{aligned}
$$

The simplified form of the DDI term in reduced dimensions has been introduced in later parts of the thesis. It has been shown that the effect of DDI, even when small compared to contact interaction, can significantly alter the confinement induced resonances due to the transverse traps [79, 80]. Quasi-1D geometries may also give rise to weakly localized states [81] and possible regimes of realisation of super-Tonks-Girardeau gas [82]. The theoretical calculations for the lower dimensional GPE have been provided in detail in appendix E.1.

1.3.4 Ground state solutions

Despite the mean-field GPE being much simpler to handle N body system, it is still quite nontrivial to solve. In certain regimes, the GPE can be further simplified and ground state solutions may be obtained. Below we look at some general and exotic solutions of the GPE. In a regime where the kinetic energy is dominant we recover the trivial case of a quantum harmonic oscillator with a Gaussian ground state solution. The interesting solutions crop up when interaction term(s) dominate.

Thomas-Fermi solution

If we consider BEC in harmonic confinement and the inter-particle interaction dominates such that kinetic energy term maybe neglected, it is called Thomas-Fermi(TF) regime. In case of a non-dipolar BEC we have a stationary GPE (1.27),

$$
\mu\psi(\mathbf{r}) = \left[V_{ext}(\mathbf{r}) + g|\psi(\mathbf{r})|^2 \right]\psi(\mathbf{r}) \quad (1.31)
$$
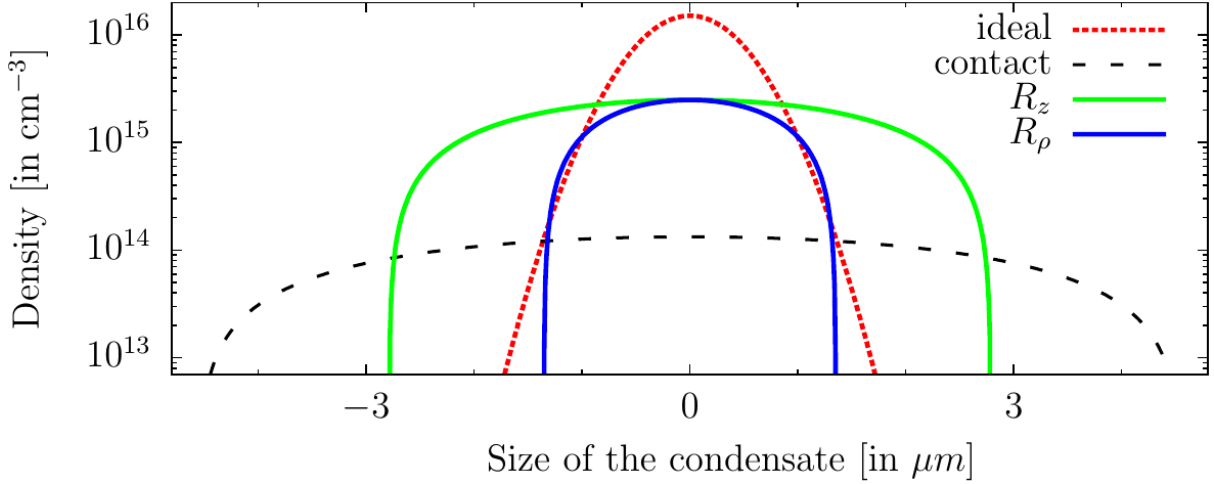
Figure 1.7:   Thomas-Fermi density profile of Chromium cloud with $N = 20000$ atoms displays the anisotropic TF profile in a spherical trap $\omega/2\pi = 500$ Hz. With just contact interaction the isotropic profile is plotted for comparison and without any interaction the Gaussian profile in a simple harmonic trap is recovered. Image taken from [85].

A solution for the density maybe obtained with $R_{x,y,z}$ defined as TF-radius in respective directions [4],

$$n(\mathbf{r}) = |\psi(r)|^2 \quad = \quad \begin{cases} \dfrac{\mu - V_{ext}(\mathbf{r})}{g} & \mu \geq V_{ext}(\mathbf{r}) \\ 0 & \text{otherwise} \end{cases} \tag{1.32}$$

$$= \quad \frac{15N}{8\pi R_x R_y R_z}\max\left[\left(1 - \frac{x^2}{R_x^2} - \frac{y^2}{R_y^2} - \frac{z^2}{R_z^2}\right), 0\right] \tag{1.33}$$

For harmonic confinement $V_{ext}(\mathbf{r}) = \dfrac{1}{2}m\omega^2 r^2$, the shape of such a solution is similar to an inverted parabola Fig. 1.7. The quantity $R_{TF} = \dfrac{\sqrt{2\mu/m}}{\omega}$ is known as the TF radius which estimates the size of the condensate. Using normalization condition, it can be shown $R_{TF} \propto N^{1/5}$, unlike the case for an ideal BEC where the size is set by the confinement alone. Clearly a large number of atoms are going to affect the condensate by increasing the size if the atoms are mutually repulsive. It is possible to smooth out the edges of the solution using a correction to the kinetic energy term [83, 84].

The solution for a dipole dominant condensate in TF regime involves more detailed calculation than the short-range case. Below only the cases where symmetry axis of a cylindrical trap coincides with the polarisation of the dipoles is shown for simplification. The TF solution for the dipolar case also takes the shape of an inverted parabola because the dipolar term only contains either constant or quadratic terms [86, 87]. But the aspect ratio is influenced by magnetostriction/electrostriction [86], or in other words by the anisotropy of the dipolar interactions. If the condensate aspect ratio is $R_\rho/R_z = \kappa$ and

trap aspect ratio $\omega_\rho/\omega_z = 1/\lambda$,

$$R_\rho = \left[\frac{15gN\kappa}{4\pi m\omega_\rho^2} \left\{ 1 + \frac{a_d}{a} \left(\frac{3\kappa^2 f(\kappa)}{2(1-\kappa^2)} - 1 \right) \right\} \right]^{1/5} \tag{1.34}$$

where a_d is the characteristic dipolar length (1.16) and

$$f(\kappa) = \frac{1 + 2\kappa^2}{1 - \kappa^2} - \frac{3\kappa^2 \tan^{-1}\sqrt{1-\kappa^2}}{(1-\kappa^2)^{3/2}} \tag{1.35}$$

This functional value is obtained from a detailed derivation using Green's function approach while recasting the dipole-dipole interaction term as a parabolic dipole potential for ease of calculation of the Thomas-Fermi radii [87]. The value for κ is solved using the following transcendental equation,

$$\frac{\kappa^2}{\lambda^2} \left[\frac{3a_d f(\kappa)}{a(1-\kappa^2)} \left(\frac{\lambda^2}{2} + 1 \right) - \frac{2a_d}{a} - 1 \right] = \frac{a_d}{a} - 1 \tag{1.36}$$

The dipolar interaction also affects the validity of TF approximation due to anisotropy depending on the trap geometry [88]. While the shape of the condensate profile remains unchanged the DDI affects the TF radii by elongating the cloud along the direction of polarisation. This aspect ratio ultimately affects the chemical potential of the condensate $\mu = gn_{peak}(1 - a_d f(\kappa)/a)$.

The expansion dynamics of the condensate is studied by releasing the gas from trap. In such situations the interaction energy is converted to kinetic energy and for accurate calculation it is prudent not to ignore the kinetic energy even in TF approximation. Instead the two kinetic terms are considered separately: the zero-point energy in trap and the kinetic energy post release of the trap. A detailed discussion may be found in [11, 89, 86, 90].

Solitons

A soliton or a solitary wave is a self-confined, non-dispersive, integrable and a non-singular solution seen in nonlinear systems. The self-focusing non-linearity can compensate the dispersion in the system leading to a stable shape-preserving wave. Solitons were first observed by John Scott Russel in 1845 in water. Extensive studies in solitons have been carried out in diverse fields such as plasma physics, meteorology, fiber optics, laser physics etc. The two main types of solitons of interest in the BEC are bright [91] and dark solitons [92].

Bright solitons:
A bright soliton has a central peak density with a zero background density. Due to
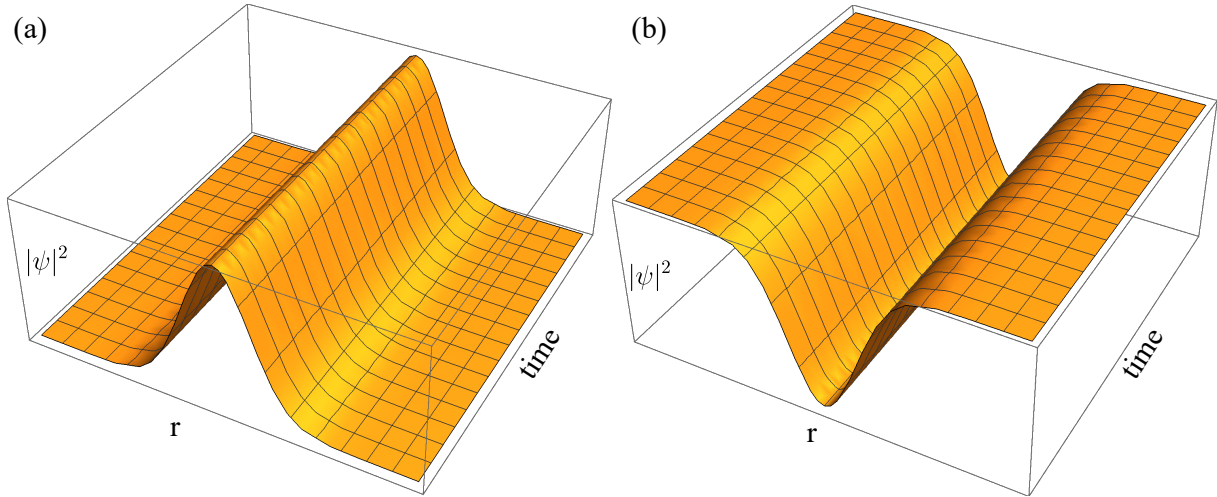
Figure 1.8:   General 1D (a) bright and (b) dark soliton density profiles.

energetically unfavourable conditions, with only short-range interactions a stable bright soliton is not possible in 3D or in quasi-2D condensates. In quasi-1D condensate the kinetic energy and an attractive short-range interaction can be balanced to obtain a self-bound soliton solution in absence of traps. Experimental observations of bright solitons were done in non-dipolar quasi-1D BECs with attractive nonlinearity [93, 94]. In presence of DDI, stable solitons are also possible in quasi-2D condensates [95, 96]. Assuming a Gaussian ansatz these claims can be easily verified by minimizing energy with respect to the variational Gaussian widths in different dimensions. The important distinction between bright solitons in non-dipolar and dipolar BECs can be identified from soliton-soliton collision which is elastic in 1D non-dipolar BECs while in dipolar BECs it is inelastic due to the lack of integrability [97]. Transfer of center-of-mass energy into internal vibrational modes can lead to soliton fusion in dipolar BECs [95].

Dark solitons:

Dark solitons(DS) are density dips with a phase shift and able to propagate without distortion on an uniform background. This is also a byproduct of competition between dispersion and nonlinearity. Unlike bright solitons, here a quasi-1D GPE allows for a DS solution when short-range interaction $g > 0$ [98–100]. The width of such a soliton is fixed by the healing length. If the transverse size of DS exceeds the healing length, it undergoes snake instability before breaking into vortices [101].

Blood cell solution

Interestingly, the Bohn group [102] found that for certain regimes with cylindrical symmetry the ground state density resembles a red blood cell, with the maximum density occurring on a ring in the radial plane. The polarising field is aligned along the pancake trap's tight direction and, 'pushing' the region DDIs of high density radially outward, the

peak density and the repulsive side-by-side DDIs are reduced. This type of solution may undergo shape deformation to dumbbell shape or multipeak structures under engineered confinements that break the cylindrical symmetry.

1.4 Beyond mean-field calculations

After the condensation of atoms with stronger magnetic moments [34] and cooling of polar molecules with high electric dipole moments the validity of mean-field has been pushed beyond its limit. Stronger interactions, accompanied by higher density and large number of atoms, demand inclusion of first-order corrections to the mean-field equation. We shall start with the full many-body Hamiltonian and calculate the correction term to the energy know as Lee-Huang-Yang (LHY) correction [103]. The beyond mean-field effects have been studied in optical lattices where their effect is enhanced [104], in non-dipolar bosonic [105] and fermionic systems [106] and recently in dipolar Erbium [107] and Dysprosium [108] condensates.

1.4.1 LHY correction

For N interacting bosons with homogeneous density the field operators (1.20) can be written in terms of plane wave [4],

$$\hat{\Psi}(\mathbf{r}) = \frac{1}{\sqrt{V}} \sum_k \hat{a}_k e^{i\mathbf{k}.\mathbf{r}} \qquad \text{and} \qquad \hat{\Psi}^\dagger(\mathbf{r}) = \frac{1}{\sqrt{V}} \sum_k \hat{a}_k^\dagger e^{-i\mathbf{k}.\mathbf{r}} \tag{1.37}$$

Replacing it in (1.19),

$$H = \sum_k \frac{\hbar^2 k^2}{2m} \hat{a}_k^\dagger \hat{a}_k + \frac{1}{2V} \sum_{p_1,p_2,k} V_k \hat{a}_{p_1+k}^\dagger \hat{a}_{p_2-k}^\dagger \hat{a}_{p_1} \hat{a}_{p_2} \tag{1.38}$$

where, $V_k = \int d\mathbf{r} V(\mathbf{r}' - \mathbf{r}) e^{-i\mathbf{k}.(\mathbf{r}'-\mathbf{r})}$. When almost all atoms are in the condensate at $T \sim 0$ i.e. $N_0 \approx N$ we are only interested in terms where $p_1, p_2, k \to 0$. In this limit, using $\hat{a}_0^\dagger = \hat{a}_0 = \sqrt{N}$, the ground state energy can be easily shown to be,

$$E_0 = \frac{V_0 N^2}{2V} \tag{1.39}$$

Extending to include the $k \neq 0$ cases, we shall only consider the cases where collision may happen between a particle with $k = 0$ and another $k \neq 0$ which is account for the first order correction. Separating the ground state and excited parts the many-body

Hamiltonian becomes,

$$
H = \frac{V_0}{2V}\hat{a}_0^\dagger\hat{a}_0^\dagger\hat{a}_0\hat{a}_0 + \sum_{k\neq 0}\frac{\hbar^2k^2}{2m}\hat{a}_k^\dagger\hat{a}_k + \frac{1}{2V}\sum_{k\neq 0}[V_0\hat{a}_0^\dagger\hat{a}_k^\dagger\hat{a}_0\hat{a}_k + V_0\hat{a}_0^\dagger\hat{a}_0^\dagger\hat{a}_k\hat{a}_0 + V_k\hat{a}_k^\dagger\hat{a}_{-k}^\dagger\hat{a}_0\hat{a}_0
$$
$$
+ V_k\hat{a}_k^\dagger\hat{a}_0^\dagger\hat{a}_0\hat{a}_k + V_k\hat{a}_0^\dagger\hat{a}_{-k}^\dagger\hat{a}_{-k}\hat{a}_0 + V_k\hat{a}_0^\dagger\hat{a}_0^\dagger\hat{a}_k\hat{a}_{-k}]
$$

In the first term we use the accurate condition $\hat{a}_0^\dagger\hat{a}_0^\dagger\hat{a}_0\hat{a}_0 = N^2 - 2N\sum_{k\neq 0}\hat{a}_k^\dagger\hat{a}_k$ while for the rest we use the approximation $\hat{a}_0^\dagger = \hat{a}_0 = \sqrt{N}$ for further simplification.

$$
H = \frac{V_0 N^2}{2V} + \sum_k\frac{\hbar^2k^2}{2m}\hat{a}_k^\dagger\hat{a}_k + \frac{N}{2V}\sum_k V_k[\hat{a}_k^\dagger\hat{a}_k + \hat{a}_{-k}^\dagger\hat{a}_{-k} + \hat{a}_k^\dagger\hat{a}_{-k}^\dagger + \hat{a}_k\hat{a}_{-k}] \qquad (1.40)
$$

The third term consists of energy of the excited states due to interaction and simultaneous creation or annihilation of particles with momentum $\hbar k$ and $-\hbar k$. In order to diagonalize this Hamiltonian we take help of Bogoliubov transformation,

$$
\hat{a}_k = u_k\hat{b}_k + \hat{v}_{-k}^*\hat{b}_{-k}^\dagger
$$
$$
\hat{a}_k^\dagger = u_k^*\hat{b}_k^\dagger + \hat{v}_{-k}\hat{b}_{-k}
$$

The new operators also follow the bosonic commutation relation and the parameters are uniquely determined by the normalization condition $u_k^2 - v_{-k}^2 = 1$ in order to cancel the off-diagonal terms of the Hamiltonian.

$$
u_k, v_{-k} = \sqrt{\frac{\hbar^2k^2/2m + nV_k}{2\epsilon(k)} \pm \frac{1}{2}} \qquad \text{where,} \qquad \epsilon(k) = \sqrt{\frac{\hbar^2k^2}{2m}\left(\frac{\hbar^2k^2}{2m} + 2nV_k\right)} \quad (1.41)
$$

The diagonalized Hamiltonian is given by,

$$
H = \frac{N^2V_0}{2V} + \frac{V}{2}\int\frac{d^3k}{(2\pi)^3}\left[\epsilon(k) - \frac{\hbar^2k^2}{2m} - nV_k\right] + \sum_k\epsilon(k)\hat{b}_k^\dagger\hat{b}_k = E_0 + \sum_k\epsilon(k)\hat{b}_k^\dagger\hat{b}_k \ (1.42)
$$

The integral term is also ultraviolet divergent [109] up to first order of potential. Hence it is necessary to consider at least up to second order in scattering potential. Then the potential is $V_k = V_{k=0} - \frac{1}{2}\int\frac{d^3k}{(2\pi)^3}\frac{V_k^2}{\hbar^2k^2/2m} + ...$ The first term is the ground state energy same as (1.39). The second term includes the fluctuations. At the end of these calculations we find, the system of interacting particles is reduced to the Hamiltonian for non-interacting quasi-particles (collective excitation) having a dispersion relation $\epsilon(k)$. With the first order correction, also known as the Lee-Huang-Yang correction the energy may be written as

$$
E_0 = \frac{N^2V_0}{2V} + \frac{V}{2}\int\frac{d^3k}{(2\pi)^3}\left[\epsilon(k) - \frac{\hbar^2k^2}{2m} - nV_k + \frac{n^2V_k^2}{2\hbar^2k^2/2m}\right] \qquad (1.43)
$$

So the energy correction term is $\Delta E = \dfrac{V}{2} \int \dfrac{d^3k}{(2\pi)^3} \left[\epsilon(k) - \dfrac{\hbar^2 k^2}{2m} - nV_k + \dfrac{n^2 V_k^2}{2\hbar^2 k^2/2m} \right]$ and correction to the chemical potential is given by

$$\Delta\mu = \frac{\partial \Delta E}{\partial N} \tag{1.44}$$

Although it has been referred to as the ground state energy, it is not true. In fact the ground state with interacting with inter-atomic potentials corresponds to a solid. The gas phase actually represents a metastable state described by the Bogoliubov theory discussed above. The theory ignores three-body collisions which, in actual systems, will eventually drive the system into the solid configuration. However, experimental verification have proved the existence of the quantum gas phase and its long lifetime for systematic measurements of many relevant physical quantities.

1.4.2 Extended Gross-Pitaevskii equation

The correction to the chemical potential due to the quantum fluctuation can be added to the GPE under the local density approximation $n \to n(\mathbf{r}, t)$. In presence of DDI,

$$
\begin{aligned}
V_k &= \int d\mathbf{r} \left(g\delta(\mathbf{r}' - \mathbf{r}) + \frac{g_d}{|\mathbf{r}' - \mathbf{r}|^3}(1 - 3\cos^2\theta) \right) e^{-i\mathbf{k}.(\mathbf{r}'-\mathbf{r})} \\
&= g + \frac{4\pi g_d}{3}(3(\hat{d} \cdot \hat{k})^2 - 1) = g_d(\beta + \mathcal{F}[\theta_k, \phi_k, \alpha)]
\end{aligned} \tag{1.45}
$$

where $\beta = g_d/g$ and $\mathcal{F}[\theta_k, \phi_k, \alpha) = 4\pi(3(\hat{d} \cdot \hat{k})^2 - 1)/3$. Using this expression in (1.44) the correction to the chemical potential can be shown to be,

$$\Delta\mu(\mathbf{r}, t) = \frac{(m/\hbar^2)^{3/2}}{3\pi^3} g_d^{5/2} n(\mathbf{r}, t)^{3/2} \int d\Omega_k [\beta + \mathcal{F}(\theta_k, \phi_k, \alpha)]^{5/2} \tag{1.46}$$

Adding this to the GPE (1.26) we obtain the extended Gross-Pitaevskii equation(eGPE),

$$
\begin{aligned}
i\hbar\frac{\partial}{\partial t}\psi(\mathbf{r}, t) = &\left[-\frac{\hbar^2\nabla^2}{2m} + V_{ext}(\mathbf{r}) + g|\psi(\mathbf{r}, t)|^2 \right. \\
&\left. + g_d \int d\mathbf{r}' \psi^*(\mathbf{r}', t) \frac{1 - 3\cos^2\theta}{|\mathbf{r}' - \mathbf{r}|^3} \psi(\mathbf{r}', t) + \Delta\mu(\mathbf{r}, t) \right] \psi(\mathbf{r}, t)
\end{aligned} \tag{1.47}
$$

This beyond mean-field equation has been able to confirm the very important role quantum fluctuations play in stabilizing a 3D BEC against collapse by formation of self-bound droplet solutions [110]. The LHY correction term has a repulsive effect in 3D, while in 1D it can become attractive by nature [111].

Chapter 2

Stability Analysis

2.1 Elementary excitations in uniform condensate

Previously, we have seen how the excitation in a system of interacting particles may be reduced to a system of non-interacting quasi-particles given by the excitation spectrum in Eq. (1.41). The study of these elementary excitations is fundamental in nature to all many-body systems in general. A lot of pioneering work related to excitations in superfluid liquid Helium was done by Landau, Bogoliubov and Feynman. The principal motive of this chapter is to understand the stability and instability of the Bose gas with the help of this dispersion relation. Both the inter-atomic interaction and the condensate dimensionality play huge role. It has to be noted that these excitations, taking place in low temperature regime, are not thermal in nature and the excited states are found from classical frequencies ω_k of the linearized GPE.

In a homogeneous gas small density perturbation is added to a constant density such that $\psi = \sqrt{n} + u(\mathbf{r})e^{i\omega_k t} + v^*(\mathbf{r})e^{-i\omega_k t}$ where, $u(\mathbf{r}), v^*(\mathbf{r})$ are complex plane wave excitation [112] and n is uniform density. Replacing this in the GPE (1.26), one may obtain the dispersion relation which gives surprising intuitions regarding whether the condensate is stable against the small density fluctuations. The instability is manifested by emergence of un-physical solutions eventually breaking down the considered model. Below we look in details about phonon and roton type excitation. Let us analyse the dispersion relation (1.41) in homogenous 3D cloud [28],

$$\epsilon(k) = \sqrt{\frac{\hbar^2 k^2}{2m}\left[\frac{\hbar^2 k^2}{2m} + 2nV_k\right]} \tag{2.1}$$

where, $V_k = g + \frac{4\pi g_d}{3}(3\cos^2\Theta - 1)$ is a factor with contributions from both short-range and long-range interactions in Fourier space. Θ is the angle between the dipole axis and the momentum $\mathbf{k}$. In the limit where we may deem the kinetic energy much stronger than the interaction term, we obtain a free particle behaviour $\epsilon(k) \approx \frac{\hbar^2 k^2}{2m}$. In the small
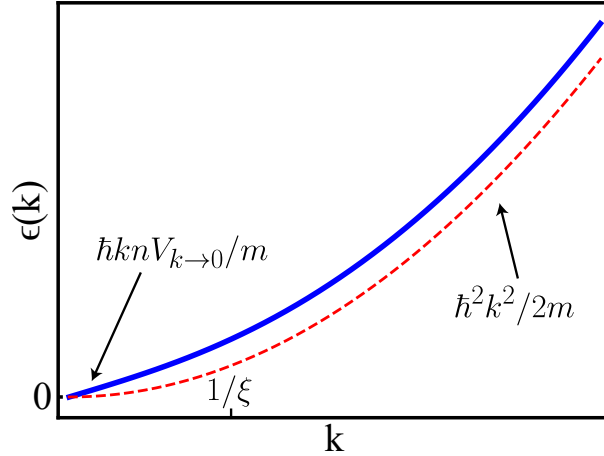
Figure 2.1: The transition between phonon and free-particle is shown in Bogoliubov dispersion relation of elementary excitations. This takes place at $k \sim 1/\xi$, where ξ is the healing length. The dashed curve shows the free particle dispersion for contrast.

momentum limit, we can obtain again a simpler expression $\epsilon(k) = \hbar k \frac{nV_{k\to 0}}{m}$. This is a phonon-like form with $\frac{nV_{k\to 0}}{m}$ representing sound speed. In non-dipolar BEC the speed acquires the popular expression $v = gn/m$. This case has been summarized well in [113]. A more detailed derivation of excitation spectrum is in Appendix B.

2.1.1 Phonons

It is clear that if V_k is negative then for low momentum values the dispersion relation gives imaginary values and the condensate becomes unstable against collapse. In absence of DDI, $g < 0$ for this to happen [4]. In presence of DDI at low momentum regimes we exactly have $\epsilon(k) \propto \sqrt{g - \frac{4\pi g_d}{3}}$ for $\Theta = \pi/2$. It can be easily derived by replacing $\Theta = \pi/2$ in the expression of V_k and then calculating (2.1). This expression becomes imaginary if $\beta > \frac{3}{4\pi}$ which is defined in Eq. (1.17). This is the result of dipole anisotropy which allows for a stable condensate parallel to the dipole orientation while density modulations take place in the direction perpendicular to the same. This is known as the phonon instability. Although homogeneous condensates are technically impossible to achieve thanks to their infinite extension condition, their simplicity describes trapped condensates if the change in density is small within the wavelength of the excitation under local density approximation.

Experimentally [48] collapse instability was studied in Chromium in expectation of manifestation of dipolar anisotropy. After preparation of BEC, the scattering length was quenched below the critical value such that phonon instability condition was satisfied. The system was allowed to evolve for an adjustable time t_{hold} before the trap was switched off and the cloud was then imaged. Initially the shape was elongated along z i.e. dipole orientation but soon it is shown to develop an expanding torus-shaped part in $x - y$ direction. Interestingly, it is found that this shape is reminiscent of the d-wave symmetry of the DDI. The collapse is restricted to the transverse direction while the condensate
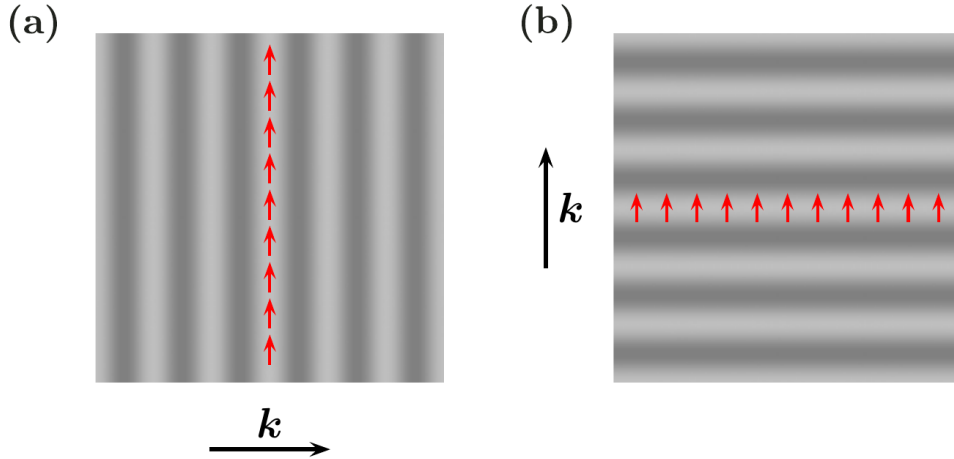
Figure 2.2: (a) A phonon with momentum perpendicular to the direction of dipoles creates planes of higher density (light gray), in which the dipoles are in the plane, corresponding to an instability. (b) For momentum parallel to the direction of dipoles the dipoles point out of the planes of high density; such a perturbation is thus stable. Image from [28].

prefers to form extremely elongated axial clouds. Once the density is extremely high, the quantum pressure tries to eject the atoms outward, resulting in an exploding condensate with anisotropic shapes. Years later, similar experiments with other dipolar atomic gases such as Erbium and Dysprosium produced strangely different results which will be discussed later.

Unlike non-dipolar case, clearly phonon instability becomes direction dependent with DDI. Potential to manipulate the anisotropy by trap geometry and changing the dipole orientation will also affect the phonon instability condition. These will be calculated and analysed in detail later in the thesis.

2.1.2 Roton and Maxon

Landau showed on the theory of superfluidity that phonons and rotons are elementary excitations of the superfluid phase. The rotons formed a local minimum of the dispersion relation $\epsilon = \Delta + \hbar^2 (k - k_0)^2 / 2\mu$, where Δ is the height of the local minima, k_0 is the roton wave number and μ determines curvature for Helium superfluid. Rotons were suspected to be the origin of vortices which is how they got their name but experiments have not confirmed anything conclusive [114]. The local maximum shown is known as maxon and the dispersion relation is known as the roton-maxon spectrum.

Roton originates from the nontrivial momentum dependency of the inter-particle interactions and is limited to long-range interactions. In search of rotons in DBEC, we present the example of quasi-2D dipolar BEC system by confining it tightly along the transverse direction i.e. perpendicular to the 2D plane of the condensate. Assuming a Gaussian distribution along the transverse direction, the modified dispersion relation will

(a) momentum dependence DI   (b) roton-maxon spectrum
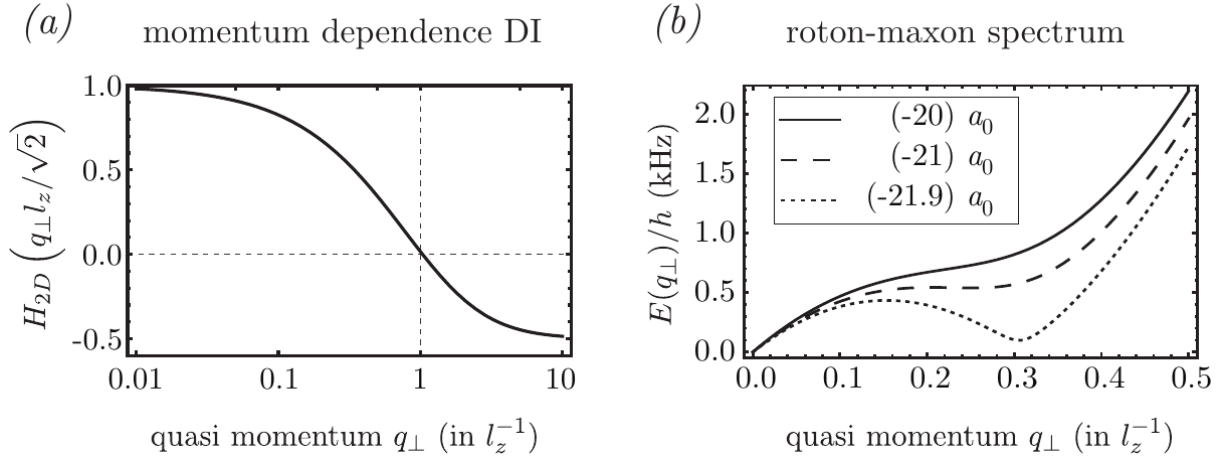
Figure 2.3:   Excitations in a 2D homogeneous dipolar BEC: (a) Function $H_{2D}(kl_z/\sqrt{2})$ captures the momentum dependence of dipolar interaction (DI) in quasi-2D. For k below l_z^{-1} DDI is effectively repulsive and vice versa. (b) Excitation spectrum of the quasi-2D dipolar BEC for three different values of scattering lengths displaying roton (dotted). The spectra are calculated for Chromium. Image taken from [115].

be,

$$\epsilon(k)^{2D} = \sqrt{\frac{\hbar^2 k^2}{2m}\left(\frac{\hbar^2 k^2}{2m} + 2n_{2D}\left[g + \frac{8\pi g_d}{3}H_{2D}\left(\frac{kl_z}{\sqrt{2}}\right)\right]\right)} \qquad (2.2)$$

where, k is limited to the transverse direction and l_z is the Gaussian widths determined by the confining trap frequency. The function $H_{2D}(x) = 1 - \frac{3\sqrt{\pi}}{2}|x|\exp[x^2]\text{erfc}[x]$. Although structurally this equation is similar to the 3D dispersion relation, an important difference can be seen in the DDI term regarding its dependence on the momentum. Due to a competition between a decreasing value of $H_{2D}(kl_z/2)$ and an increasing value of the free particle behaviour, a local minimum becomes plausible at an intermediate value of the momentum.

In analogy with the superfluid Helium dispersion relation, this local minima is known as roton [116] and the spectrum is a roton-maxon spectrum for a DBEC [78] Fig. 2.3. For this particular case of dipole orientation, if the quasi-2D condition is strictly obeyed i.e. $\mu << \hbar\omega_z$, then the system continues to remain stable. But, at the boundary of this condition when $\mu \sim \hbar\omega_z$ the system undergoes roton instability at a wave number $k > l_z^{-1}$ or in other words the dispersion relation acquires imaginary component at k. Under roton instability the unstable momentum does not necessarily include zero momentum, unlike phonon instability where the zero momentum becomes unstable. The above scenario is changed if the contact interaction is attractive. With $g < 0$, roton instability arises even under well satisfied quasi-2D condition at $k < l_z^{-1}$. Here the DDI has an effectively stabilizing effect and the attraction from the local interaction induces roton [117].

The roton instability may arise in quasi-1D conditions as well which has been theoretically studied in [118]. Presence of roton can be revealed in lowering of the superfluid critical velocity [78] in the calculation of Landau criterion and also with the help of Faraday patterns [119]. Please note that although the calculations were done for homogeneous condensates, they give a qualitative understanding for trapped condensates as well.

In some other important studies, a roton-like dispersion of the excitations was found in an oblate dipolar BEC in numerical studies [120, 65] where angular and radial rotons were found with the BEC obtaining a biconcave density profile. Interestingly, stable modulations have been shown to exist under certain trapped conditions where the distance between the density maxima is proportional to the inverse of characteristic roton momentum [121]. Post-roton instability dynamics has been researched widely in search of novel supersolid phase, i.e. self-assembled density modulations because the instability occurs at a specific value of the momentum. Driving a stable DBEC into the roton unstable regime fragments the system into a multi-peak structure [122], which is in analogy with the classical rosenweig instability phenomena. In [123] it is shown numerically that in the mean-field theory supersolid states of dipolar BEC are unstable.

2.2 Low lying excitations in trapped condensates

In trapped condensates, low-lying excitations are another indicator of stability, but the situation is vastly different. The trapped gas can demonstrate single-particle type excitations in contrast to the uniform Bose gas which has no single-particle like states at energy lower than the chemical potential [28]. In the limit when the trapping dominates the interactions the excitation spectrum recovers the harmonic oscillator excitation $\omega = n_x \omega_x + n_y \omega_y + n_z \omega_z$, where $\omega_{x,y,z}$ are harmonic trap frequencies along x, y and z direction. In case, the interaction energy dominates (for simplicity, say, the short range interaction) the trap energy a different sort of dispersion relation is obtained which are analogous of phonons [10].

One of the important oscillations that needs to be mentioned early on is the motion of the center of mass of the cloud. The motion of the center of mass is exactly decoupled from the internal degrees of freedom of the system in the presence of harmonic trapping and it oscillates with the frequency of the harmonic trap. This is a general property of interacting gas in harmonic confinements and is readily used to verify the numerical accuracy of theoretical studies as well as to test the harmonicity of the confinements during experiments [124, 125]. Here we mention that an interesting deviation from this behaviour is observed in our study consisting of multilayer dipolar BECs, a detailed analysis of which is shown in Chapter 4. While we shall limit our studies to the low energy excitations, it should be mentioned that high energy states are important tools to study the thermodynamic behaviour of the cloud.

2.2.1 Width modes

In the interaction dominated regime these excitations technically should be studied using nonlocal Bogoliubov-de Gennes equations but easier approximations have been made [26, 27] to tackle this problem. The most popular method is the dynamic variational principle, which was initially developed for a contact interacting BEC [126, 127] and extended to the case of DBEC [128]. For a start a variational ansatz is introduced,

$$\psi(x,y,z,t) = A(t) \prod_{\eta=x,y,z} e^{-\frac{\eta^2}{2\omega_\eta(t)} - i\eta^2 \beta_n(t)} \tag{2.3}$$

where dynamic variational parameters are the normalization factor $A(t)$, the Gaussian widths $\omega_\eta(t)$ and the phases $\beta_\eta(t)$. The variational parameters give equations of motion and their stationary solutions providing the BEC ground state. Small oscillations away from the ground state are the lowest lying modes, which can be indicative of the collapse and expansion instabilities. In non-dipolar BEC, the relevant modes at low energies are the two quadrupole-like modes [Fig. 2.4(Mode 1 and 3)] and a monopole mode or breathing mode (Mode 2). The latter one becomes unstable at the advent of collapse brought on by the change in sign of the scattering length. The frequency of the breathing mode goes to zero proportional to $|\gamma - \gamma_c|^{1/4}$ when γ approaches γ_c from below. Here γ denotes the ratio of the non-linear energy to the trap energy, and γ_c is correspondingly its critical value [129, 130].

The character of the modes also give an insight towards the dimensionality of the condensate. In lower dimensions, the degrees of freedom in confining directions become independent of the rest and the corresponding mode also reflects this e.g. in quasi-2D case, the axial and radial modes get independent of each other completely. Such decoupling can also be a result of strong anisotropic deformations of the cloud.

For dominantly dipolar gases the situation is similar to contact BEC case only for strongly cylindrical traps with dipoles oriented along the axis. In this situation the lowest mode is a breathing mode, and its frequency tends to zero as $|\gamma - \gamma_c|^\beta$, with $\beta \sim 1/4$. But, numerical analysis indicates that the geometry of the zero frequency mode becomes a superposition of the two quadrupole-like modes. Close to γ_c, β grows up to the value ~ 2. These results imply a completely different character of the collapse dynamics for a dipolar BEC. In later parts of the thesis, the richness in the physics of excitations shall be discussed due to the breaking of axial symmetry in dipolar BECs due to the tilting of dipoles.

In [65], an efficient method has been developed to solve the BdG equations for cylindrically symmetric DBEC. It allowed the study of excitations in both cigar and pancake-shaped traps along with condensate depletion.
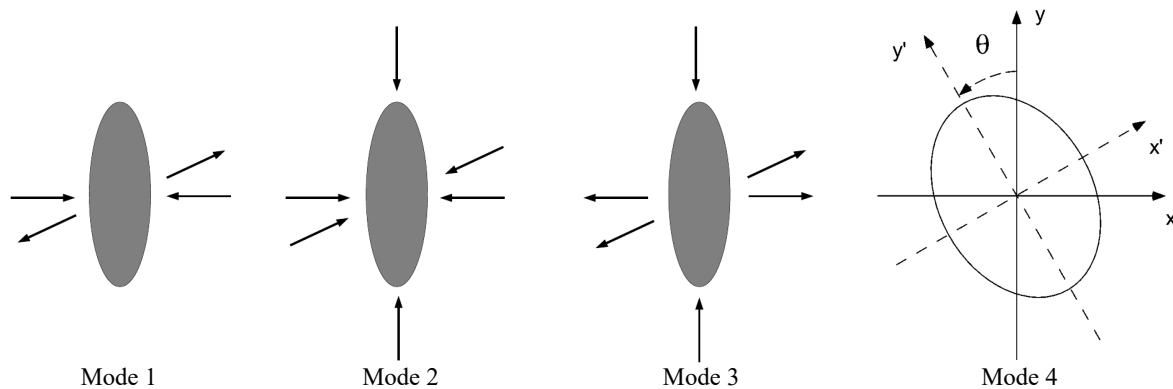
Figure 2.4: Modes 1 and 3 are 'quadrupole'-like, mode 2 is the breathing 'monopole' mode. Excitation of scissors mode (mode 4) by rotating the eigen-axis of an anisotropical trap suddenly. Image taken from [28, 131].

2.2.2 Angular mode

Aside from width oscillations, angular oscillations[Fig. 2.4(d)] also emerge in BECs which is closely linked with superfluidity as manifestations of superfluidity are associated with rotational phenomena [132, 133, 131]. This is known as the scissors mode, which is borrowed from nuclear physics where it corresponds to the out-of-phase rotation of the neutron and proton clouds [134]. For deformed potentials, the restoring force associated with the rotation of the cloud in the $x - y$ plane goes as ϵ^2 where ϵ is the deformation parameter of the trap and the mass parameter is the moment of inertia. For a superfluid system this is given by the irrotational value and is hence proportional to ϵ^2. So, although the confinement anisotropy vanishes the frequency of the oscillation approaches a non-zero value [12].

2.3 Parametrically induced excitation

Apart from natural instabilities or small perturbations in the system, excitations can also be induced via external force, often in the form of periodic driving. This allows a study of controlled excitation and manipulation to meet our desired goal. A variety of tuning parameters associated with BEC ensures experimental feasibility of parametrically induced excitation [135–139]. Depending on the geometry and the applied force the excitation maybe of local nature inducing surface modulations or may induce single particle modes or a mixture of both. Usually, small driving amplitudes have been shown to produce complicated Faraday waves in different geometries and systems while strong amplitude drive leads to chaotic and turbulent behaviour [140, 141].

2.3.1 Faraday patterns

Faraday waves are standing wave patterns on the interface of a fluid subjected to transverse oscillations. After a critical frequency of vibrations a flat hydro-static surface becomes unstable which was first described by Michael Faraday in 1831 [142]. These patterns oscillate at half the driving frequency and can take complicated structures such as stripes, hexagons and quasi-periodic patterns etc . In case of Bose gas, the transverse oscillations may be imitated by parametric modulation which results in surface patterns. Faraday patterns have been theoretical investigated in both non-dipolar [143] and dipolar homogeneous BEC [119] and have shown the resonant behaviour of the emerging patterns with the dispersion curve. Experimental probe includes liquid Helium system in which a vessel is vertically shaken in a way similar to the classical fluid case [144] and Rubidium BEC system in which Faraday waves were excited by modulation of the transverse trap frequency of a cigar-shaped BEC [145].

In the BEC experiments, which includes trap, the density is not homogeneous. External driving excites the transverse breathing mode at a frequency of 2ω where ω is the transverse trap frequency. This mode strongly couples to the density, thereby to the nonlinear interactions of the condensate resulting in the longitudinal sound waves. These sound waves create Faraday waves. Effect of both the driving frequency and amplitude has been quantitatively studied in [144]. Besides modulation of trap, modulation of scattering length with the help of Feshbach resonance allows a different method to incorporate external driving. This was done in a quasi-2D Cs BEC with both large amplitude and frequency of driving resulting in the stimulated emission of matter-wave jets [146]. In contrast, for lower modulation frequencies no resonances are found, but with strong modulation amplitude an irregular granulated distribution occurs instead of Faraday waves, which is outside the scope of a mean-field approach [147]. Instead, the granulated condensate is shown to affected by large quantum fluctuations and correlations.

2.3.2 Mode-locking

In the 17th century the Dutch physicist Christian Huygens noted synchronized motion of two clocks hanging back-to-back on the wall. Dissipative systems with competing frequencies, originating inherently or externally due to forcing, often show this kind of locking. However, if a non-dissipative trapped BEC is subjected to an external frequency sweep of quasi-periodic driving of the form $\sin \gamma t^2$, interestingly the system develops breathing mode excitation whose frequency is equal to the natural frequency of the system. The system is locked to this frequency for a long time despite the changing frequency of the external driving. In [148] the frequency locking takes places both for the ground state and excited states of the condensate. Solitons are also expected to get excited into breather states by the driving field. Mode-locking ensures that the amplitude of the resulting ex-
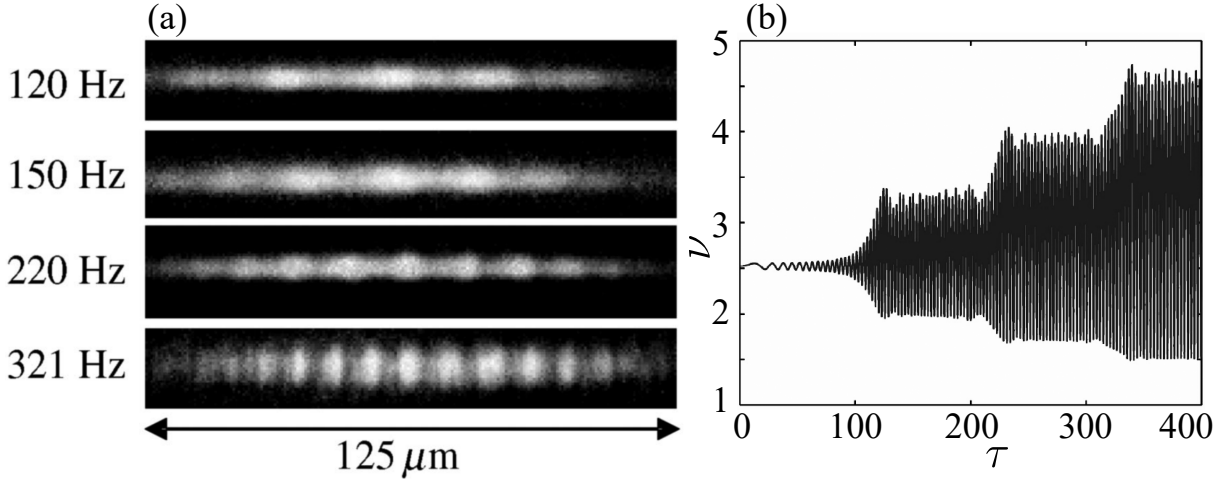
Figure 2.5: (a) In-trap absorption images of Faraday waves in a BEC. Frequency labels for each image represent the driving frequency at which the transverse trap confinement is modulated [145] (b) The dynamics of the width of the condensate: The condensate starts to respond periodically approximately $\tau \sim 111s$ but there are additional superharmonic nonlinear resonances [148].

citation is controlled and the system does not get destroyed due to heating for a long time.

Similar chirped frequency modulation has also been theoretically studied [149] in an anharmonically trapped BEC. Depending on the interplay of parameters involved, two very different kinds of excitations exist: the quantum energy ladder climbing and semi-classical autoresonance. Mode-locking is the result of a bounded phase-mismatch between the driving frequency and the self-adjusting nonlinear frequency of the system. Both the interaction of the particles and the anharmonic trap have a profound effect on the dynamics of the condensate because harmonic trap does not allow for either ladder climbing or autoresonance. The interaction affects the details of the driven-chirped excitation with applications in quantum state control. Note that for vanishing nonlinear interaction the autoresonance effect also vanishes.

In case of ladder climbing, the population is transferred from the ground quantum state to the first excited state, from first to second and so on such that only two energy eigenstates are resonantly coupled at any time. The classical counterpart of this effect is autoresonance where the energy transfer is gradual and the excitation amplitude grows continuously. Here the two level approximation breaks down and several levels can simultaneously resonate with the driving. Autoresonance has found applications in hydrodynamics [150, 151], nonlinear optic [152], plasma [153], molecular physics [154] etc.

In chapter 4, we study the quantum energy ladder climbing of two layers of non-overlapping quasi-1D BEC in harmonic trap and transfer of mode-locking between them.

Chapter 3

Dipolar Bose-Einstein condensates in Pancake-shaped Confinement

Current chapter is an adaptation of the research articles "Two-dimensional bright solitons in dipolar Bose-Einstein condensates with tilted dipoles" [155] and "Dipolar condensates with tilted dipoles in a pancake-shaped confinement" [156]. We exploit the anisotropic nature of dipole-dipole interaction in a quasi-2D dipolar BEC by tuning the polarisation angle. Its effect on stability-instability conditions, post-instability dynamics have been explored. Our results show that the roton momentum may be tuned by the tilting angle. We discover a new type of instability and a new class of solution emerging due to tunable tilting angle.

3.1   Introduction

The anisotropic nature of dipolar Bose-Einstein condensate has led to the discovery of extremely rich phenomena that are otherwise absent in a traditional short-range inter-acting BEC. In this chapter we focus on dipolar BEC in a pancake-shaped confinement geometry. We have already seen that the attractive component of dipolar BEC can lead to collapse instability in mean-field regime if it is dominant over the repulsive interactions present in the system [48]. Hence it is of a fundamental importance to understand the stability and instability properties and how it is influenced by the trapping geometry[157]. Our work aims to generalise the study by introducing the polarisation angle of the dipole moment as a tunable parameter. The tilting angle brings in new phases [158, 159] and its unique anisotropic characteristics to system properties [160, 161].

   The tilting angle is defined with respect to the axis of the condensate. We study the stability and properties shown by the condensate under the effect of this tunable polarisation angle. We begin by emphasizing the fundamental difference between a quasi-2D condensate and a purely 2D-condensate. Later, the domains of various instabilities,
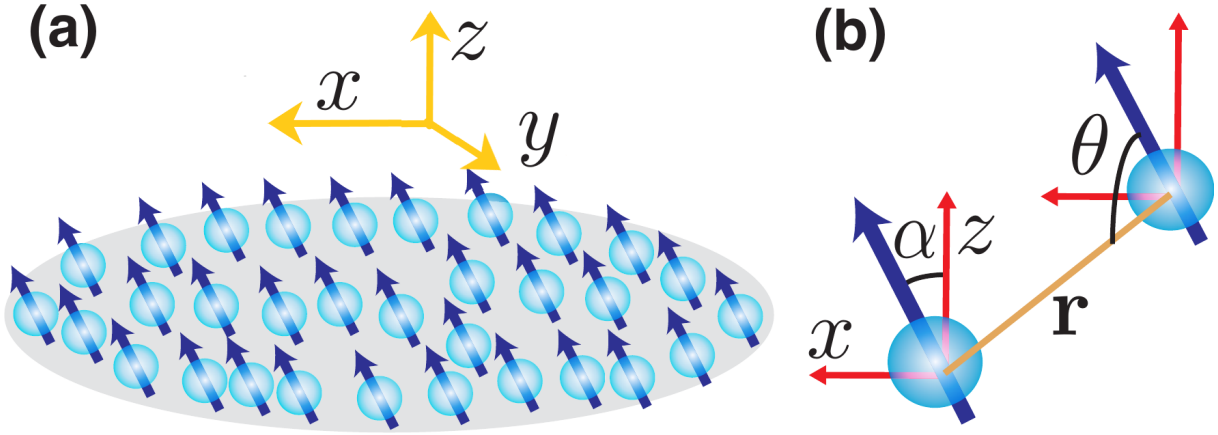
Figure 3.1: The schematic setup of dipolar BEC confined in the $x-y$ plane with a strong harmonic confinement along the z axis. (b) The dipoles are polarized in the $x-z$ plane with tilting angle α with respect to the z axis and θ is the angle between the dipole vector and the radial vector $\mathbf{r}$.

including a new one, are identified, followed by their post-instability dynamics. The effect of tilting angle on Bogoliubov spectrum brings into light the fact that roton minimum can, in fact, be varied, in contrast to the belief that it is fixed by the trapping geometry. We discuss the emergence of solitons from post-instability dynamics of phonon unstable regime followed by characterising anisotropic soliton solutions thoroughly. A new class of solution is found where a quasi-2D dipolar BEC was found to self-trap along one direction. Under sufficiently low dipolar strengths, it is found possible to have stable solitons even with attractive contact interactions.

3.2 Setup

Consider a BEC of N atoms with dipole moment d under the effect of a sufficiently large external field [Fig. 3.1(a)]. The orientation of the dipole vector is restricted in the $x-z$ plane forming an angle α with the z-axis. The DDI is described by

$$V_d(\mathbf{r}) = g_d(1 - 3\cos^2\theta)/r^3$$

where θ is the angle between the dipole vector $\mathbf{d} \equiv d(\sin\alpha \; \hat{x} + \cos\alpha \; \hat{z})$ and the radial vector $\mathbf{r}$, $g_d = \mu_0 d^2/4\pi$ is the strength of the DDI. These equations are equally valid for polar molecules as well, except the strength of the DDI changes to $g_d = d^2/4\pi\epsilon_0$. At ultracold temperatures the system can be described by a non-local Gross-Pitaevskii

equation (NLGPE):

$$i\hbar\frac{\partial}{\partial t}\Psi(\mathbf{r},t) = \left[-\frac{\hbar^2}{2m}\nabla^2 + V_t(\mathbf{r}) + g|\Psi(\mathbf{r},t)|^2 + \int d\mathbf{r}' V_d(\mathbf{r}-\mathbf{r}')|\Psi(\mathbf{r}',t)|^2\right]\Psi(\mathbf{r},t),$$

(3.1)

The total number of particles is $\int d\mathbf{r}|\Psi(\mathbf{r},t)|^2 = N$, $g = 4\pi\hbar^2 a/m$ is the two-body short-range contact interactions strength and a is the s-wave scattering length. The system is confined in a pancake-shaped trap of the form $V_t(\mathbf{r}) = m(\omega_\rho^2\rho^2 + \omega_z^2 z^2)/2$ such that $\omega_z > \omega_\rho$. If the 2D system chemical potential, $\mu_{2D} << \hbar\omega_z$, quasi-2D condition is achieved. In the absence of a radial trap $\omega_\rho = 0$, the condensate wave function can be written as $\Psi(\mathbf{r},t) = \sqrt{n_{2D}}\psi(z)e^{-i\mu t/\hbar}$ where n_{2D} is a constant homogeneous density. The radial and axial components becomes separable and we obtain an expression for $\psi(z)$ as,

$$\left(\frac{-\hbar^2}{2m}\frac{d^2}{dz^2} + \frac{m\omega_z^2 z^2}{2} + g_{eff}|\psi(z)|^2 - \mu\right)\psi(z) = 0,$$

(3.2)

where $g_{eff} = g + \frac{4\pi g_d}{3}(3\cos^2\alpha - 1)$. This derivation is shown in detail in Appendix E.1.1. This incorporates α directly in the equation. Two different regimes maybe accessed by changing g_{eff} [88]: (i) three-dimensional (3D) or Thomas-Fermi (TF) if g_{eff} is large and (ii) Q2D if g_{eff} is small.

3.2.1 2D vs quasi-2D

Quasi-2D regime restricts any dynamics along z direction and the condensate is assumed to remain in the ground state of the tight harmonic confinement. Under single mode approximation and when $\mu_{2D} << \hbar\omega_z$, we may assume $\phi(z) \propto \exp[-z^2/2l_z^2]$ where $l_z = \sqrt{\hbar/m\omega_z}$ is the characteristic length associated with ω_z. The 3D wave function may be separated as $\Psi = \phi(z)\psi(x,y)$ and an effective 2D NLGPE is obtained after integrating $\int dz$,

$$i\hbar\frac{\partial}{\partial t}\psi(x,y,t) = \left[-\frac{\hbar^2}{2m}\nabla_{x,y}^2 + \frac{m\omega_\rho^2\rho^2}{2} + \frac{g}{\sqrt{2\pi}l_z}|\psi(x,y,t)|^2 + \frac{2g_d}{3l_z}\int\frac{dk_x dk_y}{(2\pi)^2}e^{i(k_x x + k_y y)}f(k_x,k_y)\tilde{n}(k_x,k_y)\right]\psi(x,y,t)$$

(3.3)

where $\tilde{n}(k_x,k_y)$ Fourier transform of $|\psi(x,y)|^2$ and the final term is calculated after Fourier transforming the 3D DDI using convolution theorem,
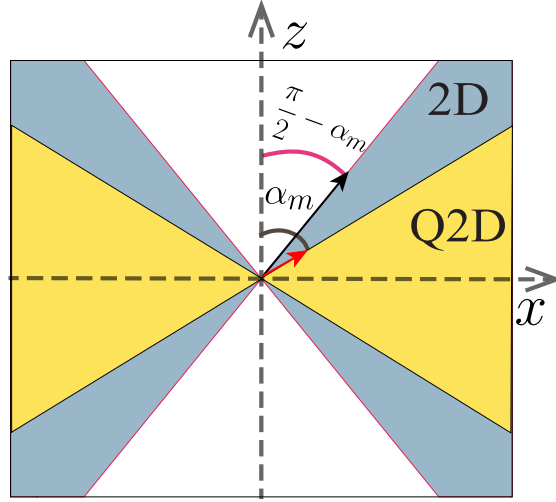
Figure 3.2:   (a) The dipoles are oriented in the xz plane forming an angle α with the z-axis. (b) For $\alpha_m < \alpha < \pi/2$ a purely Q2D dipolar condensate is unstable against collapse, indicated by smaller (yellow) shaded region, but an ideal 2D layer of dipoles is unstable when $\pi/2 - \alpha_m < \alpha < \pi/2$, indicated by the larger (gray) shaded region. Here, $g = 0$.

$$V_d(k) = \frac{4\pi g_d}{3} \left[\frac{3(k_x^2 \sin^2 \alpha + k_x k_z \sin 2\alpha + k_z^2 \cos^2 \alpha)}{k_x^2 + k_y^2 + k_z^2} - 1 \right] \tag{3.4}$$

to obtain,

$$
\begin{aligned}
f(k, \theta_k) &= \sqrt{2\pi} \left(3\cos^2 \alpha - 1 \right) + 3\pi \, e^{k^2/2} k \, \text{erfc}\left(\frac{k}{\sqrt{2}} \right) \\
&\times \left(\sin^2 \alpha \cos^2 \theta_k - \cos^2 \alpha \right),
\end{aligned} \tag{3.5}
$$

where we have used the dimensionless polar coordinates $\left(k \equiv l_z \sqrt{k_x^2 + k_y^2} \text{ and } \theta_k \right)$, and erfc$(x)$ is the complimentary error function.

Let us consider a quasi-2D homogeneous case ($\omega_\rho = 0$). In experimental scenario, this usually corresponds to the central regions of a Thomas-Fermi condensate density in a shallow radial trap. However, instead of using a Thomas-Fermi wave function in our theoretical approach the wave function maybe written as $\psi(x, y, t) = \sqrt{n_{2D}} e^{-i\mu_{2D} t/\hbar}$ where $\mu_{2D} = g_{eff} n_{2D}/\sqrt{2\pi} l_z$ under local density approximation. μ_{2D} can be easily calculated by replacing the expression for $\psi(x, y, t)$ in Eq. (3.3) and following the procedure as done in Appendix E.1.1. Note that the kinetic energy term vanishes due to uniform density and it also introduces delta functions in the final term $\tilde{n}(k_x, k_y) \propto \delta(k_x)\delta(k_y)$. For $g = 0$, the only relevant factor in DDI term is $f(k_x = 0, k_y = 0) = \sqrt{2\pi}(3\cos^2 \alpha - 1)$. For a negative chemical potential it has been shown that the homogeneous density is unstable against collapse. This may also lead to the dynamic formation of bright solitons [162]. When

$g = 0$, the instability condition is satisfied whenever $\mu_{2D} < 0$ i.e. $\alpha > \alpha_m = \cos^{-1}(1/\sqrt{3})$, where α_m is called the magic angle. Interestingly one would expect this angle to be at $\alpha > \pi/2 - \alpha_m$ at first glance. In fact, this is indeed the case for a purely ideal 2D condensate where $l_z \to 0$. It is easily seen that instability starts at $\alpha = \pi/2 - \alpha_m$ when we consider a $V_d(x, y, z = 0) = (1 - 3x^2/\rho^2)$ for a $\rho = \sqrt{x^2 + y^2}$ [159] as shown in Fig. 3.2. From this we conclude that the transverse extension of the cloud is a key factor in reducing the instability window, especially when we consider the generalised case of a tilted dipoles. This remains true for fermionic systems as well [163].

In Fig. 3.2 we show the instability region(gray area) for an ideal 2D setup and a quasi-2D set-up (overlapping yellow area). Angle $\alpha_m > \pi/2 - \alpha_m$ and clearly the effect of a nonzero spatial extension along z axis helps stabilize against the collapse of the system due to attractive interaction by the DDI. Mathematically this difference arises because for quasi-2D setup the instability condition is calculated after the $\int dz$ integration while in an ideal 2D setup it's not necessary as there's no transverse spatial extension.

3.3 Bogoliubov Excitations

To get a better picture of the stability of the quasi-2D homogeneous system we turn to calculation of Bogoliubov excitation spectrum. The details of the calculations are portrayed in Appendix B. The low-lying excitations on the homogeneous density are of the form $\sim f_\pm(z) \exp[i\mathbf{q} \cdot \rho - i\epsilon t/\hbar]$, where $\mathbf{q}$ is the quasi-momentum in the 2D surface, ϵ is the excitation energy and $f_\pm = u \pm v$ with $\{u, v\}$ are the Bogoliubov functions. The Bogoliubov-deGennes (BdG) equations are obtained by replacing it in the full NLGPE and then linearizing $f_\pm(z)$ at $\psi(z)$,

$$
\begin{aligned}
\epsilon f_-(z) &= \left[\frac{-\hbar^2}{2m} \left(\frac{\partial^2}{\partial z^2} - q^2 \right) - \mu + \frac{1}{2} m\omega_z^2 z^2 + 3n_{2D}g_{eff}|\psi(z)|^2 \right] f_+(z) \\
&\quad + 4\pi g_d n_{2D} \psi(z) \int_{-\infty}^{\infty} dz' \psi(z') e^{-q_\rho|z'-z|} \left[\frac{q_x^2}{q_\rho} \sin^2\alpha - \right. \\
&\quad \left. q_\rho \cos^2\alpha - iq_x \sin(2\alpha) \mathrm{sgn}(z'-z) \right] f_+(z') \quad (3.6) \\
\epsilon f_+(z) &= \left[\frac{-\hbar^2}{2m} \left(\frac{\partial^2}{\partial z^2} - q^2 \right) - \mu + \frac{1}{2} m\omega_z^2 z^2 + n_{2D}g_{eff}|\psi(z)|^2 \right] f_-(z). \quad (3.7)
\end{aligned}
$$

Diagonalization of the corresponding Hamiltonian matrix of the Bogoliubov equations gives the necessary excitation spectrum. The lowest eigenvalue corresponds to the lowest lying excitations in $\mathbf{q}$. One can notice that the momentum dependence stems from only the dipolar term i.e. the final term in Eq. (3.6). Subsequently for certain parameters this term also leads to emergence of roton-maxon dispersion relation [78]. In a quasi-2D
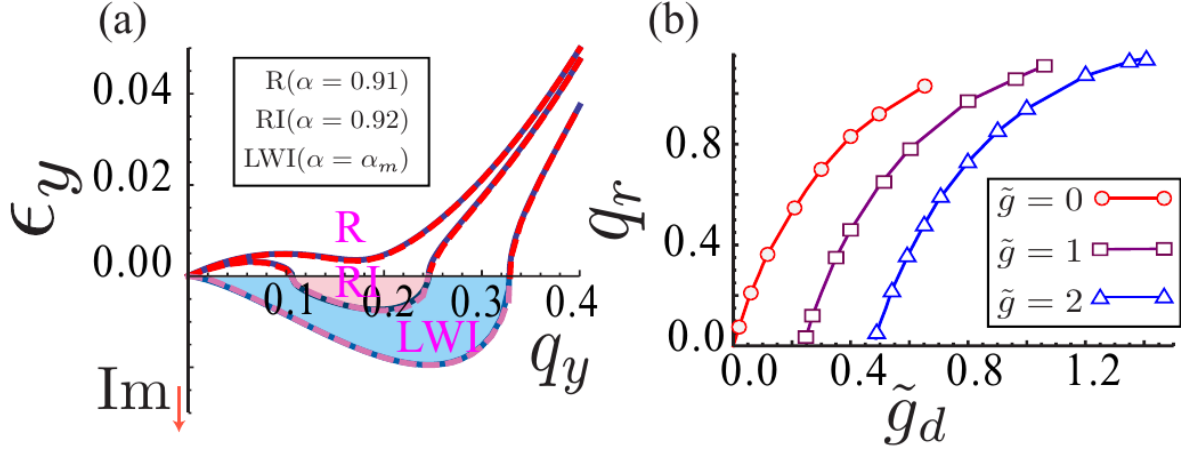
Figure 3.3:   (a) For the parameters $(\tilde{g}, \tilde{g}_d) = (0, 0.05)$ and different values of α, the Bogoliubov dispersion relation has been plotted along the q_y axis i.e. $\epsilon(q_x = 0, q_y)$. With these parameters the system satisfies the quasi-2D criteria $\mu_{2D} << \hbar\omega_z$. Comparative curves from purely 3D calculations (red dashed curve) from (??) and analytic quasi-2D calculations (solid blue curve) from (3.8) show excellent agreement. At $\alpha = \alpha_m$ the LWI instability, at $\alpha = 0.92$ rad the roton instability (RI) and at a lesser $\alpha = 0.91$ rad stable roton (R) is shown. The unstable imaginary component of $\epsilon(q_x = 0, q_y)$ is represented in the negative y-axis. (b) We define roton momentum q_r as the

regime the spectrum equations reduce to a simpler form, [161],

$$\epsilon(\mathbf{q}) = \sqrt{E_q\left\{E_q + \frac{2gn_{2D}}{\sqrt{2\pi}l_z}\left[1 + \frac{2\sqrt{2\pi}}{3}\beta f(q, \theta_q)\right]\right\}}, \tag{3.8}$$

The derivations are shown in detail in Appendix B. When $\alpha = 0$, there is no attractive component of the DDI across the 2D plane. The final term in Eq. 3.6 is negligibly small for $\alpha = 0$ when $qL << 1$ and a linear phonon spectrum can be obtained with a slope of $\sqrt{gn_{2D} + 8\pi g_d n_{2D}/3}$. The condition $qL << 1$ ensures we are in the long wavelength region where L is the width of $\psi(z)$. When we're in quasi-2D regime, $L \approx l_z$. In contrast, this slope changes when we are at $\alpha = \alpha_m$. At this magic angle if g is taken to be zero, we instead get $(E_q = 0, \alpha = \alpha_m)$

$$
\begin{aligned}
\epsilon(\mathbf{q} \to 0) \quad &\propto \quad \sqrt{f(\mathbf{q} \to 0)} \\
&\propto \quad \sqrt{g_d q(q_x^2 \sin^2\alpha_m - q^2\cos^2\alpha_m)} \\
&\propto \quad \sqrt{g_d q(q_x^2(\sin^2\alpha_m - \cos^2\alpha_m) - q_y^2\cos^2\alpha_m)} \\
&\propto \quad \sqrt{g_d q(q_x^2 - q_y^2)}
\end{aligned}
$$

We have used the relation $\sin^2\alpha_m - \cos^2\alpha_m = \cos^2\alpha_m$. Clearly, these are not standard phonon like excitations! Such excitations are characteristic to the anisotropic excitation of the DDI and can only be explored by tilting the angle to the magic angle. When

$g_d > 0$ these excitations become unstable for $q_y > q_x$ and we name it as long-wavelength instability (LWI) due to their emergence at low momenta and their nonlinear dependence on q_x and q_y with vanishing chemical potential, $\mu_{2D}(g = 0, \alpha = \alpha_m) = 0$. If g_d is increased keeping $g = 0$ and $\alpha = \alpha_m$, the region of LWI increases. However, when the tilting angle is decreased, this region is reduced such that unstable region is confined to only non-zero finite momenta. It is called roton unstable (RI) region. The maximum instability lies along the q_y axis. The system completely stabilizes upon further decrease of α and we obtain a stable roton-maxon spectrum along q_y axis. This behaviour is portrayed in Fig. 3.3 where new dimensionless parameters have been defined as $\tilde{g} = gn_{2D}/\hbar\omega_z l_z$ and $\tilde{g}_d = g_d n_{2D}/\hbar\omega_z l_z$. A comparative study between 3D calculations and quasi-2D calculation of Bogoliubov dispersion relation co-incides confirming that the parameters are in quasi-2D regime i.e. $\mu_{2D} << \hbar\omega_z$.

It is already established that the rotons are anisotropic since they're confined along q_y axis. But more importantly it is shown that quasi-2D rotons are possible even with $g = 0$ or $g > 0$ too while previously quasi-2D rotons have been explored only in the isotropic region($\alpha = 0$) with $g < 0$ [119]. It is clear that quasi-2D anisotropic rotons are purely a product of DDI. For $\alpha = 0$, it is possible to obtain rotons as well but the system doesn't remain in quasi-2D region any more as the required $\tilde{g}_d$ value is much higher and the criteria $\mu_{2D} << \hbar\omega_z$ is not well satisfied [164].

Another interesting consequence of tilting angle is the roton momentum q_r. It's generally found that $q_r \sim 1/l_z$ where l_z corresponds to the transverse length of the confining trap along z. However, previous studies were limited to $\alpha = 0$ case. Here, we show the continuous variation of q_r with respect to system parameters in Fig. 3.3(b). For each data point α has been adjusted until no such q_r can be found for $0 \leq \alpha \leq \pi/2$ as the system doesn't have stable roton any longer. The results are from a purely 3D calculation and the q_r varies from much lower values to $\sim 1/l_z$.

3.3.1 Phase diagram

All the findings have been succintly put together in the phase digrams discussed below. Our first goal is to identify the region of phonon instability(PI) for both $g < 0$ and $g > 0$. This is easily calculated by the condition $\mu_{2D} < 0$. Defining $\beta = g_d/|g|$ in Fig. 3.4 we show the PI regions in the $\alpha - \beta$ parameters space. For $g < 0$ the BEC usually collapses in the PI region (an exception is discussed later in the chapter) while post instability dynamics for $g > 0$ leads interesting solutions that will be discussed in the following sections. Henceforth we focus on only $g \geq 0$ cases. In Fig. 3.4(a) we observe two islands of PI region separated by the magic angle such that no continuous transition between the regions are possible. The bottom left region corresponds to $g_d < 0$ which is obtained with the help of rotating fields [44, 45] and the top right region corresponds to the usual
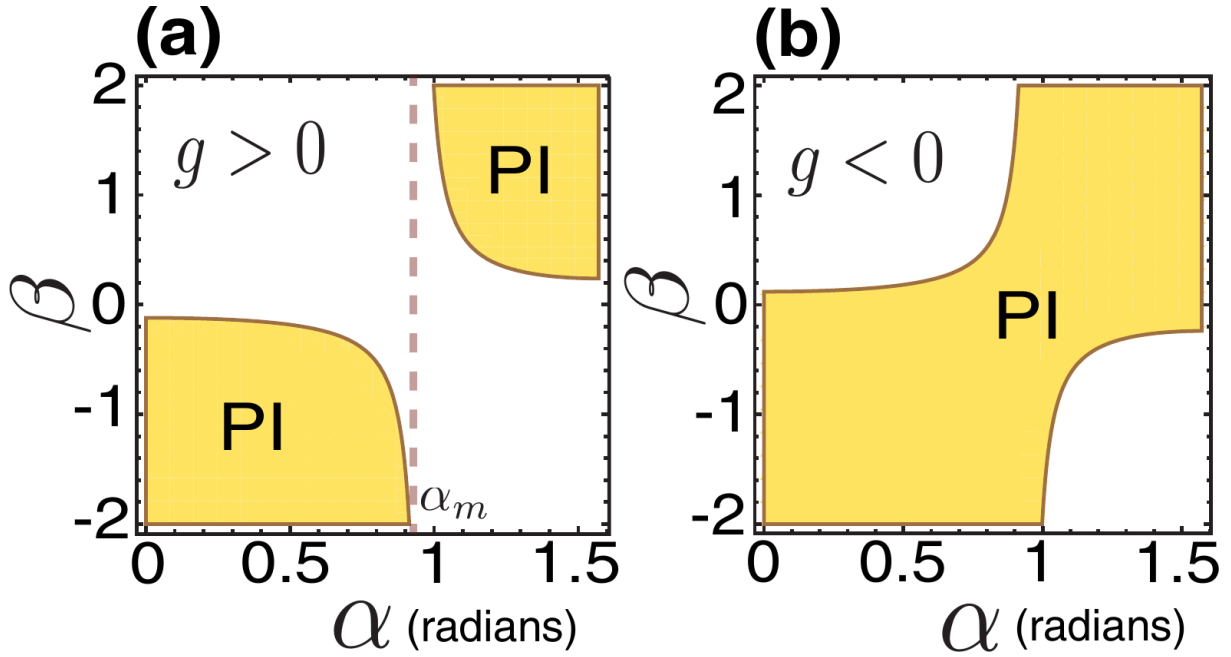
Figure 3.4:   Phonon instability region of a homogeneous quasi-2D dipolar BEC shown in $\alpha - \beta$ parameter space for (a)$g > 0$ and (b)$g < 0$. The dashed line corresponds to the magic angle α_m.

$g_d > 0$. The later island has high anisotropy compared to the former as the tilting angle is quite high and reaches the maximum value of $\pi/2$ there.

Upon finding the PI region, we now probe more thoroughly to also characterize the roton instability(RI), stable roton (R) and stable without roton(S) regions for $g_d > 0$ cases. This is done by fixing the value of $\tilde{g} = 0$ and a small positive value 0.1. For $\tilde{g} = 0$ in Fig. 3.5 The solid gray vertical line at α_m corresponds to the previously discussed LWI. This instability is changed to PI if $\alpha > \alpha_m$ for any positive value of $\tilde{g}_d$. Similarly for $\alpha < \alpha_m$ LWI shifts to RI. For $\tilde{g}_d$ less than approximately 0.48, just by changing the tilting angle one may go from S $\to$ R $\to$ RI $\to$ LWI $\to$ PI. The lower the value of $\tilde{g}_d$ the narrower the stable roton region becomes. This is because for small values of $\tilde{g}_d$, q_r arises at very small momenta and the system quickly goes to RI. LWI does not exist once $\tilde{g} \neq 0$. For $\tilde{g} > 0$, the PI region is modified as well such that it is possible to obtain stable dispersion relation even for $\alpha = \pi/2$ as long as $\tilde{g}_d$ is small enough. Introduction of a repulsive contact interaction slightly enlarges the S domain overall. While crossing from RI to PI, the nonzero finite unstable momentum region gradually increases until the zero momentum also is unstable and it's PI. The instabilities are a result of the attractive component present in the anisotropic DDI. Different types of instabilities arise due to the momentum dependence of the DDI, which is a result of its nonlocal nature. We have shown the unstable regions for the experimentally relevant dipolar atoms Chromium, Erbium and Dysprosium as well. In that case the $\tilde{g}_d$ is fixed by the dipole moment of the
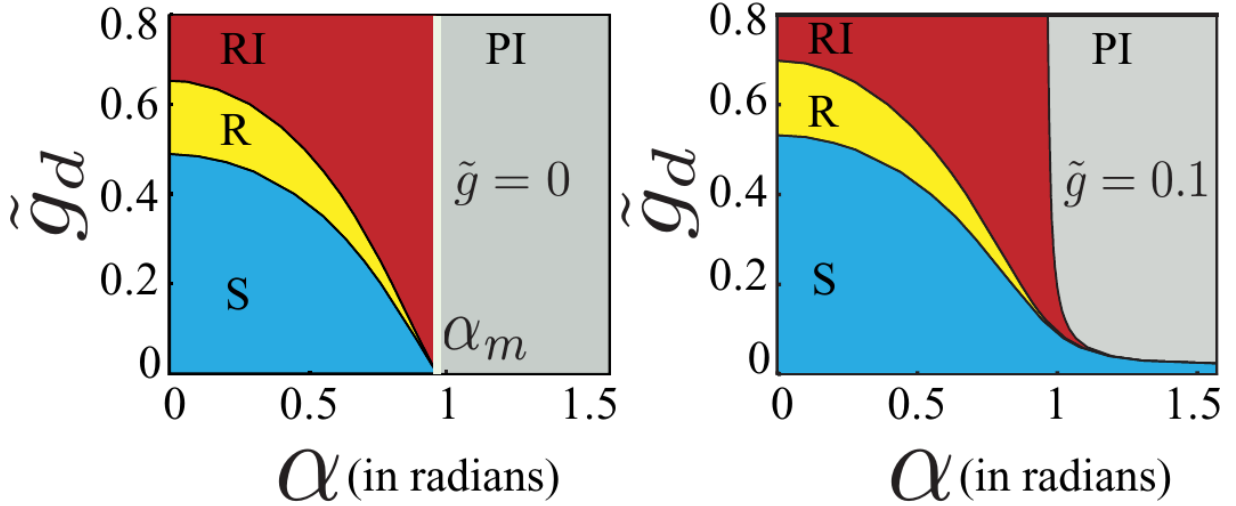
Figure 3.5:   Stability and various instability regions have been shown for a dipolar BEC tightly trapped along the z direction and homogeneous in the $x-y$ plane in the parameter space of $\alpha - \tilde{g}_d$. In left ($\tilde{g} = 0$) and in the right ($\tilde{g} = 0.1$) the stable (D), roton (R), roton unstable (RI) and phonon unstable (PI) and long-wavelength unstable (LWI) regions have been characterised. The phase diagrams have been obtained from a purely 3D Bogoliubov calculation.

atoms and the domains are plotted with respect to s-wave scattering length(a) and the tilting angle α for a homogeneous pancake-shaped condensate. The phase diagram spans over both negative and positive scattering lengths. Although the behaviour of the domain boundaries remain similar for all three atoms, the range s-wave scattering length scales to much larger magnitude for strongly dipolar Dy compared to weakly dipolar Cr. Highly negative a gives rise to PI and as it is reduced one may go from PI $\rightarrow$ RI $\rightarrow$ R $\rightarrow$ S for fixed α. For $\alpha > \alpha_m$ the R region becomes extremely negligible. It is easily noticeable that as α increases the instability boundaries move up. This can be explained using the fact that DDI gradually acquires an attractive component in the $x - y$ plane leading to stronger instability.

3.4   Post-instability Dynamics

Having discussed the various instabilities, we move on to post-instability dynamics. It was discussed for the first time that phonon instability may lead to dynamic formation of transient bright solitons [162] for $\alpha = 0$ or $\alpha = \pi/2$ case. This is in contrast to the collapse observed in phonon unstable regions in other systems such as non-dipolar BECs. For low density condensate, these solitons m ay survive for long time if they're also big enough. Such solitons also have inelastic collision properties where they merge to give larger solitons. Larger solitons can survive longer as they're more robust against atomic losses.
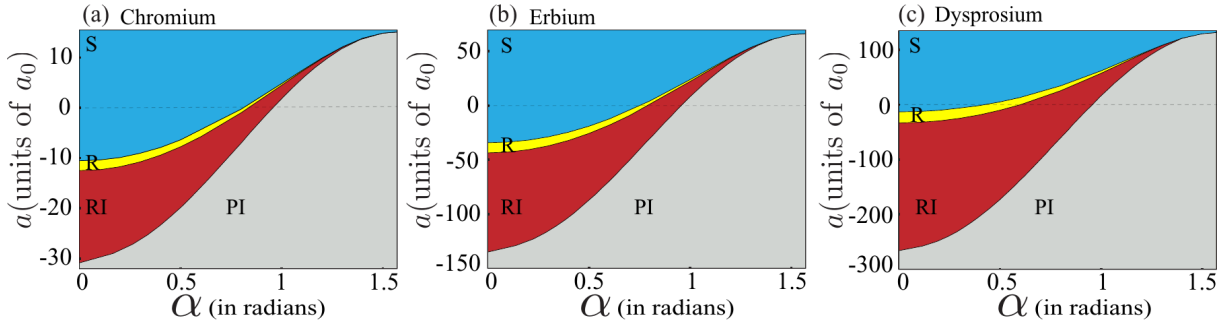
Figure 3.6:   For a fixed value of $\omega_z = 2\pi \times 800$ Hz and a low homogeneous density $n_{2D}/l_z = \sqrt{2\pi} \times 10^{20} m^{-3}$ the stability and instability regions have been identified for (a) Cr, (b) Er, and (c) Dy atom BECs. The parameter space is $\alpha - a$ and the boundaries have been obtained from a purely 3D Bogoliubov calculation.

The idea behind the formation of bright solitons is that in the nonlinear dipolar BEC system there is a balance between the repulsion and attraction which allows for the self-bound solutions. The repulsive part is obtained from the the kinetic energy, the contact interaction and the repulsive component of the long-range DDI (when $\alpha \neq 0$). The attractive part stems only from the DDI. The balance between them is in analogy with the dispersion and self-focusing nonlinearity of optical soliton in a nonlinear media. Without the DDI such a balance is not possible in quasi-2D BEC.

Here, the low density criteria also helps in maintaining the quasi-2D criterion. The phase diagram shown in Fig. 3.4 gives a first estimation of the region in which 2D solitons may be obtained.

3.4.1   Solitons formation

We simulate the NLGPE introduced in Eq. (3.3) in the PI parameter regime in real time. The real time evolution reveals the dynamic formation of transient soliton gas. The gas is metastable as these are excitations of the system and they eventually collapse in the long time scale, especially when the anisotropy is large. The metastable solutions indicate the potential existence of solitonic ground state solutions. The stability of such ground state solutions will be analysed in the next section. The real time dynamics is primarily influenced by the tilting angle and it has been shown in Fig. 3.7. We begin with homogeneous density with random local perturbations, two or three orders of magnitude less than the condensate density to characterise the Bogoliubov excitations. In real time evolution we initially observe the formation of stripe-like patterns with dislocation defects. At these defects two stripes merge into one. The density patterns in Fig. 3.7(a)-(b) is for $\alpha > \alpha_m$ generate for parameters in the top right island of Fig. 3.4(a). In this region the DDI is primarily attractive along x direction and repulsive along y. Hence the instability primarily occurs along y and the continuous symmetry is broken along y.
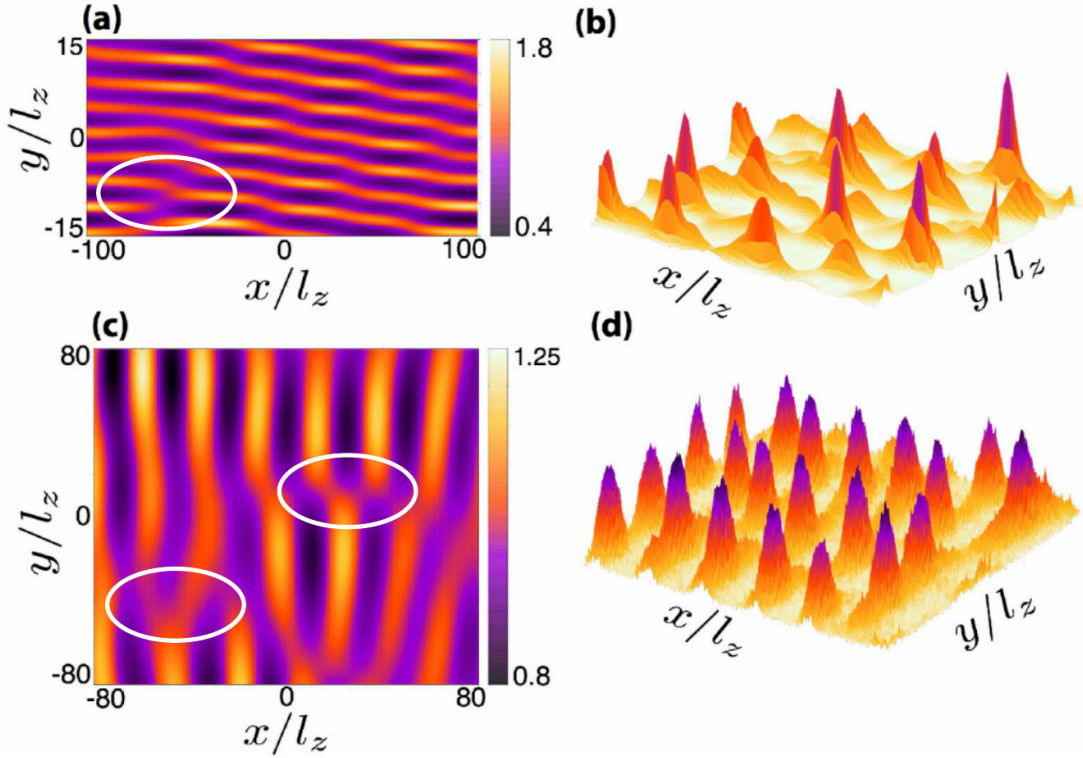
Figure 3.7: Transient stripe-like density patterns in post-PI dynamics shown for quasi-2D dipolar condensates. The top two plots have parameters $(\tilde{g}, \beta, \alpha) = (12/sqrt2\pi, 0.28, 1.35)$ at (a) $t = 13.5/\omega_z$ and (b) $t = 27/\omega_z$. The bottom two plots have parameters $(\tilde{g}, \beta, \alpha) = (40/sqrt2\pi, -0.20, 0.6)$ at (c) $t = 31/\omega_z$ and (d) $t = 90/\omega_z$. The dislocation defects have been emphasized within the ellipses.

This leads to stripe-like patterns parallel to the x-axis. In a contrasting case, for $\alpha < \alpha_m$ and parameters lying in the bottom left island of Fig. 3.4(a), the DDI is isotropically attractive for $\alpha = 0$ as β is negative. In this island for nonzero tilting angle, DDI is more attractive along y and less attractive along x. Here the stripes appear parallel to y as shown in Fig. 3.7(c)-(d). Fig. 3.7(a) and (c) depict the initial time stripe patterns which evolve into individual anisotropic solitons shown in (b) and (d) respectively at a later time scale. These anisotropic solitons may fuse into one another to form bigger solitons, however their lifetime depends on their density as already mentioned. Due to broken isotropy for any $\alpha \neq 0$ the movement of atoms are restricted and it results in a slower dynamics compared to the isotropically attractive DDI at $\alpha = 0$ case. Also, the stability of anisotropic soliton decreases as the minor axis of the soliton grows thinner.

3.4.2 Phonon vs roton instability

Here we first study the dynamics observed in RI regime and then compare it with previously shown PI dynamics. The real time evolution has been done in the RI region of Fig. 3.6(a) for a Cr atom BEC. We again evolve the Eq. 3.3 and 3.1 in real time and observe the formation of perfect stripe patterns in the post-instability dynamics. The stripes are
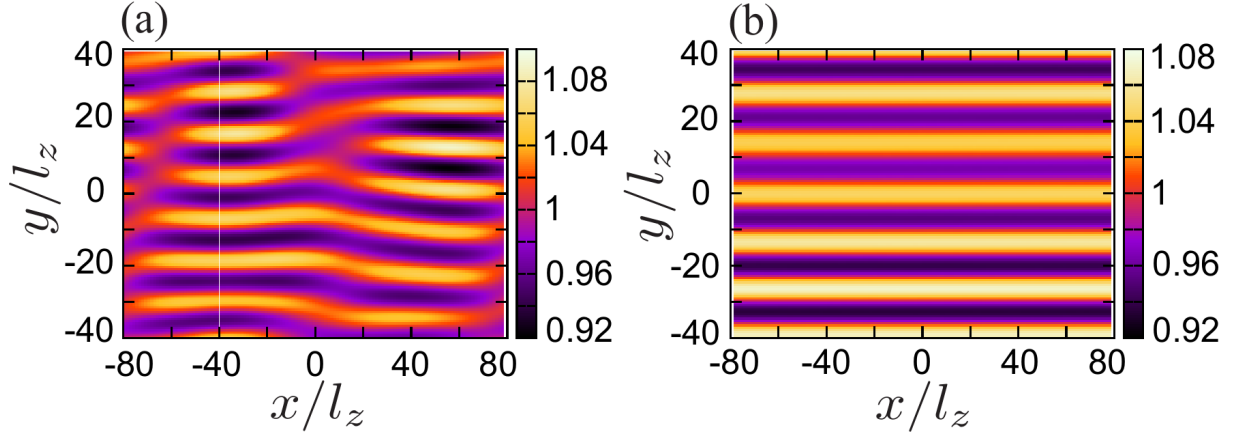
Figure 3.8: (a) The post-PI transient stripe-like density pattern with dislocation defects in a quasi-2D condensate and (b) the perfect stripe pattern without any dislocation defects in post-RI dynamics has been shown. The roton instability occurs in the q_y axis which is why the stripes are parallel to x axis. Defect-free stripes can be taken as a signature of RI. A Cr BEC has been considered with density $n_{2D}/l_z = 5\sqrt{2\pi} \times 10^{19} m^{-3}$, $\omega_z = 2\pi \times 800$Hz. For (a) $a = 0$ and $\alpha = \alpha_m + 0.14$ at $t = 100$ms while (b) $a = 5a_0$ with $\alpha = \alpha_m$ at $t = 16$ms.

parallel to the direction of attractive component of the dipole vector i.e. x-axis. The continuous translational symmetry is broken along y-direction.

The key difference between the PI and RI dynamics is the dislocation defect which is present (absent) in PI (RI) dynamics. The origin of this can be traced to the origin of the instability in Bogoliubov dispersion relation. In case RI, the most unstable momentum lies purely on the q_y axis and its q_x component is zero when DDI is attractive along x direction. This is not true for PI. Consider PI for $\alpha > \alpha_m$ where DDI is attractive along x-direction, similar to the RI case. However, the PI is inherently 2D in nature. The most unstable momentum has both q_x and q_y component although $q_y > q_x$. This results in dislocation defects. In fact, dislocation defects are good identifiers of whether the stripes are a results of PI or RI. Please note that for the isotropic case of PI and RI $q_x = q_y$. But once $\alpha \neq 0$, the most unstable momentum for RI only has q_y component.

The stripes due to RI are also transient. However they can be sustained for a longer time by adiabatically driving the system into stable roton (R) regime. The sysem, hence, takes a long time to come back to homogeneous density state by atomic losses. We also observe hopping of atoms between stripes as the background density is not zero duing intitial time evolution showing signatures of a metastable stripe supersolid state. The numerical results have been verified by both 3D and quasi-2D calculations. The time taken for the emergence of the stripes are dependent on the inverse of the unstable energy magnitude and the size of the stripes are dependent on the inverse of the unstable momentum.
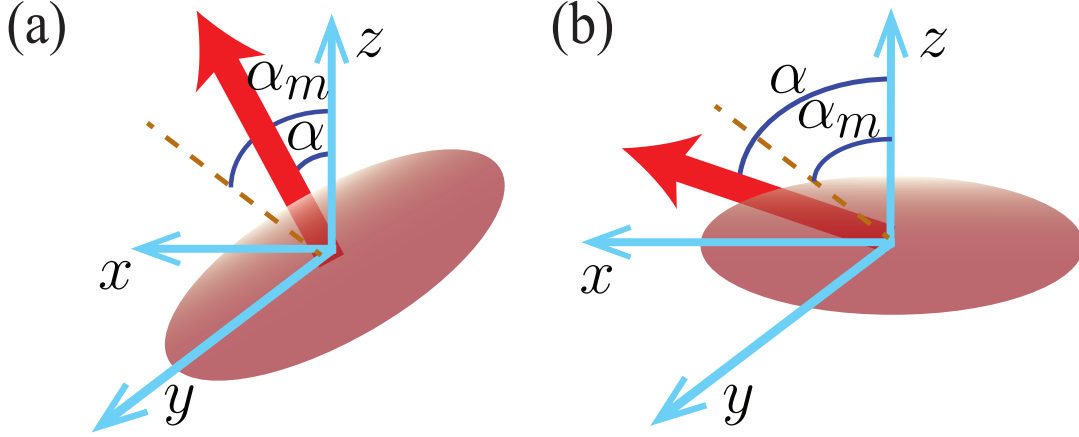
Figure 3.9: The figures (a) and (b) show the schematics of an equilibrium soliton for (a) $\beta < 0$ ($0 < \alpha < \alpha_m$) and (b) $\beta > 0$ ($\alpha_m < \alpha \leq \pi/2$). Dipole polarisation is along the red arrow in the $x - z$ plane. (a) The soliton is more elongated along the y axis and the aspect ratio is taken as $\gamma = L_x^{min}/L_y^{min}$ while for (b) the soliton major axis lies along x and aspect ratio is redefined to $\gamma = L_y^{min}/L_x^{min}$.

3.5   Stability and Properties of a Soliton

In this section we focus on the formation and stability of a single soliton in a quasi-2D scenario. We shall use fully 3D variational calculation for this purpose. We already know that solitons are stable in quasi-1D nondipolar BECs with attractive short-range interactions [93, 94, 165]. However, this is not true in higher dimensions. But for dipolar BECs for $\alpha = 0$ [162] and $\alpha = \pi/2$ stable solitons have been theoretically verified for repulsive contact interaction. Here, we shall study and seek stable solitons in a larger parameter space due to additional tuning parameter α. This allows us to discover newer soliton regime and solutions.

3.5.1   Energy minimization

We begin by considering a Gaussian ansatz to approximate a soliton solution in 2D.

$$\Psi_0(\mathbf{r}) = \frac{1}{\pi^{3/4} l_z^{3/2} \sqrt{L_x L_y L_z}} \exp\left[-\frac{1}{2l_z^2}\left(\frac{x^2}{L_x^2} + \frac{y^2}{L_y^2} + \frac{z^2}{L_z^2}\right)\right], \tag{3.9}$$

Using this the energy functional maybe evaluated,

$$E = \int d^3r \left[\frac{\hbar^2}{2m}|\nabla\Psi_0(r)|^2 + V_t(x,y,z)|\Psi_0(r)|^2 + \frac{g}{2}|\Psi_0(r)|^4 + \frac{1}{2}\int d^3r' V_d(r-r')|\Psi_0(r)|^2|\Psi_0(r')|^2\right]$$

where $V_t = \frac{m}{2}(\omega_x^2 x^2 + \omega_y^2 y^2 + \omega_z^2 z^2)$ is the 3D harmonic trap. The final expression for energy after substitution is,

$$
\begin{aligned}
\frac{E}{\hbar\omega_z} =\ & \frac{1}{4L_x^2} + \frac{1}{4L_y^2} + \frac{1}{4L_z^2} + \frac{L_z^2}{4} + \frac{\lambda_x^2 L_x^2}{4} + \frac{\lambda_y^2 L_y^2}{4} + \frac{\bar{g}}{4\pi L_x L_y L_z} \\
& + \frac{\bar{g}_d}{3L_z}\left[\frac{3\sin^2\alpha}{L_x^2 - L_y^2}\left(\sqrt{\frac{L_y^2 - L_z^2}{L_x^2 - L_z^2}} - \frac{L_y}{L_x}\right) + \frac{3\cos^2\alpha}{\sqrt{\left(L_x^2 - L_z^2\right)\left(L_y^2 - L_z^2\right)}} - \frac{1}{L_x L_y}\right] \\
& - \frac{2\bar{g}_d}{\pi}\int_0^{\pi/2} d\chi \frac{\cos^2\chi\sin^2\alpha - \cos^2\alpha}{\left[L_z^2 - \left(L_x^2\cos^2\chi + L_y^2\sin^2\chi\right)\right]^{3/2}} \\
& \qquad\qquad\qquad \times \tanh^{-1}\left(\frac{\sqrt{L_z^2 - \left(L_x^2\cos^2\chi + L_y^2\sin^2\chi\right)}}{L_z}\right), \quad (3.10)
\end{aligned}
$$

where $\lambda_{x,y} = \omega_{x,y}/\omega_z$, $\bar{g} = gN/\sqrt{2\pi}\hbar\omega_z l_z^3$ and $\bar{g}_d = g_d N/\sqrt{2\pi}\hbar\omega_z l_z^3$. Minimization of the expression gives us the ground state energy of a soliton $E^{min}[L_x^{min}, L_y^{min}, L_z^{min}]$ and its corresponding equilibrium widths. For a 2D soliton the $\lambda_x = \lambda_y = 0$. If the soliton is unstable against collapse or expansion instability we will not expect to have any equilibrium widths. This translates to non-existing finite minima for the energy functional. If the repulsive interaction dominates the soliton is unstable against an expansion and if the attractive interaction dominates it undergoes a collapse instability.

For $\alpha = 0$, stable isotropic solitons are possible only if [162],

$$
\frac{2\bar{g}_d}{3\sqrt{2\pi}} < 1 + \frac{\bar{g}}{(2\pi)^{3/2}} < \frac{-4\bar{g}_d}{3\sqrt{2\pi}}, \quad (3.11)
$$

The condition necessitates $\tilde{g}_d < 0$. For large values of g, the condition becomes $\beta < -3/8\pi$. Once $\alpha > 0$ istropy is lost, and $L_x^{min} \neq L_y^{min}$. We characterise the effect of the anisotropy on the 2D solitons by introducing the ratio $\gamma = L_i^{min}/L_j^{min}$ where $\{i,j\} \in \{x,y\}$.

Let us first consider the $\beta < 0$ cases from Fig. 3.10(a) and (c). The soliton aspect ratio is 1 at $\alpha = 0$ due to isotropic DDI. Once $\alpha > 0$, γ decreases because DDI is more attractive along y compared to x. This schematically shown in Fig. 3.9(a). As the total attractive interaction lessens in the system the size of the soliton gets bigger. The aspect ratio $\gamma = L_x^{min}/L_y^{min}$, however, shows a non-monotonous behaviour with respect to increasing tilting angle. The curve has been plotted until the soliton melts due to expansion instability. The reason there is a slight recovery in the anisotropy is because close to expansion instability the interaction energies are pretty low while the system size is pretty big. A more relevant contribution from kinetic energy helps reduce the anisotropy and hence the existence of a nonmonotonic character of the aspect ratio. Next, for $\beta > 0$ maximum anisotropy is obtained for $\alpha = \pi/2$ and then anisotropy can only be reduced
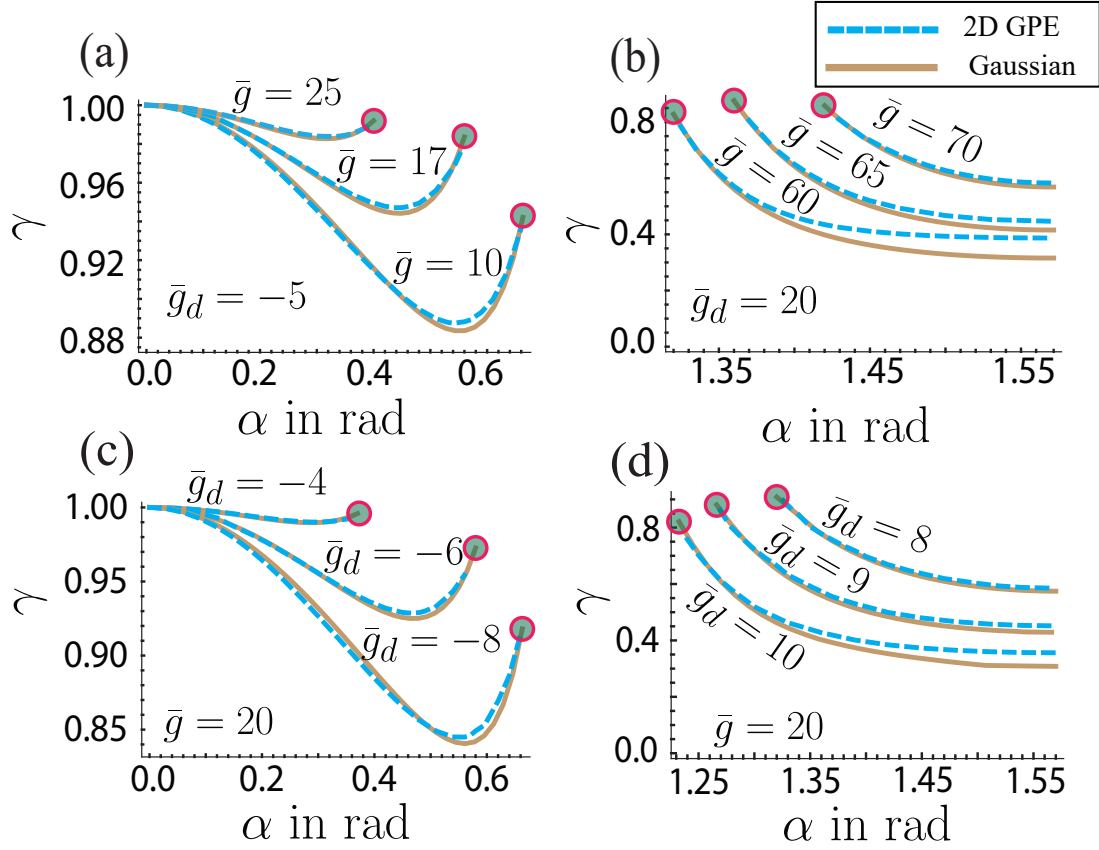
Figure 3.10: γ vs α plot shows the variation of soliton ansiotropy for different parameter regimes. Plot (a) and (c) are for $\beta < 0$ belonging to the bottom left island of Fig. 3.4 while (b) and (d) are for $\beta > 0$ from top right island of Fig. 3.4. The red dots at the end of each curve marks the stability boundaries for each curve beyond which expansion instability is met. The solid curves have been obtained from Gaussian calculations while the dashed curves are from numerics by solving Eq. (3.3).

by decreasing α. A schematic representation is shown in Fig. 3.9(b). The aspect ratio is defined as $\gamma = L_y^{min}/L_x^{min}$ for this case. This is depicted in Fig. 3.10(b) and (d). The curves gradually decreases until they meet with expansion instability. Also an increased anisotropy is related to larger values of $\bar{g}_d$ while anisotropy decreased for larger values of $\bar{g}$.

   In all subfigures in Fig. 3.10 we fix either $\bar{g}$ ($\bar{g}_d$) and have plotted for different values of $\bar{g}_d(\bar{g})$ with respect to α. The calculations are done both via Gaussian variational method (done by Meghana Raghunandan) and by solving Eq. 3.3 and found to have good agreement. The small deviations are obtained in regions where the actual solutions are less Gaussian in nature. However, the qualitative behaviours are retained by the variational method. Inclusion of α allows us to explore stable solitons with parameters where solitons were found to be unstable [95, 96]. This provides a larger parameter domain and ensures a more flexible experimentally realizable regime.
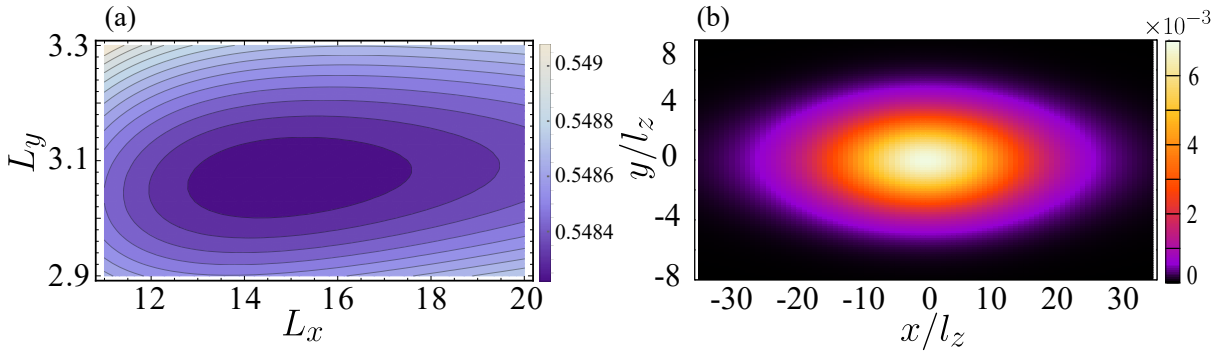
Figure 3.11: (a) The energy $E[L_x, L_y, L_z = 1]$ contours are depicted with respect to L_x and L_y showing the existence of a minimum for $\lambda_x = 0$ and $0 < \lambda_y < 1$. The parameter values are $(N, \alpha, \bar{g}, \omega_z, \omega_y) = (1000, \alpha_m, 0, 2\pi \times 800\text{Hz}, 2\pi \times 80\text{Hz})$. (b) The ground state density $|\psi(x, y)|^2$ for the same parameter regime showing self-trapping along x.

3.5.2 A new class of self-trapping

In the previous section we studied the standard quasi-2D soliton in a $x - y$ trapless condensate. We find a new class of solutions where the quasi-2D condensate is self-trapped only along one direction while it is trapped along the other. This solution is neither a traditional quasi-2D soliton because it is trapped along one direction, nor is it a quasi-1D soliton due to its 2D shape. It cannot be described by a quasi-1D GPE either. We consider trap along y and z direction and minimize the energy functional i.e. $\lambda_x = 0$ but $0 < \lambda_y < 1$. In Fig. 3.11(a), it is evident that there exists a minimum value even in the absence of any trap along x. The solution is quasi-2D in nature and in Fig. 3.11(b) we show the probability density of the same solution.

The origin of such solution can be explained by the anisotropic property of the Bogoliubov instabilities. This behaviour is further characterized by the calculation of modes of the solutions.

3.5.3 Lagrangian calculations

Here, we calculate the lowest-lying modes (ω) of the 1D self-trapped solutions using a variational method [126, 27]. The Gaussian ansatz now has time-dependent variational parameters:

$$\psi(x, y, z, t) = A(t) \prod_{\eta = x,y,z} e^{-\frac{(\eta - \eta_0(t))^2}{2w_\eta^2(t)}} e^{i\eta\alpha_\eta(t)} e^{i\eta^2\beta_\eta(t)}, \qquad (3.12)$$

where η_0, w_η, α_η and β_η are the variational parameters and $A(t) = \pi^{-3/4}/\sqrt{w_x w_y w_z}$ is the normalization constant. Applying this ansatz one needs to calculate the following Lagrangian density,

$$\mathcal{L} = \frac{i}{2}\hbar\left(\psi\frac{\partial\psi^*}{\partial t} - \psi^*\frac{\partial\psi}{\partial t}\right) + \frac{\hbar^2}{2m}|\nabla\psi(r,t)|^2 + V_t(y,z)|\psi(r,t)|^2 + \frac{g}{2}|\psi(r,t)|^2$$

$$+\frac{1}{2}|\psi(r,t)|^2\int dr' V_d(r-r')|\psi(r',t)|^2. \qquad (3.13)$$

The Lagrangian can be obtained by integrating the Lagrangian density as $L = \int d^3r\mathcal{L}$. Following this the Euler-Lagrange equations for the variational parameters can be obtained. Eliminating α_η and β_η can be done to obtain the relevant equations of motion for the widths alone. We obtain the Lagrangian:

$$L = \sum_{\eta=x,y,z}\left[\hbar\frac{\dot{\beta}_\eta w_\eta^2}{2} + \frac{\hbar^2}{2m}\left(\frac{1}{2w_\eta^2} + \alpha_\eta^2 + 2\beta_\eta^2 w_\eta^2\right)\right] + \frac{1}{2}m\omega_z^2\frac{w_z^2}{2}$$

$$+\frac{1}{2}m\omega_y^2\frac{w_y^2}{2} + \frac{g}{\sqrt{2\pi}}\frac{1}{4\pi w_x w_y w_z} + V(w_\eta),$$

$$(3.14)$$

where

$$V(w_\eta) = \frac{1}{2}\frac{1}{(2\pi)^3}\int d^3k\tilde{V}_d(\mathbf{k})\prod_{\eta=x,y,z}e^{-\frac{k_\eta^2 w_\eta^2}{2}} \qquad (3.15)$$

with $\tilde{V}_d(\mathbf{k})$ the Fourier transform the dipole-dipole potential. Then, the equations of motion for $\alpha(t)$ and $\beta(t)$ are:

$$\alpha_\eta = \frac{m}{\hbar}\left(\dot{\eta}_0 - \frac{\dot{w}_\eta \eta_0}{w_\eta}\right) \qquad (3.16)$$

$$\beta_\eta = \frac{m\dot{w}_\eta}{2\hbar w_\eta} \qquad (3.17)$$

with $\eta \in \{x,y,z\}$ and the same for the condensate widths are

$$m\ddot{w}_x = \frac{\hbar^2}{mw_x^3} + \frac{g}{(2\pi)^{3/2}w_x^2 w_y w_z} - 2\frac{\partial V}{\partial w_x} \qquad (3.18)$$

$$m\ddot{w}_y = \frac{\hbar^2}{mw_y^3} + \frac{g}{(2\pi)^{3/2}w_x w_y^2 w_z} - m\omega_y^2 y^2 - 2\frac{\partial V}{\partial w_y} \qquad (3.19)$$

$$m\ddot{w}_z = \frac{\hbar^2}{mw_z^3} + \frac{g}{(2\pi)^{3/2}w_x w_y w_z^2} - m\omega_z^2 z^2 - 2\frac{\partial V}{\partial w_z}. \qquad (3.20)$$

The above equations describe the motion of a particle with coordinates w_η in an effective potential

$$U(W_\eta) = \frac{\hbar^2}{2m}\sum_\eta\frac{1}{w_\eta^2} + \frac{1}{2}m\omega_z^2 w_z^2 + \frac{g}{(2\pi)^{3/2}w_x w_y w_z} + V(w_\eta).$$

$$(3.21)$$
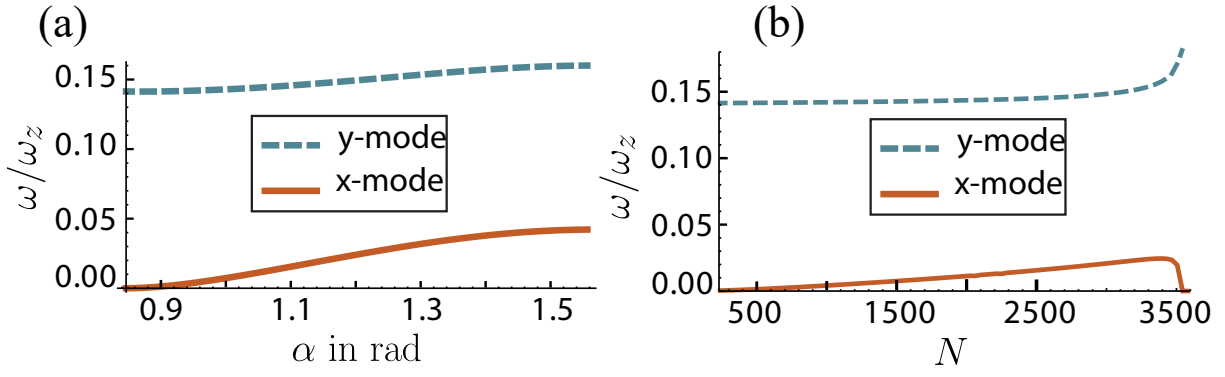
Figure 3.12: The two lowest-lying decoupled modes with respect (a)α and (b)N are depicted. The parameter values are same as Fig. 3.11.

The equilibrium widths of the condensate can also be obtained by minimizing the effective potential besides the energy functional. The low lying modes are found from diagonalization of the Hessian matrix of U. The centre of mass motion of the soliton along the z axis is de-coupled from the width modes:

$$\ddot{z}_0 = -\omega_z^2 z_0. \tag{3.22}$$

and

$$\ddot{y}_0 = -\omega_y^2 y_0. \tag{3.23}$$

For the parameters in Fig. 3.11, we calculate the two lowest lying modes with respect to α and N. The results are shown in Fig. 3.12. Due to strong anisotropy of the solution the width modes get decoupled into x and y modes i.e. they depict the oscillations along x and y respectively without affecting each other. The larger width corresponds to lower energy mode. Hence the lowest lying mode here corresponds to oscillations of w_x while the next higher mode corresponds to w_y oscillations. In Fig. 3.12(a) for lower values of α, the lowest lying mode is seen to become soft and tend to zero. This behaviour represents the onset of expansion instability. Decrease in α results in lessened attraction and hence the emergence of expansion instability. The value at which the expansion instability sets in is independent of the number of atoms, rather it depends only on the ratio g_d/g. Similarly, in Fig. 3.12(b) we show the two lowest lying modes with respect to number of atoms N. Here two different kinds of instabilities are apparent at extreme ends of the modes. When N is decreased the interaction strengths decrease and self-trapping is lost which is shown by the mode softening to zero. The solution is lost against expansion instability. At the other end, when N is quite high a stronger attractive interaction ensues and drives the system into collapse instability. Our system is focused on Chromium atoms because it is weakly dipolar. The 1D self-trapping is not seen for strongly dipolar atoms like Er and Dy from our calculations as they're unstable against collapse. However, in such systems
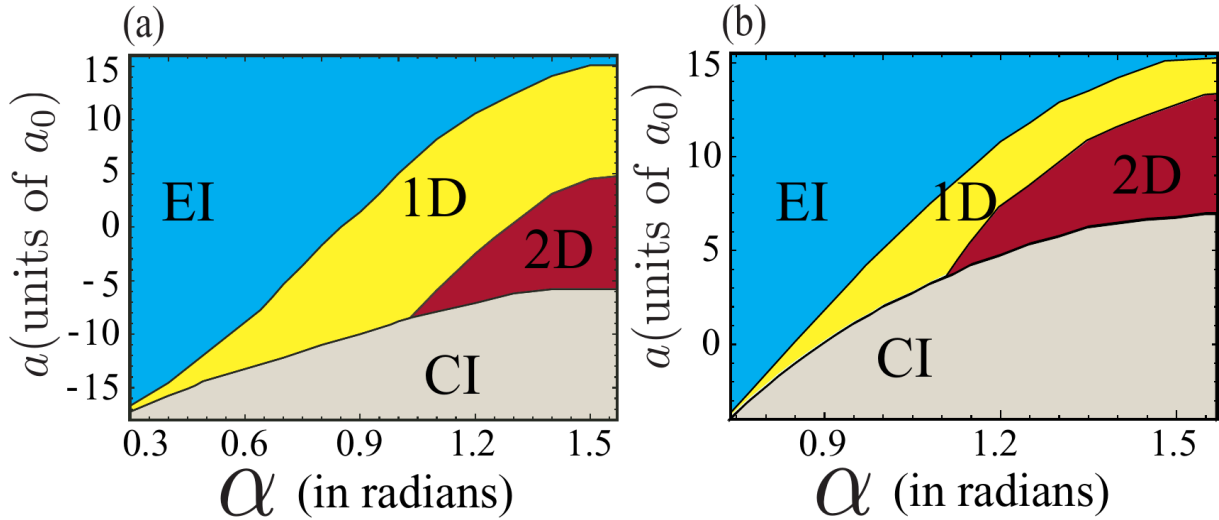
Figure 3.13: Two different kinds of self-trapped regions in quasi-2D Cr BEC in the parameter space of $\alpha - a$. The fixed parameters are $\omega_z = 2\pi \times 800$ Hz and $\omega_y = 0.1\omega_z$ with (a)$N = 1000$ and (b)$N = 5000$. EI and CI stand for expansion instability and collapse instability respectively while 1D and 2D stand for 1D and 2D self-trapped solitons in a quasi-2D scenario.

quantum fluctuations may play a bigger role [166, 110, 167] and it is beyond the scope of the current chapter. In Chromium atoms the quantum fluctuations may be neglected due to its weak dipolar nature.

All our new findings have been summarized in form of a phase diagram for Cr atomic BEC with $N = 1000$ and $N = 5000$ atoms in Fig. 3.13(a) and (b) respectively. We show the 1D self-trapping regions, the 2D soliton region bounded by expansion and collapse instabilities on both sides. It is evident that 1D self-trapping is a prominent feature which is obtained either in weak effective dipolar strength or with few number of atoms in the condensate. Comparing Fig. 3.13(a) and (b), one can note that for higher N values the stability region is narrowed as it effectively increases the dipolar interaction strength. For a fixed α value closer to $\pi/2$ by varying the scattering length one may go from expansion instability (EI)$\rightarrow$ 1D self-trapped solution to $\rightarrow$ quasi-2D anisotropic soliton $\rightarrow$ collapse instability (CI). Another important detail that comes out of the phase diagram is the existence of stable 2D solitons even for $a < 0$. For negative contact interaction it is only when the density as well as dipolar strength are sufficiently low.

3.5.4 Adiabatic preparation of solitons

Despite considerable theoretical advancements in studying the properties of quasi-2D solitons [95, 96, 162], there has been no success in finding quasi-2D solitons in laboratory. In this section we propose an experimental procedure to prepare quasi-2D solitons with advantage of the tilting angle α in real time. Below we describe the procedure.
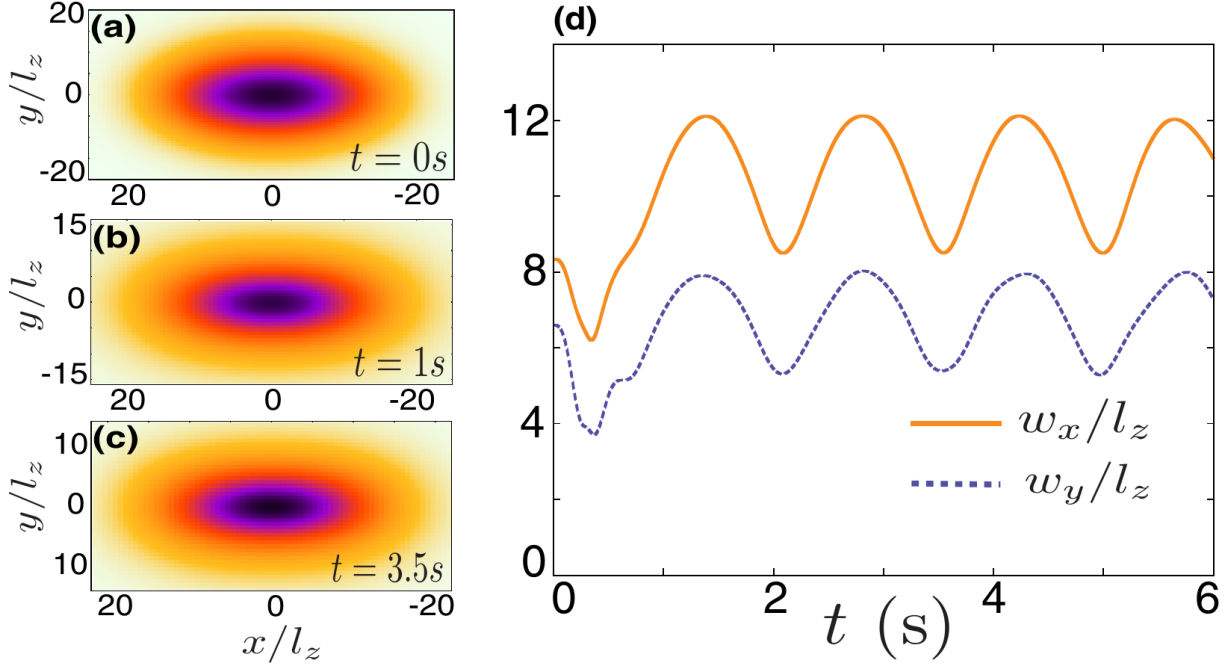
Figure 3.14:   Adiabatic preparation of soliton starting from weakly confined solution to finally self-trapped soliton is shown in Cr BEC with $N = 6000$ and $a = 9a_0$. The initial weak confinement has $\omega_{x,y} = 2\pi \times 10$Hz. Initial tilting angle $\alpha_i = 1.22$ and final tilting angle $\alpha_f = 1.32$ rad and this tuning is done in 0.3s followed by the removal of trap in 0.5s in a linar fashion. In (a)-(c) density is shown for different time scales and in (d) the width oscillations are shown with respect to time. After $t > 0.8$s self-trapping nature of soliton is observed due to stable oscillations.

We consider an external shallow trap on the $x - y$ plane with trapping frequencies $\omega_{x,y} = 2\pi \times 10$ Hz and $\omega_z = 2\pi \times 1$ kHz. A Cr BEC of $N = 6000$ atoms is an ideal setup. The condensate is initially prepared with $\alpha_i = 1.22$ radians and $a = 9a_0$, such that the condensate is in the S region of the phase diagram and there is no PI. The condensate requires the $x - y$ traps without which the cloud is unstable against expansion. In the next step, keeping everything else fixed, the tilting angle α is adiabatically tuned to a final value of $\alpha_f = 1.32$ radian. This brings the system into the PI region where a quasi-2D soliton is stable, although we still have the traps. From Fig. 3.4(a) it can be easily identified that α_i and α_f correspond to stable and PI regions respectively. Next, the trap on the xy plane are removed adiabatically. It is essential that all the tuning of parameters be done adiabatically so as to avoid any unnecessary excitations in the condensate. This exact procedure was followed numerically and we present the widths of the final solution with respect to time in Fig. 3.14(d). We observe stable oscillations of the condensate widths even after removing the confinement. This signifies self-trapping in $x - y$ plane. The oscillations are a result of slight excitation of breathing mode as the w_x and w_y oscillations are in-phase. The oscillations are stronger or suppressed depending on the adiabaticity condition. A slower tuning results in a smaller amplitude of oscillation.

The condition of adiabaticity in a system depends on the various time scales inherent to the system dynamics [168]. We ensure the following condition,

$$T_\omega \ll T \ll T_\mu \tag{3.24}$$

where, $T_\omega = \max\{1/\omega_B(\alpha(t))\}$ and $T_\mu = \max\{1/|\mu_{2D}(\alpha(t))|\}$ which are both instantaneous time dependent. T_ω is the quantum mechanical linear adiabatic time scale. Our adabatic time scale should be larger than this to avoid excitations of the breathing modes of frequency ω_B [169]. The T_μ is defined as the nonlinear time scale proportional to the inverse of chemical potential of the system. However, in our case while α changes from α_i to α_f the chemical potential also goes from a positive value to negative value respectively. This means that the $\mu_{2D} = 0$ in between and hence $T_\mu \to \infty$. This reduces our adiabaticity condition to simply $T_\omega \ll T$. In our case considered here, $T_\omega \sim 0.05$s. The soliton preparation involves two time scales, (i) for tuning α (ii) tuning $\omega_{x,y}$ to zero, both done linearly in time. We varied α in 0.3s from α_i to α_f and the trap is then removed in a duration of 0.5s.

3.6 Conclusion

The substantial effect of tilting angle (α) on the physics on quasi-2D dipolar BEC is studied in detail. We have characterized most of the relevant parameter space and shown that inclusion of the tunable parameter α ensures a larger parameter regime for the experimental exploration of the so far elusive quasi-2D solitons. The effect of tilting angle results in solitons with controllable anisotropy. Moreover, we propose an experimental sequence which allows for adiabatic preparation of anisotropic soliton without changing interactions strengths, rather by simply tilting the polarisation direction in dipolar BEC by an external polarising field. We study the stability of the solitons against collapse and expansion instabilities. We discover a new class of solutions in quasi-2D scenario which are self-trapped along only one direction. It was also found that stable quasi-2D solitons are a possibility even with negative scattering lengths as long as the number of atoms are small and the atoms are weakly dipolar. α also leads to anisotropic instability dynamics resulting in stripe patterns in phonon and roton unstable regions. Whether the patterns sport dislocation defects or not can be a signature of roton instability. The patterns due to phonon instability eventually merge into forming ansiotropic solitons. Patterns due to roton instability are transient stripes which may be sustained for longer if the system can be driven back into stable roton regions.

Our study has been in the mean-field regime and most of them are realizable in weakly dipolar systems like Cr. Recent developments in strongly dipolar Er and Dy atoms have immense potential for exploring new physics in quasi-2D scenario.

Chapter 4

Periodically Driven Quasi-1D Dipolar Bose-Einstein Condensates

Current chapter is adapted from an ongoing project. We primarily study the transfer of excitation between multiple quasi-1D layers of BECs both for homogeneous and trapped condensates. The layers are coupled via interlayer DDI. The nonlocal character of DDI gives rise to transfer of excitation between different modes of the multi-layer system. Additionally, the tilting angle of the dipole can change the nature of this interaction from repulsive to attractive. We consider both homogeneous and trapped cases. In the former case, Faraday pattern excitations are studied while in the later, we study the collective excitations and mode-locking phenomena.

4.1 Introduction

Periodically driven systems have been at the forefront of research in wide areas of condensed matter systems, atomic and molecular, optical and classical nonlinear systems. Applications of parametric oscillations have been successful in noise squeezing [170], generating squeezed light [171], enhanced detector sensitivity [172], and quantum information [173, 174]. In case of BEC, periodic driving has been implemented both experimentally [175–177] and theoretically by modulation of trap [178, 179], s-wave scattering [180–182] or the dipolar strength [183]. Under homogeneous conditions, the focus is usually on the formation self-bound structures [182, 184], stabilization [185], and generation of Faraday waves [183, 186, 187], standing waves which were initially discovered in liquid enclosed in a vibrating container. The broad motivation behind this is to study different pattern formation in nonlinear systems and also to understand the stability or instabilities of a system under periodic perturbation.

In trapped systems, the stability and nonlinearity is studied with the help of collective excitations. Controlled development of the collective excitations and manipulation of

their amplitudes [175, 176, 188] may be achieved with parametric periodic driving and they have been studied for simple BECs without dipolar interactions. Under certain conditions mode-locking can be engineered in BECs which provides tremendous control of the collective excitations or their de-excitation as well [148, 149].

We start by presenting the generalised governing equations for a multilayer quasi-1D dipolar condensates, although we restrict our studies to bilayer systems. Using Bogoliubov spectrum we identify various stability and instability regimes for a trapless bilayer system. At this point periodic driving is introduced which induces Faraday patterns. We briefly review and add to the previously studied Faraday patterns in a bilayer case where both layers are parametrically modulated [189]. But our main focus is on the study of a singly-modulated layer which shows intriguing dynamics. We observe emergence of Faraday patterns even in unmodulated layer due to the interlayer DDI and under certain modulation frequencies, interesting phenomena such as out of phase revival of Faraday patterns are demonstrated in contrast to simultaneous appearance of patterns in both layers. A complete analytic calculation has been formulated which well approximates the linear regime of excitation. These studies have been made in the stable spectrum regions. In the later half of the chapter we move on to trapped cases. Our goal is to capture the transfer of mode-locking between layers facilitated purely due to DDI and the effect of polarisation angle on the excitations transfer. As a surprising side-effect we detect coupling between width and center of mass modes in multilayer configuration and study the subsequent dynamics as well.

4.2 GPE for multilayer cigar-shaped BEC

Our study is generally focused on non-overlapping bilayer dipolar BECs in individual cigar-shaped confinements. But we present a generalised theoretical equation for a multi-layer system. The inter-layer separation $\Delta/l_\perp \geq 5$ at any time to avoid any overlapping or atom exchange where $l_\perp = \sqrt{\hbar/M\omega_\perp}$, $\omega_\perp$ is the trap frequency in the transverse direction and M is the atomic mass. We have kept the interlayer distance at least $5\sqrt{2}$ times larger than the standard deviation of the condensate in each layer along the direction of the separation. For comparison, three standard deviations along both sides from the mean of the condensate contains 99.7% of the total density. The interlayer separation limit has been determined keeping in mind a transverse Gaussian density width i.e. $\Delta >> l_\perp$. This can be modeled using the following nonlinear Gross-Pitaevskii equation(NLGPE). For a jth layer:

$$i\hbar\frac{\partial}{\partial t}\Psi_j(\mathbf{r},t) = \left[-\frac{\hbar^2}{2M}\nabla^2 + \frac{M\omega_\perp^2}{2}(x^2 + y_j^2) + g|\Psi_j(\mathbf{r},t)|^2\right.$$

$$\left. + \sum_{m=1}^{N}\int d^3\mathbf{r}'\Psi_m^*(\mathbf{r}')V_d(\mathbf{r}-\mathbf{r}')\mathbf{\Psi_m}(\mathbf{r}')\right]\Psi_j(\mathbf{r},t) \qquad (4.1)$$

where $g = 4\pi\hbar^2 a/M$ is the short-range interaction parameter proportional to s-wave scattering length a and $V_d(r)$ is the dipole-dipole interaction(DDI), $V_d(r) = g_d(1 - 3\cos^2\theta)/r^3$ where $g_d = \mu_0\mu^2/4\pi$ for atomic BEC with dipole moment μ and θ is the angle between dipole orientation and the interatomic distance. Under axially untrapped condition we restrict ourselves to satisfy the quasi-1D(Q1D) condition where the reduced chemical potential μ_{1D} is much smaller than the transverse confinement energy $\hbar\omega_\perp$. Under single mode approximation we obtain a reduced dimensional Q1D NLGPE for a jth layer:

$$i\hbar\frac{\partial}{\partial t}\psi_j(z,t) = \left[-\frac{\hbar^2}{2M}\frac{d^2}{dz^2} + \frac{g}{2\pi l_\perp^2}|\psi_j(z,t)|^2\right.$$

$$\left. + \frac{g_d}{3l_\perp^2}\sum_{m=1}^{N}\int\frac{dk_z}{2\pi}e^{izk_z}n_m(k_z)F_{m-j}(k_z)\right]\psi_j(z,t) \qquad (4.2)$$

$n_m(k_z)$ is the Fourier transform of the probability density and N is the total number of layers. The layers are separated along the y direction and the dipole vectors are restricted to the $x-y$ plane as shown in Fig. 4.1. Hence, the intralayer DDI forever remains repulsive while the interlayer interaction becomes tunable from repulsive ($\alpha = 0$) to attractive ($\alpha = \pi/2$) where α is the angle between the dipole vector and x axis. Below we show the calculations for $F_{m-j}(k_z)$. First we rewrite Eq. (4.1) with the DDI Fourier transformed,

$$i\hbar\frac{\partial}{\partial t}\Psi_j(\mathbf{r},t) = \left[-\frac{\hbar^2}{2M}\nabla^2 + \frac{M\omega_\perp^2}{2}(x^2 + y^2) + g|\Psi_j(\mathbf{r},t)|^2\right.$$

$$\left. + \sum_{m=1}^{N}\int\frac{d^3k}{(2\pi)^3}e^{i\mathbf{r}\cdot\mathbf{k}}n_m(\mathbf{k})V_d(\mathbf{k})\right]\Psi_j(\mathbf{r},t) \qquad (4.3)$$

In the transverse direction we assume a Gaussian wave function owing to the tight harmonic confinement of the form $\phi_j(x,y) = \frac{1}{\sqrt{\pi}l_\perp}e^{-\frac{x^2}{2l_\perp^2} - \frac{y_j^2}{2l_\perp^2}}$ such that $\Psi(\mathbf{r}) = \phi_j(x,y)\psi(z,t)$ and $|y_m - y_j| = |m-j|\delta$. We multiply both sides of Eq. (4.3) with $\phi_j^*(x,y)$ and integrate over $\int dx\int dy$ to obtain Eq. 4.2.

The general form of $F_{m-j}(k_z)$ is

$$F_{m-j}(k_z) = \frac{3l_\perp^2}{g_d}\int\frac{k_\perp dk_\perp d\theta_k}{(2\pi)^2}V_d(\mathbf{k})e^{-\frac{k_\perp^2 l_\perp^2}{2} - ik_\perp\sin\theta_k(m-j)\delta}$$
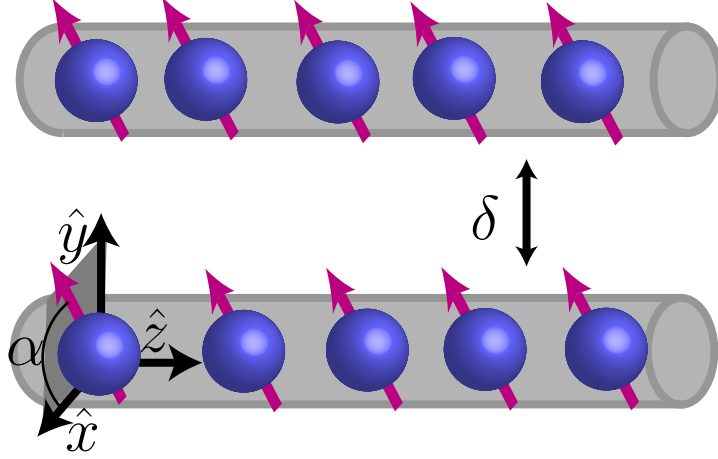
Figure 4.1: Schematics a bilayer quasi-1D dipolar BEC along z direction. The movement of dipole vector is restricted to the $x - y$ plane and the layers are separated along y direction by δ. The atoms in the layers are shown for angle α which is the angle between dipole vector and $\hat{x}$-axis.

where, $k_x = k_\perp \cos\theta_k$ and $k_y = k_\perp \sin\theta_k$ have been converted to cylindrical coordinates. $V_d(\mathbf{k})$ is the Fourier transform of $V_d(r)$. Thus,

$$V_d(\mathbf{k}) = \left(\frac{4\pi g_d}{3}\right)\left(\frac{3k_x^2\cos^2\alpha + 3k_x k_y\sin 2\alpha + 3k_y^2\sin^2\alpha}{k_x^2 + k_y^2 + k_z^2} - 1\right)$$

$$F_{m-j}(k_z) = \int dk_\perp \frac{k_\perp l_\perp^2 e^{-\frac{k_\perp^2 l_\perp^2}{2}}}{(k_\perp^2 + k_z^2)}[J_0(|m-j|\delta\ k_\perp)(k_\perp^2 - 2k_z^2)$$
$$+3k_\perp^2 J_2(|m-j|\delta\ k_\perp)\cos 2\alpha] \qquad (4.4)$$

$$\implies F_0(k_z) = 1 - \frac{3}{2}e^{\frac{k_z^2 l_\perp^2}{2}}k_z^2 l_\perp^2\Gamma\left[0, \frac{k_z^2 l_\perp^2}{2}\right]$$

$$\implies F_1(k_z) = \int dk_\perp \frac{k_\perp l_\perp^2 e^{-\frac{k_\perp^2 l_\perp^2}{2}}}{(k_\perp^2 + k_z^2)}[J_0(\delta\ k_\perp)(k_\perp^2 - 2k_z^2) + 3k_\perp^2 J_2(\delta\ k_\perp)\cos 2\alpha]$$

It is easily noticeable that $F_0(k_z)$, which represents intralayer DDI, is independent of α as it should be. Only $F_1(k_z)$ remains α dependent.

4.3 Bogoliubov dispersion relation

In this section we calculate the Bogoliubov excitation spectrum in order to identify the stability and instabilities of the system. Consider an infinitely long homogeneous distribution with plane-wave like excitations $\psi_j(z,t) = [\sqrt{n} + u_j e^{-i(zq - \omega_q t)} + v_j^* e^{i(zq - \omega_q t)}]e^{-i\mu_{1D}t/\hbar}$. n is a constant homogeneous density, u_j and v_j^* are the Bogoliubov functions. Replacing this solution in Eq. 4.2 the chemical potential is found out to be $\mu_{1D} = gn/2\pi l_\perp^2 +$
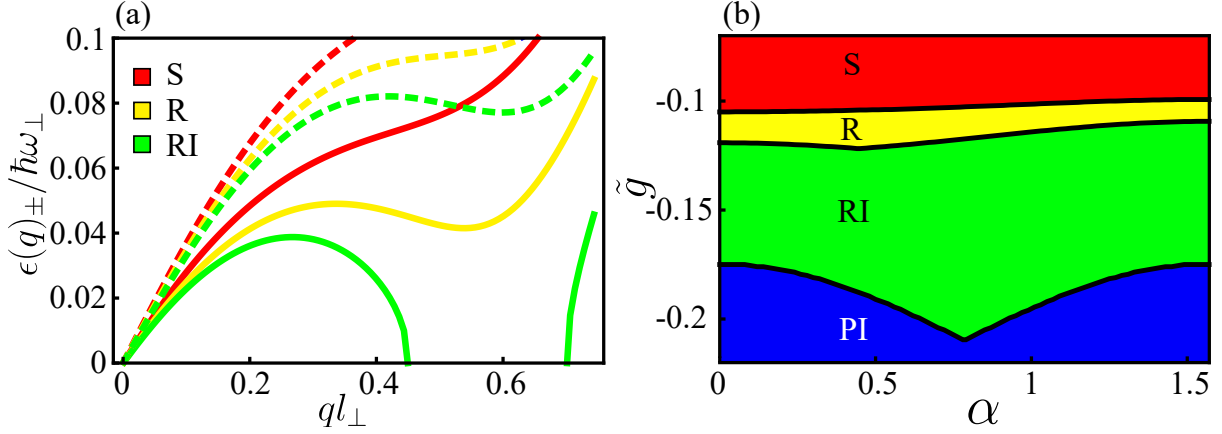
Figure 4.2: (a) Bogoliubov excitations branches for a bilayer Q1D dipolar BEC representing stable (S), roton (R) and roton instability (RI) for $\tilde{g} = -0.09, -0.106$ and -0.116 respectively at $\tilde{g}_d = 0.1, \alpha = 1.2$ rad and $\delta = 6l_\perp$. The solid curves represent the symmetric lower energy branch and the dashed curves stand for the asymmetric branch. (b) S, R, RI and phonon instability (PI) domains have been identified in the $\alpha - \tilde{g}$ domain for $\tilde{g}_d = 0.1$ and $\delta/l_\perp = 6$.

$g_d n [F_0(0) + F_1(0)]/3l_\perp$. Applying standard Bogoliubov analysis [189] multiple branches of excitation emerge owing to the coupling between the layers. The dispersion relation can be obtained by solving the following set of equations emerging from the calculations,

$$-\hbar\omega_q u_j = \frac{\hbar^2 q^2}{2M} u_j + \frac{gn}{2\pi l_\perp^2}(u_j + v_j) + \frac{g_d n}{3l_\perp^2} \sum_{m=1}^{N} F_{m-j}(q)(u_m + v_m) \qquad (4.5)$$

$$\hbar\omega_q v_j = \frac{\hbar^2 q^2}{2M} v_j + \frac{gn}{2\pi l_\perp^2}(u_j + v_j) + \frac{g_d n}{3l_\perp^2} \sum_{m=1}^{N} F_{m-j}(q)(u_m + v_m) \qquad (4.6)$$

For the simplest case of a bilayer system we have [189],

$$\epsilon(q)_\pm = \hbar\omega_{q,\pm} = \sqrt{\frac{\hbar^2 q^2}{2M}\left[\frac{\hbar^2 q^2}{2M} + 2\frac{gn}{2\pi l_\perp^2} + \frac{2g_d n}{3l_\perp^2}(F_0(q) \pm F_1(q))\right]} \qquad (4.7)$$

corresponding to the symmetric and anti-symmetric excitation branches. Along with the usual short range parameter g and dipolar parameter g_d, in a bilayer system we have two additional meaningful quantities α, the tilting angle of the dipole vector and δ, the interlayer separation. Due to anisotropic nature of the DDI, at $\alpha = \pi/2$, the interlayer interaction achieves the maximum magnitude for a fixed δ. Here, the dipoles are oriented along y, hence the interlayer interaction is attractive. As α is decreased, the magnitude and attractive nature of this interaction is reduced gradually. After a minimum value, the magnitude of the interaction increases again, however the nature of the interaction becomes repulsive. At $\alpha = 0$ the layers obtain maximum repulsion.

The phonon modes for each branch can be obtained when $\epsilon(q \to 0)_{\pm} = \hbar q \sqrt{\mu_{\pm}}/M$, where $\mu_{\pm} = gn/2\pi l_{\perp}^2 + g_d n[F_0(0) \pm F_1(0)]/3l_{\perp}$. When $\mu_{\pm}$ becomes negative, the spectrum acquires imaginary component and the phonon modes become unstable. Hence $\mu_{\pm} < 0$ gives the phonon instability (PI) condition. The simplified expressions for $F_0(0) = 1$ and $F_1(0)$ is,

$$F_1(0) = e^{-\frac{\delta^2}{2}} \left[1 + \frac{\cos 2\alpha}{\delta^2} \left\{ 6 \left(e^{\frac{\delta^2}{2}} - 1 \right) - 3\delta^2 \right\} \right] \tag{4.8}$$

which is purely δ and α dependent only.

Strictly under $Q1D$ condition we plot the dispersion relation of Eq. 4.7 in Fig. 4.2(a). For a set certain parameters there exists two branches corresponding to the symmetric and anti-symmetric component. When both the branch curves are purely real and monotonically increasing with respect to momentum it is stable (S) spectrum. If at least one of the branches show a purely real and non-monotonic behaviour such that the curve attains a minimum for a nonzero-finite value of q, we have a roton(R) spectrum. The rotonic branch may become soft and for a non-zero finite momentum the spectrum may become purely imaginary. This is called roton instability (RI). If such an instability occurs at zero momentum instead, the spectrum becomes phonon unstable (PI). When the interlayer coupling is attractive, as is the case in Fig. 4.2(a) at $\alpha = \pi/2$, the symmetric branch (solid curves) of the dispersion relation has the lowest energy and is the deciding factor of system stability. Changes in the parameters barely affect the asymmetric branch (dashed curves), especially in low momentum regime. The stable curves have been obtained for small magnitude of negative g. Once g becomes more negative, the symmetric branch acquires a rotonic character and eventually becomes roton unstable for fixed g_d, α and δ. Further increment in magnitude of attractive contact interaction results in phonon instability (not shown).

These four domains have been characterized together in the $\alpha - \tilde{g}$ parameter space for a fixed value of $\tilde{g}_d = 0.1$ and $\delta/l_{\perp} = 6$ in Fig. 4.2(b) where dimensionless quantities $\tilde{g}(\tilde{g}_d) = gn/2\pi\hbar\omega_{\perp}l_{\perp}^2 (g_d n/2\pi\hbar\omega_{\perp}l_{\perp}^2)$ have been defined. Keeping α fixed one may go from S $\to$ R $\to$ RI $\to$ PI simply by making $\tilde{g}$ more and more negative. For $\tilde{g} >\approx -0.1$ the system is always stable and for $\tilde{g} <\approx -0.21$ the system is always phonon unstable. The intermediate regions are R and RI. The RI is substantially large compared to R. Interestingly, the PI-RI and RI-R boundaries show non-monotonic behaviour with respect to α. The reason is due to anisotropic nature of the interlayer DDI. When α is close to $\pi/2$ the symmetric branch is the lowest branch and characterizes the stability and instability criteria. However, when α is close to 0 the asymmetric branch has lower energy due to interlayer repulsion and instability criteria is mediated by it. Hence, in the intermediate

region for a range of α values a crossing between the two branches occur where the interlayer interaction also becomes weak. This behaviour is reflected in the necessity of a stronger attractive contact interaction for inducing RI or PI.

To satisfy non-overlapping condition $\delta/l_\perp$ must be greater than equal to 5. For $\delta/l_\perp >$ 6 the DDI starts to become weak for our study. While it is possible to observe R and RI domains for higher magnitudes of g and g_d it drives the system out of Q1D and out of scope of our current study. From now on while applying external modulation we shall restrict the system to the purely stable regimes (S or R) only.

4.4 Faraday Patterns in Homogeneous Gas

In this section we introduce parametric driving and the resulting Faraday patterns in a homogeneous multilayer Q1D dipolar BEC. Faraday waves were briefly discussed in 2.3.1. In classical fluids external driving can lead to formation of standing waves on the fluid interface and coupling between the nonlinear waves generates patterns with different symmetries e.g. stripes, squares, hexagonal etc [141, 190–192]. Hence, Faraday patterns have proven to be a tool to explore nonlinear properties of the system. This motivates the study of Faraday patterns in a controllable nonlinear system like dipolar BEC. Here, we shall study the Faraday pattern in a bilayer system and the phenomenon of transfer of patterns formation. We look at the resonant momentum associated with these patterns and discover interesting dynamics when the parametric modulation is restricted to only one layer.

4.4.1 Doubly modulated bilayer system

We first consider the simple case of a bilayer system ($N = 2$) where both layers are parametrically modulated under the periodic driving of the s-wave scattering length. This can be done exploiting the Feshbach resonance [43] where periodically varying the external magnetic field will change the scattering length. The short-range interaction is modulated as $g(t) = \bar{g}[1 + 2\gamma \cos(2\omega t)]$ where $\bar{g}$ is the mean value. We consider a temporally modulated solution to Eq. 4.2 of the form $\psi_j(z,t) = \sqrt{n} e^{-\frac{i\mu_{1D}}{\hbar}(t + \frac{\gamma \bar{g} n}{2\pi l_\perp^2 \mu_{1D}})\frac{\sin 2\omega t}{\omega}}[1 + W_j(t)\cos(z \cdot k_z)]$ where γ is the strength of modulation, ω is the modulation frequency and $W_j(t) = u_j(t) + iv_j(t)$ is the complex perturbation amplitude and $\mu_{1D} = \frac{\bar{g}n}{2\pi l_\perp^2} + \frac{g_d}{3l_\perp^2}[F_0(0) + F_1(0)]$. This can be replaced in the Eq. (4.2) and then we segregate the real and imaginary components. Note that we always neglect higher order terms in $W(t)$. Real and imaginary

components give,

$$
\begin{aligned}
\hbar \frac{du_j}{dt} &= \frac{\hbar^2 k_z^2}{2m} v_j \\
-\hbar \frac{dv_j}{dt} &= \frac{\hbar^2 k_z^2}{2m} u_j + \frac{2\bar{g}n}{2\pi l_\perp^2} u_j + \frac{2\gamma\bar{g}n}{\pi l_\perp^2} \cos(2\omega t) u_j + \frac{2g_d}{3l_\perp^2} \sum_m F_{m-j}(k_z) u_m
\end{aligned}
$$

Eliminating v_j for each layer and adding/subtracting the second order differential equations we reduce to a symmetric and antisymmetric Matheiu equation format.

$$
\frac{d^2 u_\pm}{dt^2} + \frac{1}{\hbar^2} \left[\epsilon(k_z)_\pm^2 + \frac{\hbar^2 k_z^2}{2m} \frac{2\gamma\bar{g}n}{\pi l_\perp^2} \cos 2\omega t \right] u_\pm = 0 \tag{4.9}
$$

where, $u_\pm = u_1 \pm u_2$. Let us define $b(\omega, \gamma) = \frac{\hbar^2 k_z^2}{2m} \frac{\gamma\bar{g}n}{\pi l_\perp^2 (\hbar\omega)^2}$. By working with weak driving, we are able to linearize and obtain the Matheiu equation.

Floquet theory

Floquet theory is a powerful technique to handle periodically varying systems. The Floquet theorem can be applied to first order differential equations of the type $\dot{y} = A(t)y$ where $A(t+T) = A(t)$. In our case, solutions to Matheiu equations have the form $e^{i\sigma_\pm t} f(t)$ where $f(t + \pi/\omega) = f(t)$ according to Floquet theorem. We are interested in whether the solution is bounded or not. If the Floquet exponent σ has negative(positive) imaginary component, the solution is unstable and grows(decays) exponentially. This leads to emergence of Faraday patterns. The analytic expression for σ is given by,

$$
\begin{aligned}
\sigma_\pm &= \frac{i}{\pi} \cos^{-1} \left[\left(1 - \frac{b^4 \pi^2}{32 q^2 (1-q^2)^2} \right) \cos q\pi \right. \\
&\quad \left. + \left(-\frac{b^2 \pi}{4q(1-q^2)} + \frac{15q^4 - 35q^2 + 8}{64 q^3 (1-q^2)^3 (4-q^2)} b^4 \pi \right) \sin q\pi \right] \tag{4.10}
\end{aligned}
$$

where $q = \epsilon(k_z)_\pm^2 / (\hbar\omega)^2$. Mostly the studies are restricted to the lowest resonance $\epsilon(k_z)_\pm = \hbar\omega$, thereby we're interested in $\sigma_\pm^1$. However, for rotonic dispersion relation we shall need to consider the higher resonances i.e. $\epsilon(k_z)_\pm = n\hbar\omega$ i.e at least the second band of quasi-energy level $\sigma_\pm^2$, where n is an integer. The need for consideration of higher resonances occur solely because of the nonlocal nature of the DDI which introduces nontrivial k_z dependence in $\sigma_\pm$. The selection of the resonant momentum will correspond to the maximization of $\text{Im}(\sigma_\pm)$ for instability.

Results

In our system due to the existence of two branches, for any modulation frequency ω, there will be potentially two resonant momenta k_z^a and k_z^s in the S region, where k_z^a corresponds to the asymmetric branch and k^s to the symmetric branch. By solving Eq. (4.9) for the
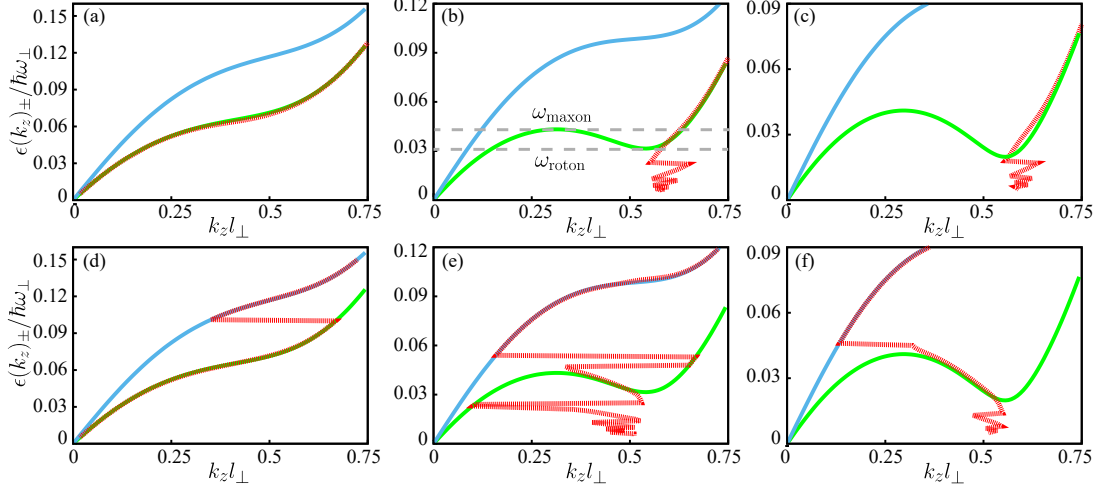
Figure 4.3: The Bogoliubov branches and most unstable mode(red) under external perturbation. (a)-(c) correspond to g modulation and (d)-(f) correspond to g_d modulation. (a) In S region for $\tilde{g} = -0.09$, the symmetric branch is the most unstable mode (b)-(c) In R region for $\tilde{g} = -0.106$ and -0.108 respectively, due to existence of roton the most unstable mode has discontinuities. (d) A switch between the most unstable modes is demonstrated for $\tilde{g} = -0.09$ at critical frequency ω_c. (e)-(f) The $\omega_c > \omega_{\text{maxon}}$ here for $\tilde{g} = -0.106$ and -0.108 respectively. When $\omega < \omega_c$ the most unstable mode shows complex selection rules due to existence of roton. However, the behaviour is markedly different for g and g_d modulation. The system parameters are $(\tilde{g}_d, \alpha, \delta/l_\rho, \gamma) = (0.1, \pi/2, 6, 0.04)$.

Floquet exponent, the most unstable momentum is found to correspond to the Bogoliubov branch which has larger imaginary component of $\sigma_\pm$. Evidently, when symmetric branch has lower energy i.e. the interlayer interaction is attractive $\text{Im}[\sigma(k_z^s)_+] > \text{Im}[\sigma(k_z^a)_-]$ and vice versa. This behaviour is shown in Fig. 4.3(a) where, $\alpha = \pi/2, \bar{\tilde{g}} = -0.09, \tilde{g}_d = 0.1$ and $\delta = 6l_\perp$.

In contrast, in the 'R' region for $\bar{\bar{g}} = -0.106$ with all other parameters being the same, where the symmetric branch acquires a rotonic character, potentially there are four resonant momenta($k_z^a < k_{z,1}^s < k_{z,2}^s < k_{z,3}^s$) if the modulation frequency satisfies $\omega_{\text{roton}} < \omega < \omega_{\text{maxon}}$. $\omega_{roton/maxon}$ has been identified in Fig. 4.3(b). k_a corresponds to momentum resonant with the anti-symmetric branch and $k_{z,i}^s (i \in (1,2,3))$ corresponds to the three resonant momenta from the symmetric branch. Again with the help of Eq. (4.9) we solve for the most unstable momentum for different modulation frequencies when $\tilde{g}$ is being modulated. The resulting picture is depicted in Fig 4.3(b) and (c). We observe that the most unstable momentum corresponds to $\epsilon(k_z)_+ = n\hbar\omega$ for some integer value of n for which $\epsilon(k_z)_+ > \omega_{\text{roton}}$.

The dynamics becomes nontrivial when $g_d(t) = \bar{g}_d[1 + 2\gamma \cos(2\omega t)]$ is modulated in-

stead. The Mathieu equation is modified as,

$$\frac{d^2 u_\pm}{dt^2} + \frac{1}{\hbar^2}\left[\epsilon(k_z)^2_\pm + \frac{\hbar^2 k_z^2}{2m}\frac{2\gamma\bar{g}_d n}{3l_\perp^2}[F_0(k_z) + F_1(k_z)]\cos 2\omega t\right] u_\pm = 0 \qquad (4.11)$$

In S region a switch between the symmetric and anti-symmetric branch selection is observed at a critical modulation frequency [189] as shown in Fig. 4.3(d) with all other parameters remaining constant as (a). It gives rise to correlated and anti-correlated patterns depending on the modulation frequency. This behaviour is shown irrespective of whether the interlayer interaction is attractive or repulsive i.e. such a behaviour is also obtained when interlayer DDI is repulsive at $\alpha = 0$ with all other parameters unchanged. In Fig. 4.3(d) when the k_z^s is selected from symmetric branch for lower ω values, correlated patterns of size $\sim 2\pi/k_z^s$ is observed in both layers. Beyond a critical modulation frequency when k_z^a becomes the resonant momentum, the patterns in the two layers also become anti-symmetric and the size of the patterns are $\sim 2\pi/k^a$.

In R region, similar to the S region, we observe a switch between the branches at a critical modulation frequency. This is observed to lie above ω_{maxon} seen in Fig. 4.3(e)(f). When modulation frequency $\omega_{\text{roton}} < \omega < \omega_{\text{maxon}}$, the most unstable momenta is found to be the middle $k_{z,2}^s$. For $\omega < \omega_{\text{roton}}$, generally the resonances occur for some min(n), where $n > 1$ is an integer, such that $n\hbar\omega > \hbar\omega_{\text{roton}}$ while k_s^2 continues to remain the most unstable mode corresponding to $n\hbar\omega$. However a small exception to this is observed in shallow rotonic spectra where $n = 1$ and the most unstable momentum is k_s^1 as can be seen in Fig. 4.3(e). Basically, the most unstable momentum does not have a monotonic increment with increment in modulation frequency. A discontinuity in most unstable momentum with respect to ω is translated to a discontinuity in pattern sizes when ω is varied as pattern sizes are inversely proportional to the resonant momentum. In other words, the size of patterns do not continuously vary for different values of modulation frequency, rather at certain frequency we see a sudden jump in the pattern sizes [119]. This is an excellent visual signature of roton in a system. For extremely small modulation frequencies the patterns often correspond to small resonant momenta and hence are large in size. The patterns also take longer time to emerge in low modulation frequency regime.

4.4.2 Singly modulated bilayer system: An analytic study

Parametric modulation of a single layer (shown schematically in Fig. 4.4(a)) is fundamentally different from modulation of both layers. In the absence of DDI, the two layers behave independently. However, presence of interlayer DDI ensures modulation of a single layer influences the second layer. In fact, real-time dynamics reveal a transfer of the Faraday patterns from the modulated layer to the unmodulated layer with a time lag dependent on the interlayer separation. We begin with two different ansatz to describe the system where

$g(t) = \bar{g}[1 + 2\gamma\cos(2\omega t)]$ is parametrically modulated in one layer which requires submicron control of interatomic interaction [193]. For the modulated and unmodulated layer we consider solutions of the form, $\psi_1(z,t) = \sqrt{n}e^{-\frac{i\mu_{1D}}{\hbar}(t+\frac{\gamma\bar{g}n}{2\pi l_\perp^2 \mu_{1D}})\frac{\sin 2\omega t}{\omega}}[1 + W_1(t)\cos(z\cdot k_z)]$ and $\psi_2(z,t) = \sqrt{n}e^{-\frac{i\mu_{1D}t}{\hbar}}[1 + W_2(t)\cos(z\cdot k_z)]$ respectively. Replacing them in Eq. 4.2 and simplifying we obtain a set of coupled equations,

$$\hbar^2\frac{d^2u_1}{dt^2} + \epsilon(k_z)^2u_1 + \frac{2g_d n}{3l_\perp^2}\frac{\hbar^2 k_z^2}{2m}F_1(k_z)u_2 + \frac{2\gamma\bar{g}n}{\pi l_\perp^2}\frac{\hbar^2 k_z^2}{2m}\cos(2\omega t)u_1 = 0 \tag{4.12}$$

$$\hbar^2\frac{d^2u_2}{dt^2} + \epsilon(k_z)^2u_2 + \frac{2g_d n}{3l_\perp^2}\frac{\hbar^2 k_z^2}{2m}F_1(k_z)u_1 = 0 \tag{4.13}$$

where $\epsilon(k_z) = \epsilon(k_z)_{\pm|F_1(k_z)\to 0|}$ is the single layer dispersion relation. Unlike the doubly modulated bilayer case, the equations cannot be decoupled into the form of Mathieu equations. Instead we reformulate the equations in the form of forced harmonic oscillators.

We, first, scale the set of equations with the tight transverse trap parameter such that $\tilde{t} = \omega_\perp t$, $\tilde{\epsilon}(k_z) = \epsilon(k_z)/\hbar\omega_\perp$ and $\tilde{g}(\tilde{g}_d) = gn/2\pi\hbar\omega_\perp l_\perp^2 (g_d n/2\pi\hbar\omega_\perp l_\perp^2)$. We introduce post-scaling variables $\mathcal{P}(k_z) = \frac{2\pi\tilde{g}_d k_z^2}{3}F_1(k_z)$ representing the coupling, $\mathcal{F}(k_z) = -2\gamma|\tilde{\bar{g}}|k_z^2$, the driving and define $\omega_D = 2\omega$, $\omega_+^2 = \epsilon(k_z)^2 + \mathcal{P}(k_z)$ and $\omega_-^2 = \epsilon(k_z)^2 - \mathcal{P}(k_z)$ for mathematical simplification. Removing the tilde and after simple algebra from Eq. 4.12 and 4.13 we get,

$$\ddot{u}_+ + \omega_+^2 u_+ = \frac{\mathcal{F}}{2}\cos(\omega_D t)(u_+ + u_-) \tag{4.14}$$

$$\ddot{u}_- + \omega_-^2 u_- = \frac{\mathcal{F}}{2}\cos(\omega_D t)(u_+ + u_-) \tag{4.15}$$

where $u_\pm = u_1 \pm u_2$. This set of differential equation has solutions of the form,

$$\begin{bmatrix} u_+ \\ u_- \end{bmatrix} = \sum_n e^{i(n\omega_D + \sigma)}\begin{bmatrix} H_n^+ \\ H_n^- \end{bmatrix} \tag{4.16}$$

Replacing Eq. 4.16 in Eq. 4.14 & 4.15 leads to two recursion relations which can be written together as [194],

$$D_n H_n + \mathcal{M}(H_{n-1} + H_{n+1}) = 0 \tag{4.17}$$

where,

$$D_n = \begin{bmatrix} \omega_+^2 - (n\omega_D + \sigma)^2 & 0 \\ 0 & \omega_-^2 - (n\omega_D + \sigma)^2 \end{bmatrix}$$

$$\mathcal{M} = \begin{bmatrix} -\mathcal{F}/4 & -\mathcal{F}/4 \\ -\mathcal{F}/4 & -\mathcal{F}/4 \end{bmatrix}$$
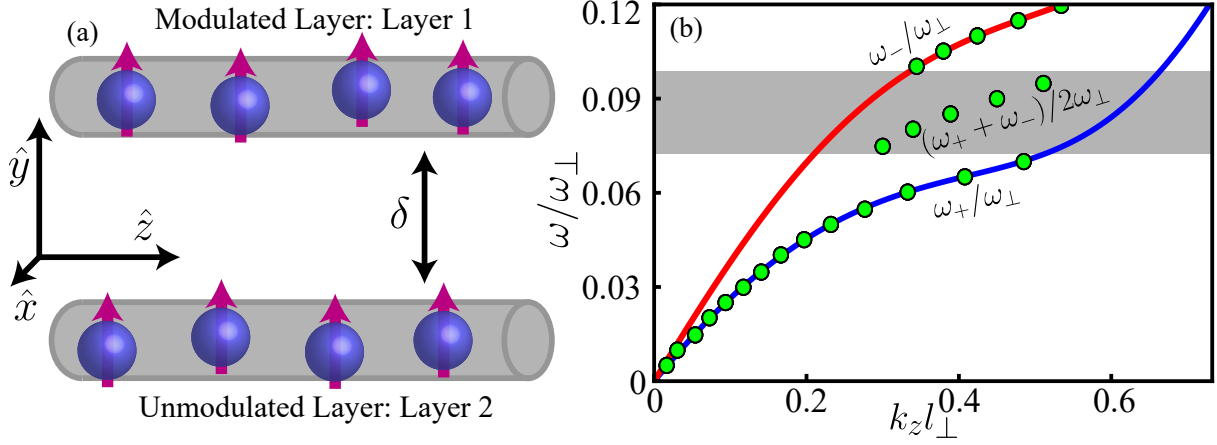
Figure 4.4: (a) Schematic diagram of a bilayer singly modulated system. The separation between the layers is δ and the dipole orientation is restricted to the $x-y$ plane while the quasi-$1D$ axis is along z-axis. Here, only Layer 1 is modulated. (b) The spectrum in 'S' region shown for a set of parameters $(\tilde{g}, \tilde{g}_d, \alpha, \delta/l_\perp) = (-0.09, 0.1, \pi/2, 6)$. The dots indicate the most unstable resonant momenta found by solving Eq. 4.21 when $\tilde{g}_d$ is modulated in Layer 1. In the gray region, a resonance is observed for momentum $k_z l_\perp$ corresponding to $(\omega_+ + \omega_-)/2\omega_\perp$, unseen in doubly modulated bilayer system.

The Eq. (4.17) can be written in an infinite dimensional matrix form. Since the parametric drive only couples the nearest neighbour Fourier components i.e. between H_n and $H_{n\pm1}$, without loss of generality we can focus on $n = 0$ case. This reduces the infinite dimensional matrix to a 4×4 minor whose 8 roots for σ can be found by imposing the condition that its determinant must vanish. From Eq. 4.16 it is clear to see that the stability criteria rests on whether σ is real or complex. We expect stable oscillatory solution if σ takes real values only and exponentially growing/decaying solution if σ has imaginary component.

$$\begin{vmatrix} \omega_+^2 - (\sigma - \omega_D)^2 & 0 & -\mathcal{F}/4 & -\mathcal{F}/4 \\ 0 & \omega_-^2 - (\sigma - \omega_D)^2 & -\mathcal{F}/4 & -\mathcal{F}/4 \\ -\mathcal{F}/4 & -\mathcal{F}/4 & \omega_+^2 - \sigma^2 & 0 \\ -\mathcal{F}/4 & -\mathcal{F}/4 & 0 & \omega_-^2 - \sigma^2 \end{vmatrix} = 0 \qquad (4.18)$$

The relevant resonances occur at $\omega = \omega_+, (\omega_+ + \omega_-)/2, |\omega_+ - \omega_-|/2$ and ω_- where Faraday instabilities arise for our system. Numerically solving for σ allows us to identify the most unstable resonance point and the corresponding momentum associated with the size of the Faraday patterns. It is found that the most unstable momentum corresponds to ω_+ i.e. the symmetric branch as long as g is modulated.

However, the situation is quite different when $g_d(t) = \bar{g}_d[1 + 2\gamma \cos(2\omega t)]$ is modulated.
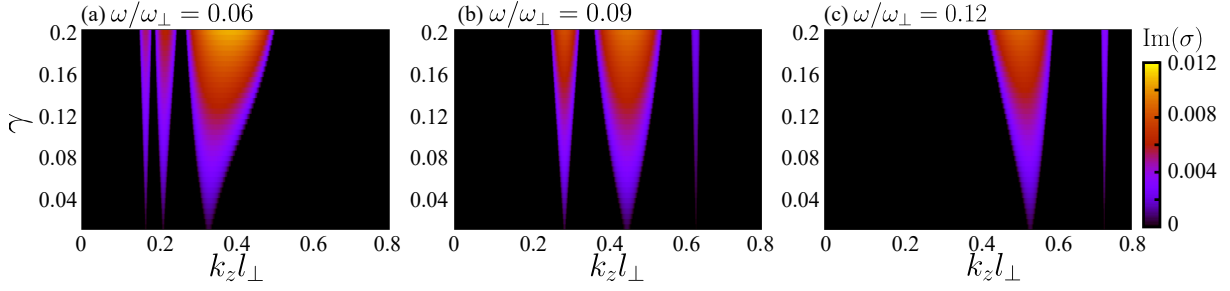
Figure 4.5: Linear instability regions in the $k_z - \gamma$ plane have been shown for three different modulation frequencies; each with most unstable momenta lying in different excitation branches. The density shows the magnitude of $\text{Im}(\sigma)$. (a) It has three unstable tongues corresponding to ω_-, $(\omega_+ + \omega_-)/2$ and ω_+ branches from left to right respectively out of which the last one contains the most unstable momentum for each γ. (b) The left unstable tongue correspond to ω_- and the most unstable tongue(right) belongs to the $(\omega_+ + \omega_-)/2$ branch. (c) The most unstable tongue here corresponds to ω_- branch. The unstable tongues for other branches lie beyond $k_z l_\perp = 0.5$, not shown in plot. The parameter values are same as used in Fig. 4.4(b).

We start by probing the existence of any sudden jumps in the most unstable resonant conditions with respect to modulation frequency, an effect reminiscent of the doubly modulated bilayer case in the 'S' region [189]. Surprisingly, we observe two jumps for the singly modulated bilayer system in contrast to only one observed for a doubly modulated bilayer system. A first switch occurs when ω_- changes to $(\omega_+ + \omega_-)/2$ mode and a subsequent one between $(\omega_+ + \omega_-)/2$ and ω_+. This new resonance at $(\omega_+ + \omega_-)/2$ gives rise to distinctly different oscillation dynamics between the layers than when only the two natural modes(ω_+ or ω_-) are selected. The modified coupled equations with g_d takes the form,

$$\ddot{u}_+ + \omega_+^2 u_+ = \cos(\omega_D t)\left(\frac{\mathcal{F}_+}{2} u_+ + \frac{\mathcal{F}_-}{2} u_-\right) \tag{4.19}$$

$$\ddot{u}_- + \omega_-^2 u_- = \cos(\omega_D t)\left(\frac{\mathcal{F}_+}{2} u_+ + \frac{\mathcal{F}_-}{2} u_-\right) \tag{4.20}$$

where, $\mathcal{F}_\pm = -\frac{4\pi g_d}{3}\gamma k_z^2 (F_0(k_z) \pm F_1(k_z))$. The analogous expression for Eq. 4.18 becomes,

$$\begin{vmatrix} \omega_+^2 - (\sigma - \omega_D)^2 & 0 & -\mathcal{F}_+/4 & -\mathcal{F}_-/4 \\ 0 & \omega_-^2 - (\sigma - \omega_D)^2 & -\mathcal{F}_+/4 & -\mathcal{F}_-/4 \\ -\mathcal{F}_+/4 & -\mathcal{F}_-/4 & \omega_+^2 - \sigma^2 & 0 \\ -\mathcal{F}_+/4 & -\mathcal{F}_-/4 & 0 & \omega_-^2 - \sigma^2 \end{vmatrix} = 0 \tag{4.21}$$
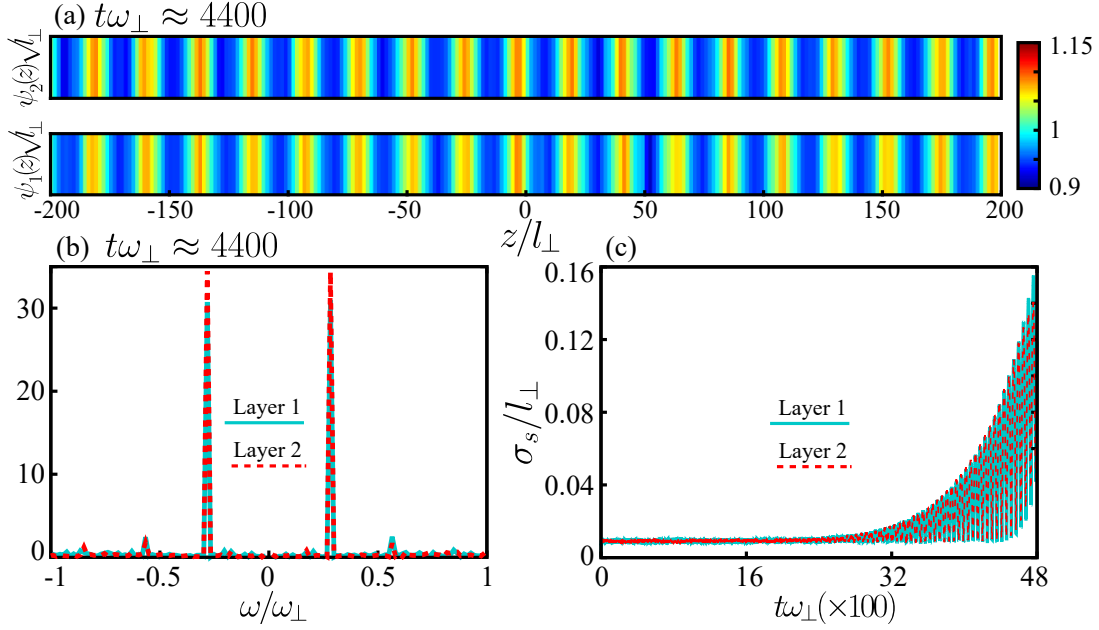
Figure 4.6: (a) Faraday patterns emerging in the unmodulated layer 2(top) spatially symmetric to layer 1(bottom), modulated with $\omega/\omega_\perp = 0.06$ at $t\omega_\perp = 4400$. (b) The most unstable momentum peaks for both layers at $k_z l_\perp \approx 0.33$. (c) The dynamic standard deviation σ_s shows in-phase growth. The periodicity of σ_s is locked to $\omega/\omega_\perp = \mathrm{Re}(\sigma) = 0.06$. $\gamma = 0.04$ for all subfigures.

4.4.3 Singly modulated bilayer system: A numerical study

In this section we simulate the singly modulated bilayer system using real time evolution and go through the different types of dynamics categorically. From Fig. 4.4(b) we pick three modulation frequencies $\omega = 0.06, 0.09$ and 0.12 such that their resonant momenta potentially covers $\omega_+, (\omega_+ + \omega_-)/2$ and ω_- branches.

For modulation frequency $\omega = 0.06$ we obtain spatially symmetric Faraday patterns(correlated) in both layers demonstrated in 4.6(a). The most unstable resonant momenta is ≈ 0.24 (4.6(b)) corresponding to the symmetric branch demonstrated in Fig. 4.5(a). At this point the only relevant root $\sigma = 0.06 \pm 0.0018i$ for a $\gamma = 0.04$ signifies that both u_+ and u_- have the same rate of parametric amplification with an oscillating frequency same as the modulation frequency ω. This behaviour is manifested in the layers such that they have in-phase dynamic oscillation and equal growth rate. It has been captured by calculating the dynamic standard deviation $\sigma_s(t) = \sqrt{\langle|\psi|^4\rangle - \langle|\psi|^2\rangle^2}$ for both layers shown in Fig. 4.6(c). Therefore the Faraday patterns in both layers undergo periodic revivals mimicking a transient time-crystal until the pattern is destroyed due to heating.

Faraday patterns emerging at modulation frequency $\omega = 0.12$(Fig. 4.7) have also similar properties except the spatial patterns in both layers have spatially anti-symmetric (or, anti-correlated) pattern owing to unstable momenta selected from ω_- branch of the
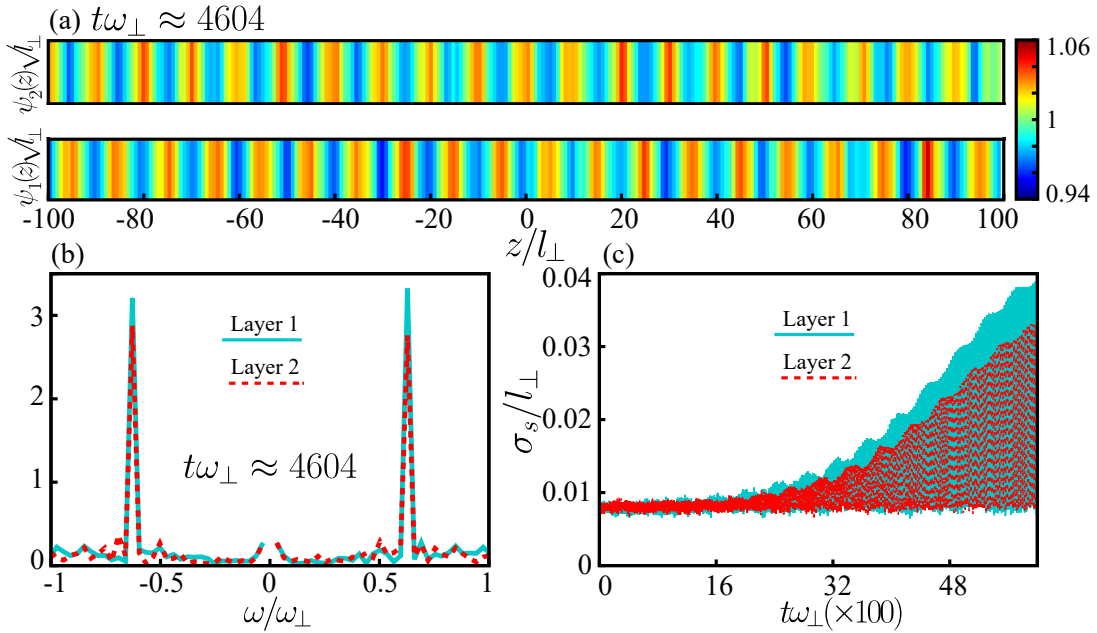
Figure 4.7: (a) Anti-symmetric patterns arising at modulation frequency $\omega/\omega_\perp = 0.12$ at $t\omega_\perp = 4604$. (b) The most unstable momentum for both layers at the same time as (a) resonant at $k_z l_\perp \approx 0.55$. (c) The periodicity of σ_s is $\omega/\omega_\perp = \mathrm{Re}(\sigma) = 0.12$ and both layers are found to oscillate and grow in-phase similar to 4.6(c). $\gamma = 0.04$ for all subfigures.

spectrum in Fig. 4.4(b). The amplitude growth occurs at a rate $\mathrm{Im}(\sigma) = 0.0016$ in Fig. 4.7(c). The size of the patterns are evidently smallers for $\omega/\omega_\perp = 0.12$ (Fig. 4.7(a)) compared to $\omega/\omega_\perp = 0.06$. Our calculations are suitable for oscillations lying in the linear regime. For longer time scales when $\sigma_s/l_\perp > 0.14$, continuous driving gives rise to high amplitude growth driving the system into nonlinear regime. Nontrivial high density waves arise due to emergence of multiple unstable momenta in this region which leads to a quick death of the patterns.

The most interesting characteristics are displayed by the intermediate range of modulation frequencies shown in Fig. 4.4(b). Numerical evidence presents that at a fixed time, density patterns in one layer is dominant while it is dormant in the other. This excitation is periodically transferred between the layers back and forth. Temporal snapshots are presented in 4.8(a)-(b). At $t\omega_\perp \approx 2316$, the patterns are dominant in the unmodulated layer (Fig. 4.8(b)). The frequency space response at the same time, shown in Fig. 4.8(c). In fact, the Fourier space of the spatial patterns in Fig. 4.8(a) reveal that the most unstable momenta corresponds to the mode $(\omega_+ + \omega_-)/2$ and not with the Bogoliubov modes(ω_+ or ω_-) of the bilayer system, as is the case with doubly-modulated case. However, weak contributions from Bogoliubov modes are also observed under this conditions, even in smaller timescales visible in Fig. 4.8(c). The opposite is observed at a slightly later time $t\omega_\perp \approx 2788$ in Fig. 4.8(b). In the dormant layer we observe a messier but a much weaker pattern due to the existence of multiple contributing frequencies e.g.
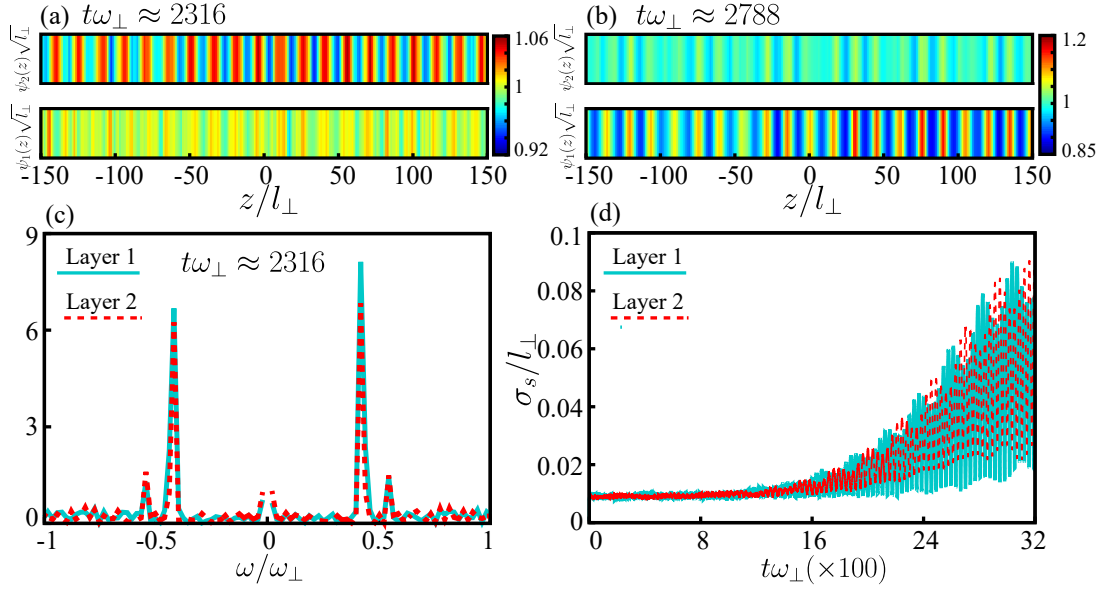
Figure 4.8: Dominant Faraday patterns in the unmodulated (a) and the modulated (b) layers shown at different temporal snapshots at $t\omega_\perp \approx 2316$ and 2788 respectively. (b) Most unstable momentum peak is at $k_z l_\perp \approx 0.45$ shown at $t\omega_\perp \approx 2316$. (c) Out-of-phase oscillations of the standard deviations of the amplitudes are shown for both the layers. It signifies dynamic energy transfer where interestingly the two relevant roots σ_1 and σ_2 of Eq. (4.21) have the property $\mathrm{Re}(\sigma_1) \neq \mathrm{Re}(\sigma_2) \neq \omega/\omega_\perp$.

at $t\omega_\perp \approx 2316$ multiple modes are weakly populated in as shown in Fig. 4.8(c). The periodic exchange of excitation, a product of interlayer dipole-dipole interaction, is best captured by the time-dependent standard deviation of amplitudes of both layers (Fig. 4.8(d)). Solving Eq. 4.21 gives two, in contrast to one, relevant roots for $\omega/\omega_\perp = 0.09$ at $\sigma_1 \approx 0.067 \pm 0.0018i$ and $\sigma_2 \approx 0.11 \pm 0.0018i$. The most important fact to be noted here is $\mathrm{Re}(\sigma_1) \neq \mathrm{Re}(\sigma_2) \neq \omega/\omega_\perp$. This is remarkable because the difference in $\mathrm{Re}(\sigma_1)$ and $\mathrm{Re}(\sigma_2)$ negates possibility of dynamically in-phase oscillations, unlike what is shown in the previous two cases. This leads to alternate revival of the patterns in the two layers or in other words, exchange of energy back and forth. However, equal magnitude of the imaginary components of the two roots signify that the rate of amplitude growth is same (Fig. 4.8(d)) but early contributions from multiple unstable frequencies drives the system into nonlinear regime faster in such a scenario.

In Fig.4.9, we have shown the dynamics of the layers close to the switching boundary values. (a)-(b) depict dynamics just below and above the switching boundaries respectively between ω_+ and $(\omega_+ + \omega_-)/2$ and (c)-(d) for the boundary between $(\omega_+ + \omega_-)/2$ and ω_-. A clear difference can be seen in terms of whether both layers show simultaneous pattern or if there is collapse and revival behaviour showing pattern is active in only one layer at a time.
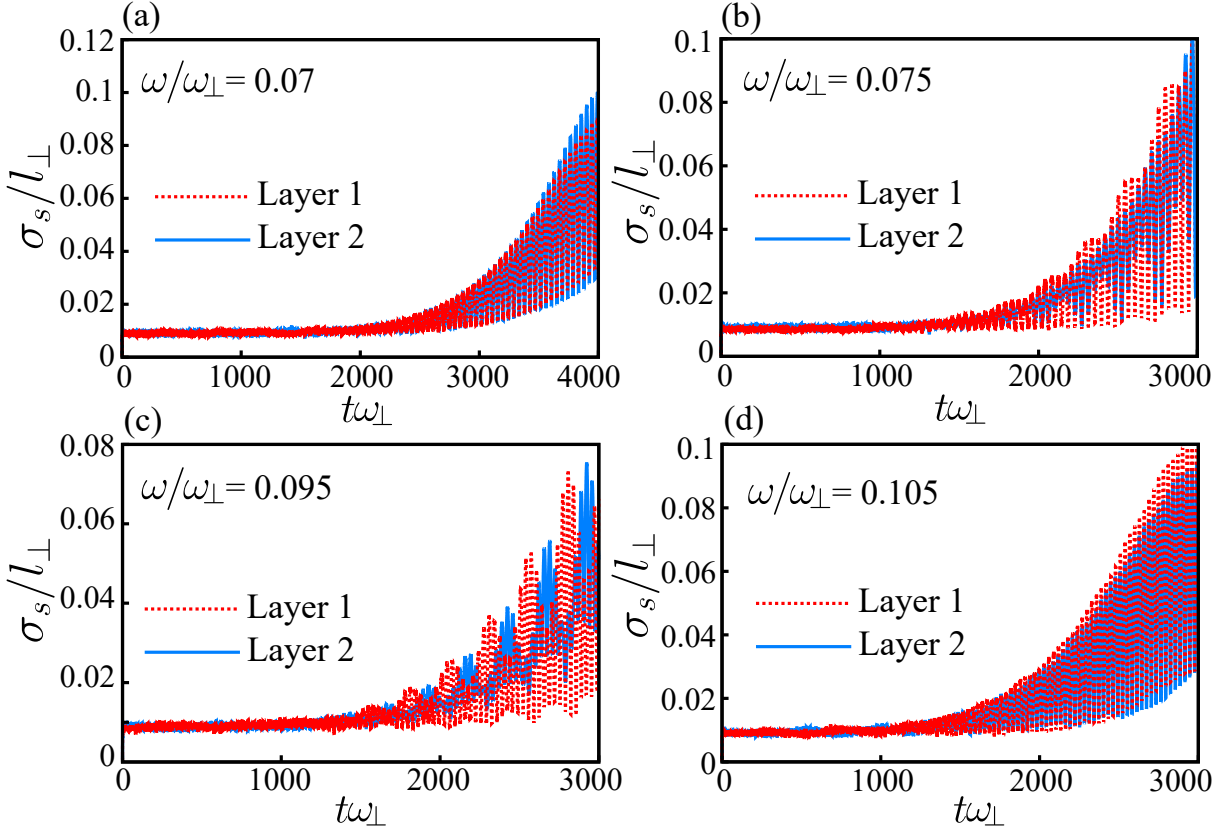
Figure 4.9: (a) and (b) show σ_s plot with respect to time just below and above the switching boundary between ω_+ and $(\omega_+ + \omega_-)/2$ modes. (c) and (d) show the dynamics just below and above the switching boundary between $(\omega_+ + \omega_-)/2$ and ω_- modes. While (a) and (d) show in-phase growth in amplitude, (b) and (c), corresponding to $(\omega_+ + \omega_-)/2$ mode, show amplitude transfer between the layers. Parameters are same as Fig. 4.4 with $\gamma = 0.04$.

4.4.4 Effect of tilting angle

Our results so far have been for an $\alpha = \pi/2$. In this subsection we show the effect of the tilting angle. The tuning of the polarisation angle α brings a change in the Bogoliubov spectrum as the interlayer interaction can be changed from attractive ($\alpha = \pi/2$) to repulsive ($\alpha = 0$). The interlayer interaction $F_1(k_z)$ is plotted in Fig. 4.10(b) inset with respect to k_z for contrasting $\alpha = 0$ (purple, top), $\alpha = 0.5$ (orange, middle) and $\alpha = \pi/2$ (yellow, bottom). For $\alpha = 0$ rad, F_1 is purely positive and the interaction is repulsive between the layers. For $\alpha = \pi/2$, interlayer interaction is purely negative and is reflected in the negative values of $F_1(k_z)$ for any k_z. For the intermediate $\alpha = 0.5$ rad, $F_1(k_z)$ becomes zero for some value of $k_z \approx 0.45$ and its overall magnitude remains close to zero for most k_z values. From this we can conclude that around $\alpha = 0.5$, interlayer interaction changes sign and its nature of interaction.

At $\alpha = 0$ rad, due to strong repulsive interlayer interaction the anti-symmetric branch
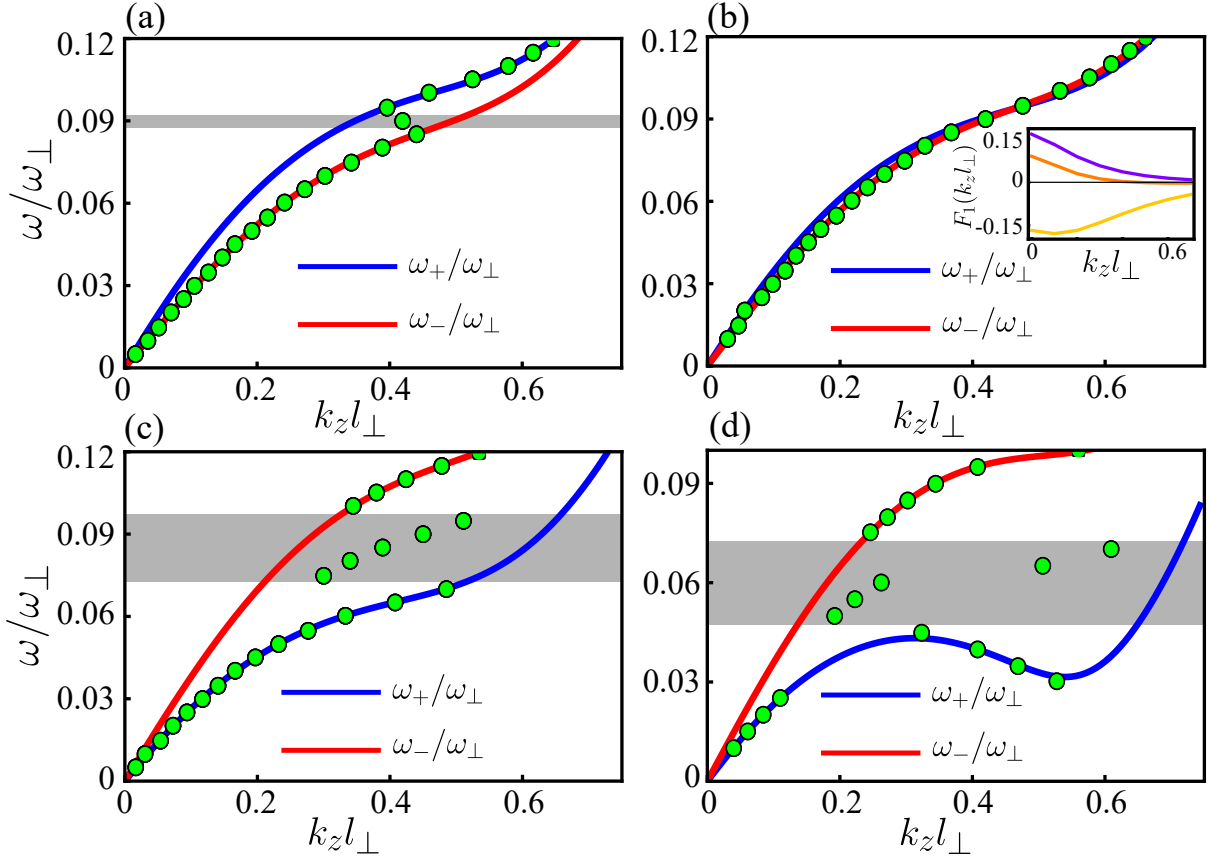
Figure 4.10: Solid curves in (a)-(c) depicts the Bogoliubov spectrum for $\alpha = 0, 0.6$ and $\pi/2$ rad respectively. The dots obtained by solving Eq. (4.21) represent the most unstable modes under g_d modulation. The common parameters are $(\tilde{g}, \tilde{g}_d, \delta, \gamma) = (-0.05, 0.1, 4, 0.04)$. In (b) the function $F_1(k_z l_\perp)$ has been plotted for the above three α. The gray area shows the region where the most unstable mode corresponds to $(\omega_+ + \omega_-)/2$ mode.

of the Bogoliubov spectrum acquires a lower energy than the symmetric branch. In Fig. 4.10(a) we observe the two switches in the most unstable mode (green dots). This is similar to what has been described so far except the symmetric and anti-symmetric branches are flipped. Also since branches are close to each other, the region in which $(\omega_+ + \omega_-)/2$ becomes the most unstable mode is quite thin, shown in gray area in the figure. As polarisation angle changes from 0 rad, the interlayer repulsion gradually decreases. The magnitude of the interlayer interaction is also weakened. At $\alpha = 0.5$ rad, the two branches become quasi-degenerate, a trait which is also observed when interlayer separation $\delta/l_\perp$ is large. At $k_z l_\perp \approx 0.45$ the two branches cross each other or in other words, they're exactly degenerate, shown in Fig. 4.10(b). This point exactly coincides with when $F_1(k_z)$ is exactly zero for $\alpha = 0.6$ shown in the inset. Hence, the degeneracy is a consequence of vanishing interlayer interaction. The most unstable mode lies in the asymmetric branch for any modulation frequency and no switches are observed. If frequency modulation

is done for $\omega \approx 0.095\omega_\perp$ which corresponds to resonant momentum $k_z \approx 0.45$, due to vanishing interlayer interaction the excitation transfer is weak and the unmodulated layer has lesser growth amplitude than the modulated layer at any given time. The transfer will not be completely halted as the system parameters are modulated around the mean value of the parameter for which the particular dispersion relation is valid. Next, for attractive interlayer interaction as is the case in Fig. 4.10(c) the symmetric branch acquires lower energy. This spectrum has been already discussed previously and shown here for contrast.

Keeping $\alpha = \pi/2$ if we change the value of $\tilde{g}$ to more negative, we enter the R region [Fig. 4.10(d)]. Here the behaviour of most unstable mode is different than what was obtained for a doubly-modulated bilayer case. For example, when $\omega < \omega_{\mathrm{roton}}$ the most unstable mode for doubly-modulated system correspond to $n\omega$ such that $\omega_{\mathrm{roton}} < n\omega < \omega_{\mathrm{maxon}}$ and the most unstable momenta is $k_{z,2}^s$ corresponding to the symmetric branch. This means $n > 1$. In contrast, for a singly modulated case, $n = 1$ or in other words for a modulation frequency $\omega < \omega_{\mathrm{roton}}$, most unstable mode remains unaffected by the existence of rotonic character. For modulation frequency $\omega > \omega_{\mathrm{maxon}}$ the usual switches are retrieved from ω_+ to $(\omega_+ + \omega_-)/2$ and then to ω_-. However, for the intermediate values of modulation frequency in the gray region ($\omega_{\mathrm{roton}} < \omega < \omega_{\mathrm{maxon}}$), $k_{z,2}^s$ are selected as the most unstable momenta, similar to the doubly-modulated scenario.

So far our studies have focused on bilayer systems. Study of more than two layers is also bound to make the dynamical transfer of excitations a more interesting process. Concluding the basic understanding of a homogeneous bilayer system, we now move on to a trapped system.

4.5   Trapped BEC: Lagrangian Equations of Motion

A different aspect of external perturbation to the system can be observed in trapped condensates. The system under weak external forcing develops collective excitations and we aim to study the controlled excitations of these frequencies and their manipulation. With the addition of a harmonic confinement of frequency $\omega_z = \lambda\omega_\perp$ along the z direction, Eq. (4.2) for j^{th} layer is,

$$
\begin{aligned}
i\hbar \frac{\partial}{\partial t}\psi_j(z,t) &= \left[-\frac{\hbar^2}{2M}\frac{d^2}{dz^2} + \frac{M}{2}\lambda^2 z^2 + \frac{g}{2\pi l_\perp^2}|\psi_j(z,t)|^2 \right. \\
&\qquad \left. + \frac{g_d}{3l_\perp^2}\sum_{m=1}^{N}\int \frac{dk_z}{2\pi}e^{izk_z}n_m(k_z)F_{m-j}(k_z) \right]\psi_j(z,t) \qquad (4.22)
\end{aligned}
$$

Unlike the homogeneous case, the parametric modulation considered here is with a chirped frequency. Chirping introduces mode-locking in the system [148, 149] which remains unexplored for the case of dipolar BEC. An analytic study of quasi $1D$ BEC layers under chirped modulation is carried out. We write the Lagrangian density for describing the

system assuming we have Gaussian wave functions where the widths and their center of masses are some of the variational parameters. We solve for the Euler-Lagrange equations of motion for the variational parameters after obtaining the Lagrangian $L = \int dz \mathcal{L}$. These dynamic equations allow further study regarding mode-locking under chirped condition as we discuss below in details. For the jth layer:

$$\mathcal{L}_j = \frac{i\hbar}{2}\left(\psi_j \frac{\partial \psi_j^*}{\partial t} - \psi_j^* \frac{\partial \psi_j}{\partial t}\right) + \frac{\hbar^2}{2M}|\partial_z \psi_j|^2 + \frac{M\lambda^2 z^2}{2}|\psi_j|^2 + \frac{g}{4\pi l_\perp^2}|\psi_j|^4$$
$$+ \sum_m \frac{g_d}{6l_\perp^2}|\psi_j|^2 \int \frac{dk_z}{2\pi} e^{izk_z} n_m(k_z) F_{m-j}(k_z) \tag{4.23}$$

where the Gaussian variational ansatz is,

$$\psi_j = \frac{1}{\pi^{\frac{1}{4}}\sqrt{W_j(t)}} \exp\left[-\frac{(z-z_j(t))^2}{2W_j(t)^2} + iz\alpha_j(t) + iz^2\beta_j(t)^2\right] \tag{4.24}$$

where the variational parameters are W_j, z_j, α_j and β_j. $z_j(t)$ is the time-dependent center of mass of the solution. Please note that to faithfully describe the dynamics of the system using this variational ansatz under periodic perturbation, there should not be local excitations or density modulations arising in the condensate i.e. the macroscopic shape of should adhere to that of a Gaussian ansatz qualitatively. After integration, we obtain a simplified Lagrangian,

$$L_j = \left[\frac{\hbar}{2}(W_j^2 \dot{\beta}_j + 2z_j^2 \dot{\beta}_j + 2z_j \dot{\alpha}_j)\right] + \left[\frac{\hbar^2}{2M}\left(\frac{1}{2W_j^2} + 2W_j^2 \beta_j^2 + \alpha_j^2 + 4z_j \alpha_j \beta_j + 4z_j^2 \beta_j^2\right)\right]$$
$$+ \frac{M\lambda^2}{4}(W_j^2 + 2z_j^2) + \frac{g}{4\pi l_\perp^2}\frac{1}{\sqrt{2\pi}W_j} + \frac{g_d}{6l_\perp^2}\sum_m \int \frac{dk_z}{2\pi} n_m(k_z) n_j(k_z) F_{m-j}(k_z) \tag{4.25}$$

The variational parameters α_j and β_j may be eliminated by transformation $L_j \to L_j - \frac{d\mathcal{G}_j}{dt}$. Solving the equations of motion for α_j and β_j simultaneously gives,

$$\alpha_j = \frac{M}{\hbar}\left(\dot{z}_j - \frac{z_j \dot{W}_j}{W_j}\right)$$
$$\beta_j = \frac{M}{\hbar}\frac{\dot{W}_j}{2W_j}$$

For a $\mathcal{G}_j = \frac{\hbar \beta_j W_j^2}{2} + \hbar(\alpha_j z_j + \beta_j z_j^2)$ the transformed Lagrangian becomes,

$$L_j = \frac{M}{2}\left(\frac{\hbar^2}{2M^2W_j^2} - \frac{\dot{W}_j^2}{2}\right) - \frac{M\dot{z}_j^2}{2} + \frac{M\lambda^2}{4}(W_j^2 + 2z_j^2) + \frac{g}{\sqrt{2\pi}4\pi l_\perp^2 W_j} + V(W_j, z_j, W_m, z_m)$$

(4.26)

where $V(W_j, z_j, W_m, z_m) = \frac{g_d}{6l_\perp^2}\sum_m \int \frac{dk_z}{2\pi}n_m(k_z)n_j(k_z)F_{m-j}(k_z)$. We obtain the Euler-Lagrange equations for the width and the center of mass,

$$M\ddot{W}_j = \frac{\hbar^2}{MW_j^3} + \frac{2g}{4\pi l_\perp^2}\left(\frac{1}{\sqrt{2\pi}W_j^2}\right) - M\lambda^2 W_j - 2\frac{\partial V(W_j, z_j, W_m, z_m)}{\partial W_j}$$

(4.27)

$$M\ddot{z}_j = -M\lambda^2 z_j - \frac{\partial V(W_j, z_j, W_m, z_m)}{\partial z_j}$$

(4.28)

An interesting result comes into light in the form of coupling between the center of mass and width dynamics of multi-layer dipolar BECs. This is not seen for a single layer as the center of mass term gets eliminated. The last terms in Eq. (4.27) and (4.28) are the dipolar coupling terms and we expect to see new dynamics as a result which will be studied in later sections.

4.6 Mode-locking

We have come across mode-locking already in 2.3.2 in introductory chapter. A BEC, parametrically modulated with chirped frequency, gets collectively excited at a steep rate when the modulation frequency equals its natural mode frequency. Once mode-locked, the system continues to oscillate at the natural frequency even after the modulation frequency has crossed the resonance window. Below we aim to capture the physics analytically. We start from the equation of motion we calculated in the previous section. We eventually are able to construct a Hamiltonian which mimics a particle in an effective potential whose ground state corresponds to the condition for mode-locking.

4.6.1 Single Layer: An analytic study

We study the simplistic case of a single layer of quasi-$1D$ dipolar BEC parametrically modulated with a chirped frequency as $g(t) = g(1 + \gamma \sin \Delta t^2/2)$. The equation of motion in Eq. (4.27) is modified as,

$$M\ddot{W} = \frac{\hbar^2}{MW^3} + \frac{2g(t)}{4\pi l_\perp^2}\left(\frac{1}{\sqrt{2\pi}W^2}\right) - M\lambda^2 W - 2\frac{\partial V(W)}{\partial W_j}$$

(4.29)

Linearization under the assumption that the width oscillates around equilibrium value $\bar{W}$ by a small amount ϵ gives the following equations,

$$M\ddot{\epsilon} + \left[\frac{3\hbar^2}{M\bar{W}^4} + \frac{g}{\pi\sqrt{2\pi}l_\perp^2\bar{W}^3} + M\lambda^2 + V'(\bar{W}) \right]\epsilon = \frac{2g\gamma}{4\pi l_\perp^2} \frac{1}{\sqrt{2\pi}\bar{W}^2} \sin \Delta t^2/2$$

$$\implies \ddot{\epsilon} + \omega_0^2\epsilon = \frac{2g\gamma}{4\pi m l_\perp^2} \frac{1}{\sqrt{2\pi}\bar{W}^2} \sin \Delta t^2/2 \quad (4.30)$$

where,

$$V'(W) = \frac{g_d}{6l_\perp^2} \int \frac{dk_z}{2\pi} k_z^2 \bar{W} n(k_z)^2 F_{m-j}(k_z)$$

$$\omega_0 = \left[\frac{3\hbar^2}{M^2\bar{W}^4} + \frac{g}{\pi M\sqrt{2\pi}l_\perp^2\bar{W}^3} + \lambda^2 + \frac{V'(\bar{W})}{M} \right]^{1/2} \quad (4.31)$$

Here, ω_0 is clearly the system's natural frequency. And the right hand side of Eq. (4.30) refers to the external forcing. For the following calculations we follow the procedure in [148] which is solved for the case of a forced non-dipolar BEC and [195] which is for classical nonlinear systems. We assume a solution of the type $\epsilon = a(t)\sin\phi(t) = a(t)\text{Im}[e^{i\phi(t)}]$ where $a(t)^2 = I$ can be defined as the action variable. At resonance $\dot{\phi}(t) = \omega_0$ and we assume $\ddot{\phi}(t) \approx 0$. We shall restrict our study near the resonance which captures the essential physics. Replacing the guess solution in Eq. (4.30),

$$2i\dot{a}\dot{\phi} + ia\ddot{\phi} - a\dot{\phi}^2 + \omega_0^2 a = \frac{2g\gamma}{4\pi m l_\perp^2} \frac{1}{\sqrt{2\pi}\bar{W}^2} e^{i\left(\frac{\Delta t^2}{2} - \phi(t)\right)}$$

Separating real and imaginary parts,

$$\omega_0 - \dot{\phi} = \frac{2g\gamma}{4\pi M l_\perp^2} \frac{1}{a(t)\sqrt{2\pi}\bar{W}^2} \cos\left(\frac{\Delta t^2}{2} - \phi\right) \quad (4.32)$$

$$\frac{d(a^2\dot{\phi})}{dt} = \frac{2g\gamma}{4\pi M l_\perp^2} \frac{a(t)}{\sqrt{2\pi}\bar{W}^2} \sin\left(\frac{\Delta t^2}{2} - \phi\right) \quad (4.33)$$

The phase mismatch $\Phi(t) = \frac{\Delta t^2}{2} - \phi$ can be defined as the angle variable. The above equations can be recast in form of action-angle variables as,

$$\dot{\Phi}(t) = \Delta t - \omega_0 + \frac{2g\gamma}{4\pi M l_\perp^2} \frac{1}{\sqrt{2\pi I(t)}\bar{W}^2} \cos\Phi \quad (4.34)$$

$$\dot{I}(t) = \frac{2g\gamma}{4\pi M l_\perp^2} \frac{\sqrt{I(t)}}{\sqrt{2\pi}\bar{W}^2} \sin\Phi \quad (4.35)$$

To uphold the mode-locking condition at resonance($t = \omega_0/\Delta$) there should not be any change in the phase mismatch i.e. $\dot{\Phi} = 0$. This is possible when $\Phi = 0$ or π. To obtain an intuitive picture we can formulate an effective Hamiltonian from the perturbations of the action-angle variables. If the energy for the Hamiltonian is minimised for the specific values of $\Phi = \pi$ the system will prefer to stay mode-locked (We ignore $\Phi = 0$ case because eventually it can be seen that energy is maximised in this case). Let $I = I_0 + \delta I$ and $\Phi = \Phi_0 + \delta\Phi$. Under mode-locked condition we would expect $\delta\Phi = 0$ as the modulation frequency and . Replacing in the above equations we get,

$$
\begin{aligned}
\dot{\delta\Phi} &= \delta I \, S \\
\dot{\delta I} &= -A\sin\delta\Phi + \frac{\Delta}{S}
\end{aligned}
$$

where, $S = \frac{2g\gamma}{4\pi M l_\perp^2} \frac{1}{I^{3/2}\sqrt{2\pi \bar{W}^2}}$ and $A = \frac{2g\gamma}{4\pi M l_\perp^2} \frac{\sqrt{I(t)}}{\sqrt{2\pi \bar{W}^2}}$. The corresponding Hamiltonian becomes,

$$
\mathcal{H} = \frac{S\delta I^2}{2} - A\cos\delta\Phi - \frac{\Delta}{S}\delta\Phi \tag{4.36}
$$

depicting a particle of mass $1/S$ moving in a pseudo-potential $-A\cos\delta\Phi - \frac{\Delta}{S}\delta\Phi$. This potential has a minimum for $\delta\Phi = 0$ and this corresponds to the condition for mode-locking as we predicted. An extensive calculations for multi-layer systems is a future goal which is nontrivial as it involves multiple coupled equations and needs appropriate guess solutions.

4.6.2 Single Layer: Numerical results

Before we show the transfer of mode-locked excitation between layers, we briefly review results showing mode-locking in a single layer in order to understand and characterize its properties. Mode-locking is an excellent technique to identify and excite natural frequencies of the system in a controlled fashion. This can be achieved in either trapped condensates or self-bound soliton solutions. Solitons are stable only for very weak modulation strength, so we focus on stable trapped cases. However note that extremely strong modulations may give rise to local density patterns, eventually breaking the BEC even for trapped cases. We strive for a balanced perturbation where we observe mode-locking without inducing local density fluctuations. Mode-locking in BEC is a long time dynamics, surviving without heating up. This is a result of the system not absorbing more energy from the modulation once mode-locking has been achieved. The amplitude of oscillations remain constant after resonance condition is achieved and the BEC undergoes a breathing mode. In case of higher dimensional condensates, where there are multiple natural frequencies (breathing mode, quadrupole mode etc), it is possible to excite each mode
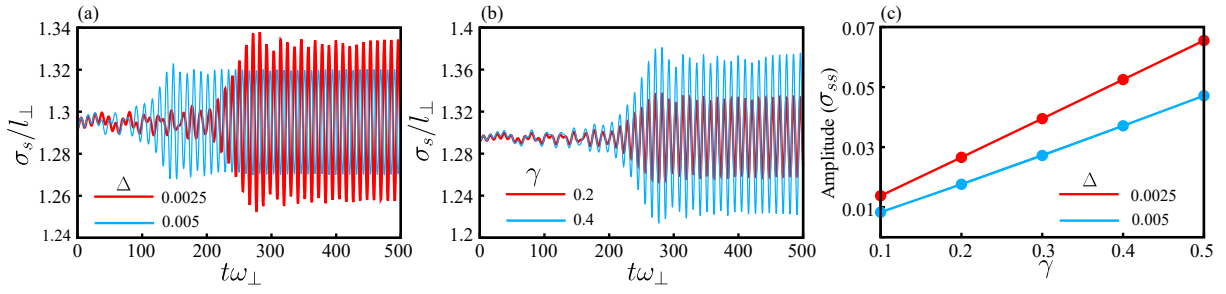
Figure 4.11: Mode-locking in a single quasi-$1D$ dipolar BEC layer is shown. (a) We vary Δ and plot σ_s(width) with respect to time. It is observed that for a lower value of Δ the system takes longer to mode-lock for a fixed $\gamma = 0.2$. Interestingly, a slower chirping is also accompanied by a larger mode-locked amplitude. This is because the system is allowed to spend more time around the resonance. (b) For a constant $\Delta = 0.0025$, we vary the strength of modulation. Clearly a stronger modulation results in higher energy transfer and higher amplitude. (c) We plot the standard deviation of $\sigma_s(t)$, which gives us the averaged maximum amplitude. As already mentioned, a slower chirping rate shows higher amplitude for any γ. All plots have been obtained for $(\tilde{g}, \tilde{g}_d, \alpha, \lambda) = (0.05, 0.1, \pi/2, 0.3)$.

one by one when the external frequency is adiabatically swept through the spectrum via chirping. For instance, in a quasi-2D dipolar BEC where the condensate is anisotropic in the 2D plane due to a tilted dipole vector as discussed thoroughly in previous chapter, one can easily observe excitation of quadrupole mode via mode-locking.

In Fig. 4.11, we characterize the basic properties shown by a mode-locked BEC. A dynamic variation in Fig. 4.11(a) shows the width of the condensate with respect to time for two different value of the parameter Δ, the chirping rate. When $\Delta t^2/2 < \omega_0$, both the natural and driving frequencies exist in the system with comparable strength. However in the resonance window $\Delta t^2/2 \approx \omega_0$, massive energy transfer occurs from the driving to the natural frequency such that ω_0 becomes dominant in the post-resonance period. The system is less affected by frequencies $\Delta t^2/2 >> \omega_0$. This is reflected in the small fluctuations in σ_s in small time period after mode-locking has been achieved, while the fluctuations are suppressed in long time period. The energy transfer mechanism is strongly dependent on the time spent in the small resonance window. To achieve a larger energy transfer it is vital that Δ must be small. Fig. 4.11(b) characterizes the comparative effect of different driving strengths on the mode-locking. It is easy to see that a stronger driving will be able to pump more energy into the system which in turn results in a higher amplitude of collective mode oscillation for the condensate. A very strong amplitude, however, may result in an ineffective mode-locking and inevitable loss of the condensate.

4.6.3   Bilayer: Numerical Results

Expansion and propagation of collective modes in multilayer condensates are one of the least explored topics in dipolar BEC. Although there have been many studies regarding the anisotropic effect of DDI, impact of its long-range nature has been undervalued [196–198]. In this section we study the resonant energy transfer between two quasi-1D dipolar BEC layers where we show the transfer of mode-locked wave back and forth, possible due to long-range dipolar interaction between them.
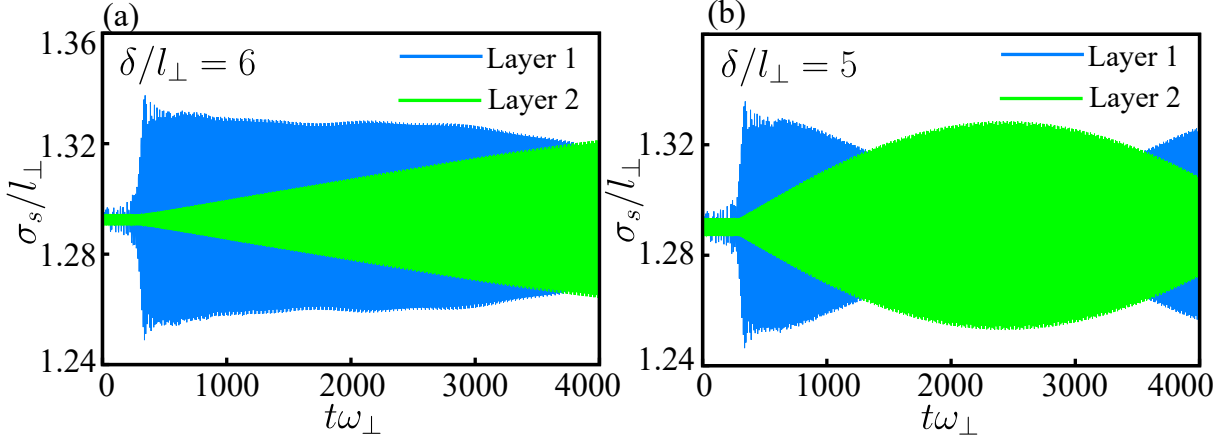
Figure 4.12: Mode-locking in a singly-modulated(Layer 1) bilayer quasi-$1D$ dipolar BEC layer. Layer 1 gets mode-locked to its natural frequency (which is verified by a simple Fourier transform of the $\sigma_s(t)$) first. However due to interlayer coupling this energy is slowly transferred to the unmodulated Layer 2 which also gets mode-locked to natural frequency. As the separation between the layers increase, the interlayer DDI lessens. The resulting rate of energy transfer decreases as shown in (a)-(b). All plots have been obtained for $(\tilde{g}, \tilde{g}_d, \alpha, \lambda, \gamma, \Delta) = (0.05, 0.1, \pi/2, 0.3, 0.2, 0.002)$.

We again restrict our dipole vector to the $x - y$ plane as done for the homogeneous case. We first consider the case where $\alpha = \pi/2$ and the interlayer interaction is attractive. This provides a stronger interaction than $\alpha = 0$ case due to the inherent anisotropy of the DDI term.

After the onset of frequency chirping, mode-locking takes place at the natural frequency. Once mode-locking has been achieved, a smooth and continuous energy transfer takes place between the two layers while the maximum amplitude remains equal and fixed between the layers. Changing the separation between the layers manifests in the change in rate of energy transfer demonstrated in Fig. 4.12. The closer the layers, the faster is the energy transfer between the layers and vice versa. Usually a faster energy transfer between the layers also means an inefficient energy transfer. However for $\delta/l_\perp > 5$ the rate of transfer is already quite slow. Please note that, although higher harmonics maybe excited when both layers are modulated, it is usually suppressed when only one layer is
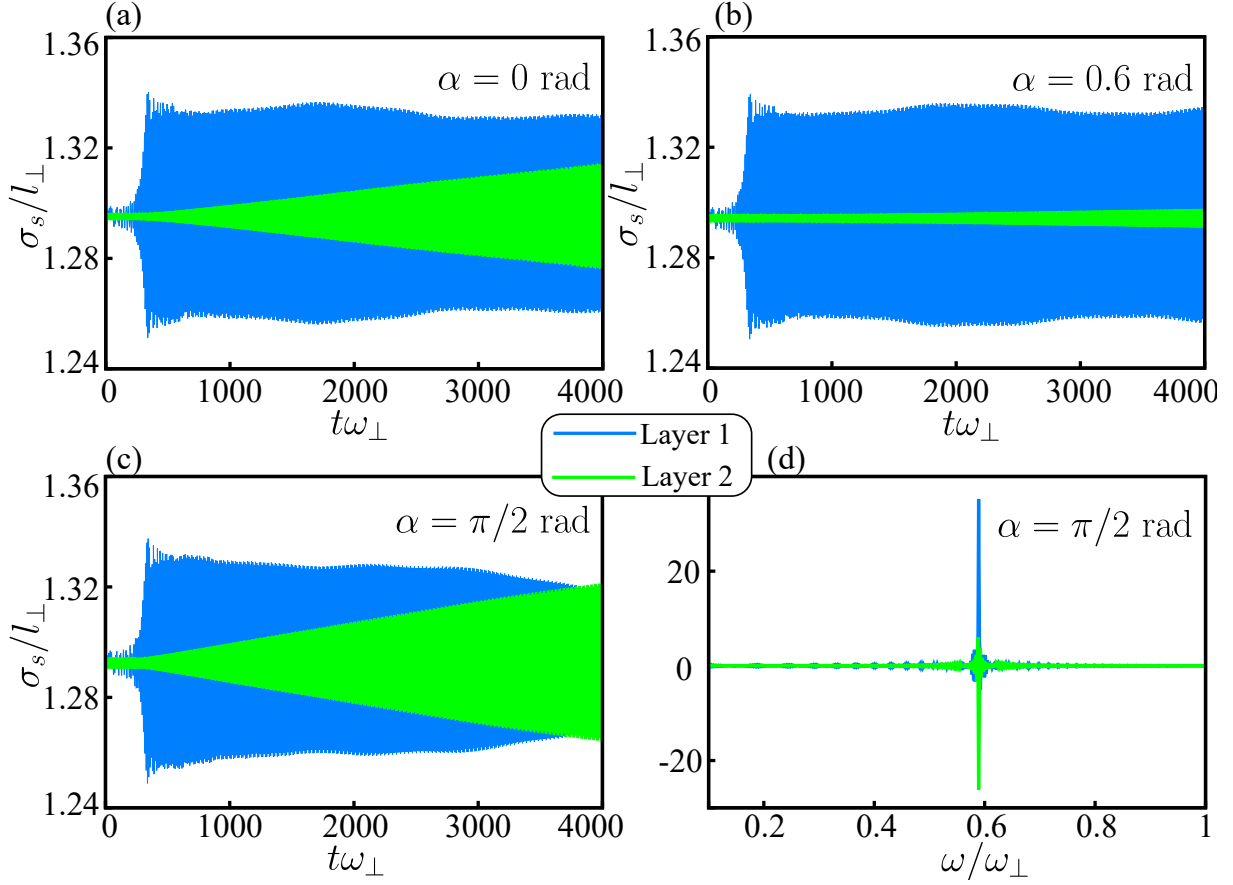
Figure 4.13: Mode-locking in a singly-modulated(Layer 1) bilayer quasi-1D dipolar BEC layer. From (a)-(c), we have shown the energy transfer from Layer 1 to Layer 2 for various α. At $\alpha = 0$ the interlayer interaction is repulsive and at $\alpha = \pi/2$ the interlayer interaction is attractive. The interaction changes from positive to negative as α goes from 0 to $\pi/2$. (d) The frequency response of (c) showing the mode-locked frequency for both layers. All plots have been obtained for $(\tilde{g}, \tilde{g}_d, \delta/l_\perp, \lambda, \gamma, \Delta) = (0.05, 0.1, 6, 0.3, 0.2, 0.002)$.

pumped.

4.6.4   Effect of tilting angle

The angle α is another tunable parameter in the system. Fig. 4.13(a)-(d) shows transfer of mode-locking between two layers for a series of tilting angle $\alpha = 0, 0.6$ and $\pi/2$ rad. This changes the interlayer interaction from repulsive (positive value) to attractive (negative value) gradually. In the intermediate region when interlayer DDI is close to zero, the layers interact only weakly even if the interlayer separation is not large. Under this condition the transfer of mode-locking is suppressed as seen in Fig. 4.13(b). A representative frequency space plot in Fig. 4.13(d) confirms that both layers are oscillating locked to a single frequency giving a sustainable energy transfer process.

If interlayer interaction is purely attractive for $\alpha = \pi/2$, the mode-locking maybe

destroyed easily compared to the purely repulsive $\alpha = 0$ case when δ is small even though the condensates are non-overlapping. In the later case mode-locking can be lost if the driving amplitude is very high, similar to the single layer case. In that case, the condensate starts to develop density patterns due to excitation of multiple frequencies. Mode-locking allows us to excite the low lying modes in a controllable fashion as we have multiple tunable parameters such as the strength of modulations, chirping rate, δ etc.

4.7 Center of Mass Oscillations

So far we have covered the collective excitation of width modes. We observed transfer of mode-locking phenomenon due to DDI. Here, we briefly take up the study of excitation of the center of mass. Propagation of center of mass mode has been previously studied regarding multilayer dipolar condensates [198]. However, here we not only study the propagation of the excitation between the layers but also between different modes.

In case of a single layer BEC, the width and center of mass modes decouple from each other. However, a coupling between the modes is retained once multilayer configuration is considered as already calculated in section 4.5 Eq. (4.27) and Eq. (4.28). It was hinted earlier that it leads to interesting dynamics; here, we discuss and demonstrate the behaviour of these excitations under external modulation. Strikingly, we observe the transfer of energy between center of mass and width modes due to the existing coupling between the modes arising due to dipole-dipole interaction. The modulation is now done with a constant frequency instead of a chirped frequency.

Unlike the interlayer coupling of width modes, coupling between width and center of mass (c.o.m.) mode is extremely weak. Modulation of the usual parameters g or g_d as it has been done so far fails to amplify the transfer of excitation. Modulating g, g_d or even trap frequency ω_z leads to emergence of width modes such as breathing mode and the center of mass remains negligibly affected. Instead of expecting to observe any substantial transfer of energy from width modes to c.o.m. mode, we try to modulate the trap center in order to first excite the center of mass and expect energy transfer from c.o.m. mode to width modes. This turns out to be a successful endeavor. We consider periodically modulated trap $\frac{1}{2}m\omega_z^2(z - z_0(t))^2$, where the center $z_0(t) = \gamma \cos \omega t$ is time-dependent. This results in the vibration of the potential minimum for the condensate, hence the periodic shift in the c.o.m. of the condensate. The natural mode of c.o.m. is $\approx \omega_z$ when ω_z is strong compared to contact and dipolar interactions.

4.7.1 Excitation transfer between c.o.m. and width modes

Numerical analysis of the bilayer case with modulation of trap center reveals excitation of width modes along with the usual c.o.m. excitation thanks to the nontrivial DDI
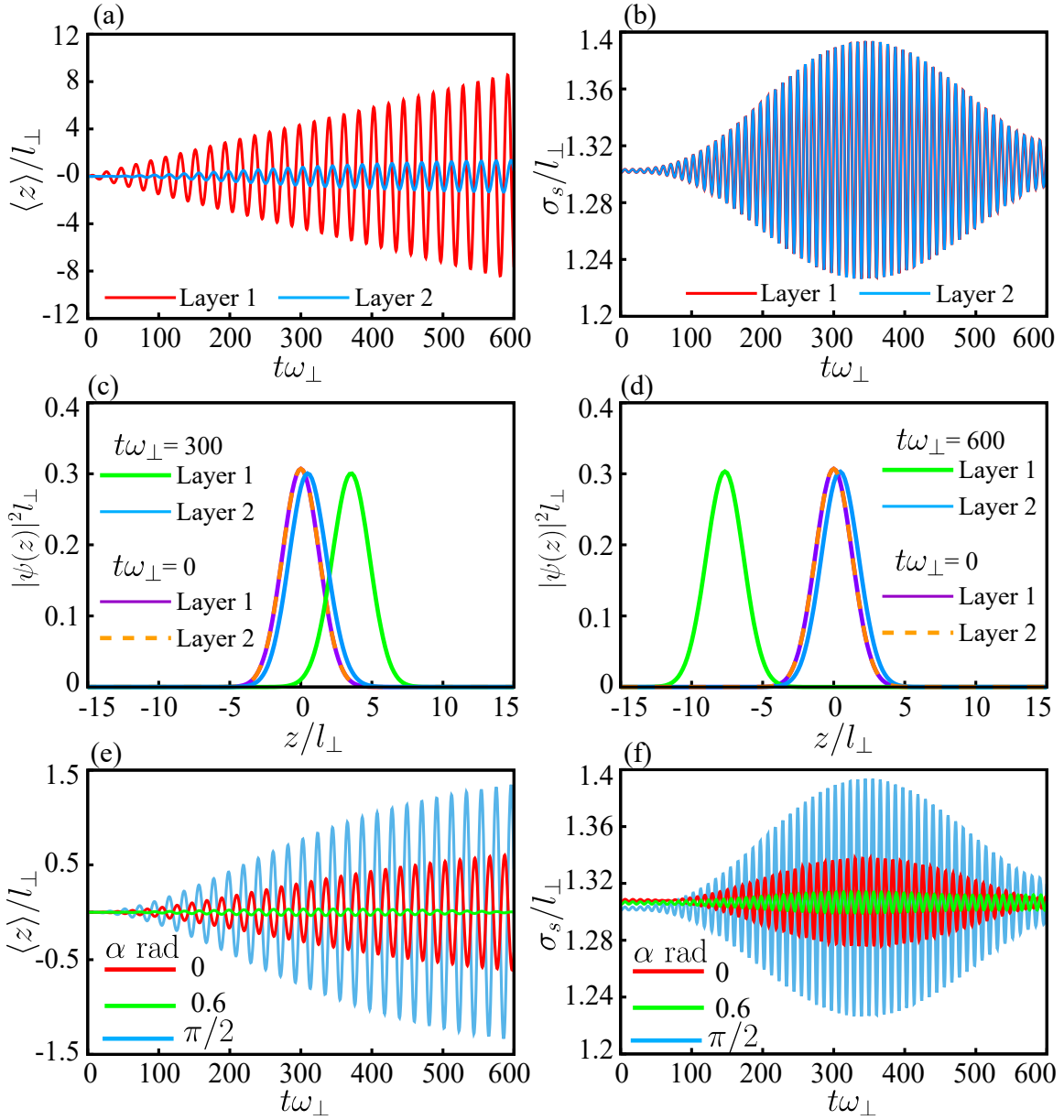
Figure 4.14: We modulated Layer 1 by periodically changing the trap center and observe the dynamics of excited modes. (a) Center of mass oscillations of both layers with respect to time. The amplitude gradually increases as we modulated at $\omega = \omega_z$. (b) The width of the layers described by σ_s shows a collapse and revival behaviour with time signifying energy exchange between center of mass and width modes. The width oscillations are in-phase here. We compare various temporal snapshots of the density distributions of the two layers with their $t\omega_\perp = 0$ state in (c)-(d). We observe clear change in center of mass in (c)-(d). At large time scales due to continuous pumping, the system starts to develop density defects. So we have shown the dynamics till $t\omega_\perp < 600$. Here $(\tilde{g}, \tilde{g}_d, \alpha, \delta/l_\perp, \lambda, \gamma, \Delta) = (0.05, 0.1, \pi/2, 6, 0.3, 0.1, 0.3)$. In (e) and (f) we show the center of mass and width oscillations respectively for only the unmodulated Layer 2. Here $(\tilde{g}, \tilde{g}_d, \delta/l_\perp, \lambda, \gamma, \Delta) = (0.05, 0.1, 6, 0.3, 0.1, 0.3)$. At $\alpha = 0.6$ the transfer is heavily suppressed because of extremely weak interlayer DDI.

coupling. The width mode excitations are induced by transfer of excitation energy from c.o.m. mode. The energy transfer is very weak such that the interlayer separation has to be quite less to see significant energy transfer. To maximize the interlayer interaction, we fix $\alpha = \pi/2$. We modulate only one layer (Layer 1) as done previously. The parametric values are such that the unmodulated system is in stable region.

In Fig. 4.14 we depict the c.o.m. and width dynamics of both modulated and unmodulated layer. The c.o.m. of the unmodulated layer starts oscillating almost immediately and the excitation of Layer 1 and 2 are shown in Fig. 4.14(a). In Fig. 4.14(b) the width oscillations are gradually seen to grow and show a collapse-revival pattern which is a signature of energy transfer between the c.o.m. modes and width modes. The width oscillations in both layers have similar growth rate and they oscillate in-phase. The condensate densities at initial time $t\omega_\perp = 0$ and at a later time are compared in Fig. 4.14(c)-(d). At large time scales, the condensate densities develop local patterns and the oscillations are no more purely collective so the dynamics shown here are restricted to $t\omega_\perp < 600$.

The major difference in c.o.m. oscillations and the width oscillations are in their amplitude. The c.o.m. oscillations show an almost monotonic growth with time when modulation frequency $\omega = \omega_z$ [Fig. 4.14(a)]. The c.o.m. amplitude of Layer 1 is much larger compared to the c.o.m. amplitude of Layer 2 due to weak transfer of energy. The amplitude of width oscillations are even weaker. For lower values of $\delta/l_\perp$ this can be substantially improved.

4.8 Conclusion

Periodic modulation of various systems has been at the forefront of research for decades now. Nonlinear systems often do not behave predictably under periodic modulations, providing key insight into the system's properties. Bose-Einstein condensates provide a coherent system to analyse such nonlinear properties and acts as a simulator for many classical and quantum systems of interest. Morever, dipolar BEC with tunable polarization angle provides extreme controllability. In the first part of the chapter, a homogeneous condensate develops Faraday patterns and we present a detailed analysis in a bilayer system where the pattern shows nontrivial dynamics. In the second half, the concept of mode-locking has been introduced for a trapped condensate and the transfer of excitations between two layers is shown. We characterize the effect of polarization angle as it may change the nature of interlayer interaction from repulsive to attractive and affect the transfer of excitation. We demonstrate numerically the energy transfer between the center of mass and width modes in a bilayer system due to interlayer DDI. Ongoing work includes further analytic calculation to characterise the behaviour of bilayer trapped systems when only a single layer is modulated.

Chapter 5

Self-bound Doubly-Dipolar Bose-Einstein Condensates

Current chapter is an adaptation of the research article "Self-Bound Doubly Dipolar Bose-Einstein Condensates" [199]. In this article, a doubly-dipolar BEC is explored for the first time along with the necessary LHY correction. For Dysprosium atom, droplet solutions have been shown to undergo a dimensional crossover in tune with the angle between the two dipole moments i.e. the magnetic dipole moment and the induced electric dipole moment.

5.1   Introduction

Despite the success of Bose-Einstein condensates in magnetic dipolar atoms, it cannot be ignored that BEC of electric dipolar polar molecules are yet to be achieved although ultra-cold polar molecules have been established as promising systems for exploring quantum chemistry [200] and many-body physics [201]. This has encouraged search for magnetic dipole moment in ultracold polar molecules giving rise to a complex doubly dipolar system [202, 203] for studying trapping, collision and chemical reactions. Recently a long-lived fermionic polar molecule with magnetic dipole moment has been observed to sustain for a long time of 4.6 sec [203]. The exact opposite scenario i.e. inducing electric dipole moment in traditional magnetic dipolar Dysprosium atoms is a newer proposal by [42]. Since atomic setups are traditionally more feasible for realization of dipolar BEC, it can be potentially extrapolated to doubly dipolar atoms as well. The doubly dipolar interaction enriches the anisotropy and parametric control of the system and opens up potentially new research paths.

In this chapter we begin by briefly reviewing how a doubly dipolar Dy atom maybe engineered followed by a thorough analysis of the resulting in doubly dipole-dipole interaction (DDDI). This potential displays rich, yet highly controllable, anisotropy that is
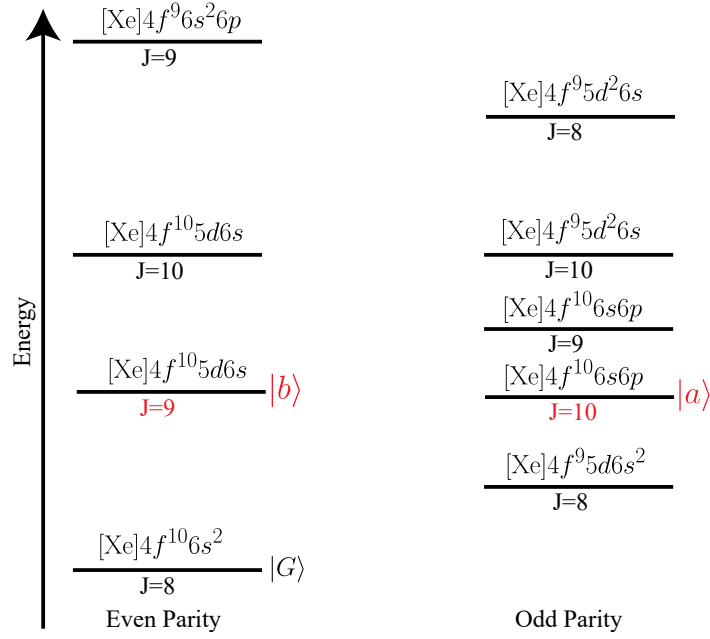
Figure 5.1: Relevant electronic structure of Dy atom. We work with quasi-degenerate $|a\rangle$ and $|b\rangle$ levels. One may reach $|a\rangle$ by spontaneous transition from a high-lying even parity state which can be initially reached via two-photon transition from the ground state $|G\rangle$. It's also possible to Raman transition from $|G\rangle$ to $|b\rangle$ via $4f^{10}6s6p(J = 9)$ or $4f^{9}5d^{2}6s(J = 8)$ states.

drastically different than that of a single DDI. The effect of DDDI on the currently relevant topic of quantum droplets is probed next. After introducing quantum droplets, which are traditionally cigar-shaped in singly dipolar BECs, we discover a transition to pancake-shaped droplets in presence of doubly dipolar BEC. This structural transformation can be carried out by tuning the angle (α) between the magnetic and electric dipole moments which are individually controlled by a magnetic and an electric field respectively. Further we prove that not only a structural transition, but also it is a dimensional crossover. We determine the dimensions of the droplet by showing that a cigar-shaped droplet changes only axially on a linear scale, a feature characteristic to quasi-1D solutions, with respect to the number of atoms in the droplet while a pancake-shaped droplet changes radially with square root dependence which is of quasi-2D nature.

Typically a dimensional crossover of a condensate can be facilitated by changing the confinement geometry [204]. In lower dimensions, the tightly trapped direction remains in the ground state of the confinement and the degrees of freedom decouple from other direction(s). However, in the absence of trap this is a completely different and remarkable scenario. Here, a self-bound solution undergoes dimensional crossover purely enabled by internal interactions alone. We conclude the chapter with a brief note on trapped solutions of DDDI BEC with the extended GPE.
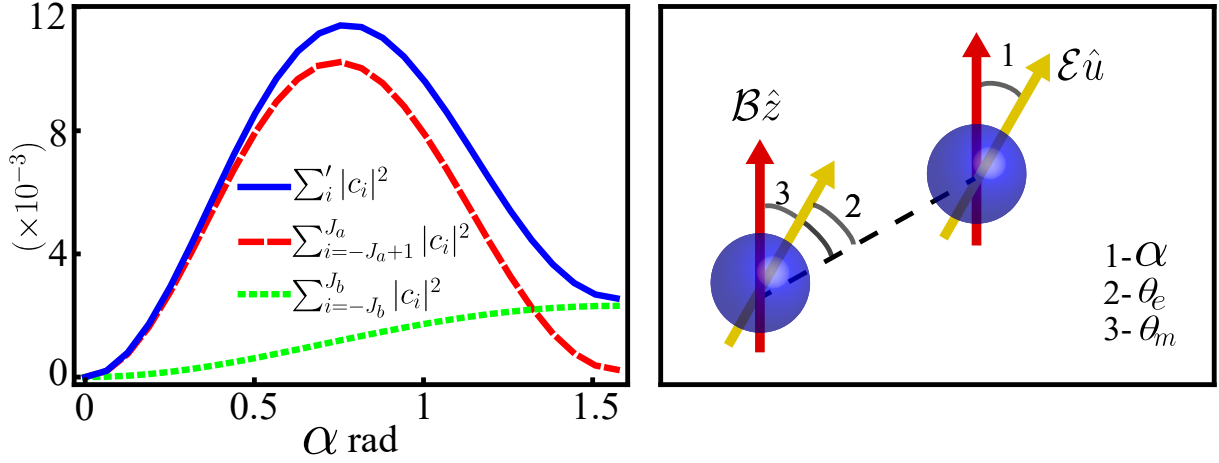
Figure 5.2: The probability of finding state $|S\rangle$ in states other than $|M_a = -10\rangle$ is found to be quite small such that the maximum $\sum_i' |c_i|^2/|c_0|^2 \approx 0.0116$. The plot is for $\mathcal{B} = 100G$ and electric field $\mathcal{E} = 2.68kV/cm$ with respect to the angle, α, between the magnetic and electric dipoles. In the right side we show a schematic displaying the angles involved in calculations.

5.1.1   Doubly-dipolar Dysprosium Atoms

We discuss the preparation of a doubly-dipolar Dy atom [42] and lay down a suitable parameter regime for further studies which is also experimentally viable. Dy atom has a permanent magnetic dipole moment ($\approx 10\mu_B$) [34] which is approximately an order of magnitude higher than alkali atoms. Among other strongly magnetic atoms where BEC has been achieved, Dy continues to have the strongest magnetic dipolar interaction. In [42], it has been calculated that Dy is a candidate for inducing electric dipole moment as well. This is done by considering a pair of opposite parity states $|a\rangle, |b\rangle$ with energies E_a, E_b very close to each other respectively. In presence of magnetic field, the two energy levels E_a and E_b divide into Zeeman sub-levels and on application of external electric field, these sub-levels of opposite parities are allowed to couple which induces an electric dipole moment via the transition dipole moment.

The energy levels considered are $E_a = 17513.33cm^{-1}$ and $E_b = 17514.5cm^{-1}$ for $|a\rangle = $ [Xe]$4f^{10}6s6p$ and $|b\rangle = $ [Xe]$4f^{10}5d6s$ with total angular momentum $J_a = 10$ and $J_b = 9$ respectively shown in Fig. 5.1. This pair of states have a high transition dipole moment of $8.16D$. A uniform magnetic field $\mathcal{B}\hat{z}$ is considered to be the quantization axis and it splits $|a\rangle$ into $2J_a + 1(= 21)$ states $|M_a = -J_a\rangle, ..., |M_a = J_a\rangle$ and $|b\rangle$ into $2J_b + 1(= 19)$ states $|M_b = -J_b\rangle, ..., |M_b = J_b\rangle$. Now an external electric field is applied $\mathcal{E}\hat{u}$ such that $\hat{z}.\hat{u} = \cos\alpha$. This mixes the Zeeman sublevels of $|a\rangle$ and $|b\rangle$ among each other. For $\alpha = 0$, only $|M_a = -9\rangle, ..., |M_a = 9\rangle$ states can get mixed with $|M_b = -9\rangle, ..., |M_b = 9\rangle$ due to selection rule. However, once the quantization axis symmetry is broken by introducing nonzero angle between the external fields, the state $|M_a\rangle = -10$ is weakly coupled to
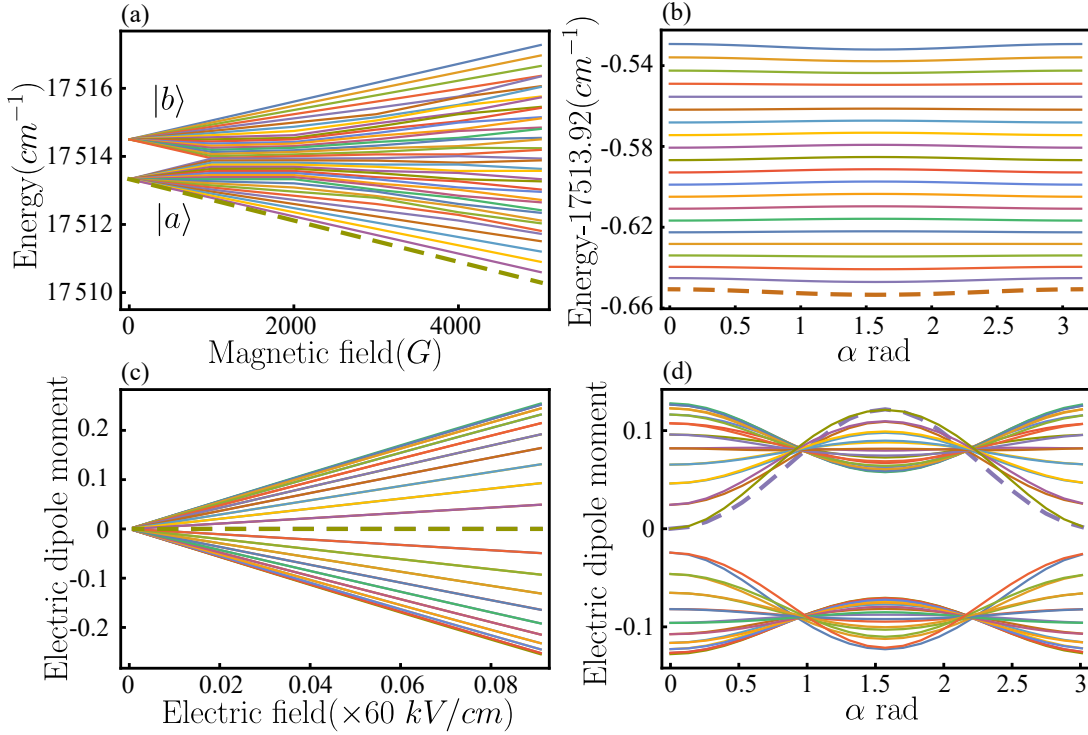
Figure 5.3: (a) Eigenvalues of the atom-field Hamiltonian with respect to magnetic field and zero electric field. At $\mathcal{B} = 0$, we observe two quasi-degenerate energy levels E_a and E_b. In presence of magnetic field their Zeeman sublevels are split. For very high magnetic fields, the energy levels overlap but due to opposite parity any interaction is impossible. (b) The lowest 21 energy levels have been shown with respect to the angle between the magnetic($\mathcal{B} = 100G$) and electric field($\mathcal{E} = 2.68kV/cm$). (c) The electric dipole moment of all sublevels have been plotted with respect to electric field strengths for $\mathcal{B} = 100G$ and $\alpha = 0$. The relevant $|M_a\rangle = -10$ state doesn't have induced electric dipole moment(EDM) in this case. (d) But once α is varied (for the same parameters as (b)), we observe induced EDM gradually increases and reaches a maximum when the external fields are perpendicular to each other for the lowest energy state. The dashed curve represents the lowest energy state $|M_a\rangle = -10$ in all subfigures.

other states such that the lowest eigenstate becomes $|S\rangle = c_0|M_a = -10\rangle + \sum_i' c_i|i\rangle$. This provides us with an ideal scenario of exploring induced electric dipole moment (EDM) in our systems as long as $\sum_i' |c_i|^2/|c_0|^2 \ll 1$ where the sum is over all the remaining 39 sub-levels. The Hamiltonian is,

$$\hat{H} = E_a \sum_{M_a=-J_a}^{J_a} |M_a\rangle\langle M_a| + E_b \sum_{M_b=-J_b}^{J_b} |M_b\rangle\langle M_b| + \mu_B B(g_a M_a + g_b M_b) + \hat{H}_{stark} \quad (5.1)$$

where, $g_a = 1.3$ and $g_b = 1.32$ are the Landé g factors. The last term represents the Stark Hamiltonian which captures the electric field-atom interaction,

$$\langle M_a|\hat{H}_{stark}|M_b\rangle = -\sqrt{\frac{4\pi}{3(2J_a+1)}}\langle a||\hat{d}||b\rangle\mathcal{E} \times Y^*_{1,M_a-M_b}(\alpha,0)C^{J_aM_a}_{J_bM_b,1,M_a-M_b} \qquad (5.2)$$

where, $\langle a||\hat{d}||b\rangle$ is the reduced transition dipole moment with a value $8.16D$, $Y_{l,m}(\theta,\phi)$ are the spherical harmonics and the Cs are Clebsch-Gordan coefficients. The eigenvalues of the Hamiltonian has been plotted in Fig. 5.3(a-b) with respect to magnetic field and the angle α respectively for the experimentally viable [205, 206] fields $\mathcal{B} = 100$ G and $\mathcal{E} = 2.68$ kV/cm. The contributions to the state $|S\rangle$ from the $|M_b\rangle$ predominantly determines the lifetime which is calculated as

$$\tau = \left(\sum_{i=a,b}\Gamma_i\sum_{M_i=-J_i}^{J_i}|c_{M_i}|^2\right)^{-1} \qquad (5.3)$$

as the natural linewidths are $\Gamma_a \approx 0$ and $\Gamma_b = 2.98 \times 10^4 s^{-1}$. The lifetime is shown in the inset of 5.5(a) which is found to be a function of angle α as well.

The magnetic and electric dipole moments of Dy atom in $|S\rangle$ is calculated as,

$$d_m = -\mu_B\left(g_a\sum_{M_a=-J_a}^{J_a}|c_{M_a}|^2M_a + g_b\sum_{M_b=-J_b}^{J_b}|c_{M_b}|^2M_b\right) \qquad (5.4)$$

$$d_e = -\frac{1}{\mathcal{E}}\sum_{M_a,M_b}c^*_{M_a}c_{M_b}\langle M_a|\hat{H}_{stark}|M_b\rangle + c.c. \qquad (5.5)$$

The permanent magnetic dipole moment (MDM) of an atom in $|S\rangle$ is $d_m = d_m\hat{z}$ ($d_m \approx 13\mu_B$), and the induced EDM is $d_e = d_e\hat{u}$. Note that $\hat{d}_m$ is even higher than the current value of $10\mu_B$ for Dy. In Fig. 5.3(c) and (d), we show the dipole moments as a function of electric field and α respectively. The field values are taken same as Fig. 5.3(a) and (b).

5.1.2 Doubly dipole potential

Having understood how to engineer a doubly dipolar Dy atom, we shall probe the resulting DDDI which is rich in its anisotropic profile. For a Dy atoms we assume the MDM ($\hat{d}_m$) is always aligned along $\hat{z}$ and the EDM ($\hat{d}_e$) is along $\hat{u}$ which is a unit vector lying in the $x-z$ plane. In this scenario the DDDI, $V_d(r)$, is always repulsive along $\hat{y}$.

$$V_d(r) = \frac{g_m}{r^3}(1-3\cos^2\theta_m) + \frac{g_e}{r^3}(1-3\cos^2\theta_e) \qquad (5.6)$$

where $g_m = \mu_0 d_m^2/4\pi$ and $g_e = d_e^2/4\pi\epsilon_0$ are the magnetic and electric dipolar interaction strengths respectively. r is the inter-atomic distance and $\theta_m(\theta_e)$ are the angle between the

dipole vector and r. We define $\gamma = g_e/g_m$. Fig. 5.4 show the 2D xz potential [$V_d^{y=0}(r)$] as a function of α and γ. It becomes purely attractive [Figs. 5.4(d),(g),(h)& (l)] when $\alpha > \alpha_a$ but remains anisotropic except when $\alpha = \pi/2$ and $\gamma = 1$ [Fig. 5.4(h)]. The angle α_a separates the regime of the purely attractive xz potential ($\alpha > \alpha_a$) and an anisotropic xz potential exhibiting both repulsive and attractive lobes. The attractive and repulsive lobes in the potential are separated by two intersecting straight lines satisfying $V_d^{y=0}(r,\theta) = 0$, see Fig. 5.4(a)-(c). Writing the equation for these straight lines as $z = m_\pm x$, where the slopes $m_\pm$ can be found from the condition $V_d^{y=0}(r,\theta) = 0$ as,

$$m_\pm = -\frac{3\gamma\sin 2\alpha \pm \sqrt{2(4 - \gamma + 4\gamma^2 + 9\gamma\cos 2\alpha)}}{4 + \gamma + 3\gamma\cos 2\alpha}$$

When the xz potential becomes purely attractive the two lines merges into one, i.e., $m_+ = m_-$, and we obtain

$$\alpha_a = \frac{1}{2}\cos^{-1}\left[\frac{\gamma - 4(1 + \gamma^2)}{9\gamma}\right] \tag{5.7}$$

For the previously discussed fixed magnetic field ($\mathcal{B} = 100G$) and electric field ($\mathcal{E} = 2.68kV/cm$) values we show the magnetic and electric dipole moments and the ratio between the strengths of the interactions ($\gamma = g_e/g_m$) with respect to α in Fig. 5.5(a). The lifetime of such a state decreases with increase in α due to higher level of mixing between previously discussed $|a\rangle$ and $|b\rangle$ states. We identify an effective polarization axis, depicted by grey arrows [Fig. 5.4], along the direction in which the atoms are maximally attractive and is determined by an angle

$$\theta_p(\alpha,\gamma) = \cos^{-1}\left[\frac{1}{\sqrt{2}}\sqrt{1 + \frac{1 + \gamma\cos 2\alpha}{\sqrt{1 + \gamma^2 + 2\gamma\cos 2\alpha}}}\right], \tag{5.8}$$

with the +ve z-axis. It is obtained by minimizing $V_d^{y=0}(r,\theta)$ w.r.t. θ and exhibits a monotonous behaviour as a function of α for $\gamma \geq 1$. For $\gamma < 1$, θ_p obtains a maximum, $\theta_p^{max} = \cos^{-1}\sqrt{\frac{1}{2}[1 + \sqrt{1 - \gamma^2}]}$, at $\alpha = \frac{1}{2}\cos^{-1}(-\gamma)$ before decreasing back to zero at $\alpha = \pi/2$. A linear relation, $\theta_p = \alpha/2$ holds for $\gamma = 1$ [see Fig. 5.5(b)]. When $\alpha = \pi/2$ and $\gamma = 1$, we have isotropic interaction, $V_d^{y=0}(r) = -1/r^3$ and θ_p is not uniquely defined due to the radial symmetry in the xz-plane. As a consequence, θ_p changes abruptly from zero to $\pi/2$ across $\gamma = 1$ for $\alpha = \pi/2$ [Fig. 5.5(b)].

5.2   Homogeneous DDBEC

We consider a gas of N bosons of mass M with both electric and magnetic dipole moment, which are polarized, respectively, by an external electric and magnetic field, which form
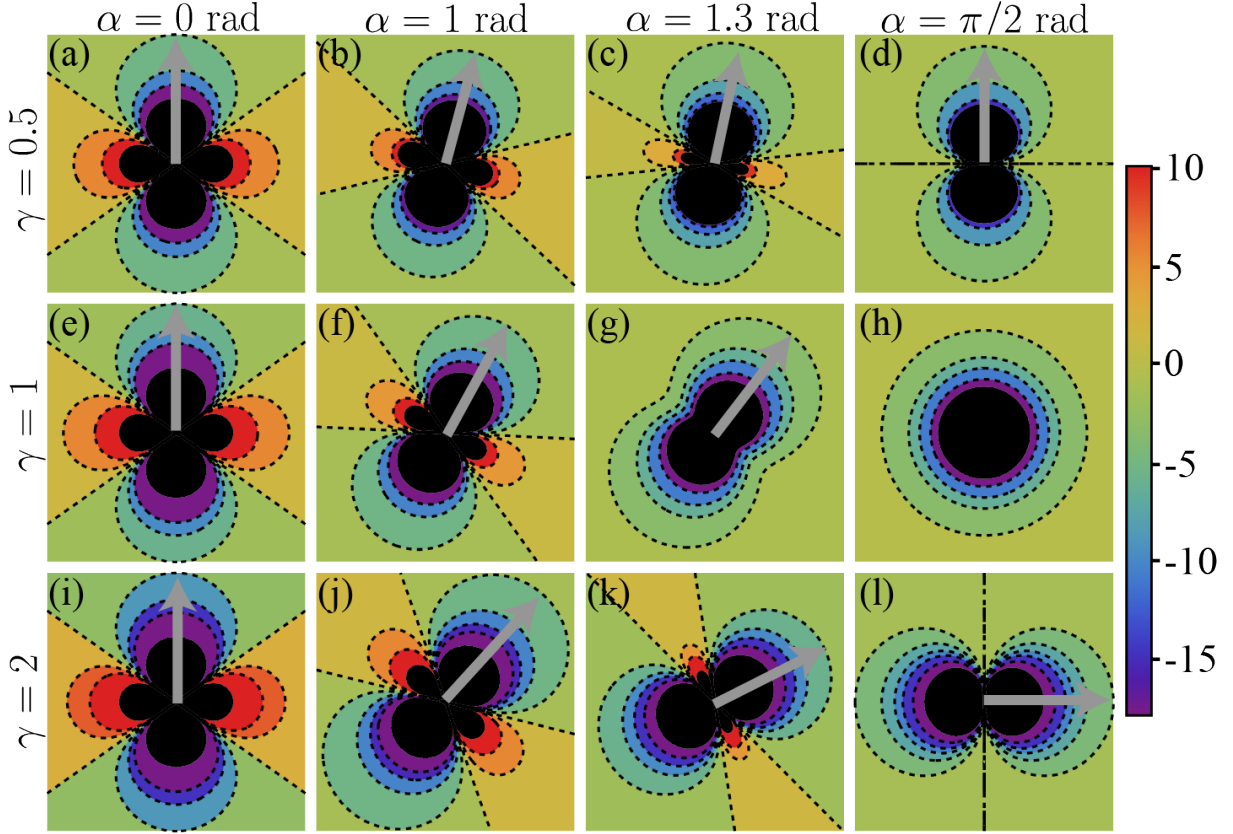
Figure 5.4:   Shown here are the anisotropic interactions $V_d^{y=0}(r)$ for two dipoles in the $x - z$ plane for various $\{\alpha, \gamma\}$ combinations. In (d) and (l) we show the cases when $m_+ = m_-$ and the dashed lines correspond to the vanishing of the repulsive lobe i.e. $\alpha_a = \pi/2$ for $\gamma = 0.5$ and $\gamma = 1$. For $\gamma < 1$, (a)-(d) shows θ_p attaining a maximum before falling back to zero again while for $\gamma > 1$,(i)-(l) shows a nonlinear and monotonous increase in θ_p.

an angle α between them. At very low temperatures, the system is described in mean field, by a nonlocal Gross-Pitaevskii equation (NLGPE): $i\hbar\dot\psi(r,t) = \mathcal{H}\psi(r,t)$, where

$$\mathcal{H} = \frac{-\hbar^2\nabla^2}{2M} + \int d^3r'\psi(r',t)V(r-r')\psi(r',t) \tag{5.9}$$

where $V(r) = g\delta(r) + V_d(r)$ is the interaction potential. The parameter $g = 4\pi\hbar^2 a_s N/M$ determines the contact interaction strength, with a_s being the s-wave scattering length. Here, $g_m = N\mu_0 d_m^2/4\pi$ and $g_e = N d_e^2/4\pi\epsilon_0$ as we are now dealing with N atoms.

The dispersion law of elementary excitations of a uniform DDBEC with density n_0 is

$$\varepsilon_k = \sqrt{\frac{\hbar^2 k^2}{2M}\left(\frac{\hbar^2 k^2}{2M} + 2g_m n_0\left[\beta + \mathcal{F}(\theta_k, \phi_k, \alpha)\right]\right)} \tag{5.10}$$
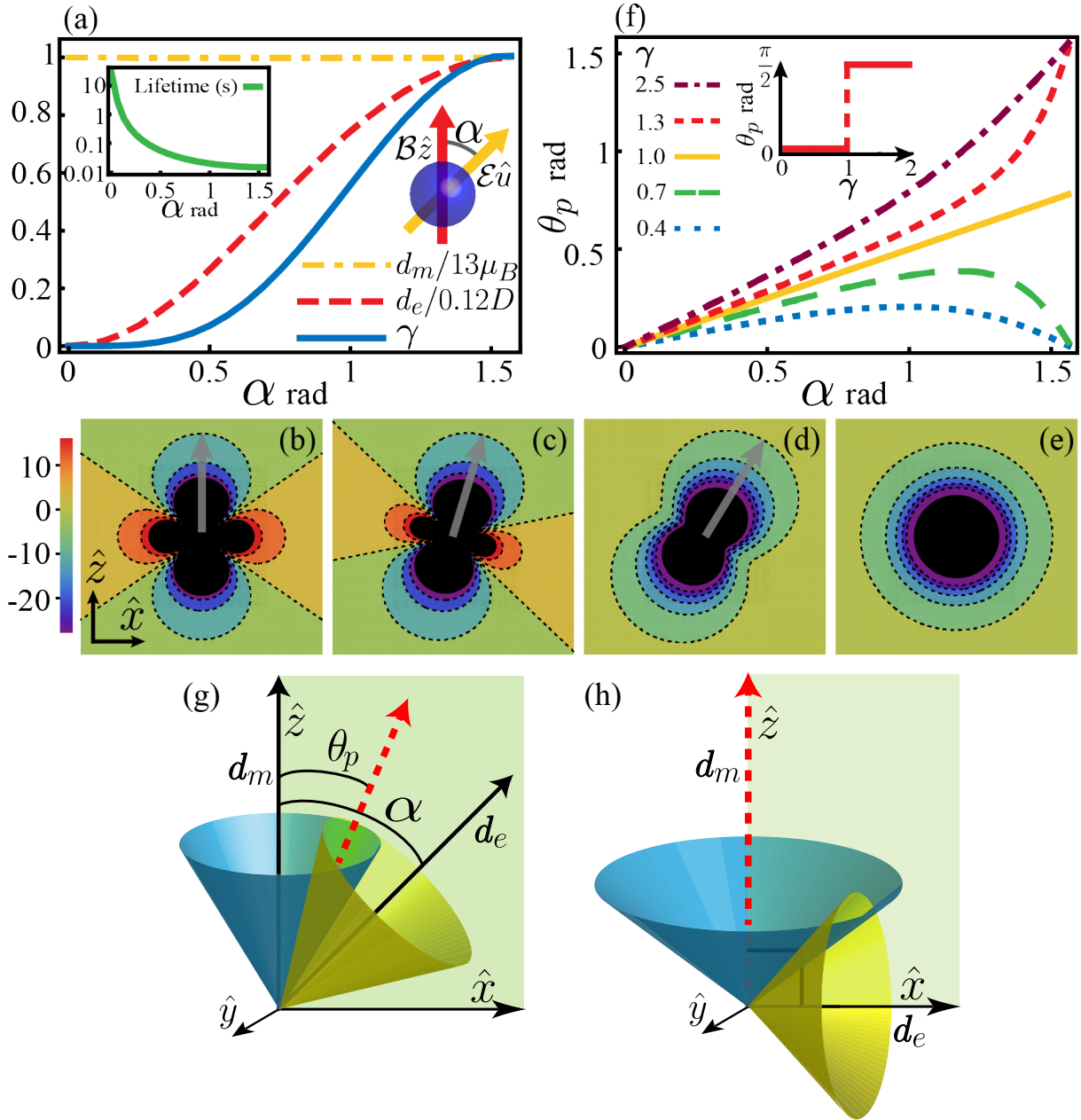
Figure 5.5:   (a) The dipole moments d_m and d_e of a Dy atom in the stretched state $|S\rangle$ as a function of α for $\mathcal{B} = 100$ G and $\mathcal{E} = 2.68$ kV/cm. With these field strengths the maximum values of d_m and d_e attained are $13\mu_B$ and 0.12 Debye respectively. The solid line shows the ratio $\gamma = g_e/g_m$. The inset shows the lifetime (in s) of the state $|S\rangle$. The 2D potential, $V_d^{y=0}(r)$ (in arbitrary units), taking d_m and d_e from (a) for (b) $\alpha = 0$, (c) $\alpha = 1$ rad, $\alpha = 1.3$ rad and $\alpha = \pi/2$ rad. For $\alpha > \alpha_a = 1.239$ rad, $V_d^{y=0}(r)$ is purely attractive, see (d) and (e). The thick arrow shows the effective polarization direction. (f) Polarization angle θ_p vs α for different γ; the inset shows θ_p as a function of γ for $\alpha = \pi/2$. (g) Orientation of the electric and magnetic dipoles and an effective polarization have been shown. The cones display the volume of attractive DDI. Both type of DDIs are equally strong with an angle α between them. (h) Here $\alpha = \pi/2$ and the effective polarization axis lies along the axis (z-axis) of the strongest dipole strength. In case of equally strong polarization, such an axis is undefined.
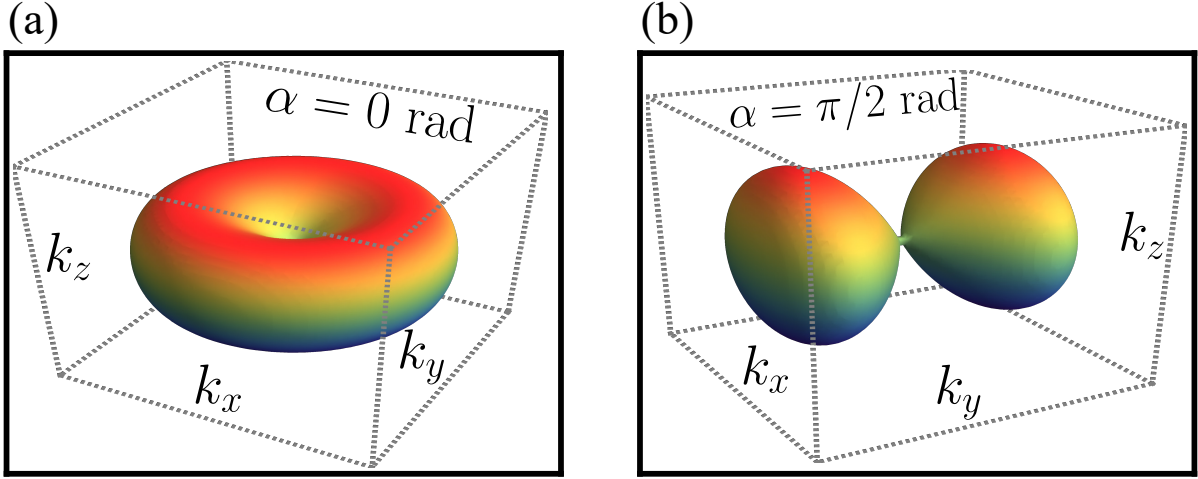
Figure 5.6: (a) and (b) depict regions in momentum space where $\varepsilon_k^2 < 0$ for $\gamma = 1$ and $\beta = 4\pi/3$.

where $\beta = g/g_m$ and

$$
\begin{aligned}
\mathcal{F}(\theta_k, \phi_k, \alpha) &= \frac{4\pi\gamma}{3}\left[3\left(\cos\alpha\cos\theta_k + \sin\alpha\sin\theta_k\cos\phi_k\right)^2 - 1\right] \\
&\quad + \frac{4\pi}{3}(3\cos^2\theta_k - 1).
\end{aligned} \tag{5.11}
$$

with θ_k and ϕ_k the angular coordinates in momentum space. The long-wavelength excitations (phonons) are: $\varepsilon_{k\to0} = c(\theta_k, \phi_k)\hbar k$ with the angle-dependent sound velocity (Fig. 5.7)

$$
c(\theta_k, \phi_k) = \left[g_m n_0\left(\beta + \mathcal{F}(\theta_k, \phi_k, \alpha)\right)/M\right]^{1/2}. \tag{5.12}
$$

The hard phonons propagate along the effective polarization axis whereas the softer ones propagate in a perpendicular direction. The phonons along the y-axis are always softer which sets the stability criteria for the condensate $c^2(\pi/2, \pi/2) = \frac{g_m n_0}{M}\left[\beta - \frac{4\pi}{3}(1+\gamma)\right] > 0$. Thus, a homogeneous DDBEC becomes unstable against local collapses if $\beta < \frac{4\pi}{3}(1+\gamma)$. Though, the instability criteria is independent of α, the unstable modes and the post-instability dynamics depends significantly on it as evident from Fig. 5.6(a)-(b). The dominant contribution of unstable momenta changes drastically from $k_x - k_y$ plane for $\alpha = 0$ to only k_y in $\alpha = \pi/2$ case. This remarkable transition in anisotropic direction dependence manifests in the post-instability dynamics of the condensate as shown later in the paper.

5.2.1 Quantum fluctuations

The above discussion regarding instabilities is insufficient unless one considered the newly discovered effects of beyond mean-field effects. Although there had been a theoretical
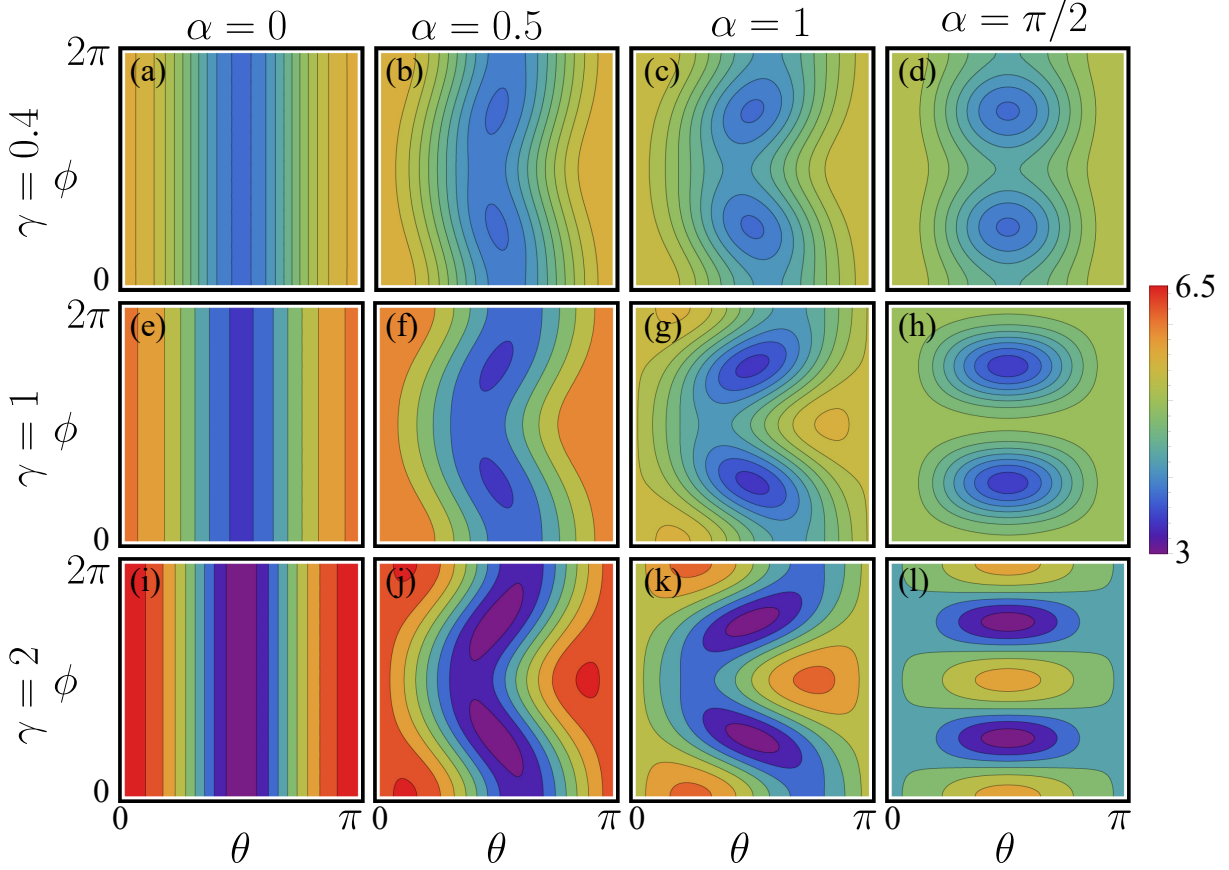
Figure 5.7:   The sound velocity function $c(\theta, \phi)$ plotted for arbitrary value of $\beta = 20$ with respect to θ and ϕ for various (α, γ) combinations. Always the minimum lies along $\theta = \pi/2$ while the function varies along ϕ depending on the configuration. If there exists a minimum along ϕ axis, it is found at $\pi/2$ and $3\pi/2$ symmetrically. So the stability condition $c(\pi/2, \pi/2)^2 > 0$ is a logical conclusion.

framework of beyond mean-field calculations(or, LHY correction) for decades now, there effects in dipolar Bose-Einstein condensates had gone unobserved for a long time. A detailed derivation of such work corresponding to singly dipolar BECs have been carried out by Lima and Pelster [109] which has been discussed previously in section 1.4. In 2016 it was experimentally discovered that a repulsive Lee-Huang-Yang(LHY) correction has been shown to arrest this post-instability collapse of an unstable condensate which then stabilize into an array of quantum droplets in a $3D$ trap [108]. Using the dispersion (5.10), we obtain the beyond mean field LHY correction to the chemical potential ($\Delta\mu$):

$$\Delta\mu = \frac{1}{3\pi^3 N} \left(\frac{M}{\hbar^2}\right)^{3/2} n_0^{3/2} g_m^{5/2} \int d\Omega_k \left[\beta + \mathcal{F}(\theta_k, \phi_k, \alpha)\right]^{\frac{5}{2}} \tag{5.13}$$

where $\int d\Omega_k = \int_0^{2\pi} d\phi_k \int_0^{\pi} d\theta_k \sin\theta_k$. The current expression for correction to the chemical potential is modified to incorporate a doubly dipolar potential and it brings further nuances into the quantum fluctuations. Due to the $n_0^{3/2}$ dependence, the repulsive LHY
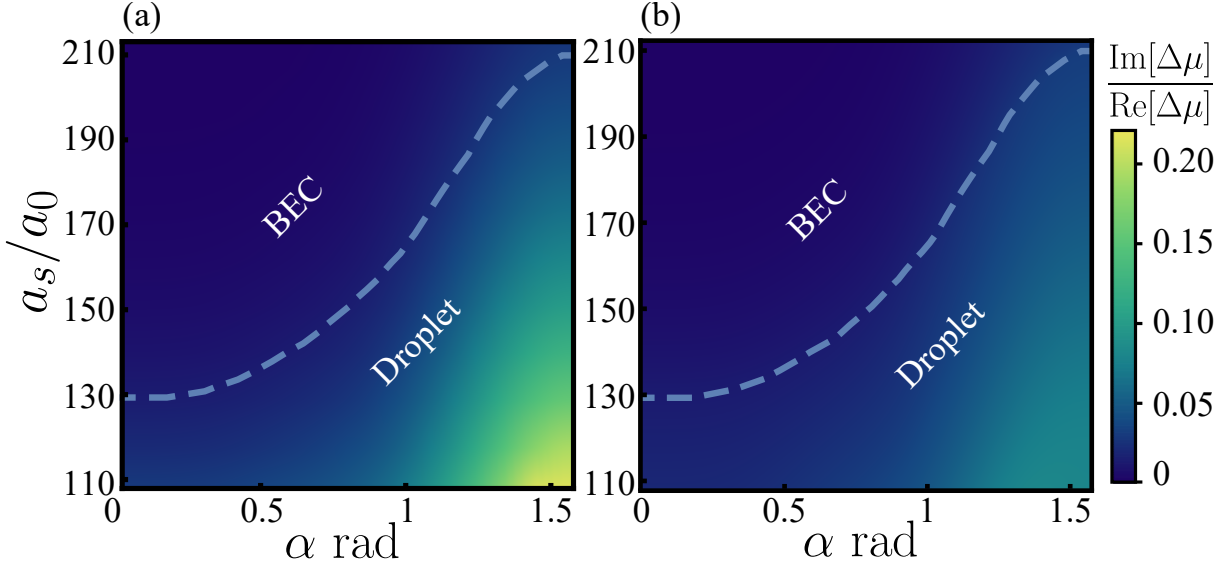
Figure 5.8: (a) The ratio $\mathrm{Im}[\Delta\mu]/\mathrm{Re}[\Delta\mu]$ for a homogeneous condensate in the $a_s - \alpha$ parameter space for a Dysprosium atom BEC. (b) The ratio $\mathrm{Im}[\Delta\mu^c]/\mathrm{Re}[\Delta\mu^c]$ shows a significant reduction in the ignored imaginary component.

correction becomes significant at high densities, and halts the condensate collapse, stabilizing it into a quantum droplet [110, 167, 207, 208]. The LHY correction can be incorporated to the NLGPE using local density approximation $[n_0 \rightarrow n(r,t)]$ [110, 167, 207, 208, 166], leading to the generalized equation:

$$i\hbar\dot{\psi}(r,t) = (\mathcal{H} + \Delta\mu\,[n(r,t)])\,\psi(r,t). \tag{5.14}$$

It is easy to notice that due to the Bogoliubov instabilities, the LHY correction terms will acquire imaginary components. Usually the imaginary part is small enough to be ignored when the we're close to the boundary of instability. We shall be working within this region so that our beyond-mean-field calculations and the local density approximation is valid. Additionally, finite size effects are shown to diminish the effect of this imaginary component while weakly affecting the real part of the quantum fluctuation term[167]. This happens as in reality we do not work with infinitely large systems. By assuming a finite size for the condensate, we need to exclude a small region around the momentum space origin in the integration in Eq. (5.13). The limits change from $[0,\infty]$ to $[k_c,\infty]$, where $k_c(\theta_k, \phi_k)$ is a cut-off momentum. This cut-off region is an ellipsoid in our case with the following expression,

$$k_c(\theta_k, \phi_k) = \left[\frac{(\sin\theta_k\cos\phi_k\cos\theta_p - \cos\theta_k\sin\theta_p)^2}{C_x^2} + \frac{\sin^2\theta_k\sin^2\phi_k}{C_y^2}\right.$$
$$\left. + \frac{(\cos\theta_k\cos\theta_p + \sin\theta_k\cos\phi_k\sin\theta_p)^2}{C_z^2}\right]^{-\frac{1}{2}} \tag{5.15}$$

where, C_x, C_y and C_z are the cut-offs along the axes of the ellipsoid. Replacing this cutoff in the integral of Eq. (5.13), the LHY correction is obtained as,

$$
\begin{aligned}
\Delta\mu^c &= \frac{1}{3\pi^3 N}\left(\frac{M}{\hbar^2}\right)^{3/2} g_m^{5/2} n_0^{3/2} \times \\
&\left[\frac{1}{16\sqrt{2}}\int_0^{2\pi} d\phi_k \int_0^{\pi}\sin\theta_k d\theta_k \left\{2[\beta + \mathcal{F}(\theta_k,\phi_k,\alpha)]k_c(\theta_k,\phi_k)^2\{5k_c(\theta_k,\phi_k)\right.\right. \\
&\left.-2\sqrt{2[\beta + \mathcal{F}(\theta_k,\phi_k,\alpha)] + k_c(\theta_k,\phi_k)^2}\} + 6k_c(\theta_k,\phi_k)^4\{k_c(\theta_k,\phi_k)\right. \\
&\left.-\sqrt{2(\beta + \mathcal{F}(\theta_k,\phi_k,\alpha)) + k_c(\theta_k,\phi_k)^2}\}\right. \\
&\left.\left.+[\beta + \mathcal{F}(\theta_k,\phi_k,\alpha)]^2\{16\sqrt{2[\beta + \mathcal{F}(\theta_k,\phi_k,\alpha)] + k_c(\theta_k,\phi_k)^2} - 15k_c(\theta_k,\phi_k)\}\right\}\right]
\end{aligned}
$$

(5.16)

This complex expression, although gives a lower value of imaginary component, the qualitative results remain unaffected. Hence we proceed with the much simpler and widely accepted expression in Eq. (5.13).

5.2.2   Quantum droplets in DBEC

At this point we introduce the quantum droplets which are a unique ground state solutions of the extended-GPE beyond the mean-field approximation. In 2016, Tilman Pfau's group from Stuttgart [209] discovered that strongly dipolar Dy atoms form metastable crystal structures inside a pancake shaped trap when the scattering length of the BEC is quenched to very small values compared to characteristic dipolar length scales. This spontaneous breaking of translational symmetry to a crystalline phase is a remarkable phenomenon in superfluid where the symmetry of phase invariance is also broken. The individual crystal filaments are droplet solutions which occurs due to a balance between the effective attractive interactions present in the system and the quantum fluctuations represented by the LHY correction [207, 167]. Realization of crystal states in a superfluid leads to the inevitable probe of the elusive supersolid state, a counter-intuitive phenomena where global phase coherence is maintained despite the breaking of translational symmetry. Quantum droplets turn out to be excellent candidates for exploring supersolidity as there has been substantial progress in last couple of years both theoretically [210] and experimentally [211–215].

In absence of a confinement geometry the situation is quite different. The BEC is found to form a single giant droplet when the scattering length is adiabatically lowered below a threshold [216, 107]. These self-bound structures are ideal to study properties such as quantum depletion, collective oscillations and expansion dynamics etc. We are interested in analogous studies for the case of doubly dipolar BEC. Naturally we begin by probing in a self-bound droplet scenario without any confinement.

5.3 Lagrangian and equation of motion

A time-dependent variational Gaussian ansatz is used to predict the key properties of doubly-dipolar droplets:

$$\psi(r,t) = \frac{1}{\pi^{3/4}\sqrt{L_x L_y L_z}} \exp\left[-\frac{x'^2}{2L_x^2} - \frac{y^2}{2L_y^2} - \frac{z'^2}{2L_z^2} + ix'^2\beta_x + iy^2\beta_y + iz'^2\beta_z + ix'z'\beta_{xz}\right]$$

(5.17)

where $x' = x\cos\theta - z\sin\theta$, $z' = x\sin\theta + z\cos\theta$. We take such a generalized ansatz because the condensate is expected to tilt away from z-axis as α is varied. We show how the major axis of the condensate changes with α for $\mathcal{B} = 100G$ and $\mathcal{E} = 2.68kV/cm$ in Fig. 5.9. Inputting the ansatz into the Lagrangian density describing a DDBEC,

$$\mathcal{L} = \frac{i\hbar}{2}\left(\psi\dot{\psi}^* - \dot{\psi}\psi^*\right) + \frac{\hbar^2}{2m}|\nabla\psi|^2 + \frac{g}{2}|\psi|^4 + \frac{1}{2}|\psi|^2\int d^3r' V_d(r-r')|\psi(r')|^2$$
$$+ \frac{2M^{3/2}}{15\pi^3\hbar^3 N}g_m^{5/2}|\psi|^5\int d\Omega_k[\beta + \mathcal{F}(\theta_k,\phi_k,\alpha)]^{5/2} \quad (5.18)$$

We obtain the Lagrangian $L = \int d^3r\mathcal{L}$. After the transformation $L \to L - \frac{d}{dt}\left(\frac{\hbar}{2}\sum_i \beta_i L_i^2\right)$ the equations of motion, $\frac{d}{dt}\left(\frac{\partial L}{\partial \dot{Q}}\right) - \frac{\partial L}{\partial Q} = 0$ with $Q \in \{L_x, L_y, L_z, \theta\}$ are

$$M\ddot{L}_x = \frac{\hbar^2}{ML_x^3} + \frac{ML_x\dot{\theta}^2}{(L_x^2+L_z^2)^2}(L_x^4 + 2L_x^2 L_z^2 - 3L_z^4) + \frac{g}{(2\pi)^{3/2}L_x^2 L_y L_z}$$
$$- g_m\frac{\partial}{\partial L_x}\int\frac{d^3k}{(2\pi)^3}\mathcal{F}(\theta_k,\phi_k,\alpha)n^2(k)$$
$$+ \left(\frac{2}{5}\right)^{5/2}\frac{(M/\hbar)^{3/2}}{N\pi^{21/4}}\frac{g_m^{5/2}\int d\Omega_k[\beta + \mathcal{F}(\theta_k,\phi_k,\alpha)]^{5/2}}{L_x(L_x L_y L_z)^{3/2}} \quad (5.19)$$

$$M\ddot{L}_y = \frac{\hbar^2}{ML_y^3} + \frac{g}{(2\pi)^{3/2}L_x L_y^2 L_z} - g_m\frac{\partial}{\partial L_y}\int\frac{d^3k}{(2\pi)^3}\mathcal{F}(\theta_k,\phi_k,\alpha)n^2(k)$$
$$+ \left(\frac{2g_m}{5}\right)^{5/2}\frac{(M/\hbar)^{3/2}}{N\pi^{21/4}}\frac{\int d\Omega_k[\beta + \mathcal{F}(\theta_k,\phi_k,\alpha)]^{5/2}}{L_y(L_x L_y L_z)^{3/2}} \quad (5.20)$$
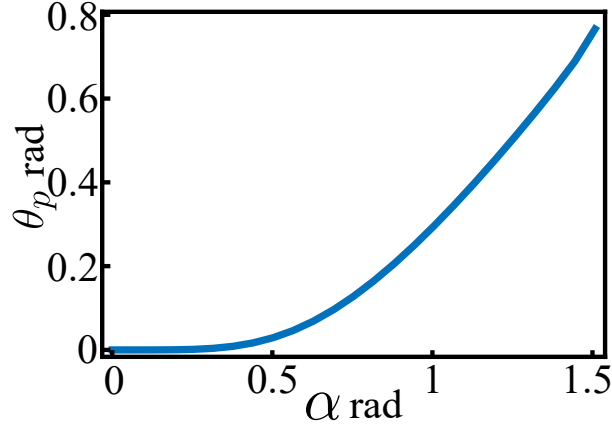
Figure 5.9: The effective polarization angle θ_p vs α for $\mathcal{B} = 100G$ and $\mathcal{E} = 2.68kV/cm$. For $\alpha = 0$, θ_p is also 0. For maximum $\alpha = \pi/2$, θ_p increases nonlinearly and reaches a maximum value $\pi/4$.

$$
\begin{aligned}
M\ddot{L}_z &= \frac{\hbar^2}{ML_z^3} + \frac{ML_z\dot{\theta}^2}{(L_x^2 + L_z^2)^2}(L_z^4 + 2L_x^2L_z^2 - 3L_x^4) + \frac{g}{(2\pi)^{3/2}L_xL_yL_z^2} \\
&\quad - g_m\frac{\partial}{\partial L_z}\int\frac{d^3k}{(2\pi)^3}\mathcal{F}(\theta_k, \phi_k, \alpha)n^2(k) \\
&\quad + \left(\frac{2}{5}\right)^{5/2}\frac{(M/\hbar)^{3/2}}{N\pi^{21/4}}\frac{g_m^{5/2}\int d\Omega_k[\beta + \mathcal{F}(\theta_k, \phi_k, \alpha)]^{5/2}}{L_z(L_xL_yL_z)^{3/2}}
\end{aligned}
\tag{5.21}
$$

$$
\begin{aligned}
\frac{(L_x^2 - L_z^2)^2}{L_x^2 + L_z^2}M\ddot{\theta} &= -\frac{\partial}{\partial\theta}\left(g_m\int\frac{d^3k}{(2\pi)^3}\mathcal{F}(\theta_k, \phi_k, \alpha)n^2(k)\right) \\
&\quad - 2M\dot{\theta}\frac{(L_x^2 - L_z^2)}{(L_x^2 + L_z^2)^2}[L_x\dot{L}_x(3L_z^2 + L_x^2) - L_z\dot{L}_z(3L_x^2 + L_z^2)]
\end{aligned}
\tag{5.22}
$$

At the equilibrium the first derivatives vanishes. Thus, for the vicinity of the equilibrium point we can approximately write the equations of motion as $d^2Q'/dt^2 = -\partial V_{eff}/\partial Q'$ with $Q' \in \{x', y, z', \theta'\}$ and $\theta' = \left([(L_x^0)^2 - (L_z^0)^2]/\sqrt{(L_x^0)^2 + (L_z^0)^2}\right)\theta$, where,

$$
\begin{aligned}
V_{eff} &= \frac{\hbar^2}{2M}\sum_i\frac{1}{L_i^2} + \frac{g}{(2\pi)^{3/2}L_xL_yL_z} + g_m\int\frac{d^3k}{(2\pi)^3}\mathcal{F}(\theta_k, \phi_k, \alpha)n^2(k) \\
&\quad + 2\left(\frac{2}{5}\right)^{5/2}\frac{(M/\hbar)^{3/2}}{3N\pi^{21/4}}\frac{g_m^{5/2}\int d\Omega_k[\beta + \mathcal{F}(k, \alpha)]^{5/2}}{(L_xL_yL_z)^{3/2}}
\end{aligned}
\tag{5.23}
$$

The effective potential can be minimized to evaluate the equilibrium widths (L_i^0) and the orientation (θ^0) where $\theta^0 = \theta_p$ as predicted. Fig. 5.9 shows the minimized θ_p vs α value for $\mathcal{B} = 100$ G and $\mathcal{E} = 2.68$ kV/cm. In absence of LHY correction the L_i^0 in unstable region tends to zero post-minimization as minimum energy tends to negative
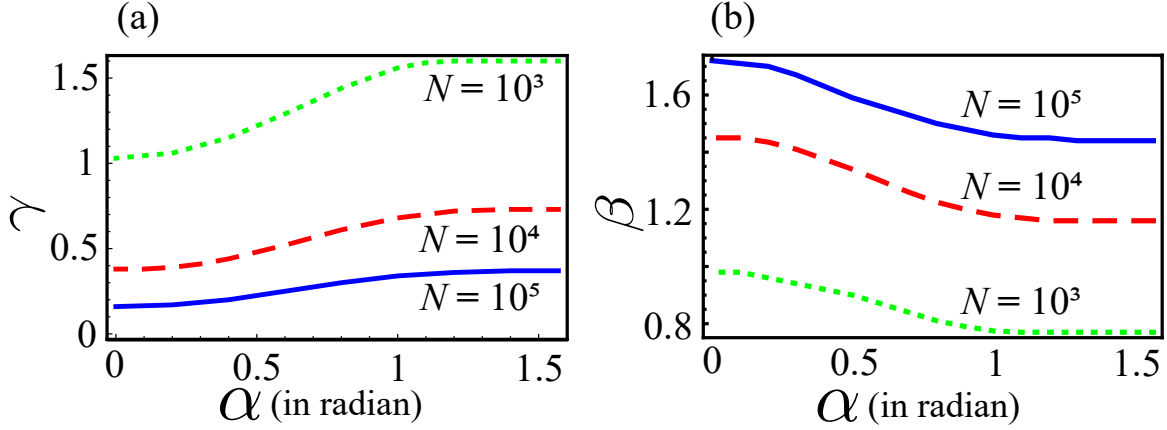
Figure 5.10: For different atom numbers $N = 10^3, 10^4$ and 10^5 , we show phase boundaries for negative energy regime in which stable self-bound droplets are possible. (a) Keeping $\beta = 1$ we find γ for which $E/E_0 = 0$ and (b) keeping $\gamma = 1$ we find the same boundary by varying β for $0 < \alpha < \pi/2$. For the former(later) case, $E/E_0 < 0$ above(below) the boundary lines.

infinity monotonically. Once a nontrivial density dependent $n^{3/2}$ in the LHY correction is added, we observe that energy now tends to positive infinity as $L_i \to 0$. However, a minima for finite unique values of L_i is only observed under a certain threshold value of $a_s(a_{cr})$ which lies below the standard phonon instability curve at $a_s = a_m(1 + \gamma)$. This represents a stable droplet solution. Above this threshold, in presence of LHY only stable BEC exists equivalent of expansion instability corresponding to a self-bound structure. In Fig. 5.10 and Fig. 5.11(a) this stable/unstable region has been depicted for a self-bound droplet in a Dy DDBEC. In the former we show the boundaries for parameter domains of γ and β vs α while in the later it is plotted as a function of a_s and α, for number of atoms $N = 2000$ and the dipole moments corresponding to Fig. 5.5(a). These are results from a variational calculation with a Gaussian ansatz, obtained by minimizing Eq. (5.23). It is clear to see that a large-enough a_s results in a stable BEC as it can dominate the attractive DDDI with the help of a repulsive quantum fluctuation term. But if $a_s < a_{cr}$ then the effective interaction in the system becomes attractive in nature. This attractive part is then balanced by the repulsive LHY term to result in a self bound droplet. As we increase α, we also introduce gradually a stronger electric dipole moment thereby raising the a_{cr} as α varies. It is also reflected in the Fig. 5.5(b)-(e) where the total attractive region due to the DDDI is shown to increase with α. a_{cr} is also a function of number of atoms. A larger number of atoms leads to a larger a_{cr} as the total attractive part of DDDI becomes stronger for large number of atoms. We show the curves of a_{cr} keeping $\gamma = 1$ or $\beta = 1$ with respect to α for different number of atoms.
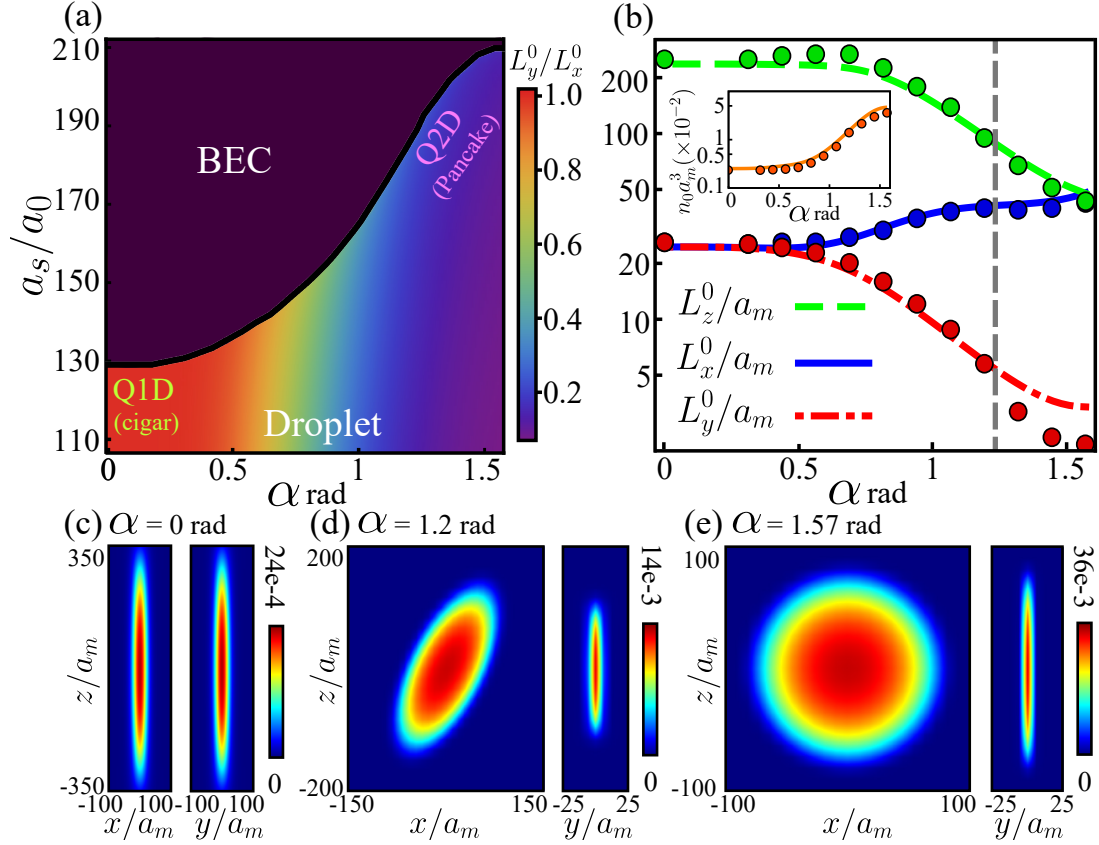
Figure 5.11: (a) Stable/unstable region for a self-bound (Gaussian) droplet of Dy atoms in the state $|S\rangle$, for $\mathcal{B} = 100$ G, $\mathcal{E} = 2.68$ kV/cm and $N = 2000$, as function of the scattering length a and α. The stable regime is partitioned using L_y^0/L_x^0. (b) Equilibrium widths as a function of α for $a = 110a_0$ where a_0 is the Bohr radius and other parameters as in (a). The inset shows the peak density of the droplet as a function of α. The solid lines are from the Gaussian calculations, and filled circles are from the full 3D numerical simulations of Eq. (5.14). The angle α_a is shown by a dashed vertical line. The widths are scaled by the length $a_m = \mu_0 m d_m^2/12\pi\hbar^2 \simeq 222a_0$. (c)-(e) show the density plots for the droplet ground state from the 3D numerics for different α, indicating a structural crossover from cigar to pancake-shaped droplet.

5.3.1   Dimensional crossover

Below we shall consider only cases where the magnetic field and electric field are fixed at $\mathcal{B} = 100G$ and $\mathcal{E} = 2.68kV/cm$ respectively. This effectively fixes the γ for each tilting angle α as shown in 5.5(a). The most important concepts of self-bound droplets discussed below are captured by the tunable parameter α. The traditional case is when $\alpha = 0$ and $\gamma = 0$. In presence of only magnetic field, the droplets are cigar shaped along the $\hat{z}$ axis such that $L + x^0 = L_y^0 << L_z^0$. The widths are shown in 5.11(b) and the density profile is is plotted in 5.11(c). The θ_p lies along $\hat{z}$ coinciding with α. Once α is non-zero, the effective polarization is no longer aligned with α accompanied by the breaking of radial symmetry of the droplets. The L_y^0 and L_z^0, both decrease by almost an order of magnitude each monotonically while L_x^0 slowly increases until $L_x^0 = L_z^0$ at $\alpha = \pi/2$ as shown in Fig.

5.11(b) and (e). An intermediate density profile is shown in Fig. 5.11(d). The droplet doesn't have any structural symmetry in the intermediate region and it is tilted along the effective polarization direction θ_p. The Fig. 5.11(c)-(e) demonstrate the structural crossover from a cigar-shaped droplet to pancake-shaped droplet clearly and this change is accompanied by a change in the peak density of the droplet shown in the inset of Fig. 5.11(b). Although the droplet density profiles are not Gaussian, an approximation with Gaussian variational calculation gives suitable predictions and maybe used for qualitative understanding. The structural transition is summed up for all parameters in the phase diagram Fig. 5.11(a) where we plot the ratio L_y^0/L_x^0 which can attain a maximum value 1 at $\alpha = 0$ while it tends to a small value (≈ 0.1) for a perfectly pancake-shaped droplet at $\alpha = \pi/2$. The color density shows this structural crossover. The solid black curve separates the droplet region from the BEC region of expanding gas. This also corresponds to $\langle H \rangle = 0$ curve which means the self-bound droplets start to appear when the chemical potential corrected for quantum fluctuation goes negative.

Below we study this structural transition more rigorously. Although finding collective excitations remains a standard procedure, it is an extremely valuable tool to check for the stability and other properties of a solution.

5.4 Collective Excitations

The collective excitation frequencies can be obtained from the Lagrangian equations of motion that we have already calculated in (5.19)-(5.22). This is done by linearizing the equations around the equilibrium values of the variational parameters. This allows us to impose $L_i(\theta) = L_i^0(\theta_p) + \delta_i(\delta\theta)$ where $i \in x, y, z$ where derivatives of equilibrium values vanish and so does product terms such as $\dot{\theta}\dot{L}_i$. In the end we may express the resulting four equations in form a matrix and solve for its eigenvalues and eigenvectors. The eigenvalues give us the four lowest lying frequencies and the eigenvectors represent the nature of oscillations. Out of the four modes we obtain, one corresponds to the scissors mode oscillation and is effectively decoupled from the rest three eigenvectors corresponding to width oscillations. The scissor mode oscillations are angular oscillations around the polarization axis along θ_p. A detailed analysis regarding scissor mode is experimentally done by the Stuttgart group [217] and we discuss this more in the following subsection. First we shall focus on the rest three eigenmodes which are plotted in Fig. 5.12(a). The chemical potential (μ) is plotted for reference as well. This will become an important factor when we study the dimensions of a droplet solution. It is important to realise that cigar-shaped(pancake-shaped) solutions need not be quasi-$1D$(quasi-$2D$) in general.

For a cigar-shaped droplet we observe that the lowest eigenvalue corresponds to the axial mode along the elongated direction for $\alpha \approx 0$ region. There are two quasi-degenrate transverse modes ω_1(breathing mode) and ω_2 (quadrupole mode) where ω_1 being slightly
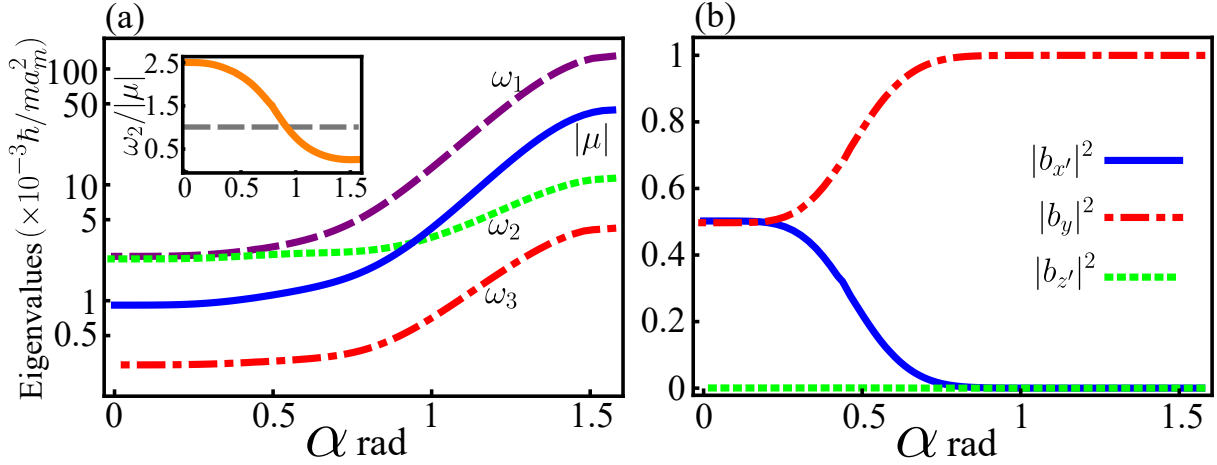
Figure 5.12: (a) Excitation frequencies of the Dy droplet obtained from the Gaussian variational calculations as a function of α for the same parameters as in Fig. 5.11(b). The inset shows $\omega_2/|\mu|$ as a function of α. (b) The eigenvector $\sum_{j=x',y,z'} b_j \vec{e}_j$ corresponding to ω_1 as a function of α. It changes from being a breathing mode on the xy-plane for $\alpha = 0$ to a pure y-oscillation as α approaches $\pi/2$.

higher than ω_2. These modes are restricted to $x - y$ plane. The important thing to notice is $\mu < \omega_2$ by a factor of ≈ 2.5. At this point we draw an analogy with a condensate in a cigar-shaped trap where $\mu << \omega_{\mathrm{radial}}$ imposes quasi1D condition. In such a trap the transverse oscillations are close to the transverse trap frequencies ω_{radial}. Similarly we see that our droplet solutions for $\alpha \approx 0$ has $\mu < \omega_2$ (inset of Fig. 5.12(a)) which proves that they are in a quasi-1D regime. In contrast, for $\alpha \approx \pi/2$ we have a pancake-shaped droplet which we prove is quasi-2D. The lowest two frequencies ω_2 and ω_3 correspond to breathing and quadrupole modes respectively in the $x - z$ plane while ω_1 is the transverse mode along y and strongly decoupled from the radial modes. We see that $\mu < \omega_1$ by a factor of 2.8 which proves its two dimensional character. The eigenvector character of the ω_1 for all α has been demonstrated in Fig. 5.12(b). At $\alpha \approx 0$, it has only radial component in the $x - y$ plane and it completely decoupled from the axial component while at $\alpha \approx \pi/2$, the highest eigenvalue acquires a transverse character along y and is completely decoupled from the $x - z$ component as predicted.

It reveals that we observe not only a structural crossover of droplets from a cigar-shape to pancake-shape but also it undergoes a dimensional crossover from quasi-1D to quasi-2D. Another method to obtain the dimensional crossover is by keeping $\alpha = \pi/2$ and varying γ instead. This can be done by changing the electric field strength. When $\gamma \approx 0$ we have an elongated quasi-1D along z. When γ approaches unity, we obtain back the current quasi-2D droplet. Please note that if $\gamma > 1$, the droplet again starts to break the radial symmetry and starts to elongate along x. However a stronger γ may increase experimental difficulty by introducing strong coupling between the Zeeman sublevel and reducing the lifetime of the doubly dipolar Dy atoms.
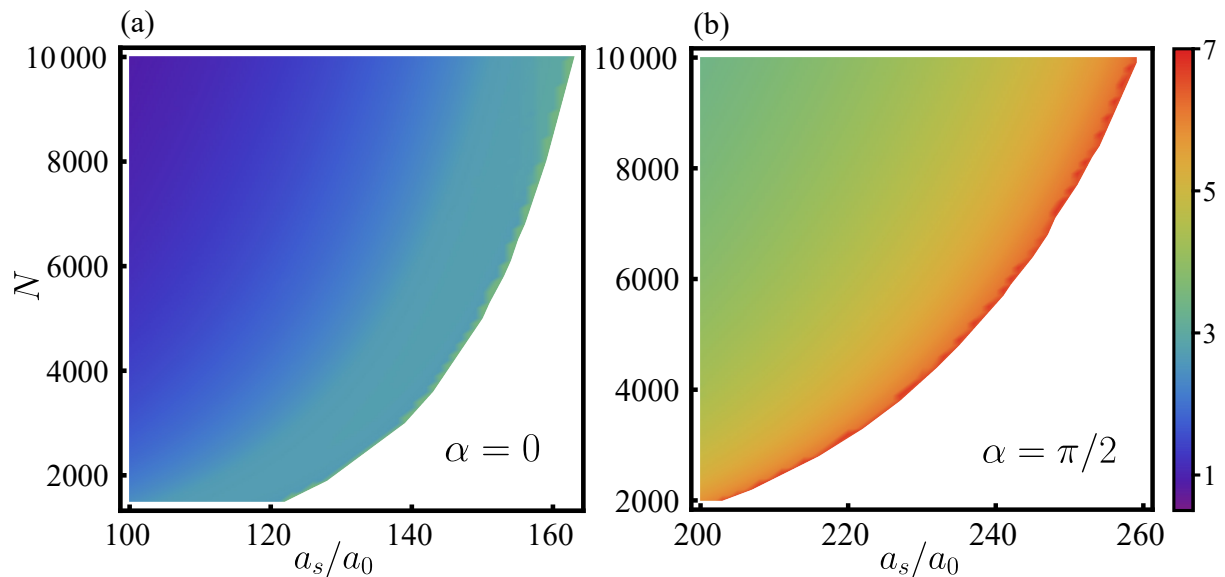
Figure 5.13: (a) We show $|\mu|/\omega_2$ ratio for $\alpha = 0$ rad and (b) ω_1/μ for $\alpha = \pi/2$ in the a_s vs N parameter space. The white region corresponds to expansion instability for a droplet i.e. stable homogenous BEC exists.

5.4.1 Scissors mode

In a traditional trapped BEC, scissors mode corresponds to a shape-preserving oscillation around a principal axis of the trap. We had introduced it in 2.2.2. Its origin lies in interactions and it vanishes in presence of symmetric traps. In doubly-dipolar self-bound droplets scissors mode is a natural occurrence due to the inherently rich anisotropy of the DDDI even though we do not have any trap. We observe scissors mode with respect to the polarization direction in the $x - z$ plane for any $\alpha \in [0, \pi/2)$. This is obvious because at $\alpha = \pi/2$ the droplets obtain symmetry in $x - z$ plane negating the concept of scissors mode.

The scissors mode frequency is obtained from the Gaussian variational calculation and found to be decoupled from the width modes for any value of alpha under linear response theory. The magnitude of the frequency increases with α, however this behaviour is not trivially explained due to the variation of the underlying variable γ.

5.5 N-dependence

In this section, we solidify our claim that the droplet undergoes a dimensional crossover by analyzing the dependence of droplets widths with respect to number of atoms N. Any solution which is quasi-1D(quasi-2D) have their dynamics frozen in the tightly trapped radial (transverse) direction. Addition to number of atoms to the solution results in expansion of the solution along the axial (radial) direction while the tightly trapped width
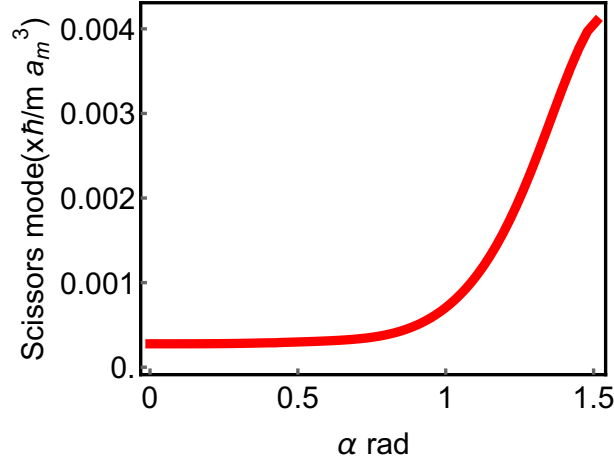
Figure 5.14:   Scissors mode frequency with respect to α for $a_s/a_0 = 110$, obtained from the Gaussian variational calculation. At $\alpha = \pi/2$ it is not defined.

remains independent of N. In analogy, we consider the $Q1D$ and $Q2D$ solutions at $\alpha = 0$ and $\alpha = \pi/2$ respectively. Numerically we show that for $Q1D$ droplets the axial width increases with N while the radial widths ($L_x = L_y \approx \sqrt{2\hbar/m\omega_1}$) remain independent of it. The relation of L_z with N is found to be linear. These results are summarized in Fig. 5.15(a). Similarly, for $\alpha = \pi/2$, the transverse width remains independent of N as shown in Fig. 5.15(b). Unlike the $Q1D$ case, the radial widths depend on $\sqrt{N}$ instead.

We perform analytic calculation to confirm the N dependence of the widths by employing a hybrid Gaussian-TF density profile. Considering the $\alpha = 0$ case first, we assume a Gaussian profile in $x-y$ plane while a TF profile along the z-axis.

$$n(\rho, z, t) = \frac{3}{4\pi L_\rho^2 R_z}\left(1 - \frac{z^2}{R_z^2}\right)\exp\left(-\frac{\rho^2}{L_\rho^2}\right)e^{-i\mu t}, \tag{5.24}$$

where R_z is the TF radius and $L_\rho = L_x = L_y$ are the Gaussian widths. Using this ansatz in Eq. (5.14), we can ignoring the kinetic energy along the z-direction due to TF approximation. Integrating in the $x-y$ plane we arrive at,

$$
\begin{aligned}
\mu &= \frac{\hbar^2}{2ML_\rho^2} + \frac{3g}{8\pi L_\rho^2 R_z}\left(1 - \frac{z^2}{R_z^2}\right) \\
&\quad + \frac{\sqrt{3}g_m^{5/2}}{20N\pi^{9/2}}\left(\frac{m}{R_z L_\rho^2 \hbar^2}\right)^{3/2}\int d\Omega_k[\beta + \mathcal{F}(\theta_k, \phi_k, 0)]^{5/2}\left(1 - \frac{z^2}{R_z^2}\right)^{3/2} \\
&\quad + \left(\frac{\pi g_m}{R_z^3}\right)\int \frac{dk_z}{2\pi}\int \frac{dk_x}{2\pi}\int \frac{dk_y}{2\pi}\left(\frac{3k_z^2}{k_x^2 + k_y^2 + k_z^2} - 1\right) \\
&\quad \times e^{-k_\rho^2 L_\rho^2/2}\frac{4(\sin k_z R_z - k_z R_z \cos k_z R_z)}{k_z^3}e^{izk_z}. \tag{5.25}
\end{aligned}
$$

Next, we expand around $z = 0$ and equate the coefficients of the z^0 and z^2 terms. For z^0
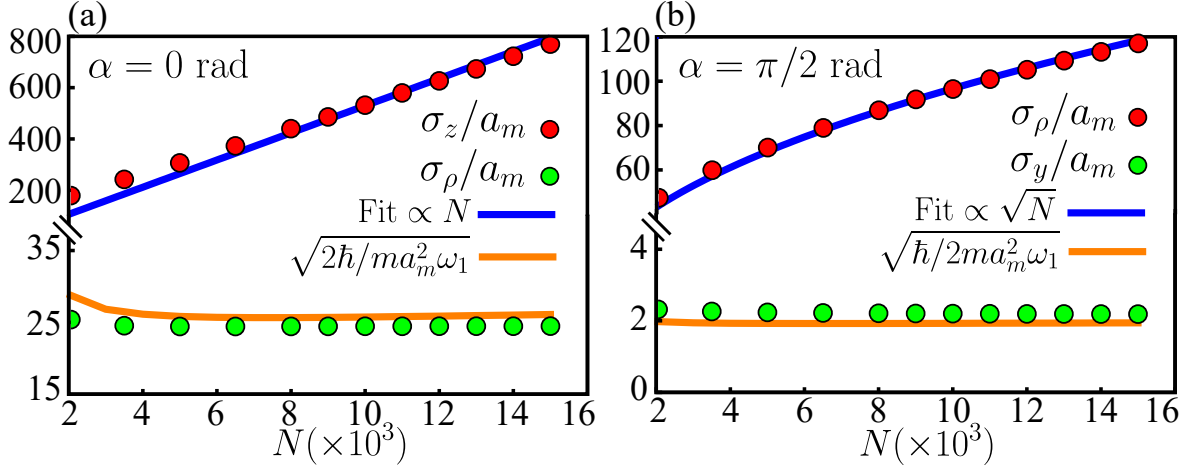
Figure 5.15:   The N-dependence of the droplet widths at $\alpha = 0$ and $\alpha = \pi/2$ is shown in (a) and (b) respectively. We have defined $\sigma_\rho = \sqrt{\int d^3r(x^2 + y^2)|\psi(r)|^2}$, $\sigma_y = \sqrt{\int d^3ry^2|\psi(r)|^2}$ and $L_y = \sqrt{2}\sigma_y$.

we get,

$$
\begin{aligned}
\mu \;=\; & \frac{\hbar^2}{2ML_\rho^2} + \frac{3}{8\pi L_\rho^2 R_z}\left(g - \frac{4\pi g_m}{3}\right) \\
& + \frac{\sqrt{3}g_m^{5/2}}{20N\pi^{9/2}}\left(\frac{M}{R_z L_\rho^2 \hbar^2}\right)^{3/2}\int d\Omega_k[\beta + \mathcal{F}(\theta_k, \phi_k, 0)]^{5/2} \\
& - \frac{6g_m}{4R_z^2 L_\rho}\left(\sqrt{2\pi}e^{R_z^2/2L_\rho^2}\mathrm{erfc}\left[\frac{R_z}{\sqrt{2}L_\rho}\right] - \frac{\pi L_\rho}{R_z}\mathrm{erfi}\left[\frac{R_z}{\sqrt{2}L_\rho}\right] \right. \\
& \left. \qquad\qquad + \frac{R_z}{L_\rho}\;_pF_q\left(\{1,1\};\left\{\frac{3}{2},2\right\};\frac{R_z^2}{2L_\rho^2}\right)\right) \quad (5.26)
\end{aligned}
$$

and for z^2 we have,

$$
\begin{aligned}
\frac{1}{2\pi L_\rho^2 R_z}\left(\beta - \frac{4\pi}{3}\right) + \frac{\sqrt{3N}}{10\pi^3 L_\rho^3}\left(\frac{3a_m}{\pi R_z}\right)^{3/2}\int d\Omega_k[\beta + \mathcal{F}(\theta_k, \phi_k, 0)]^{5/2} \\
+ \left(\frac{2}{R_z L_\rho^2} - \frac{\sqrt{2\pi}}{L_\rho^3}e^{\frac{R_z^2}{2L_\rho^2}}\mathrm{erfc}\left[\frac{R_z}{\sqrt{2}L_\rho}\right]\right) \\
- \frac{1}{\pi R_z^3}\int dx\; e^{\frac{x^2 L_\rho^2}{2R_z^2}}\Gamma\left[0, \frac{x^2 L_\rho^2}{2R_z^2}\right]x^2\cos x = 0 \quad (5.27)
\end{aligned}
$$

where erfi and erfc are the imaginary and complimentary error functions respectively, $_pF_q()$ is the generalized hypergeometric function and $\Gamma[]$ is the incomplete gamma function. Eq. (5.27) is the important equation which gives us the N-dependence. The first

term corresponds to the effective short-range interactions coming from both the *s*-wave scattering and from the DDI, the second term is from the LHY correction. The last two terms come from the non-local character of the DDI. Here we impose the limit $R_z \gg L_\rho$. Under this condition the last two terms may be neglected which simplifies our equation to,

$$R_z \simeq \frac{81a_m^3 N}{25\pi^7 L_\rho^2 (4\pi/3 - \beta)^2} \left[\int d\Omega_k \left[\beta + \mathcal{F}(\theta_k, \phi_k, 0) \right]^{5/2} \right]^2. \tag{5.28}$$

Similarly, for $\alpha = \pi/2$, in the Q2D regime, we use an ansatz where the radial density profile is TF while the transverse profile is assumed to be Gaussian.

$$n(\rho, z, t) = \frac{3}{4\sqrt{\pi}R_\perp^2 L_y} \left(1 - \frac{\rho^2}{R_\perp^2} \right) e^{-y^2/L_y^2} e^{-i\mu t}, \tag{5.29}$$

Following the same procedure as above we get,

$$R_\perp \simeq \frac{9a_m^{3/2}}{2\pi^{13/4}} \sqrt{\frac{N}{5L_y}} \frac{\int d\Omega_k [\beta + \mathcal{F}(\theta_k, \phi_k, \pi/2)]^{5/2}}{(8\pi/3 - \beta)}. \tag{5.30}$$

5.6 Trapped Droplets

We briefly show the trapped doubly dipolar droplets. The situation is different as trap allows for formation of droplet crystals. In singly dipolar case, this has recently proved to be an excellent candidate to study the supersolid phase. We have studied the droplets by keeping $\gamma = 1$ and varying α. Please note that the electric field strength needs to be different for different α to satisfy the condition. For $\alpha = 0$, this is impossible, however the situation can be easily mimicked by magnetic dipole moment alone easily. We begin by finding the ground state using imaginary time evolution in a stable BEC region where $a_s/a_m > (1+\gamma)$. In real time we quench into sufficiently deep unstable region by decreasing a_s, a procedure which is similar to the experimental sequence for a singly dipolar BEC.

Expectedly, we observe gradual formation of droplet crystals. However, the above discussed structural transformation with respect to α is manifested here as well. An interesting consequence of this is that a $2D$ crystal structure of the droplets gets transitioned to a $1D$ crystal structure from $\alpha = 0$ to $\alpha = \pi/2$ respectively. This is well depicted in Fig. 5.16. In (a), z is the tightly trapped axis, allowing small movement of droplets in the $x - y$ plane while in (d), the droplet movements are restricted along y-axis alone. Unlike self-bound droplets, trap-bound droplet structures are surrounded by a dilute gas. The size and number of droplets forming in the post-quench dynamics are additionally trap dependent along with their usual dependence on β and N.
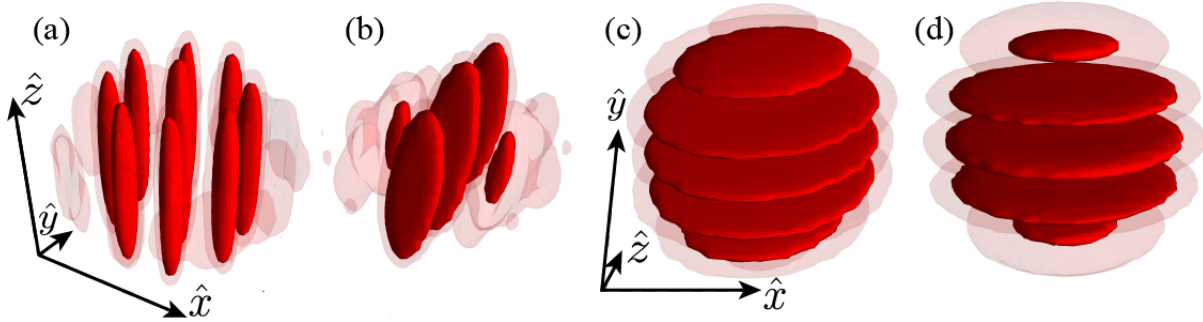
Figure 5.16: Formation of droplets in the post-instability dynamics of a Dy 3D DDBEC. (a)-(d) show the isosurfaces for the density in the post instability dynamics with $\gamma = 1$ and $N = 15000$. The instability is induced by quenching the s-wave scattering from $a_s^i = 262.9a_0$ to a_s^f over a period of $t = 3$ms where $a_s^i > a_s^f$. For (a) and (b) $a_s^f = 137.4a_0$ and the trap frequencies $(\omega_x, \omega_y, \omega_z) = 2\pi \times (44, 44, 133)$ Hz, for (c) and (d) $a_s^f = 161.75a_0$ and $(\omega_x, \omega_y, \omega_z) = 2\pi \times (133, 44, 133)$ Hz. The angle α is (a) 0, (b) 0.6 rad, (c) 1.3 rad and (d) $\pi/2$ rad.

5.7 Conclusions

In this chapter we explore the rich and nontrivial anisotropic properties of the DDBEC which features new kind of self-bound droplet structures. We discover a structural crossover from cigar to pancake shaped droplets with respect to the changing angle between the electric and magnetic dipole moments of the Dy atom BEC. We prove that this transition is in fact a dimensional crossover where the traditionally known $Q1D$ self-bound droplet can transition to a new $Q2D$ droplet structure. The dimensional crossover has been verified with the help of calculation of collective excitations and N-dependence of the widths of the droplets. This is interesting because, dimensional crossover has been usually observed in presence of confining geometries. Here a purely interaction induced dimensional crossover is shown which opens up possibilities of new quantum phenomena both in continuous and discrete ultracold medium. Future outlooks include studying the roton excitations, sound velocity, and vortex lattices etc under such rich anisotropy. The trapped case scenario can be extremely potent field for the study of super-solid properties.

Chapter 6

Summary and Outlook

The wealth of physics born out of dipolar Bose-Einstein condensates is enormous. The experimental and theoretical efforts in this field have, so far, proceeded collaboratively. This has resulted in a thriving research community where theoretical predictions are verified in the lab and models are continuously being updated to explain novel experimental observations. So it is imperative to understand the fundamentals of the system from each and every aspect. A small fraction of it has been uncovered in this thesis. While a large amount of literature exists regarding the long-range and anisotropic nature of the dipolar interaction in dipolar BEC, our focus is on the potential effects of tuning the anisotropy. Our work pertains to understanding the effect of tunable anisotropy, achieved by controlling the polarisation direction of the dipole moment of atoms. Effect of anisotropy varies dramatically depending on the trapping geometry. We have probed the effect in various geometries e.g. i) quasi-2D ii) quasi-1D and in iii) 3D with suitable variations. We employ theoretical techniques such as 'imaginary time evolution', 'real time evolution', 'variational methods' to capture the system under the mean-field approximation and in the last chapter, beyond mean-field approximation as well.

Tunability of polarisation direction of dipole moment adds another dimension to the parameter space. The first course of action is to scope out this dimension thoroughly and summarize the results in suitable and experimentally relevant phase diagrams. This is done using the Bogoliubov analysis by formulating the dispersion relation for a uniformly dense condensate. Uniform density approximation allows a first qualitative understanding of a realistic system. A purely real excitation spectrum with respect to momentum indicates a stable system while imaginary components in the spectrum makes the system unstable. We analyse the stability and instability regions using the dispersion spectrum in the new parameter space. The stable region is largely comprised of non-rotonic stable region and rotonic stable region. The distinction between them lies in whether the dispersion curve is monotonic or not respectively. In a quasi-2D non-monotonic roton spectrum the momentum corresponding to the roton minima is considered fixed by the transverse trap. However, we show that it can be varied by changing the dipole polarisa-

tion angle from lower values upto the inverse of characteristic trap length. The unstable regions can be segregated into roton instability, phonon instability or long-wavelength instability. Phonon instability occurs when the low momentum phonon modes acquire imaginary values and roton instability arises when the spectrum goes soft at non-zero finite momentum. These two instabilities have been observed previously in other systems with non-local interactions as well. However, the long-wavelength instability is a new kind of instability which is found in quasi-2D geometry by tilting the dipole orientation to a fixed angle i.e. the magic angle when there is no short-range interaction in the system. The post-instability dynamics have been studied and the visual cues were identified to distinguish between roton instability and phonon instability in the form of dislocation defects. In phonon unstable region in quasi-2D dynamic formation of anisotropic bright solitons is observed. We characterise the anisotropy and stability of a single soliton as well with the help of variational methods. The low-lying excitations are studied as well as an adiabatic experimental procedure was prescribed for the formation of the elusive quasi-2D soliton in the lab.

Response of a system to a continuous external driving is another fundamental study that helps understand the inherent nonlinearity, nonlocality and anisotropy of the system. For this we choose a multilayer quasi-1D dipolar BEC. The polarisation angle allows us to tune the long-range interlayer dipolar interaction from attractive to repulsive. First we study the surface waves on the uniform condensate, known as Faraday patterns, generated by periodically varying either the short-range contact interaction or by varying the dipolar coupling strength. Both symmetric and anti-symmetric spatial patterns are observed depending on the tunable interlayer DDI and external modulation frequency. In a simplistic bilayer case, when both the layers are modulated, it is apparent that Faraday waves appear in both layers. Interestingly in a singly-modulated bilayer system the unmodulated layer can also develop Faraday patterns as the interlayer DDI couples the layers and energy transfer can take place. Different pattern dynamics are found for different modulation frequencies compared to the doubly-modulated case. We have probed the system in both non-rotonic and rotonic regions. Next, under trapped conditions, the collective excitations in a bilayer system show coupling between the center of mass and the width modes, absent in a single layer BEC. We periodically perturb a trapped bilayer system in order to exploit this unique feature. Due to the coupling, an energy transfer takes place from the center of mass mode to the width modes even when only a single layer is being modulated. If the bilayer system is modulated with a chirped frequency instead, the mode-locking phenomenon kicks in and it is shown to propagate between the layers back and forth. Tuning the dipole moments is found to enhance or suppress this excitation transfer.

Keeping pace with current progress we also include beyond-mean-field effects in our final study. Here we introduce a doubly-dipolar BEC for the first time in the community,

following a recent proposal to induce electric dipole moment in the Dysprosium atom which already has a permanent magnetic dipole moment. This opens up a whole new avenue of research. Our goal is to capture of effect of beyond mean-field approximation in a doubly-dipolar BEC. In 3D dipolar BECs, beyond mean-field quantum fluctuations have led to formation of droplet solutions, found both experimentally and theoretically. In absence of confinement, the traditional droplets acquire quasi-1D cigar-like shapes. In doubly dipolar BEC, by tuning the polarisation angle we show a structural transition from cigar to pancake-shaped droplets. In fact we prove that this not simply a structural transition but a dimensional crossover from quasi-1D to quasi-2D. The uniqueness of this dimensional crossover lies in the fact that it is purely mediated by internal interactions, not by any external potential which is usually the case otherwise. We identify the phase boundary between the BEC and droplet phases in doubly-dipolar case with respect to the tunable polarisation angle between the two dipole vectors. The widths of the droplets are then plotted with respect to the number of atoms in the droplet. This dependence characterizes the dimensionality of the droplets.

We have studied the doubly-dipolar interaction in 3D. However the rich anisotropy is bound to give rise to new physics in lower-dimensions as well. A thorough analysis of it can be done in quasi-1D and quasi-2D geometries. The Dysprosium atoms are strongly dipolar, hence it would necessitate the calculations to include beyond mean-field effects. Gaussian variational methods, at this point, can give only very qualitative understanding on the system. It becomes imperative to improve upon the theoretical methodologies of local density approximation and extended-Gross-Pitaevskii equation with the help of involved quantum Monte-Carlo simulations. Another direction of study could include probing the dispersion relation in elongated non-axissymmetric traps. The rotonic momentum is associated with the characteristic trap length scales. Under two different dipole moments, the roton momentum is expected to show peculiar behaviour.

The study of supersolidity has taken over the dipolar BEC community after the discovery of droplets. The quasi-2D droplets, due to their one-dimensional degree of freedom in a cigar-shaped confinement, can prove to be excellent candidates for a supersolid. Further expansion would be the study of vortex lattices as quasi-2D droplets have an extended surface, unlike the traditional quasi-1D droplets.

Appendix A

Efficiency Boosting Techniques

A.1   Fourier transform of DDI

The DDI term has a $1/r^3$ factor which diverges as $r \to 0$. To avoid this DDI is usually dealt with in momentum space. Below the Fourier transform of DDI is briefly outlined. We start by expressing the DDI in terms of spherical harmonics,

$$V_d(\mathbf{r}) = \frac{g_d}{r^3} \left(-4\sqrt{\frac{\pi}{5}} \right) Y_{20}(\theta) \tag{A.1}$$

where Y_{lm} are the spherical harmonics. Before moving on to Fourier transform, the plane wave expansion is introduced first,

$$e^{-i\mathbf{k}\cdot\mathbf{r}} = 4\pi \sum_{l=0}^{\infty} i^l j_l(kr) \sum_{m=-l}^{l} Y_{lm}^*(\theta, \phi) Y_{lm}(\theta_k, \phi_k) \tag{A.2}$$

where, $\mathbf{k}$ is the polar axis in momentum space. Incorporating orthogonality condition of spherical harmonic functions $\int \sin\theta d\theta \int d\phi Y_{lm}^* Y_{l',m'} = \delta_{ll'}\delta mm'$ and the relation $\int dr j_2(kr)/r = 1/3$, the Fourier transform of DDI becomes,

$$V_d(k) = \int d\mathbf{r} V_d(\mathbf{r}) e^{-i\mathbf{k}\cdot\mathbf{r}} = \frac{4\pi g_d}{3}(3\cos^2\theta_k - 1) \tag{A.3}$$

where θ_k represents the angle between $\mathbf{k}$ and the dipole orientation. In contrast to contact interaction, DDI not only has a momentum dependence, but also it shall vary according to the system's dimensionality as will be discussed later. This momentum dependence plays a key role in the origin of rotonic dispersion relation 2.1.2. Assuming the dipole moment is restricted to $x - z$ plane such that it makes an angle α with z, then the general DDI expression in cartesian coordinates is,

$$V_d(\mathbf{k}) = \frac{4\pi g_d}{3} \left(\frac{3k_z^2\cos^2\alpha + 3k_xk_z\sin 2\alpha + 3k_x^2\sin^2\alpha}{k^2} - 1 \right) \tag{A.4}$$

While working with lower dimension ($0 < D < 3$) where the tightly confined region has a Gaussian distribution of the wave function, we may obtain explicit form of a low-dimensional DDI expression,

$$V_d^D(\mathbf{k}) = \int \frac{dk^{3-D}}{(2\pi)^{3-D}} V_d(\mathbf{k}) n_{3-D}(\mathbf{k})^2 \tag{A.5}$$

A.2 Cut-off for DDI

While the divergence in real space is eliminated, this Fourier transformed DDI has a discontinuity at the origin where it reaches its maximum value. This discontinuity is a result of the anisotropic nature of the DDI. Below a technique is proposed to tackle this in numerical simulations to improve accuracy and speed of convergence. The cut-off introduces a finite radius R for the DDI in 3D such that outside this range $V_d(r > R) \approx 0$ in the spherical region. This approximation holds well as long as $R >$ system size. The truncated form becomes,

$$V_d(\mathbf{k})^{\text{cut R}} = \frac{4\pi g_d}{3} \left(1 + 3\frac{\cos Rk}{R^2 k^2} - \frac{\sin kR}{k^3 R^3} \right) (3\cos^2 \theta_k - 1) \tag{A.6}$$

For pancake-shaped traps with axis along z, the truncation region also has to be of similar shape. Although not an exact, but a partially helpful solution for DDI in cylindrical trap is,

$$V_d(\mathbf{k})^{\text{cut z}} = \frac{4\pi g_d}{3}(3\cos^2 \theta_k - 1) + 4\pi e^{-Zk_\rho}[\sin^2 \theta_k \cos Zk_z - \sin \theta_k \cos \theta_k \sin Zk_z] \tag{A.7}$$

The Z value can now be small enough to only cover the condensate.

Appendix B

Bogoliubov Dispersion Relation

B.1   Uniform gas confined along one direction

We begin with an ansatz of the form mentioned in 2.1 where spatial dependence remains only along the trapped direction,

$$
\begin{aligned}
\psi(r,t) &= \sqrt{n_{2D}}[\psi_0(z) + \chi(r,t)]\exp{-i\mu t/\hbar} \\
&= \sqrt{n_{2D}}[\psi_0(z) + u(z)\exp(i(\rho \cdot q_\rho - \epsilon t/\hbar)) + v(z)^*\exp(-i(\rho \cdot q_\rho - \epsilon t/\hbar))]e^{-i\mu t/\hbar}
\end{aligned}
$$

where $\rho = \sqrt{x^2 + y^2}$ and $r = \sqrt{x^2 + y^2 + z^2}$ and replace it in the relevant $3D$ GPE,

$$
i\hbar\frac{\partial}{\partial t}\psi(r,t) = \left\{-\frac{\hbar^2}{2m}\Delta + \frac{m}{2}\omega^2 z^2 + g|\psi(r,t)|^2 + \int dr' V_d(r - r')|\psi(r',t)|^2\right\}\psi(r,t) \quad \text{(B.1)}
$$

While dealing with the rest of the terms are straight forward, the DDI term has been explicitly calculated below,

$$
\begin{aligned}
&\int dr' V_d(r - r')|\psi(r',t)|^2 \\
=\ &\int dr' V_d(r - r')n_{2D}\left[\psi_0^2(z') + \psi_0(z')\left\{u(z') + v(z')\right\}e^{i(q_\rho \cdot \rho' - \omega t)}\right. \\
&\qquad\qquad \left. + \psi_0(z')\left\{u^*(z') + v^*(z')\right\}e^{-i(q_\rho \cdot \rho' - \omega t)}\right] \quad \text{(B.2)}
\end{aligned}
$$

Expanding term by term, the first term is

$$
\begin{aligned}
\int dr' V_d(r - r')\psi_0^2(r') &= \int \frac{d^3k}{(2\pi)^3}V_d(k)n(k)e^{ik\cdot r} \\
&= \int \frac{dk_z}{2\pi}V_d(k_z,0,0)n(k_z)e^{izk_z} \\
&= \frac{4\pi g_d}{3}(3\cos^2\alpha - 1)\psi_0^2(z)
\end{aligned}
$$

Second term,

$$\int dr' \psi_0(z')\{u(z') + v(z')\}V_d(r - r')e^{i(q_\rho \cdot \rho' - \omega t)} \quad = \quad \int \frac{d^3k}{(2\pi)^3}V_d(k)f(k)e^{ik\cdot r}$$

where,

$$
\begin{aligned}
f(k) &= \int d^3r' \exp(-i\vec{k}\cdot\vec{r'})\psi_0(z')\{u(z') + v(z')\}\exp(i(q_\rho.\rho' - \omega t)) \\
&= 4\pi^2\delta(k_x - q_x)\delta(k_y - q_y)\int dz' \; e^{-i(k_z z')}\psi_0(z')\{u(z') + v(z')\}e^{-i\omega t}
\end{aligned}
$$

Replacing $f(k)$ in the above equation and simplifying gives us,

$$
\begin{aligned}
&\int \frac{d^3k}{2\pi}\delta(k_x - q_x)\delta(k_y - q_y)\int dz'\psi_0(z')\{u(z') + v(z')\}e^{-ik_z z'}V_d(k_x, k_y, k_z)e^{i\vec{k}\cdot\vec{r} - i\omega t} \\
=\; &\frac{2g_d}{3}\int dz'\psi_0(z')\{u(z') + v(z')\}e^{i\rho q_\rho - i\omega t}\left[\frac{3\pi}{q_\rho}(q_x^2\sin^2\alpha - q_\rho^2\cos^2\alpha)e^{-q_\rho|z'-z|}\right. \\
&\left. -i3\pi q_x\sin 2\alpha \; sign(z' - z)e^{-q_\rho|z'-z|}\right] + \frac{2g_d}{3}\psi_0(z)\{u(z) + v(z)\}(3\cos^2\alpha - 1)e^{i(\rho k_\rho - \omega t)}
\end{aligned}
$$

Similarly third term can be calculated and the full dipolar term can be written together as:

$$
\begin{aligned}
&\frac{4\pi g_d n_{2D}}{3}(3\cos^2\alpha - 1)\psi_0^2(z) + \frac{2g_d n_{2D}}{3}\psi_0(z)\{u(z) + v(z)\}(3\cos^2\alpha - 1)e^{i(\rho q_\rho - \omega t)} \\
&+\frac{2g_d n_{2D}}{3}\int dz'\psi_0(z')\{u(z') + v(z')\}e^{i\rho q_\rho - i\omega t} \\
&\qquad\times\left[\frac{3\pi}{q_\rho}(q_x^2\sin^2\alpha - q_\rho^2\cos^2\alpha)e^{-q_\rho|z'-z|} - i3\pi q_x\sin(2\alpha) \; sign(z' - z)e^{-q_\rho|z'-z|}\right] \\
&+\frac{2g_d n_{2D}}{3}\psi_0(z)\{u(z)^* + v(z)^*\}(3\cos^2\alpha - 1)e^{-i(\rho q_\rho - \omega t)} \\
&+\frac{2g_d n_{2D}}{3}\int dz'\psi_0(z')\{u^*(z') + v^*(z')\}e^{-i\rho q_\rho + i\omega t} \\
&\qquad\times\left[\frac{3\pi}{q_\rho}(q_x^2\sin^2\alpha - q_\rho^2\cos^2\alpha)e^{-q_\rho|z'-z|} + i3\pi q_x\sin(2\alpha) \; sign(z' - z)e^{-q_\rho|z'-z|}\right]
\end{aligned}
$$

Taking the zeroth order term from both left and right hand sides of the simplified GPE we obtain:

$$
\begin{aligned}
\mu\psi_0(z) &= -\frac{\hbar^2}{2m}\Delta + \frac{1}{2}m\omega^2 z^2 + gn_{2D}|\psi_0(z)|^2\psi_0(z) \\
&\qquad +\frac{4\pi g_d n_{2D}}{3}(3\cos^2\alpha - 1)\psi_0(z)^2\psi_0(z)
\end{aligned}
\tag{B.3}
$$

Collecting coefficients of $e^{-i\omega t}$ and $e^{i\omega t}$ followed by simple algebra gives us dispersion

relations:

$$
\begin{aligned}
\epsilon f_-(z) &= -\frac{\hbar^2}{2m}\left(\frac{\partial^2}{\partial z^2} - q^2\right)f_+(z) - \mu f_+(z) + \frac{1}{2}m\omega^2 z^2 f_+(z) \\
&\quad + 3\left\{gn_{2D} + \frac{4\pi g_d n_{2D}}{3}(3\cos^2\alpha - 1)\right\}|\psi_0(z)|^2 f_+(z) \\
&\quad + 4\pi g_d n_{2D}\psi_0(z)\int_{-\infty}^{\infty} dz'\psi_0(z')e^{-q_\rho|z'-z|} \\
&\quad \times \left\{\frac{q_x^2}{q_\rho}\sin^2\alpha - q_\rho\cos^2\alpha - iq_x\sin(2\alpha)\ sign(z'-z)\right\}f_+(z) \quad \text{(B.4)}
\end{aligned}
$$

$$
\begin{aligned}
\epsilon f_+(z) &= -\frac{\hbar^2}{2m}\left(\frac{\partial^2}{\partial z^2} - q^2\right)f_-(z) - \mu f_-(z) + \frac{1}{2}m\omega^2 z^2 f_-(z) \\
&\quad + \left\{gn_{2D} + \frac{4\pi g_d n_{2D}}{3}(3\cos^2\alpha - 1)\right\}|\psi_0(z)|^2 f_-(z) \quad \text{(B.5)}
\end{aligned}
$$

B.2   Uniform gas confined along two directions

We begin with an ansatz where spatial dependence remains along the radially trapped direction,

$$
\begin{aligned}
\psi_j(r,t) &= \sqrt{n_{1D}}\left[\psi_j(x,y) + u_j(x,y)e^{i(zk_z-\omega t)} + v_j^*(x,y)e^{-i(zk_z-\omega t)}\right]e^{-i\mu_j t/\hbar} \\
&= \sqrt{n_{1D}}\left[\psi_j(\rho) + u_j(\rho)e^{i(zk_z-\omega t)} + v_j^*(\rho)e^{-i(zk_z-\omega t)}\right]e^{-i\mu_j t/\hbar}
\end{aligned}
$$

where $\rho = \sqrt{x^2 + y^2}$, $r = \sqrt{x^2 + y^2 + z^2}$ and the index $j \in [1,N]$ where N is the number of layers. For a single layer $j = 1$. Replacing it in the $3D$ NLGPE,

$$
i\hbar\frac{\partial\psi_j(r,t)}{\partial t} = \left[-\frac{\hbar^2}{2m}\nabla^2 + \frac{1}{2}m\omega^2\rho^2 + g|\psi_j(r,t)|^2 + \int d^3r'V_d(r-r')|\psi_m(r',t)|^2\right]\psi_j(r,t) \quad \text{(B.6)}
$$

We show calculations only for the DDI term below.

$$
\begin{aligned}
&\sum_m\int d^3r'V_d(r-r')|\psi_m(r')|^2\psi_j(r,t) \\
&= \sum_m\int d^3r'V_d(r-r')n_{1D}\left[\psi_m(\rho')^2 + \psi_m(\rho')\{u_m^*(\rho') + v_m^*(\rho')\}e^{-i(z'k_z-\omega t)}\right. \\
&\quad \left. + \psi_m(\rho')\{u_m(\rho') + v_m(\rho')\}e^{i(z'k_z-\omega t)}\right]\psi_j(r,t)
\end{aligned}
$$

$$= \sum_m \int d^3r' V_d(r-r') n_{1D} \psi_m(\rho')^2 \psi_j(r,t)$$

$$+ \sum_m \int d^3r' V_d(r-r') n_{1D} \left[\psi_m(\rho') \{u_m^*(\rho') + v_m^*(\rho')\} e^{-i(z'k_z - \omega t)} \right] \psi_j(r,t)$$

$$+ \sum_m \int d^3r' V_d(r-r') n_{1D} \left[\psi_m(\rho') \{u_m(\rho') + v_m(\rho')\} e^{i(z'k_z - \omega t)} \right] \psi_j(r,t) \quad \text{(B.7)}$$

Let us look at the three terms one by one,

a

$$\sum_m \int d^3r' V_d(r-r') n_{1D} \psi_m(\rho')^2 \psi_j(r,t)$$

$$= \sum_m \int \frac{d^3k}{(2\pi)^3} e^{ik.r} V_d(k) n_{1D} 2\pi \delta(k_z) n_m(k_\rho) \psi_j(r,t)$$

$$= \sum_m \int \frac{d^2k}{(2\pi)^2} e^{ik.\rho} V_d(k_\rho, 0) n_m(k_\rho) n_{1D} \sqrt{n_{1D}}$$

$$\times \left[\psi_j(\rho) + u_j(\rho) e^{i(zk_z - \omega t)} + v_j^*(\rho) e^{-i(zk_z - \omega t)} \right] e^{-i\mu_j t/\hbar} \quad \text{(B.8)}$$

b

$$\sum_m \int d^3r' V_d(r-r') n_{1D} \left[\psi_m(\rho') \{u_m^*(\rho') + v_m^*(\rho')\} e^{-i(z'k_z - \omega t)} \right] \sqrt{n_{1D}}$$

$$\times \left[\psi_j(\rho) + u_j(\rho) e^{i(zk_z - \omega t)} + v_j^*(\rho) e^{-i(zk_z - \omega t)} \right] e^{-i\mu_j t/\hbar}$$

$$= n_{1D} \sqrt{n_{1D}} \sum_m \int d^3r' V_d(r-r') \left[\psi_m(\rho') \{u_m^*(\rho') + v_m^*(\rho')\} e^{-i(z'k_z - \omega t)} \right] \psi_j(\rho)$$

$$= n_{1D} \sqrt{n_{1D}} \sum_m \int d^2\rho' \left[\psi_m(\rho') \{u_m^*(\rho') + v_m^*(\rho')\} \right] \int dz' e^{-i(z'k_z - \omega t)} V_d(\rho - \rho', z - z') \psi_j(\rho)$$

$$= n_{1D} \sqrt{n_{1D}} \sum_m \int d^2\rho' \left[\psi_m(\rho') \{u_m^*(\rho') + v_m^*(\rho')\} \right] \int dz' e^{-i(z'k_z - \omega t)} \int \frac{dq_z}{2\pi} e^{i(z-z')q_z} V_d(\rho - \rho', q_z) \psi_j(\rho)$$

$$= n_{1D} \sqrt{n_{1D}} \sum_m \int d^2\rho' \left[\psi_m(\rho') \{u_m^*(\rho') + v_m^*(\rho')\} \right] \int \frac{dq_z}{2\pi} e^{i(zk_z + \omega t)} V_d(\rho - \rho', q_z) \int dz' e^{iz'(q_z + k_z)} \psi_j(\rho)$$

$$= n_{1D} \sqrt{n_{1D}} \sum_m \int d^2\rho' \left[\psi_m(\rho') \{u_m^*(\rho') + v_m^*(\rho')\} \right] \int \frac{dq_z}{2\pi} e^{i(zk_z + \omega t)} V_d(\rho - \rho', q_z) 2\pi \delta(k_z + q_z) \psi_j(\rho)$$

$$= n_{1D} \sqrt{n_{1D}} \sum_m \int d^2\rho' \left[\psi_m(\rho') \{u_m^*(\rho') + v_m^*(\rho')\} \right] e^{-i(zk_z - \omega t)} V_d(\rho - \rho', -k_z) \psi_j(\rho)$$

Similarly,

c

$$\sum_m \int d^3r' V_d(r - r') n_{1D} \left[\psi_m(\rho') \{u_m(\rho') + v_m(\rho')\} e^{i(z'k_z - \omega t)} \right] \sqrt{n_{1D}}$$

$$\times \left[\psi_j(\rho) + u_j(\rho) e^{i(zk_z - \omega t)} + v_j^*(\rho) e^{-i(zk_z - \omega t)} \right] e^{-i\mu_j t/\hbar}$$

$$= n_{1D}\sqrt{n_{1D}} \sum_m \int d^3r' V_d(r - r') \left[\psi_m(\rho') \{u_m(\rho') + v_m(\rho')\} e^{i(z'k_z - \omega t)} \right] \psi_j(\rho)$$

$$= n_{1D}\sqrt{n_{1D}} \sum_m \int d^2\rho' \left[\psi_m(\rho') \{u_m(\rho') + v_m(\rho')\} \right] e^{i(zk_z - \omega t)} V_d(\rho - \rho', k_z) \psi_j(\rho)$$

$V_d(\rho - \rho', q_z)$:

We shall start with the full 3D dipolar term.

$$V_d(r_1 - r_2) = \frac{g_d}{(r_1 - r_2)^3} (1 - 3(\hat{d} \cdot (\hat{r}_1 - \hat{r}_2))^2)$$

$$= \frac{g_d}{r^3} (1 - 3(\hat{d} \cdot \hat{r})^2)$$

$$= \frac{g_d}{(x^2 + y^2 + z^2)^{\frac{3}{2}}} \left[1 - 3 \frac{\{(\cos\alpha\hat{x} + \sin\alpha\hat{z}) \cdot (x\hat{x} + y\hat{y} + z\hat{z})\}^2}{x^2 + y^2 + z^2} \right]$$

$$= \frac{g_d}{(x^2 + y^2 + z^2)^{\frac{3}{2}}} \left[1 - 3 \frac{\{x\cos\alpha + z\sin\alpha\}^2}{x^2 + y^2 + z^2} \right]$$

$$= \frac{g_d}{(x^2 + y^2 + z^2)^{\frac{3}{2}}} \left[1 - 3 \left(\frac{x^2\cos^2\alpha + xz\sin 2\alpha + z^2\sin^2\alpha}{x^2 + y^2 + z^2} \right) \right]$$

Now we shall take the Fourier transform only along the z direction.

$$V_d(x, y, k_z) = \int dz e^{-izk_z} V_d(r)$$

$$= \int dz e^{-izk_z} \frac{g_d}{(x^2 + y^2 + z^2)^{\frac{3}{2}}} \left[1 - 3 \left(\frac{x^2\cos^2\alpha + xz\sin 2\alpha + z^2\sin^2\alpha}{x^2 + y^2 + z^2} \right) \right]$$

$$= g_d \int dz e^{-izk_z} \left[\frac{1}{(x^2 + y^2 + z^2)^{\frac{3}{2}}} - 3 \left(\frac{x^2\cos^2\alpha + xz\sin 2\alpha + z^2\sin^2\alpha}{(x^2 + y^2 + z^2)^{\frac{5}{2}}} \right) \right]$$

$$= g_d \left[\frac{2|k_z|(3\cos^2\alpha - 2)K_1(\sqrt{x^2 + y^2}|k_z|)}{\sqrt{x^2 + y^2}} + 2ixk_z|k_z|\sin 2\alpha \frac{K_1(\sqrt{x^2 + y^2}|k_z|)}{\sqrt{x^2 + y^2}} \right.$$

$$\left. + \frac{2k_z^2\{(x^2 + y^2)\sin^2\alpha - x^2\cos^2\alpha\}K_2(\sqrt{x^2 + y^2}|k_z|)}{x^2 + y^2} \right] \tag{B.9}$$

B.2.1   Alternately:

b

$$\sum_m \int d^3r' V_d(r-r') n_{1D} \left[\psi_m(\rho') \{ u_m^*(\rho') + v_m^*(\rho') \} e^{-i(z'k_z - \omega t)} \right] \sqrt{n_{1D}}$$

$$\times \left[\psi_j(\rho) + u_j(\rho) e^{i(zk_z - \omega t)} + v_j^*(\rho) e^{-i(zk_z - \omega t)} \right] e^{-i\mu_j t/\hbar}$$

$$= n_{1D}\sqrt{n_{1D}} \sum_m \int d^2\rho' \left[\psi_m(\rho') \{ u_m^*(\rho') + v_m^*(\rho') \} \right] e^{-i(zk_z - \omega t)} \int \frac{d^2q}{(2\pi)^2} e^{iq(\rho - \rho')} V_d(q_\rho, -k_z) \psi_j(\rho)$$

Similarly,

c

$$\sum_m \int d^3r' V_d(r-r') n_{1D} \left[\psi_m(\rho') \{ u_m(\rho') + v_m(\rho') \} e^{i(z'k_z - \omega t)} \right] \sqrt{n_{1D}}$$

$$\times \left[\psi_j(\rho) + u_j(\rho) e^{i(zk_z - \omega t)} + v_j^*(\rho) e^{-i(zk_z - \omega t)} \right] e^{-i\mu_j t/\hbar}$$

$$= n_{1D}\sqrt{n_{1D}} \sum_m \int d^2\rho' \left[\psi_m(\rho') \{ u_m(\rho') + v_m(\rho') \} \right] e^{i(zk_z - \omega t)} \int \frac{d^2q}{(2\pi)^2} e^{iq(\rho - \rho')} V_d(q_\rho, k_z) \psi_j(\rho)$$

Taking the zeroth order term from both left and right hand sides of the simplified GPE we obtain:

$$\mu_j \psi(\rho) = -\frac{\hbar^2}{2m} \nabla_\rho^2 \psi_j(\rho) + \frac{1}{2} m\omega^2 \rho^2 \psi_j(\rho) + gn|\psi_j(\rho)|^2 \psi_j(\rho)$$
$$+ \sum_m \int \frac{d^2k}{(2\pi)^2} e^{ik\cdot\rho} V_d(k_\rho, 0) n_m(k_\rho) n_{1D} \psi_j(\rho) \qquad (B.10)$$

Collecting coefficients of $e^{i\omega t}$,

$$(\mu_j - \hbar\omega) v_j = -\frac{\hbar^2}{2m} (\nabla_x^2 + \nabla_y^2 - k_z^2) v_j + \frac{1}{2} m\omega^2 \rho^2 v_j + 2gn|\psi_j|^2 v_j + gn|\psi_j|^2 u_j$$
$$+ \sum_m \int \frac{d^2k}{(2\pi)^2} e^{-ik\cdot\rho} V_d(k_\rho, 0) n_m^*(k_\rho) n_{1D} v_j(\rho)$$
$$+ n_{1D} \sum_m \int d^2\rho' \left[\psi_m(\rho') \{ u_m(\rho') + v_m(\rho') \} \right] \int \frac{d^2q}{(2\pi)^2} e^{-iq(\rho - \rho')} V_d(q_\rho, -k_z) \psi_j(\rho)$$
$$(B.11)$$

Taking a conjugate over the whole equation to convert v^* to v adds a negative sign to $e^{iq(\rho - \rho')}$ of the last term.

And coefficients of $e^{-i\omega t}$,

$$
\begin{aligned}
(\mu_j + \hbar\omega)u_j &= -\frac{\hbar^2}{2m}(\nabla_x^2 + \nabla_y^2 - k_z^2)u_j + \frac{1}{2}m\omega^2\rho^2 u_j + 2gn|\psi_j|^2 u_j + gn|\psi_j|^2 v_j \\
&\quad + \sum_m \int \frac{d^2k}{(2\pi)^2} e^{ik.\rho} V_d(k_\rho, 0) n_m^*(k_\rho) n_{1D} u_j(\rho) \\
&\quad + n_{1D} \sum_m \int d^2\rho' \left[\psi_m(\rho')\{u_m(\rho') + v_m(\rho')\}\right] \int \frac{d^2q}{(2\pi)^2} e^{iq(\rho-\rho')} V_d(q_\rho, k_z)\psi_j(\rho)
\end{aligned}
$$

(B.12)

Adding and subtracting Eq. (B.11) and (B.12) for one layer($j = 1$) gives:

$$
\begin{aligned}
\hbar\omega f_-(x, y) &= -\frac{\hbar^2}{2m}(\nabla_x^2 + \nabla_y^2 - k_z^2)f_+(x, y) + \left(\frac{1}{2}m\omega^2\rho^2 - \mu_j\right)f_+(x, y) \\
&\quad + 3gn|\psi_j|^2 f_+(x, y) + \sum_m \int \frac{d^2k}{(2\pi)^2} e^{-ik.\rho} V_d(k_\rho, 0) n_m^*(k_\rho) n_{1D} f_+(\rho) \\
&\quad + 2n_{1D} \sum_m \int d^2\rho' \psi_m(\rho') f_+(\rho') \int \frac{d^2q}{(2\pi)^2} e^{iq(\rho-\rho')} V_d(q_\rho, k_z)\psi_j(\rho) \\
\hbar\omega f_+(x, y) &= -\frac{\hbar^2}{2m}(\nabla_x^2 + \nabla_y^2 - k_z^2)f_-(x, y) + \left(\frac{1}{2}m\omega^2\rho^2 - \mu_j\right)f_-(x, y) \\
&\quad + gn|\psi_j|^2 f_-(x, y) + \sum_m \int \frac{d^2k}{(2\pi)^2} e^{-ik.\rho} V_d(k_\rho, 0) n_m^*(k_\rho) n_{1D} f_-(\rho)
\end{aligned}
$$

Dispersion relation for quasi-2D, quasi-1D and purely uniform 3D condensates starting from quasi-2D and quasi-1D and 3D GPE have been discussed inside the chapters 3, 4, and 5 respectively.

Appendix C

Calculation of Modes

The lagrangian density for a trapped 3D gas is,

$$
\mathcal{L} = \frac{i\hbar}{2}\left(\psi\frac{d\psi^*}{dt} - \psi^*\frac{d\psi}{dt}\right) + \frac{\hbar^2}{2m}|\nabla\psi|^2 + \frac{g}{2}|\psi|^4 + \frac{1}{2}|\psi(r)|^2\int d^3r' V_d(r-r')|\psi(r')|^2
$$
$$
+ \frac{2(m/\hbar^2)^{3/2}}{15\pi^3 N}g_m^{5/2}|\psi|^5\int d\Omega_k[\beta + \mathcal{F}(\theta_k,\phi_k,\alpha)]^{5/2}
$$

$$(C.1)$$

We use an ansatz normalized to 1. It is general expression to mix the x and z coordinates using the rotation angle θ,

$$
\psi(x,y,z) = \frac{1}{\pi^{3/4}\sqrt{L_x L_y L_z}}\exp\left[-\frac{x'^2}{2L_x^2} - \frac{z'^2}{2L_z^2} - \frac{y^2}{2L_y^2} + ix'^2\beta_x + iy^2\beta_y + iz'^2\beta_z + ix'z'\beta_{xz}\right]
$$

where,

$$
\begin{bmatrix} \cos\theta_p & 0 & -sin\theta_p \\ 0 & 1 & 0 \\ \sin\theta_p & 0 & \cos\theta_p \end{bmatrix}\begin{bmatrix} x \\ y \\ z \end{bmatrix} = \begin{bmatrix} x' \\ y' \\ z' \end{bmatrix}
$$

$$(C.2)$$

Replacing the ansatz in the Lagrangian and simplifying,

$$
\begin{aligned}
L = {} & \frac{\hbar}{2}(L_x^2\dot\beta_x + L_y^2\dot\beta_y + L_z^2\dot\beta_z) + \frac{\hbar}{2}(L_x^2 - L_z^2)\beta_{xz}\dot\theta_p \\
& + \frac{\hbar^2}{4m}\left(\frac{1}{L_x^2} + \frac{1}{L_y^2} + \frac{1}{L_z^2} + (4\beta_x^2 + \beta_{xz}^2)L_x^2 + 4\beta_y^2 L_y^2 + (4\beta_z^2 + \beta_{xz}^2)L_z^2\right) \\
& + \frac{m}{8}[2\omega_y^2 L_y^2 + (L_x^2 + L_z^2)(\omega_x^2 + \omega_z^2) + (L_x^2 - L_z^2)(\omega_x^2 - \omega_z^2)\cos 2\theta_p] \\
& + \frac{g}{2(2\pi)^{3/2}L_x L_y L_z} + \frac{V_{DDI}}{2} + \left(\frac{2}{5}\right)^{5/2}\frac{(m/\hbar)^{3/2}}{3N\pi^{21/4}}\frac{g_m^{5/2}\int d\Omega_k[\beta + \mathcal{F}(k,\alpha)]^{5/2}}{(L_x L_y L_z)^{3/2}}
\end{aligned}
$$

The Euler-Lagrange equations for variational parameter β becomes,

$$\frac{d}{dt}\left(\frac{\partial L}{\partial \dot{\beta_i}}\right) - \frac{\partial L}{\partial \beta_i} = 0$$

$$\implies \beta_i = \frac{m}{2\hbar}\frac{\dot{L_i}}{L_i} \tag{C.3}$$

And,

$$\beta_{xz} = \frac{m}{\hbar}\left(\frac{L_z^2 - L_x^2}{L_z^2 + L_x^2}\right)\dot{\theta}_p \tag{C.4}$$

We do the transformation $L' = L - \dfrac{d\mathcal{G}}{dt}$ where $\mathcal{G} = \dfrac{\hbar}{2}\sum_i \beta_i L_i^2$. Replacing the expressions for β_i's, the new Lagrangian becomes,

$$
\begin{aligned}
L =\ & \frac{\hbar^2}{4m}\left(\frac{1}{L_x^2} + \frac{1}{L_y^2} + \frac{1}{L_z^2}\right) - \frac{m}{4}(\dot{L_x}^2 + \dot{L_y}^2 + \dot{L_z}^2) + \frac{g}{2(2\pi)^{3/2}L_xL_yL_z} + \frac{V_{DDI}}{2} \\
& + \frac{m}{4}[\omega_y^2 L_y^2 + \omega_x^2(L_x^2\cos^2\theta_p + L_z^2\sin^2\theta_p) + \omega_z^2(L_z^2\cos^2\theta_p + L_x^2\sin^2\theta_p)] + \frac{\gamma_{QF}g_m^{5/2}Q_5}{(L_xL_yL_z)^{3/2}} \\
& - \frac{m}{4}\frac{(L_x^2 - L_z^2)^2}{(L_x^2 + L_z^2)}\dot{\theta}_p^2 \tag{C.5}
\end{aligned}
$$

Next we obtain the Euler-Lagrange Equations of L_i and θ_p,

$$
\begin{aligned}
m\ddot{L}_x =\ & \frac{\hbar^2}{mL_x^3} - mL_x(\omega_x^2\cos^2\theta_p + \omega_z^2\sin^2\theta_p) + \frac{mL_x\dot{\theta}_p^2}{(L_x^2 + L_z^2)^2}(L_x^4 + 2L_x^2L_z^2 - 3L_z^4) \\
& + \frac{g}{(2\pi)^{3/2}L_x^2L_yL_z} - \frac{\partial V_{DDI}}{\partial L_x} + \frac{3\gamma_{QF}g_m^{5/2}Q_5}{L_x(L_xL_yL_z)^{3/2}} \tag{C.6}
\end{aligned}
$$

$$
m\ddot{L}_y = \frac{\hbar^2}{mL_y^3} - mL_y\omega_y^2 + \frac{g}{(2\pi)^{3/2}L_xL_y^2L_z} - \frac{\partial V_{DDI}}{\partial L_y} + \frac{3\gamma_{QF}g_m^{5/2}Q_5}{L_y(L_xL_yL_z)^{3/2}} \tag{C.7}
$$

$$
\begin{aligned}
m\ddot{L}_z =\ & \frac{\hbar^2}{mL_z^3} - mL_z(\omega_z^2\cos^2\theta_p + \omega_x^2\sin^2\theta_p) + \frac{mL_z\dot{\theta}_p^2}{(L_x^2 + L_z^2)^2}(L_z^4 + 2L_x^2L_z^2 - 3L_x^4) \\
& + \frac{g}{(2\pi)^{3/2}L_xL_yL_z^2} - \frac{\partial V_{DDI}}{\partial L_z} + \frac{3\gamma_{QF}g_m^{5/2}Q_5}{L_z(L_xL_yL_z)^{3/2}} \tag{C.8}
\end{aligned}
$$

$$
\begin{aligned}
\frac{(L_x^2 - L_z^2)^2}{L_x^2 + L_z^2}m\ddot{\theta}_p =\ & \frac{m}{2}(\omega_x^2 - \omega_z^2)(L_x^2 - L_z^2)\sin 2\theta_p - \frac{\partial V_{DDI}}{\partial \theta_p} \\
& - 2m\dot{\theta}_p\frac{(L_x^2 - L_z^2)}{(L_x^2 + L_z^2)^2}[L_x\dot{L}_x(3L_z^2 + L_x^2) - L_z\dot{L}_z(3L_x^2 + L_z^2)] \tag{C.9}
\end{aligned}
$$

Appendix D

Energy Functional

The 3D energy functional for a doubly-dipolar BEC has the following expression:

$$
\begin{aligned}
E \;=\; & \int d^3r \frac{\hbar^2}{2m}|\nabla\psi|^2 + \frac{g}{2}\int d^3r|\psi|^4 + \frac{1}{2}\int d^3r|\psi(r)|^2 \int d^3r' V_d(r-r')|\psi(r')|^2 \\
& + \frac{2(m/\hbar^2)^{3/2}}{15\pi^3 N} g_m^{5/2} \int d^3r|\psi|^5 \int d\Omega_k [\beta + \mathcal{F}(\theta_k,\phi_k,\alpha)]^{5/2}
\end{aligned}
\tag{D.1}
$$

Ansatz

We use a general Gaussian expression with tilted major axis in the $x-z$ coordinates by an angle θ_p. This angle mixes the x and z components.

$$
\psi(x,y,z) \;=\; \frac{1}{\pi^{3/4}\sqrt{L_x L_y L_z}} \exp\left[-\frac{(x\cos\theta_p - z\sin\theta_p)^2}{2L_x^2} - \frac{(x\sin\theta_p + z\cos\theta_p)^2}{2L_z^2} - \frac{y^2}{2L_y^2} \right]
\tag{D.2}
$$

We have used the following rotating matrix for the argument in the ansatz.

$$
\begin{bmatrix} \cos\theta_p & 0 & -sin\theta_p \\ 0 & 1 & 0 \\ \sin\theta_p & 0 & \cos\theta_p \end{bmatrix} \begin{bmatrix} x \\ y \\ z \end{bmatrix} = \begin{bmatrix} x' \\ y' \\ z' \end{bmatrix}
\tag{D.3}
$$

Non-dipolar Energies

$$
E_{kin} = \frac{\hbar^2}{4m}\left(\frac{1}{L_x^2} + \frac{1}{L_y^2} + \frac{1}{L_z^2} \right)
\tag{D.4}
$$

$$
E_{trap} \;=\; \frac{m}{8}[2\omega_y^2 L_y^2 + (L_x^2 + L_z^2)(\omega_x^2 + \omega_z^2) + (L_x^2 - L_z^2)(\omega_x^2 - \omega_z^2)\cos 2\theta_p]
\tag{D.5}
$$

$$E_c = \frac{g}{2(2\pi)^{3/2} L_x L_y L_z} \tag{D.6}$$

Dipolar Energy

$$
\begin{aligned}
E_{DDI} &= = \frac{1}{2} \int \frac{d^3 k}{(2\pi)^3} V_d(k) n(k)^2 \\
&= \frac{g_m}{(2\pi)^{3/2}} \int_0^{2\pi} d\theta \left[-\frac{1+\gamma}{3 L_y B(\theta, \theta_p)} + \frac{\cos^2\theta + \gamma \cos(\alpha-\theta)^2}{(B(\theta,\theta_p) - L_y^2)} \right. \\
&\qquad \left. \times \left(\frac{\tan^{-1}\left(\frac{\sqrt{B(\theta,\theta_p) - L_y^2}}{L_y} \right)}{\sqrt{B(\theta,\theta_p) - L_y^2}} - \frac{L_y}{B(\theta,\theta_p)} \right) \right] \\
&= \frac{V_{DDI}}{2}
\end{aligned}
\tag{D.7}
$$

where,

$$B(\theta, \theta_p) = \sin^2\theta (L_z^2 \sin^2\theta_p + L_x^2 \cos^2\theta_p) + \cos^2\theta (L_z^2 \cos^2\theta_p + L_x^2 \sin^2\theta_p) + \sin\theta \cos\theta (L_z^2 - L_x^2) \sin 2\theta_p$$

LHY Energy

$$E_{LHY} = \left(\frac{2}{5} \right)^{5/2} \frac{(m/\hbar)^{3/2}}{3N\pi^{21/4}} \frac{g_m^{5/2} \int d\Omega_k [\beta + \mathcal{F}(k,\alpha)]^{5/2}}{(L_x L_y L_z)^{3/2}} \tag{D.8}$$

Total Energy

$$
\begin{aligned}
E &= \frac{\hbar^2}{4m} \left(\frac{1}{L_x^2} + \frac{1}{L_y^2} + \frac{1}{L_z^2} \right) + \frac{m}{8} [2\omega_y^2 L_y^2 + (L_x^2 + L_z^2)(\omega_x^2 + \omega_z^2) + (L_x^2 - L_z^2)(\omega_x^2 - \omega_z^2)\cos 2\theta_p] \\
&\quad + \frac{g}{2(2\pi)^{3/2} L_x L_y L_z} + \frac{V_{DDI}}{2} + \left(\frac{2}{5} \right)^{5/2} \frac{(m/\hbar)^{3/2}}{3N\pi^{21/4}} \frac{g_m^{5/2} \int d\Omega_k [\beta + \mathcal{F}(k,\alpha)]^{5/2}}{(L_x L_y L_z)^{3/2}}
\end{aligned}
\tag{D.9}
$$

Appendix E

Miscellaneous

E.1 Dimensional Reduction of GPE with Tilted Dipoles

E.1.1 From 3D to Quasi-2D

Below we demonstrate the procedure to reduce a 3D GPE to a quasi-2D GPE where in z direction the condensate is tightly trappedso that the motion is effectively frozen. We employ the factorisation, $\psi(r) = \psi(x, y, t)\phi_0(z)$ where $\phi_0(z) = \frac{1}{\sqrt{l_z}\pi^{1/4}}e^{-z^2/2l_z^2}$ is the Gaussian ground state solution of 1D harmonic trap with frequency ω_z and $l_z = \sqrt{\hbar/m\omega_z}$. We replace it in the 3D GPE,

$$
\begin{aligned}
i\hbar\frac{\partial}{\partial t}(\psi(x, y, t)\phi_0(z)) &= \left[\frac{-\hbar^2}{2m}(\nabla_{x,y}^2 + \nabla_z^2) + \frac{1}{2}m\omega_z^2 z^2 + g|\psi(x, y, t)|^2|\phi_0(z)|^2 \right. \\
&\left. + \int dr' V_d(r - r')|\psi(x', y', t)|^2|\phi_0(z')|^2\right]\psi(x, y, t)\phi_0(z) \quad \text{(E.1)}
\end{aligned}
$$

Now

$$
\left[\frac{\partial^2}{\partial z^2} + \frac{1}{2}m\omega_z^2 z^2\right]\phi_0(z) = \frac{1}{2}\hbar\omega_z\phi_0(z) \quad \text{(E.2)}
$$

Multiplying both sides of the equation by $\phi_0^*(z)$ and taking integral over dz we obtain,

$$
\begin{aligned}
i\hbar\frac{\partial}{\partial t}\psi(x, y, t) &= -\frac{\hbar^2}{2m}\nabla_{xy}^2\psi(x, y, t) + \frac{1}{2}\hbar\omega_z + g|\psi(x, y, t)|^2\int|\phi_0(z)|^4 dz \\
&+ \int dr' V_d(r - r')|\psi(x', y', t)|^2|\phi_0(z')|^2\int|\phi_0(z)|^2 dz
\end{aligned}
$$

We shall only explicitly calculate the dipole-dipole interaction,

$$\int \left[\int dr' V_d(r - r') |\psi(x', y', t)|^2 |\phi_0(z')|^2 \right] |\phi_0(z)|^2 dz$$

$$= \int \left[\int \frac{d^3 k}{(2\pi)^3} V_d(k) n(k_x, k_y) n(k_z) e^{i(xk_x + yk_y + zk_z)} \right] |\phi_0(z)|^2 dz \qquad \text{(E.3)}$$

$$= \int \frac{dk_x dk_y dk_z}{(2\pi)^3} V_d(k) n(k_x, k_y) n^2(k_z) e^{i(xk_x + yk_y)}$$

$$= \frac{1}{(2\pi)^2} \frac{2g_d}{3} \int dk_x dk_y dk_z \left[\frac{3(k_x^2 \sin^2 \alpha + k_x k_z \sin 2\alpha + k_z \cos^2 \alpha)}{k_x^2 + k_y^2 + k_z^2} - 1 \right]$$

$$\times n(k_x, k_y) e^{-\frac{k_z^2 l_z^2}{2}} e^{i(xk_x + yk_y)}$$

Now taking the dk_z integral and converting to cylindrical coordinates,

$$f(k_x, k_y) = \int \left[\frac{3(k_x^2 \sin^2 \alpha + k_x k_z \sin 2\alpha + k_z \cos^2 \alpha)}{k_x^2 + k_y^2 + k_z^2} - 1 \right] e^{-\frac{k_z^2 l_z^2}{2}} dk_z$$

$$= \int \left[\frac{3(k_\rho^2 \cos^2 \theta_k \sin^2 \alpha + k_\rho k_z \cos \theta_k \sin 2\alpha + k_z^2 \cos^2 \alpha)}{k_\rho^2 + k_z^2} - 1 \right] e^{-\frac{k_z^2 l_z^2}{2}} dk_z$$

$$= \sqrt{2\pi}(3\cos^2 \alpha - 1) + 3\pi k e^{\frac{k^2}{2}} \text{Erfc} \left[\frac{k}{\sqrt{2}} \right] (\sin^2 \alpha \cos^2 \theta_k - \cos^2 \alpha)$$

where $k = k_\rho l_z$ and $k_\rho = \sqrt{k_x^2 + k_y^2}$. So the nonlinear GPE is reduced to,

$$i\hbar \frac{\partial \psi(x, y, t)}{\partial t} = \left[\frac{-\hbar^2}{2m} \nabla_{x,y}^2 + \frac{g}{\sqrt{2\pi} l_z} |\psi(x, y, t)|^2 \right.$$

$$\left. + \frac{2g_d}{3l_z} \int \frac{d^2 k}{(2\pi)^2} e^{i(xk_x + yk_y)} f(k_x, k_y) \tilde{n}(k_x, k_y) \right] \psi(x, y, t)$$

$$\text{(E.4)}$$

GPE along z-axis

For a condensate uniform in $x - y$ plane and trapped tightly along z the wave function gets separated as $\Psi(\mathbf{r}) = \sqrt{n} \psi(z) e^{-i\mu t/\hbar}$. Note that we do not assume a Gaussian ansatz

along z-axis, rather we are interested in the true density profile of $\psi(z)$.

$$
\begin{aligned}
i\hbar\frac{\partial}{\partial t}\Psi(\mathbf{r},t) &= \left[-\frac{\hbar^2}{2m}\nabla^2 + V_t(\mathbf{r}) + g|\Psi(\mathbf{r},t)|^2 + \int d\mathbf{r}' V_d(\mathbf{r}-\mathbf{r}')|\Psi(\mathbf{r}',t)|^2\right]\Psi(\mathbf{r},t) \\
\implies \mu\psi(z) &= \left[-\frac{\hbar^2\partial_z^2}{2m} + V_t(z) + gn|\psi(z)|^2 + \int \frac{d^3k}{(2\pi)^3}e^{ik.r}V_d(k)(2\pi)^2 n\delta(k_x)\delta(k_y)n(k_z)\right]\psi(z) \\
\implies \mu\psi(z) &= \left[-\frac{\hbar^2\partial_z^2}{2m} + V_t(z) + gn|\psi(z)|^2 + n\int \frac{dk_z}{2\pi}e^{izk_z}V_d(k_x=0, k_y=0, k_z)n(k_z)\right]\psi(z) \\
\implies \mu\psi(z) &= \left[-\frac{\hbar^2\partial_z^2}{2m} + V_t(z) + gn|\psi(z)|^2 + \frac{4\pi g_d n}{3}(3\cos^2\alpha - 1)\int \frac{dk_z}{2\pi}e^{izk_z}n(k_z)\right]\psi(z) \\
\implies \mu\psi(z) &= \left[-\frac{\hbar^2\partial_z^2}{2m} + V_t(z) + gn|\psi(z)|^2 + \frac{4\pi g_d n}{3}(3\cos^2\alpha - 1)|\psi(z)|^2\right]\psi(z) \\
0 &= \left[-\frac{\hbar^2\partial_z^2}{2m} + V_t(z) + g_{eff}n|\psi(z)|^2 - \mu\right]\psi(z) \quad\text{(E.5)}
\end{aligned}
$$

where, $g_{eff} = g + \dfrac{4\pi g_d}{3}(3\cos^2\alpha - 1)$.

E.1.2 From 3D to Quasi-1D

The procedure to reduce a 3D GPE to a quasi-1D GPE is similar to the calculations in previous section. Here the factorisation, $\psi(r) = \psi(z,t)\phi_0(x,y)$ where $\phi_0(x,y) = \frac{1}{l\sqrt{\pi}}e^{-(x^2+y^2)/2l_\rho^2}$

$$
\begin{aligned}
i\hbar\frac{\partial}{\partial t}(\psi(z,t)\phi_0(x,y)) &= \left[\frac{-\hbar^2}{2m}(\nabla_{x,y}^2 + \nabla_z^2) + \frac{1}{2}m\omega_\rho^2(x^2+y^2) + g|\psi(z,t)|^2|\phi_0(x,y)|^2 \right. \\
&\quad \left. + \frac{2g_d}{3}\int dr' V_d(r-r')|\psi(z,t)|^2|\phi_0(x,y)|^2\right]\psi(z,t)\phi_0(x,y) \quad\text{(E.6)}
\end{aligned}
$$

Multiplying both sides of the equation by $\phi_0^*(x,y)$ and taking integral over $dx\,dy$ we obtain,

$$
\begin{aligned}
i\hbar\frac{\partial}{\partial t}\psi(z,t) &= -\frac{\hbar^2}{2m}\nabla_z^2\psi(z,t) + \hbar\omega_\rho + g|\psi(z,t)|^2\int\int|\phi_0(x,y)|^4 dx\,dy \\
&\quad + \int dr' V_d(r-r')|\psi(z',t)|^2|\phi_0(x',y')|^2\int\int|\phi_0(x,y)|^2 dx\,dy
\end{aligned}
$$

We shall only explicitly calculate the dipole-dipole interaction,

$$\int dr' V_d(r-r')|\psi(z',t)|^2|\phi_0(x',y')|^2 \int\int |\phi_0(x,y)|^2 dx\ dy$$

$$= \int\left[\int \frac{d^3k}{(2\pi)^3} V_d(k)n(k_z)n(k_x,k_y)e^{i(xK_x+yk_y+zk_z)}\right]|\phi_0(x,y)|^2 dz$$

$$= \int \frac{dk_x dk_y dk_z}{(2\pi)^3} V_d(k)n(k_z)n^2(k_x,k_y)e^{i(zk_z)}$$

$$= \frac{1}{2\pi}\frac{g_d}{3\pi}\int dk_x dk_y dk_z \left[\frac{3(k_x^2\sin^2\alpha + k_x k_z\sin 2\alpha + k_z\cos^2\alpha)}{k_x^2+k_y^2+k_z^2}-1\right]$$

$$\times n(k_z)e^{-\frac{k_\rho^2 l_\rho^2}{2}}e^{i(zk_z)}$$

Now taking the dk_z integral and converting to cylindrical coordinates,

$$
\begin{aligned}
f(k_z) &= \int\int \left[\frac{3(k_x^2\sin^2\alpha + k_x k_z\sin 2\alpha + k_z\cos^2\alpha)}{k_x^2+k_y^2+k_z^2}-1\right]e^{-\frac{(k_x^2+k_y^2)l_\rho^2}{2}}dk_x dk_y \\
&= \int\int k_\rho\left[\frac{3(k_\rho^2\cos^2\theta_k\sin^2\alpha + k_\rho k_z\cos\theta_k\sin 2\alpha + k_z^2\cos^2\alpha)}{k_\rho^2+k_z^2}-1\right]e^{-\frac{k_\rho^2 l_\rho^2}{2}}dk_\rho d\theta_k \\
&= \frac{\pi(1+3\cos 2\alpha)}{2}\left(\frac{3}{2}e^{k_z^2/2}k_z^2\Gamma\left[0,\frac{k_z^2}{2}\right]-1\right)
\end{aligned}
\tag{E.7}
$$

where $k_z = k_z l_\rho$.

So the nonlinear GPE is reduced to,

$$
i\hbar\frac{\partial\psi(z,t)}{\partial t} = \left[\frac{-\hbar^2}{2m}\nabla_z^2 + \frac{g}{2\pi l_\rho^2}|\psi(z,t)|^2 + \frac{g_d}{3\pi}\int \frac{dk_z}{2\pi}e^{izk_z}f(k_z)\tilde{n}(k_z)\right]\psi(z,t)
\tag{E.8}
$$

E.2   Scaling the Quasi-2D GPE w.r.t. Chemical Potential

The 2D chemical potential→

$$\mu = \frac{gn}{\sqrt{2\pi}l_z}\left[1 + \frac{4\pi\beta}{3}(3\cos^2\alpha - 1)\right] = \frac{\hbar^2}{2m\xi^2} \tag{E.9}$$

where ξ is the healing length and $\beta = g_d/g$. Now to make the 2D NLGPE dimensionless w.r.t. μ, let us first consider the L.H.S. of the Eq. (E.4)

$$\frac{i\hbar}{\mu}\frac{\partial}{\partial t}\psi = i\frac{\partial\psi}{\partial\tilde{t}} \tag{E.10}$$

Now let us consider the R.H.S.,

The first term→

$$\frac{\hbar^2 k^2}{2m\mu} = \frac{\hbar^2}{2m}\frac{2m\xi^2}{\hbar^2}k^2 = (k\xi)^2 = \tilde{k}^2 \tag{E.11}$$

The second term →

$$
\begin{aligned}
\frac{g[1 + 2\alpha_s\cos(2\omega t)]|\psi|^2}{\sqrt{2\pi}l_z\mu} &= \frac{g|\psi|^2}{\sqrt{2\pi}l_z}\frac{[1 + 2\alpha_s\cos(2\omega t)]}{\dfrac{gn}{\sqrt{2\pi}l_z}\left[1 + \dfrac{4\pi\beta}{3}(3\cos^2\alpha - 1)\right]} \\
&= \frac{|\tilde{\psi}|^2[1 + 2\alpha_s\cos(2\omega t)]}{\tilde{n}\left[1 + \dfrac{4\pi\beta}{3}(3\cos^2\alpha - 1)\right]}
\end{aligned} \tag{E.12}
$$

The third term→

$$
\begin{aligned}
&\frac{2g_d}{3l_z\mu}\int\frac{d^2k}{(2\pi)^2}e^{i(xk_x+yk_y)}f(k_x,k_y)\tilde{n}(k_x,k_y) \\
&= \frac{2g_d}{3\sqrt{2\pi}l_z}\frac{\int\dfrac{d^2k}{(2\pi)^2}e^{i(xk_x+yk_y)}\sqrt{2\pi}f(k_x,k_y)\tilde{n}(k_x,k_y)}{\dfrac{gn}{\sqrt{2\pi}l_z}\left[1 + \dfrac{4\pi\beta}{3}(3\cos^2\alpha - 1)\right]} \\
&= \frac{2\beta}{3}\frac{\int\dfrac{d^2k}{(2\pi)^2}e^{i(xk_x+yk_y)}\sqrt{2\pi}f(k_x,k_y)\tilde{n}(k_x,k_y)}{\tilde{n}\left[1 + \dfrac{4\pi\beta}{3}(3\cos^2\alpha - 1)\right]}
\end{aligned} \tag{E.13}
$$

We expand $f(k_x, k_y) = f_0 + f_1(k_x, k_y)$ into a momentum independent and dependent part respectively, where $f_0 = \sqrt{2\pi}(3\cos^2\alpha - 1)$ and $f_1(k_x, k_y) = 3\pi k e^{\frac{k^2}{2}}\text{Erfc}\left[\frac{k}{\sqrt{2}}\right](\sin^2\alpha\cos^2\theta_k - \cos^2\alpha)$.

$$= \frac{2\beta}{3} \frac{\int \frac{d^2k}{(2\pi)^2} e^{i(xk_x+yk_y)} \sqrt{2\pi}(f_0 + f_1(k_x,k_y))\tilde{n}(k_x,k_y)}{\tilde{n}\left[1 + \frac{4\pi\beta}{3}(3\cos^2\alpha - 1)\right]}$$

$$= \frac{2\beta}{3} \frac{\int \frac{d^2k}{(2\pi)^2} e^{i(xk_x+yk_y)} \sqrt{2\pi}[\sqrt{2\pi}(3\cos^2\alpha - 1) + f_1(k_x,k_y)]\tilde{n}(k_x,k_y)}{\tilde{n}\left[1 + \frac{4\pi\beta}{3}(3\cos^2\alpha - 1)\right]}$$

$$= \frac{4\pi\beta}{3} \frac{(3\cos^2\alpha - 1)\int \frac{d^2k}{(2\pi)^2} e^{i(xk_x+yk_y)}\tilde{n}(k_x,k_y)}{\tilde{n}\left[1 + \frac{4\pi\beta}{3}(3\cos^2\alpha - 1)\right]} + \frac{2\beta}{3} \frac{\int \frac{d^2k}{(2\pi)^2} e^{i(xk_x+yk_y)} \sqrt{2\pi} f_1(k_x,k_y)\tilde{n}(k_x,k_y)}{\tilde{n}\left[1 + \frac{4\pi\beta}{3}(3\cos^2\alpha - 1)\right]}$$

$$= \frac{4\pi\beta}{3} \frac{(3\cos^2\alpha - 1)|\psi|^2}{\tilde{n}\left[1 + \frac{4\pi\beta}{3}(3\cos^2\alpha - 1)\right]} + \frac{2\beta}{3} \frac{\int \frac{d^2k}{(2\pi)^2} e^{i(xk_x+yk_y)} \sqrt{2\pi} f_1(k_x,k_y)\tilde{n}(k_x,k_y)}{\tilde{n}\left[1 + \frac{4\pi\beta}{3}(3\cos^2\alpha - 1)\right]} \tag{E.14}$$

Now writing second and third terms together after simplifying we will obtain,

$$\frac{|\tilde{\psi}|^2[1 + 2\alpha_s\cos(2\omega t) + \frac{4\pi\beta}{3}(3\cos^2\alpha - 1)]}{\tilde{n}\left[1 + \frac{4\pi\beta}{3}(3\cos^2\alpha - 1)\right]} + \frac{2\beta}{3} \frac{\int \frac{d^2k}{(2\pi)^2} e^{i(xk_x+yk_y)} \sqrt{2\pi} f_1(k_x,k_y)\tilde{n}(k_x,k_y)}{\tilde{n}\left[1 + \frac{4\pi\beta}{3}(3\cos^2\alpha - 1)\right]} \tag{E.15}$$

Hence, the dimensionless 2D NLGPE becomes,

$$i\frac{\partial\tilde{\psi}}{\partial\tilde{t}} = \left[\tilde{k}^2 + \frac{|\tilde{\psi}|^2[1 + 2\alpha_s\cos(2\omega t) + \frac{4\pi\beta}{3}(3\cos^2\alpha - 1)]}{\tilde{n}\left[1 + \frac{4\pi\beta}{3}(3\cos^2\alpha - 1)\right]}\right.$$

$$\left. + \frac{2\beta}{3} \frac{\int \frac{d^2k}{(2\pi)^2} e^{i(xk_x+yk_y)} \sqrt{2\pi} f_1(k_x,k_y)\tilde{n}(k_x,k_y)}{\tilde{n}\left[1 + \frac{4\pi\beta}{3}(3\cos^2\alpha - 1)\right]}\right]\tilde{\psi} \tag{E.16}$$

Bibliography

1. Einstein, A. Quantentheorie des einatomigen idealen Gases, zweite Abhandlung. *Berliner Berichte,* 3–14 (1925).

2. Bose, S. N. Plancks Gesetz und Lichtquantenhypothese. *Zeitschrift für Physik* **26,** 178–181 (1924).

3. LANDAU, L. & LIFSHITZ, E. in *Statistical Physics (Third Edition)* (Butterworth-Heinemann, Oxford, 1980). ISBN: 978-0-08-057046-4.

4. Pıétajevskıéj, L., S. Stringari, L., Pitaevskii, L., Stringari, S., Stringari, S. & Press, O. U. *Bose-Einstein Condensation* ISBN: 9780198507192 (Clarendon Press, 2003).

5. Stwalley, W. C. & Nosanow, L. H. Possible "New" Quantum Systems. *Phys. Rev. Lett.* **36,** 910–913 (15 Apr. 1976).

6. Phillips, W. D. Nobel Lecture: Laser cooling and trapping of neutral atoms. *Rev. Mod. Phys.* **70,** 721–741 (3 July 1998).

7. Anderson, M. H., Ensher, J. R., Matthews, M. R., Wieman, C. E. & Cornell, E. A. Observation of Bose-Einstein Condensation in a Dilute Atomic Vapor. *Science* **269,** 198–201. ISSN: 0036-8075 (1995).

8. Davis, K. B., Mewes, M. .-.-O., Andrews, M. R., van Druten, N. J., Durfee, D. S., Kurn, D. M. & Ketterle, W. Bose-Einstein Condensation in a Gas of Sodium Atoms. *Phys. Rev. Lett.* **75,** 3969–3973 (22 Nov. 1995).

9. Bradley, C. C., Sackett, C. A., Tollett, J. J. & Hulet, R. G. Evidence of Bose-Einstein Condensation in an Atomic Gas with Attractive Interactions. *Phys. Rev. Lett.* **75,** 1687–1690 (9 Aug. 1995).

10. Dalfovo, F., Giorgini, S., Pitaevskii, L. P. & Stringari, S. Theory of Bose-Einstein condensation in trapped gases. *Rev. Mod. Phys.* **71,** 463–512 (3 Apr. 1999).

11. Castin, Y. *Bose-Einstein Condensates in Atomic Gases: Simple Theoretical Results* in *Coherent atomic matter waves* (eds Kaiser, R., Westbrook, C. & David, F.) (Springer Berlin Heidelberg, Berlin, Heidelberg, 2001), 1–136. ISBN: 978-3-540-45338-3.

12. Pethick, C. & Smith, H. *Bose-Einstein Condensation in Dilute Gases* ISBN: 9780521665803 (Cambridge University Press, 2002).

13. Weiner, J., Bagnato, V. S., Zilio, S. & Julienne, P. S. Experiments and theory in cold and ultracold collisions. *Rev. Mod. Phys.* **71,** 1–85 (1 Jan. 1999).

14. Huang, K. *Statistical mechanics* ISBN: 9780471815181 (Wiley, 1987).

15. Stwalley, W. C. Stability of Spin-Aligned Hydrogen at Low Temperatures and High Magnetic Fields: New Field-Dependent Scattering Resonances and Predissociations. *Phys. Rev. Lett.* **37,** 1628–1631 (24 Dec. 1976).

16. Roberts, J. L., Claussen, N. R., Burke, J. P., Greene, C. H., Cornell, E. A. & Wieman, C. E. Resonant Magnetic Field Control of Elastic Scattering in Cold ^{85}Rb. *Phys. Rev. Lett.* **81,** 5109–5112 (23 Dec. 1998).

17. Inouye, S., Andrews, M. R., Stenger, J., Miesner, H.-J., Stamper-Kurn, D. M. & Ketterle, W. Observation of Feshbach resonances in a Bose-Einstein condensate. *Nature* **392,** 151–154. ISSN: 1476-4687 (1998).

18. Moerdijk, A. J., Verhaar, B. J. & Axelsson, A. Resonances in ultracold collisions of ^{6}Li, ^{7}Li, and ^{23}Na. *Phys. Rev. A* **51,** 4852–4861 (6 June 1995).

19. Moerdijk, A. J., Verhaar, B. J. & Nagtegaal, T. M. Collisions of dressed ground-state atoms. *Phys. Rev. A* **53,** 4343–4351 (6 June 1996).

20. Marinescu, M. & You, L. Controlling Atom-Atom Interaction at Ultralow Temperatures by dc Electric Fields. *Phys. Rev. Lett.* **81,** 4596–4599 (21 Nov. 1998).

21. Fedichev, P. O., Kagan, Y., Shlyapnikov, G. V. & Walraven, J. T. M. Influence of Nearly Resonant Light on the Scattering Length in Low-Temperature Atomic Gases. *Phys. Rev. Lett.* **77,** 2913–2916 (14 Sept. 1996).

22. Bohn, J. L. & Julienne, P. S. Semianalytic treatment of two-color photoassociation spectroscopy and control of cold atoms. *Phys. Rev. A* **54,** R4637–R4640 (6 Dec. 1996).

23. Enomoto, K., Kasa, K., Kitagawa, M. & Takahashi, Y. Optical Feshbach Resonance Using the Intercombination Transition. *Phys. Rev. Lett.* **101,** 203201 (20 Nov. 2008).

24. Thalhammer, G., Theis, M., Winkler, K., Grimm, R. & Denschlag, J. H. Inducing an optical Feshbach resonance via stimulated Raman coupling. *Phys. Rev. A* **71,** 033403 (3 Mar. 2005).

25. Yan, M., DeSalvo, B. J., Ramachandhran, B., Pu, H. & Killian, T. C. Controlling Condensate Collapse and Expansion with an Optical Feshbach Resonance. *Phys. Rev. Lett.* **110,** 123201 (12 Mar. 2013).

26. Yi, S. & You, L. Trapped atomic condensates with anisotropic interactions. *Phys. Rev. A* **61,** 041604 (4 Mar. 2000).

27. Yi, S. & You, L. Trapped condensates of atoms with dipole interactions. *Phys. Rev. A* **63,** 053607 (5 Apr. 2001).

28. Lahaye, T., Menotti, C., Santos, L., Lewenstein, M. & Pfau, T. The physics of dipolar bosonic quantum gases. *Reports on Progress in Physics* **72,** 126401 (Nov. 2009).

29. Koashi, M. & Ueda, M. Exact Eigenstates and Magnetic Response of Spin-1 and Spin-2 Bose-Einstein Condensates. *Phys. Rev. Lett.* **84,** 1066–1069 (6 Feb. 2000).

30. Vengalattore, M., Leslie, S. R., Guzman, J. & Stamper-Kurn, D. M. Spontaneously Modulated Spin Textures in a Dipolar Spinor Bose-Einstein Condensate. *Phys. Rev. Lett.* **100,** 170403 (17 May 2008).

31. Świsłocki, Brewczyk, M., Gajda, M. & Rzą żewski, Spinor condensate of ^{87}Rb as a dipolar gas. *Phys. Rev. A* **81,** 033604 (3 Mar. 2010).

32. Griesmaier, A., Werner, J., Hensler, S., Stuhler, J. & Pfau, T. Bose-Einstein Condensation of Chromium. *Phys. Rev. Lett.* **94,** 160401 (16 Apr. 2005).

33. Aikawa, K., Frisch, A., Mark, M., Baier, S., Rietzler, A., Grimm, R. & Ferlaino, F. Bose-Einstein Condensation of Erbium. *Phys. Rev. Lett.* **108,** 210401 (21 May 2012).

34. Lu, M., Burdick, N. Q., Youn, S. H. & Lev, B. L. Strongly Dipolar Bose-Einstein Condensate of Dysprosium. *Phys. Rev. Lett.* **107,** 190401 (19 Oct. 2011).

35. Weinstein, J. D., deCarvalho, R., Guillet, T., Friedrich, B. & Doyle, J. M. Magnetic trapping of calcium monohydride molecules at millikelvin temperatures. *Nature* **395,** 148–150. ISSN: 1476-4687 (1998).

36. Doyle, J. M., Friedrich, B., Kim, J. & Patterson, D. Buffer-gas loading of atoms and molecules into a magnetic trap. *Phys. Rev. A* **52,** R2515–R2518 (4 Oct. 1995).

37. Carr, L. D., DeMille, D., Krems, R. V. & Ye, J. Cold and ultracold molecules: science, technology and applications. *New Journal of Physics* **11,** 055049 (May 2009).

38. Vogt, T., Viteau, M., Zhao, J., Chotia, A., Comparat, D. & Pillet, P. Dipole Blockade at Förster Resonances in High Resolution Laser Excitation of Rydberg States of Cesium Atoms. *Phys. Rev. Lett.* **97,** 083003 (8 Aug. 2006).

39. Heidemann, R., Raitzsch, U., Bendkowsky, V., Butscher, B., Löw, R. & Pfau, T. Rydberg Excitation of Bose-Einstein Condensates. *Phys. Rev. Lett.* **100,** 033601 (3 Jan. 2008).

40. Żuchowski, Aldegunde, J. & Hutson, J. M. Ultracold RbSr Molecules Can Be Formed by Magnetoassociation. *Phys. Rev. Lett.* **105,** 153201 (15 Oct. 2010).

41. Barry, J. F., McCarron, D. J., Norrgard, E. B., Steinecker, M. H. & DeMille, D. Magneto-optical trapping of a diatomic molecule. *Nature* **512,** 286– (Aug. 2014).

42. Lepers, M., Li, H., Wyart, J.-F., Quéméner, G. & Dulieu, O. Ultracold Rare-Earth Magnetic Atoms with an Electric Dipole Moment. *Phys. Rev. Lett.* **121,** 063201 (6 Aug. 2018).

43. Chin, C., Grimm, R., Julienne, P. & Tiesinga, E. Feshbach resonances in ultracold gases. *Rev. Mod. Phys.* **82,** 1225–1286 (2 Apr. 2010).

44. Giovanazzi, S., Görlitz, A. & Pfau, T. Tuning the Dipolar Interaction in Quantum Gases. *Phys. Rev. Lett.* **89,** 130401 (13 Sept. 2002).

45. Tang, Y., Kao, W., Li, K.-Y. & Lev, B. L. Tuning the Dipole-Dipole Interaction in a Quantum Gas with a Rotating Magnetic Field. *Phys. Rev. Lett.* **120,** 230401 (23 June 2018).

46. Glaum, K., Pelster, A., Kleinert, H. & Pfau, T. Critical Temperature of Weakly Interacting Dipolar Condensates. *Phys. Rev. Lett.* **98,** 080407 (8 Feb. 2007).

47. Glaum, K. & Pelster, A. Bose-Einstein condensation temperature of dipolar gas in anisotropic harmonic trap. *Phys. Rev. A* **76,** 023604 (2 Aug. 2007).

48. Lahaye, T., Metz, J., Fröhlich, B., Koch, T., Meister, M., Griesmaier, A., Pfau, T., Saito, H., Kawaguchi, Y. & Ueda, M. *d*-Wave Collapse and Explosion of a Dipolar Bose-Einstein Condensate. *Phys. Rev. Lett.* **101,** 080401 (8 Aug. 2008).

49. Cooper, N. R., Rezayi, E. H. & Simon, S. H. Vortex Lattices in Rotating Atomic Bose Gases with Dipolar Interactions. *Phys. Rev. Lett.* **95,** 200402 (20 Nov. 2005).

50. Ho, T.-L. Spinor Bose Condensates in Optical Traps. *Phys. Rev. Lett.* **81,** 742–745 (4 July 1998).

51. Kawaguchi, Y., Saito, H. & Ueda, M. Spontaneous Circulation in Ground-State Spinor Dipolar Bose-Einstein Condensates. *Phys. Rev. Lett.* **97,** 130404 (13 Sept. 2006).

52. Vengalattore, M., Leslie, S. R., Guzman, J. & Stamper-Kurn, D. M. Spontaneously Modulated Spin Textures in a Dipolar Spinor Bose-Einstein Condensate. *Phys. Rev. Lett.* **100,** 170403 (17 May 2008).

53. Kawaguchi, Y., Saito, H. & Ueda, M. Einstein–de Haas Effect in Dipolar Bose-Einstein Condensates. *Phys. Rev. Lett.* **96,** 080405 (8 Mar. 2006).

54. Gawryluk, K., Brewczyk, M., Bongs, K. & Gajda, M. Resonant Einstein–de Haas Effect in a Rubidium Condensate. *Phys. Rev. Lett.* **99,** 130401 (13 Sept. 2007).

55. Fattori, M., D'Errico, C., Roati, G., Zaccanti, M., Jona-Lasinio, M., Modugno, M., Inguscio, M. & Modugno, G. Atom Interferometry with a Weakly Interacting Bose-Einstein Condensate. *Phys. Rev. Lett.* **100,** 080405 (8 Feb. 2008).

56. Van Otterlo, A. & Wagenblast, K.-H. Coexistence of diagonal and off-diagonal long-range order: A Monte Carlo study. *Phys. Rev. Lett.* **72,** 3598–3601 (22 May 1994).

57. Batrouni, G. G., Scalettar, R. T., Zimanyi, G. T. & Kampf, A. P. Supersolids in the Bose-Hubbard Hamiltonian. *Phys. Rev. Lett.* **74,** 2527–2530 (13 Mar. 1995).

58. Dalla Torre, E. G., Berg, E. & Altman, E. Hidden Order in 1D Bose Insulators. *Phys. Rev. Lett.* **97,** 260401 (26 Dec. 2006).

59. Menotti, C., Trefzger, C. & Lewenstein, M. Metastable States of a Gas of Dipolar Bosons in a 2D Optical Lattice. *Phys. Rev. Lett.* **98,** 235301 (23 June 2007).

60. Wang, D.-W., Lukin, M. D. & Demler, E. Quantum Fluids of Self-Assembled Chains of Polar Molecules. *Phys. Rev. Lett.* **97,** 180413 (18 Nov. 2006).

61. Astrakharchik, G. E., Boronat, J., Kurbakov, I. L. & Lozovik, Y. E. Quantum Phase Transition in a Two-Dimensional System of Dipoles. *Phys. Rev. Lett.* **98,** 060405 (6 Feb. 2007).

62. Mora, C., Parcollet, O. & Waintal, X. Quantum melting of a crystal of dipolar bosons. *Phys. Rev. B* **76,** 064511 (6 Aug. 2007).

63. Bloch, I., Dalibard, J. & Zwerger, W. Many-body physics with ultracold gases. *Rev. Mod. Phys.* **80,** 885–964 (3 July 2008).

64. Roudnev, V. & Cavagnero, M. Resonance phenomena in ultracold dipole–dipole scattering. *Journal of Physics B: Atomic, Molecular and Optical Physics* **42,** 044017 (Feb. 2009).

65. Ronen, S., Bortolotti, D. C. E., Blume, D. & Bohn, J. L. Dipolar Bose-Einstein condensates with dipole-dependent scattering length. *Phys. Rev. A* **74,** 033611 (3 Sept. 2006).

66. Wang, D.-W. An effective many-body theory for strongly interacting polar molecules. *New Journal of Physics* **10,** 053005 (May 2008).

67. Mora, C. & Castin, Y. Extension of Bogoliubov theory to quasicondensates. *Phys. Rev. A* **67,** 053615 (5 May 2003).

68. Luxat, D. L. & Griffin, A. Dynamic correlation functions in one-dimensional quasicondensates. *Phys. Rev. A* **67,** 043603 (4 Apr. 2003).

69. Andersen, J. O., Al Khawaja, U. & Stoof, H. T. C. Phase Fluctuations in Atomic Bose Gases. *Phys. Rev. Lett.* **88,** 070407 (7 Feb. 2002).

70. Petrov, D. S., Shlyapnikov, G. V. & Walraven, J. T. M. Regimes of Quantum Degeneracy in Trapped 1D Gases. *Phys. Rev. Lett.* **85,** 3745–3749 (18 Oct. 2000).

71. Görlitz, A. *et al.* Realization of Bose-Einstein Condensates in Lower Dimensions. *Phys. Rev. Lett.* **87,** 130402 (13 Sept. 2001).

72. Cataliotti, F. S., Burger, S., Fort, C., Maddaloni, P., Minardi, F., Trombettoni, A., Smerzi, A. & Inguscio, M. Josephson Junction Arrays with Bose-Einstein Condensates. *Science* **293,** 843–846. ISSN: 0036-8075 (2001).

73. Hänsel, W., Hommelhoff, P., Hänsch, T. W. & Reichel, J. Bose-Einstein condensation on a microelectronic chip. *Nature* **413,** 498–501. ISSN: 1476-4687 (2001).

74. Ott, H., Fortagh, J., Schlotterbeck, G., Grossmann, A. & Zimmermann, C. Bose-Einstein Condensation in a Surface Microtrap. *Phys. Rev. Lett.* **87,** 230401 (23 Nov. 2001).

75. Ticknor, C. Two-dimensional dipolar scattering. *Phys. Rev. A* **80,** 052702 (5 Nov. 2009).

76. Ticknor, C. Quasi-two-dimensional dipolar scattering. *Phys. Rev. A* **81,** 042708 (4 Apr. 2010).

77. Ticknor, C., Wilson, R. M. & Bohn, J. L. Anisotropic Superfluidity in a Dipolar Bose Gas. *Phys. Rev. Lett.* **106,** 065301 (6 Feb. 2011).

78. Santos, L., Shlyapnikov, G. V. & Lewenstein, M. Roton-Maxon Spectrum and Stability of Trapped Dipolar Bose-Einstein Condensates. *Phys. Rev. Lett.* **90,** 250403 (25 June 2003).

79. Sinha, S. & Santos, L. Cold Dipolar Gases in Quasi-One-Dimensional Geometries. *Phys. Rev. Lett.* **99,** 140406 (14 Oct. 2007).

80. Giannakeas, P., Melezhik, V. S. & Schmelcher, P. Dipolar Confinement-Induced Resonances of Ultracold Gases in Waveguides. *Phys. Rev. Lett.* **111,** 183201 (18 Oct. 2013).

81. Kim, J. I., Schmiedmayer, J. & Schmelcher, P. Quantum scattering in quasi-one-dimensional cylindrical confinement. *Phys. Rev. A* **72,** 042711 (4 Oct. 2005).

82. Astrakharchik, G. E. & Lozovik, Y. E. Super-Tonks-Girardeau regime in trapped one-dimensional dipolar gases. *Phys. Rev. A* **77,** 013404 (1 Jan. 2008).

83. Fetter, A. L. & Feder, D. L. Beyond the Thomas-Fermi approximation for a trapped condensed Bose-Einstein gas. *Phys. Rev. A* **58,** 3185–3194 (4 Oct. 1998).

84. Zambelli, F. & Stringari, S. Quantized Vortices and Collective Oscillations of a Trapped Bose-Einstein Condensate. *Phys. Rev. Lett.* **81,** 1754–1757 (9 Aug. 1998).

85. Metz, J. *Collapse of dipolar Bose-Einstein condensates for different trap geometries* PhD thesis (Jan. 2010).

86. O'Dell, D. H. J., Giovanazzi, S. & Eberlein, C. Exact Hydrodynamics of a Trapped Dipolar Bose-Einstein Condensate. *Phys. Rev. Lett.* **92,** 250401 (25 June 2004).

87. Eberlein, C., Giovanazzi, S. & O'Dell, D. H. J. Exact solution of the Thomas-Fermi equation for a trapped Bose-Einstein condensate with dipole-dipole interactions. *Phys. Rev. A* **71,** 033618 (3 Mar. 2005).

88. Parker, N. G. & O'Dell, D. H. J. Thomas-Fermi versus one- and two-dimensional regimes of a trapped dipolar Bose-Einstein condensate. *Phys. Rev. A* **78,** 041601 (4 Oct. 2008).

89. Castin, Y. & Dum, R. Bose-Einstein Condensates in Time Dependent Traps. *Phys. Rev. Lett.* **77,** 5315–5319 (27 Dec. 1996).

90. Giovanazzi, S., Pedri, P., Santos, L., Griesmaier, A., Fattori, M., Koch, T., Stuhler, J. & Pfau, T. Expansion dynamics of a dipolar Bose-Einstein condensate. *Phys. Rev. A* **74,** 013621 (1 July 2006).

91. Strecker, K. E., Partridge, G. B., Truscott, A. G. & Hulet, R. G. Bright matter wave solitons in Bose–Einstein condensates. *New Journal of Physics* **5,** 73–73 (June 2003).

92. Frantzeskakis, D. J. Dark solitons in atomic Bose–Einstein condensates: from theory to experiments. *Journal of Physics A: Mathematical and Theoretical* **43,** 213001 (May 2010).

93. Strecker, K. E., Partridge, G. B., Truscott, A. G. & Hulet, R. G. Formation and propagation of matter-wave soliton trains. *Nature* **417,** 150–153. ISSN: 1476-4687 (2002).

94. Khaykovich, L., Schreck, F., Ferrari, G., Bourdel, T., Cubizolles, J., Carr, L. D., Castin, Y. & Salomon, C. Formation of a Matter-Wave Bright Soliton. *Science* **296,** 1290–1293. ISSN: 0036-8075 (2002).

95. Pedri, P. & Santos, L. Two-Dimensional Bright Solitons in Dipolar Bose-Einstein Condensates. *Phys. Rev. Lett.* **95,** 200404 (20 Nov. 2005).

96. Tikhonenkov, I., Malomed, B. A. & Vardi, A. Anisotropic Solitons in Dipolar Bose-Einstein Condensates. *Phys. Rev. Lett.* **100,** 090406 (9 Mar. 2008).

97. Krolikowski, W., Bang, O., Rasmussen, J. J. & Wyller, J. Modulational instability in nonlocal nonlinear Kerr media. *Phys. Rev. E* **64,** 016612 (1 June 2001).

98. Burger, S., Bongs, K., Dettmer, S., Ertmer, W., Sengstock, K., Sanpera, A., Shlyapnikov, G. V. & Lewenstein, M. Dark Solitons in Bose-Einstein Condensates. *Phys. Rev. Lett.* **83,** 5198–5201 (25 Dec. 1999).

99. Denschlag, J. *et al.* Generating Solitons by Phase Engineering of a Bose-Einstein Condensate. *Science* **287,** 97–101. ISSN: 0036-8075 (2000).

100. Becker, C., Stellmer, S., Soltan-Panahi, P., Dörscher, S., Baumert, M., Richter, E.-M., Kronjäger, J., Bongs, K. & Sengstock, K. Oscillations and interactions of dark and dark-bright solitons in Bose-Einstein condensates. *Nature Physics* **4,** 496–501. ISSN: 1745-2481 (2008).

101. Brand, J. & Reinhardt, W. P. Solitonic vortices and the fundamental modes of the "snake instability": Possibility of observation in the gaseous Bose-Einstein condensate. *Phys. Rev. A* **65,** 043612 (4 Apr. 2002).

102. Ronen, S., Bortolotti, D. C. E. & Bohn, J. L. Radial and Angular Rotons in Trapped Dipolar Gases. *Phys. Rev. Lett.* **98,** 030406 (3 Jan. 2007).

103. Lee, T. D., Huang, K. & Yang, C. N. Eigenvalues and Eigenfunctions of a Bose System of Hard Spheres and Its Low-Temperature Properties. *Phys. Rev.* **106,** 1135–1145 (6 June 1957).

104. Xu, K., Liu, Y., Miller, D. E., Chin, J. K., Setiawan, W. & Ketterle, W. Observation of Strong Quantum Depletion in a Gaseous Bose-Einstein Condensate. *Phys. Rev. Lett.* **96,** 180405 (18 May 2006).

105. Papp, S. B., Pino, J. M., Wild, R. J., Ronen, S., Wieman, C. E., Jin, D. S. & Cornell, E. A. Bragg Spectroscopy of a Strongly Interacting ^{85}Rb Bose-Einstein Condensate. *Phys. Rev. Lett.* **101,** 135301 (13 Sept. 2008).

106. Altmeyer, A., Riedl, S., Kohstall, C., Wright, M. J., Geursen, R., Bartenstein, M., Chin, C., Denschlag, J. H. & Grimm, R. Precision Measurements of Collective Oscillations in the BEC-BCS Crossover. *Phys. Rev. Lett.* **98,** 040401 (4 Jan. 2007).

107. Chomaz, L., Baier, S., Petter, D., Mark, M. J., Wächtler, F., Santos, L. & Ferlaino, F. Quantum-Fluctuation-Driven Crossover from a Dilute Bose-Einstein Condensate to a Macrodroplet in a Dipolar Quantum Fluid. *Phys. Rev. X* **6,** 041039 (4 Nov. 2016).

108. Ferrier-Barbut, I., Kadau, H., Schmitt, M., Wenzel, M. & Pfau, T. Observation of Quantum Droplets in a Strongly Dipolar Bose Gas. *Phys. Rev. Lett.* **116,** 215301 (21 May 2016).

109. Lima, A. R. P. & Pelster, A. Beyond mean-field low-lying excitations of dipolar Bose gases. *Phys. Rev. A* **86,** 063609 (6 Dec. 2012).

110. Wächtler, F. & Santos, L. Quantum filaments in dipolar Bose-Einstein condensates. *Phys. Rev. A* **93,** 061603 (6 June 2016).

111. Edler, D., Mishra, C., Wächtler, F., Nath, R., Sinha, S. & Santos, L. Quantum Fluctuations in Quasi-One-Dimensional Dipolar Bose-Einstein Condensates. *Phys. Rev. Lett.* **119,** 050403 (5 Aug. 2017).

112. Bogolyubov, N. N. On the theory of superfluidity. *J. Phys.(USSR)* **11.** [Izv. Akad. Nauk Ser. Fiz.11,77(1947)], 23–32 (1947).

113. Ozeri, R., Katz, N., Steinhauer, J. & Davidson, N. Colloquium: Bulk Bogoliubov excitations in a Bose-Einstein condensate. *Rev. Mod. Phys.* **77,** 187–205 (1 Apr. 2005).

114. Feynman, R. P. Atomic Theory of the Two-Fluid Model of Liquid Helium. *Phys. Rev.* **94,** 262–277 (2 Apr. 1954).

115. Müller, S. *Stability and collapse dynamics of dipolar Bose-Einstein condensates in one-dimensional optical lattices* PhD thesis (Jan. 2013).

116. Landau, L. Theory of the Superfluidity of Helium II. *Phys. Rev.* **60,** 356–358 (4 Aug. 1941).

117. Klawunn, M. & Santos, L. Hybrid multisite excitations in dipolar condensates in optical lattices. *Phys. Rev. A* **80,** 013611 (1 July 2009).

118. Giovanazzi, S. & O'Dell, D. H. J. Instabilities and the roton spectrum of a quasi-1D Bose-Einstein condensed gas with dipole-dipole interactions. *The European Physical Journal D - Atomic, Molecular, Optical and Plasma Physics* **31,** 439–445. ISSN: 1434-6079 (Nov. 2004).

119. Nath, R. & Santos, L. Faraday patterns in two-dimensional dipolar Bose-Einstein condensates. *Phys. Rev. A* **81,** 033626 (3 Mar. 2010).

120. Wilson, R. M., Ronen, S. & Bohn, J. L. Critical Superfluid Velocity in a Trapped Dipolar Gas. *Phys. Rev. Lett.* **104,** 094501 (9 Mar. 2010).

121. Werner, F. & Castin, Y. Unitary gas in an isotropic harmonic trap: Symmetry properties and applications. *Phys. Rev. A* **74,** 053604 (5 Nov. 2006).

122. Wilson, R. M., Ronen, S. & Bohn, J. L. Angular collapse of dipolar Bose-Einstein condensates. *Phys. Rev. A* **80,** 023614 (2 Aug. 2009).

123. Komineas, S. & Cooper, N. R. Vortex lattices in Bose-Einstein condensates with dipolar interactions beyond the weak-interaction limit. *Phys. Rev. A* **75,** 023623 (2 Feb. 2007).

124. Fetter, A. L. & Rokhsar, D. Excited states of a dilute Bose-Einstein condensate in a harmonic trap. *Phys. Rev. A* **57,** 1191–1201 (2 Feb. 1998).

125. Kimura, T., Saito, H. & Ueda, M. A Variational Sum-Rule Approach to Collective Excitations of a Trapped Bose-Einstein Condensate. *Journal of the Physical Society of Japan* **68,** 1477–1480 (1999).

126. Pérez-Garcíéa, V. M., Michinel, H., Cirac, J. I., Lewenstein, M. & Zoller, P. Low Energy Excitations of a Bose-Einstein Condensate: A Time-Dependent Variational Analysis. *Phys. Rev. Lett.* **77,** 5320–5323 (27 Dec. 1996).

127. Pérez-Garcíéa, V. M., Michinel, H., Cirac, J. I., Lewenstein, M. & Zoller, P. Dynamics of Bose-Einstein condensates: Variational solutions of the Gross-Pitaevskii equations. *Phys. Rev. A* **56,** 1424–1432 (2 Aug. 1997).

128. Góral, K. & Santos, L. Ground state and elementary excitations of single and binary Bose-Einstein condensates of trapped dipolar gases. *Phys. Rev. A* **66,** 023613 (2 Aug. 2002).

129. Bergeman, T. Hartree-Fock calculations of Bose-Einstein condensation of ^{7}Li atoms in a harmonic trap for $T > 0$. *Phys. Rev. A* **55,** 3658–3669 (5 May 1997).

130. Singh, K. G. & Rokhsar, D. S. Collective Excitations of a Confined Bose Condensate. *Phys. Rev. Lett.* **77,** 1667–1670 (9 Aug. 1996).

131. Stringari, S. Phase Diagram of Quantized Vortices in a Trapped Bose-Einstein Condensed Gas. *Phys. Rev. Lett.* **82,** 4371–4375 (22 May 1999).

132. Hess, G. B. & Fairbank, W. M. Measurements of Angular Momentum in Superfluid Helium. *Phys. Rev. Lett.* **19,** 216–218 (5 July 1967).

133. Stringari, S. Moment of Inertia and Superfluidity of a Trapped Bose Gas. *Phys. Rev. Lett.* **76,** 1405–1408 (9 Feb. 1996).

134. Iudice, N. L. & Palumbo, F. New Isovector Collective Modes in Deformed Nuclei. *Phys. Rev. Lett.* **41,** 1532–1534 (22 Nov. 1978).

135. Morsch, O. & Oberthaler, M. Dynamics of Bose-Einstein condensates in optical lattices. *Rev. Mod. Phys.* **78,** 179–215 (1 Feb. 2006).

136. Lignier, H., Sias, C., Ciampini, D., Singh, Y., Zenesini, A., Morsch, O. & Arimondo, E. Dynamical Control of Matter-Wave Tunneling in Periodic Potentials. *Phys. Rev. Lett.* **99,** 220403 (22 Nov. 2007).

137. Wang, G.-F., Fu, L.-B. & Liu, J. Periodic modulation effect on self-trapping of two weakly coupled Bose-Einstein condensates. *Phys. Rev. A* **73,** 013619 (1 Jan. 2006).

138. Saito, H. & Ueda, M. Dynamically Stabilized Bright Solitons in a Two-Dimensional Bose-Einstein Condensate. *Phys. Rev. Lett.* **90,** 040403 (4 Jan. 2003).

139. Belmonte-Beitia, J., Pérez-Garcíéa, V. M., Vekslerchik, V. & Konotop, V. V. Localized Nonlinear Waves in Systems with Time- and Space-Modulated Nonlinearities. *Phys. Rev. Lett.* **100,** 164102 (16 Apr. 2008).

140. Keolian, R., Turkevich, L. A., Putterman, S. J., Rudnick, I. & Rudnick, J. A. Subharmonic Sequences in the Faraday Experiment: Departures from Period Doubling. *Phys. Rev. Lett.* **47,** 1133–1136 (16 Oct. 1981).

141. Ciliberto, S. & Gollub, J. P. Pattern Competition Leads to Chaos. *Phys. Rev. Lett.* **52,** 922–925 (11 Mar. 1984).

142. Faraday, M. XVII. On a peculiar class of acoustical figures; and on certain forms assumed by groups of particles upon vibrating elastic surfaces. *Philosophical Transactions of the Royal Society of London* **121,** 299–340 (1831).

143. Staliunas, K., Longhi, S. & de Valcárcel, G. J. Faraday Patterns in Bose-Einstein Condensates. *Phys. Rev. Lett.* **89,** 210406 (21 Nov. 2002).

144. Abe, H., Ueda, T., Morikawa, M., Saitoh, Y., Nomura, R. & Okuda, Y. Faraday instability of superfluid surface. *Phys. Rev. E* **76,** 046305 (4 Oct. 2007).

145. Engels, P., Atherton, C. & Hoefer, M. A. Observation of Faraday Waves in a Bose-Einstein Condensate. *Phys. Rev. Lett.* **98,** 095301 (9 Feb. 2007).

146. Clark, L. W., Gaj, A., Feng, L. & Chin, C. Collective emission of matter-wave jets from driven Bose-Einstein condensates. *Nature* **551,** 356– (Nov. 2017).

147. Nguyen, J. H. V., Tsatsos, M. C., Luo, D., Lode, A. U. J., Telles, G. D., Bagnato, V. S. & Hulet, R. G. Parametric Excitation of a Bose-Einstein Condensate: From Faraday Waves to Granulation. *Phys. Rev. X* **9,** 011052 (1 Mar. 2019).

148. Nicolin, A. I., Jensen, M. H. & Carretero-González, R. Mode locking of a driven Bose-Einstein condensate. *Phys. Rev. E* **75,** 036208 (3 Mar. 2007).

149. Batalov, S. V., Shagalov, A. G. & Friedland, L. Autoresonant excitation of Bose-Einstein condensates. *Phys. Rev. E* **97,** 032210 (3 Mar. 2018).

150. Friedland, L. Control of Kirchhoff vortices by a resonant strain. *Phys. Rev. E* **59,** 4106–4111 (4 Apr. 1999).

151. Assaf, M. & Meerson, B. Parametric autoresonance in Faraday waves. *Phys. Rev. E* **72,** 016310 (1 July 2005).

152. Barak, A., Lamhot, Y., Friedland, L. & Segev, M. Autoresonant Dynamics of Optical Guided Waves. *Phys. Rev. Lett.* **103,** 123901 (12 Sept. 2009).

153. Fajans, J., Gilson, E. & Friedland, L. Autoresonant (Nonstationary) Excitation of the Diocotron Mode in Non-neutral Plasmas. *Phys. Rev. Lett.* **82,** 4444–4447 (22 May 1999).

154. Marcus, G., Friedland, L. & Zigler, A. From quantum ladder climbing to classical autoresonance. *Phys. Rev. A* **69,** 013407 (1 Jan. 2004).

155. Raghunandan, M., Mishra, C., Łakomy, K., Pedri, P., Santos, L. & Nath, R. Two-dimensional bright solitons in dipolar Bose-Einstein condensates with tilted dipoles. *Phys. Rev. A* **92,** 013637 (1 July 2015).

156. Mishra, C. & Nath, R. Dipolar condensates with tilted dipoles in a pancake-shaped confinement. *Phys. Rev. A* **94,** 033633 (3 Sept. 2016).

157. Santos, L., Shlyapnikov, G. V., Zoller, P. & Lewenstein, M. Bose-Einstein Condensation in Trapped Dipolar Gases. *Phys. Rev. Lett.* **85,** 1791–1794 (9 Aug. 2000).

158. Wu, Z., Block, J. K. & Bruun, G. M. Liquid crystal phases of two-dimensional dipolar gases and Berezinskii-Kosterlitz-Thouless melting. *Scientific Reports* **6,** 19038. ISSN: 2045-2322 (2016).

159. Macia, A., Hufnagl, D., Mazzanti, F., Boronat, J. & Zillich, R. E. Excitations and Stripe Phase Formation in a Two-Dimensional Dipolar Bose Gas with Tilted Polarization. *Phys. Rev. Lett.* **109,** 235307 (23 Dec. 2012).

160. Bismut, G., Laburthe-Tolra, B., Maréchal, E., Pedri, P., Gorceix, O. & Vernac, L. Anisotropic Excitation Spectrum of a Dipolar Quantum Bose Gas. *Phys. Rev. Lett.* **109,** 155302 (15 Oct. 2012).

161. Ticknor, C., Wilson, R. M. & Bohn, J. L. Anisotropic Superfluidity in a Dipolar Bose Gas. *Phys. Rev. Lett.* **106,** 065301 (6 Feb. 2011).

162. Nath, R., Pedri, P. & Santos, L. Phonon Instability with Respect to Soliton Formation in Two-Dimensional Dipolar Bose-Einstein Condensates. *Phys. Rev. Lett.* **102,** 050401 (5 Feb. 2009).

163. Bruun, G. M. & Taylor, E. Quantum Phases of a Two-Dimensional Dipolar Fermi Gas. *Phys. Rev. Lett.* **101,** 245301 (24 Dec. 2008).

164. Fischer, U. R. Stability of quasi-two-dimensional Bose-Einstein condensates with dominant dipole-dipole interactions. *Phys. Rev. A* **73,** 031602 (3 Mar. 2006).

165. Cornish, S. L., Thompson, S. T. & Wieman, C. E. Formation of Bright Matter-Wave Solitons during the Collapse of Attractive Bose-Einstein Condensates. *Phys. Rev. Lett.* **96,** 170401 (17 May 2006).

166. Lima, A. R. P. & Pelster, A. Quantum fluctuations in dipolar Bose gases. *Phys. Rev. A* **84,** 041604 (4 Oct. 2011).

167. Bisset, R. N., Wilson, R. M., Baillie, D. & Blakie, P. B. Ground-state phase diagram of a dipolar condensate with quantum fluctuations. *Phys. Rev. A* **94,** 033619 (3 Sept. 2016).

168. Band, Y. B., Malomed, B. & Trippenbach, M. Adiabaticity in nonlinear quantum dynamics: Bose-Einstein condensate in a time-varying box. *Phys. Rev. A* **65,** 033607 (3 Feb. 2002).

169. Pu, H., Maenner, P., Zhang, W. & Ling, H. Y. Adiabatic Condition for Nonlinear Systems. *Phys. Rev. Lett.* **98,** 050406 (5 Feb. 2007).

170. Rugar, D. & Grütter, P. Mechanical parametric amplification and thermomechanical noise squeezing. *Phys. Rev. Lett.* **67,** 699–702 (6 Aug. 1991).

171. Yurke, B. Use of cavities in squeezed-state generation. *Phys. Rev. A* **29,** 408–410 (1 Jan. 1984).

172. Caves, C. M. Quantum-mechanical noise in an interferometer. *Phys. Rev. D* **23,** 1693–1708 (8 Apr. 1981).

173. Furusawa, A., Sørensen, J. L., Braunstein, S. L., Fuchs, C. A., Kimble, H. J. & Polzik, E. S. Unconditional Quantum Teleportation. *Science* **282,** 706–709. ISSN: 0036-8075 (1998).

174. Ralph, T. C. Continuous variable quantum cryptography. *Phys. Rev. A* **61,** 010303 (1 Dec. 1999).

175. Mewes, M.-O., Andrews, M. R., van Druten, N. J., Kurn, D. M., Durfee, D. S., Townsend, C. G. & Ketterle, W. Collective Excitations of a Bose-Einstein Condensate in a Magnetic Trap. *Phys. Rev. Lett.* **77,** 988–991 (6 Aug. 1996).

176. Jin, D. S., Ensher, J. R., Matthews, M. R., Wieman, C. E. & Cornell, E. A. Collective Excitations of a Bose-Einstein Condensate in a Dilute Gas. *Phys. Rev. Lett.* **77,** 420–423 (3 July 1996).

177. Pollack, S. E., Dries, D., Hulet, R. G., Magalhães, K. M. F., Henn, E. A. L., Ramos, E. R. F., Caracanhas, M. A. & Bagnato, V. S. Collective excitation of a Bose-Einstein condensate by modulation of the atomic scattering length. *Phys. Rev. A* **81,** 053627 (5 May 2010).

178. Yukalov, V. I., Novikov, A. N. & Bagnato, V. S. Formation of granular structures in trapped Bose–Einstein condensates under oscillatory excitations. *Laser Physics Letters* **11,** 095501 (July 2014).

179. Eckardt, A., Jinasundera, T., Weiss, C. & Holthaus, M. Analog of Photon-Assisted Tunneling in a Bose-Einstein Condensate. *Phys. Rev. Lett.* **95,** 200401 (20 Nov. 2005).

180. Abdullaev, F. K., Kamchatnov, A. M., Konotop, V. V. & Brazhnyi, V. A. Adiabatic Dynamics of Periodic Waves in Bose-Einstein Condensates with Time Dependent Atomic Scattering Length. *Phys. Rev. Lett.* **90,** 230402 (23 June 2003).

181. Nguyen, J. H. V., Tsatsos, M. C., Luo, D., Lode, A. U. J., Telles, G. D., Bagnato, V. S. & Hulet, R. G. Parametric Excitation of a Bose-Einstein Condensate: From Faraday Waves to Granulation. *Phys. Rev. X* **9,** 011052 (1 Mar. 2019).

182. Saito, H. & Ueda, M. Dynamically Stabilized Bright Solitons in a Two-Dimensional Bose-Einstein Condensate. *Phys. Rev. Lett.* **90,** 040403 (4 Jan. 2003).

183. Nath, R. & Santos, L. Faraday patterns in two-dimensional dipolar Bose-Einstein condensates. *Phys. Rev. A* **81,** 033626 (3 Mar. 2010).

184. Kasamatsu, K. & Tsubota, M. Modulation instability and solitary-wave formation in two-component Bose-Einstein condensates. *Phys. Rev. A* **74,** 013617 (1 July 2006).

185. Sabari, S., Jisha, C. P., Porsezian, K. & Brazhnyi, V. A. Dynamical stability of dipolar Bose-Einstein condensates with temporal modulation of the *s*-wave scattering length. *Phys. Rev. E* **92,** 032905 (3 Sept. 2015).

186. Staliunas, K., Longhi, S. & de Valcárcel, G. J. Faraday Patterns in Bose-Einstein Condensates. *Phys. Rev. Lett.* **89,** 210406 (21 Nov. 2002).

187. Nicolin, A. I., Carretero-González, R. & Kevrekidis, P. G. Faraday waves in Bose-Einstein condensates. *Phys. Rev. A* **76,** 063609 (6 Dec. 2007).

188. Edwards, M., Ruprecht, P. A., Burnett, K., Dodd, R. J. & Clark, C. W. Collective Excitations of Atomic Bose-Einstein Condensates. *Phys. Rev. Lett.* **77,** 1671–1674 (9 Aug. 1996).

189. Łakomy, K., Nath, R. & Santos, L. Faraday patterns in coupled one-dimensional dipolar condensates. *Phys. Rev. A* **86,** 023620 (2 Aug. 2012).

190. Christiansen, B., Alstro?m, P. & Levinsen, M. T. Ordered capillary-wave states: Quasicrystals, hexagons, and radial waves. *Phys. Rev. Lett.* **68,** 2157–2160 (14 Apr. 1992).

191. Douady, S. & Fauve, S. Pattern Selection in Faraday Instability. *Europhysics Letters (EPL)* **6,** 221–226 (June 1988).

192. Rajchenbach, J., Clamond, D. & Leroux, A. Observation of Star-Shaped Surface Gravity Waves. *Phys. Rev. Lett.* **110,** 094502 (9 Feb. 2013).

193. Yamazaki, R., Taie, S., Sugawa, S. & Takahashi, Y. Submicron Spatial Modulation of an Interatomic Interaction in a Bose-Einstein Condensate. *Phys. Rev. Lett.* **105,** 050405 (5 July 2010).

194. Calvanese Strinati, M., Bello, L., Pe'er, A. & Dalla Torre, E. G. Theory of coupled parametric oscillators beyond coupled Ising spins. *Phys. Rev. A* **100,** 023835 (2 Aug. 2019).

195. Fajans, J. & Frièdland, L. Autoresonant (nonstationary) excitation of pendulums, Plutinos, plasmas, and other nonlinear oscillators. *American Journal of Physics* **69,** 1096–1102 (2001).

196. Gallemi, A., Guilleumas, M., Mayol, R. & Pi, M. Propagation of collective modes in non-overlapping dipolar Bose-Einstein Condensates. *Journal of Physics: Conference Series* **497,** 012035 (Apr. 2014).

197. Matveeva, N., Recati, A. & Stringari, S. Dipolar drag in bilayer harmonically trapped gases. *The European Physical Journal D* **65,** 219–222. ISSN: 1434-6079 (2011).

198. Huang, C.-C. & Wu, W.-C. Center motions of nonoverlapping condensates coupled by long-range dipolar interaction in bilayer and multilayer stacks. *Phys. Rev. A* **82,** 053612 (5 Nov. 2010).

199. Mishra, C., Santos, L. & Nath, R. Self-Bound Doubly Dipolar Bose-Einstein Condensates. *Phys. Rev. Lett.* **124,** 073402 (7 Feb. 2020).

200. Carr, L. D., DeMille, D., Krems, R. V. & Ye, J. Cold and ultracold molecules: science, technology and applications. *New Journal of Physics* **11,** 055049 (May 2009).

201. Baranov, M. A., Dalmonte, M., Pupillo, G. & Zoller, P. Condensed Matter Theory of Dipolar Quantum Gases. *Chemical Reviews* **112.** PMID: 22877362, 5012–5061 (2012).

202. Abrahamsson, E., Tscherbul, T. V. & Krems, R. V. Inelastic collisions of cold polar molecules in nonparallel electric and magnetic fields. *The Journal of Chemical Physics* **127,** 044302 (2007).

203. Rvachov, T. M., Son, H., Sommer, A. T., Ebadi, S., Park, J. J., Zwierlein, M. W., Ketterle, W. & Jamison, A. O. Long-Lived Ultracold Molecules with Electric and Magnetic Dipole Moments. *Phys. Rev. Lett.* **119,** 143001 (14 Oct. 2017).

204. Parker, N. G. & O'Dell, D. H. J. Thomas-Fermi versus one- and two-dimensional regimes of a trapped dipolar Bose-Einstein condensate. *Phys. Rev. A* **78,** 041601 (4 Oct. 2008).

205. Maier, T., Ferrier-Barbut, I., Kadau, H., Schmitt, M., Wenzel, M., Wink, C., Pfau, T., Jachymski, K. & Julienne, P. S. Broad universal Feshbach resonances in the chaotic spectrum of dysprosium atoms. *Phys. Rev. A* **92,** 060702 (6 Dec. 2015).

206. Ni, K.-K., Ospelkaus, S., Wang, D., Quéméner, G., Neyenhuis, B., de Miranda, M. H. G., Bohn, J. L., Ye, J. & Jin, D. S. Dipolar collisions of polar molecules in the quantum regime. *Nature* **464,** 1324–1328. ISSN: 1476-4687 (2010).

207. Wächtler, F. & Santos, L. Ground-state properties and elementary excitations of quantum droplets in dipolar Bose-Einstein condensates. *Phys. Rev. A* **94,** 043618 (4 Oct. 2016).

208. Saito, H. Path-Integral Monte Carlo Study on a Droplet of a Dipolar Bose–Einstein Condensate Stabilized by Quantum Fluctuation. *Journal of the Physical Society of Japan* **85,** 053001 (2016).

209. Kadau, H., Schmitt, M., Wenzel, M., Wink, C., Maier, T., Ferrier-Barbut, I. & Pfau, T. Observing the Rosensweig instability of a quantum ferrofluid. *Nature* **530,** 194–197. ISSN: 1476-4687 (2016).

210. Roccuzzo, S. M. & Ancilotto, F. Supersolid behavior of a dipolar Bose-Einstein condensate confined in a tube. *Phys. Rev. A* **99,** 041601 (4 Apr. 2019).

211. Böttcher, F., Schmidt, J.-N., Wenzel, M., Hertkorn, J., Guo, M., Langen, T. & Pfau, T. Transient Supersolid Properties in an Array of Dipolar Quantum Droplets. *Phys. Rev. X* **9,** 011051 (1 Mar. 2019).

212. Guo, M., Böttcher, F., Hertkorn, J., Schmidt, J.-N., Wenzel, M., Büchler, H. P., Langen, T. & Pfau, T. The low-energy Goldstone mode in a trapped dipolar supersolid. *Nature* **574,** 386–389. ISSN: 1476-4687 (2019).

213. Ilzhöfer, P., Sohmen, M., Durastante, G., Politi, C., Trautmann, A., Morpurgo, G., Giamarchi, T., Chomaz, L., Mark, M. J. & Ferlaino, F. Phase coherence in out-of-equilibrium supersolid states of ultracold dipolar atoms. *arXiv e-prints,* arXiv:1912.10892 (Dec. 2019).

214. Natale, G., van Bijnen, R. M. W., Patscheider, A., Petter, D., Mark, M. J., Chomaz, L. & Ferlaino, F. Excitation Spectrum of a Trapped Dipolar Supersolid and Its Experimental Evidence. *Phys. Rev. Lett.* **123,** 050402 (5 Aug. 2019).

215. Tanzi, L., Roccuzzo, S. M., Lucioni, E., Famà, F., Fioretti, A., Gabbanini, C., Modugno, G., Recati, A. & Stringari, S. Supersolid symmetry breaking from compressional oscillations in a dipolar quantum gas. *Nature* **574,** 382–385. ISSN: 1476-4687 (2019).

216. Schmitt, M., Wenzel, M., Böttcher, F., Ferrier-Barbut, I. & Pfau, T. Self-bound droplets of a dilute magnetic quantum liquid. *Nature* **539,** 259–262. ISSN: 1476-4687 (2016).

217. Ferrier-Barbut, I., Wenzel, M., Böttcher, F., Langen, T., Isoard, M., Stringari, S. & Pfau, T. Scissors Mode of Dipolar Quantum Droplets of Dysprosium Atoms. *Phys. Rev. Lett.* **120,** 160402 (16 Apr. 2018).